Micromechanical failure in fiber-reinforced composites

Ashouri Vajari, Danial

Publication date:
2014

Document Version
Publisher's PDF, also known as Version of record

Micromechanical failure in fiber-reinforced composites

PhD Thesis

$$(EIv'')'' = q - \rho A\ddot{v}$$

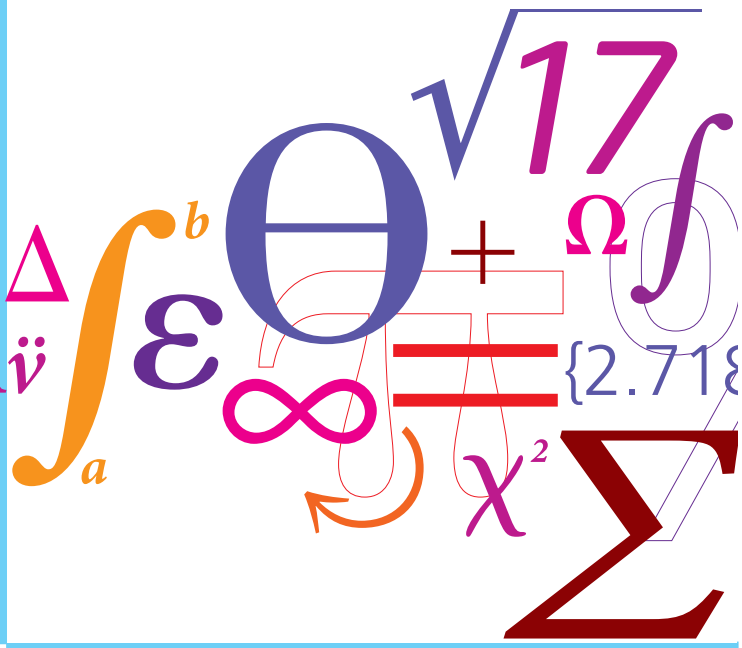

Danial Ashouri Vajari
DCAMM Special Report No. S164
March 2014

DTU Mechanical Engineering
Department of Mechanical Engineering

Micromechanical failure in fiber-reinforced composites

by

Danial Ashouri Vajari

DEPT. OF MECHANICAL ENGINEERING
Solid Mechanics

TECHNICAL UNIVERSITY OF DENMARK

Title of the thesis:
Micromechanical failure in fiber-reinforced composites

Ph.D. student:
Danial Ashouri Vajari
E-mail: dvaj@mek.dtu.dk

Supervisors:
Brian Nyvang Legarth
E-mail: bnl@mek.dtu.dk

Bent F. Sørensen
E-mail: bsqr@dtu.dk

Christian F. Niordson
E-mail: cn@mek.dtu.dk

Christian Berggreen
E-mail: cbe@mek.dtu.dk

Address:
Department of Mechanical Engineering, Solid Mechanics
Technical University of Denmark
Nils Koppels Allé, Building 404, 2800 Kgs. Lyngby, Denmark

Preface

This thesis is submitted in partial fulfillment of the requirements for obtaining the degree of Ph.D. in mechanical engineering at the Technical University of Denmark (DTU). The Ph.D. project was funded by the Danish Council for Strategic Research (grant no.: 09-067212) under the Danish Center for Composite Structures and Materials for Wind Turbines (DCCSM) and carried out at the Department of Mechanical Engineering, Solid Mechanics, and the Department of Wind Energy at DTU in the period April 1st 2011 - March 31st 2014. Supervisors on the project were Associate Professor Ph.D. Brian Nyvang Legarth, Associate Professor Ph.D. Christian F. Niordson and Associate Professor Ph.D. Christian Berggreen from the Mechanical Engineering Department and Professor Dr.techn. Bent F. Sørensen from the Department of Wind Energy, section of Composites and Materials Mechanics.

I am very grateful to my supervisors for their inspiring support and for always taking their time to discuss the work and the results during the project. I would also like to thank Professor Javier Llorca and Dr. Carlos González who were hosting me at IMDEA Materials Institute, Madrid, Spain, during my PhD external stay in the period October 2013- January 2014, for our beneficial collaboration.

I would like to thank the colleagues from the Department of Wind Energy at Risø campus: Johannes S. Bang, Tom L. Andersen, Christen M. Markussen, Jonas K. Heininge, Erik Vogeley and Christian H. Madsen for the successful collaboration and for their assistance in the experimental part of my study.

I am also thankful to my colleagues in the section of Solid Mechanics and in particular the other phd-students for creating a cheerful and inspiring working environment.

Finally, I wish to express my deepest gratitude to my lovely wife, Masoomeh, for all her support and understanding during my PhD and my best teachers, my mother and my father.

Kgs. Lyngby, March 31st 2014.

Danial Ashouri Vajari

Resumé

Mikromekaniske brudmekanismer, som forekommer i fiberforstærkede kompositmaterialer, er undersøgt ved hjælp af finite element metoden og eksperimentelt. Analyserne fokuserer på effekten af mikro-skala mekanismer såsom delaminering af fiber/matrix interface, revner i matrix-materialet og mikroporøsiteter og deres indflydelse på det mikroskopiske og makroskopiske mekaniske respons af kompositmaterialer. Til dette formål er der ved hjælp af kohæsiv zone modellering først udført en numerisk analyse for at undersøge mulighederne for at stabilisere revnevækst i interfacet under dominerende Mode-I brud. Som resultat af dette, fremsættes forslag til en metode til at bestemme egenskaber i normalretningen til interfacet. For at evaluere effekten af mikro-skala mekanismerne på den samlede spændings-/tøjningsrespons i kompositter, etableres to forskellige numeriske metoder: (I) ensartet fiberfordeling og (II) vilkårlig fiberfordeling. I den første fremgangsmåde, er J2 plasticitetsteori implementeret, for at modellere den elasto-plastiske opførsel af matrix-materialet, mens den modificerede Drucker-Prager plasticitetsmodel anvendes i den anden strategi for at modellere den tilnærmelsesvis skøre og trykafhængige opførsel af epoxy. Desuden er skadeslocus for den kompositmaterialet bestemt ved hjælp af numerisk mikromekanik under forskellige belastningsforhold og sammenlignet med Puck's model. Resultaterne er i meget god overensstemmelse med Puck's model for forskellige svigtmekanismer. For direkte at validere den numeriske mikrostrukturelle tilgang blev de numeriske resultater sammenlignet med eksperimentelle forsøg. Det blev konstateret, at den mikromekaniske model kan nøjagtigt forudsige revnedannelse som udspringer fra mikroporøsiteter samt revneudbredelse langs et fiber/matrix interface. Resultaterne af denne afhandling viser, at styrken af kompositmaterialer reduceres betydeligt ved svage interface-egenskaber samt tilstedeværelsen af porøsiteter. Størrelsen og formen af mikroporøsiteterne kan også føre til forskellige mikroskopiske revneveje. Afslutningsvist konkluderes det, at den foreliggende numeriske strategi, synes at være en lovende kandidat som redskab til at forudsige det makroskopiske og mikroskopiske mekaniske respons af kompositmaterialer.

Abstract

Micromechanical failure mechanisms occurring in unidirectional fiber-reinforced composites are studied by means of the finite element method as well as experimental testing. This study highlights the effect of micro-scale features such as fiber/matrix interfacial debonding, matrix cracking and microvoids on the microscopic and macroscopic mechanical response of composite materials. To this end, first a numerical study is carried out to explore ways to stabilize interfacial crack growth under dominant Mode-I fracture using the cohesive zone model. Consequently, this study suggests a method to determine the normal interfacial properties. Afterward, two different numerical approaches (I) the regular fiber distribution approach and (II) the random fiber distribution strategy are established to evaluate the effect of the micro-scale features on the overall stress-strain response of unidirectional composites. In the first approach, the J_2 plasticity model is implemented to model the elasto-plastic behavior of the matrix while in the second strategy the modified Drucker-Prager plasticity model is utilized to account for brittle-like and pressure dependent behavior of an epoxy matrix. In addition, the failure locus of the composite lamina under different loading conditions is obtained by means of computational micromechanics and compared with the predictions of Puck's model. The results are in very good agreement with the predictions of Puck's model under different interfiber failure modes. In order to validate the numerical microstructral approach accurately, an experimental test was carried out to be compared with the numerical results. It was found that the micromechanical model could accurately predict the crack initiation emanating from microvoids as well as crack propagation along the interfaces. The results of this thesis show that the strength of composite is significantly reduced by weak interfacial properties and the presence of voids. The size and shape of microvoids can also microscopically lead to different crack paths. Finally, the present numerical strategy seems to be a promising tool to predict the macroscopic and microscopic mechanical response of composites.

Publications

The following publications are part of the thesis

[P1] D. Ashouri Vajari, K. Martyniuk, B. F. Sørensen and B. N. Legarth, Experimental and numerical studies of the micro-mechanical failure in composites, Proceedings of the 19th International Conference on Composite Materials, Montréal, Canada, 28 July-02 August, 2013. P.5853-5863.

[P2] D. Ashouri Vajari, B. F. Sørensen and B. N. Legarth, Effect of fiber positioning on mixed-mode fracture of interfacial debonding in composites, *Submitted to International Journal of Solids and Structures*, 2014.

[P3] D. Ashouri Vajari, B. N. Legarth and C. F. Niordson Micromechanical modeling of unidirectional composites with uneven interfacial strengths, *European Journal of Mechanics - A/Solids*, Vol. 42, P. 241-250, 2013.

[P4] D. Ashouri Vajari, C. González, J. Llorca and B. N. Legarth, A numerical study of the influence of microvoids in the transverse mechanical response of unidirectional composites, *Journal of Composites Science and Technology*, Vol. 97, P. 46-54, 2014.

[P5] D. Ashouri Vajari, A micromechanical study of porous composites under longitudinal shear and transverse normal loading, *Submitted to Journal of Composites-A*, 2014.

Contents

Chapter 1
Introduction

1.1 Background

A preliminary definition of composites can be given as a combination of two or more distinct constituent materials with different material properties which together lead to a new material with better mechanical characteristics needed for desired applications. From the early stage of human civilization, wood as a natural composite has being widely used. Wood consists of an arrangement of cellulose fibers in a matrix of lignin. The fibers provide the wood tensile strength while the matrix provides lateral support to the fibers and compressive resistance. The first recorded man-made composites were straw and mud burnt together to form bricks for construction purposes (Herakovich, 1998). The ancient Egyptians used plywood when they realised that wood could be rearranged to achieve superior strength and resistance to thermal expansion as well as to swelling caused by the absorption of moisture (Jones, 1999). The advantage of composite materials is that, if well designed, they usually exhibit the best qualities of their components or constituents and often some quantities that neither constituent possesses (Jones, 1999). Nowadays, advanced Fiber Reinforced Composites (FRC's) are increasingly becoming potential candidates for replacing conventional metallic materials in weight sensitive applications. High ratios of stiffness-to-weight and strength-to-weight are demanded such as in aerospace, ship and wind turbine industries.

The combination of stiff carbon- or glass-fibers embedded in low density polymers lead to light-weight FRC's with outstanding stiffness, strength and creep resistance. However, the high brittle nature of epoxy, specially thermosets, used as matrices makes the material prone to failure by interply delamination, limits the impact resistance and leads to a brittle behavior of lamina subjected to transverse tensile stresses (Canal et al., 2009). Furthermore, due to the non-homogeneous nature of these materials, problems can arise during their manufacture and handling, which result in defects. Void content/porosity, fiber-matrix interfacial debonding, delamination and matrix cracks are just some of the common composite material defects. Characterization of these defects are important for determining the quality of a composite structure, as these parameters have a signicant effect on the mechanical properties of the material and can lead to failure initiation (Ghiorse, 1993). In addition, FRC's present different physical failure mechanisms as function of loading conditions. Thus, it is essential to clearly understand the limitations of composites due to failure in order to improve the reliability of these materials.

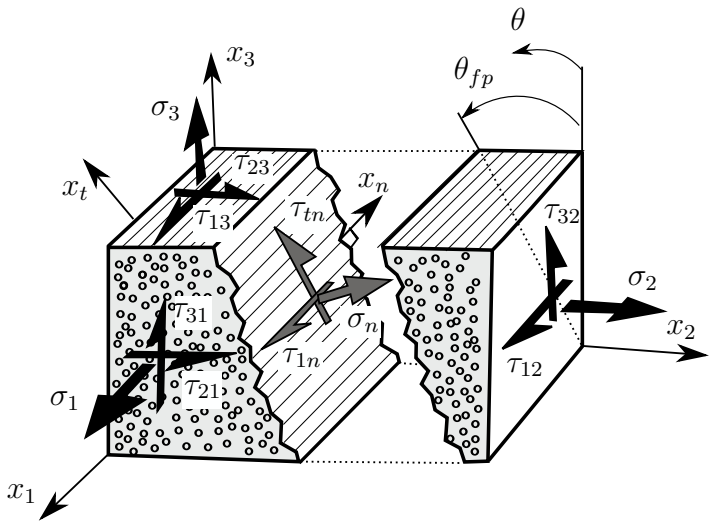

Figure 1.1 a) Illustration of the coordinate systems used in Puck's models. The (x_1, x_n, x_t) coordinate system is rotated by the fracture angle, θ_{fp}, with respect to the (x_1, x_2, x_3) coordinate system.

1.2 Analytical solutions

Starting in the 1950s, there has been a steady stream of research related to the failure of composite materials (Hinton and Soden, 1998). Several efforts have been pursued to propose an analytical criterion to provide accurate predictions of failure in composites. According to the World-Wide Failure Exercise (WWFE), Hinton et al. (2004) compared 19 different theoretical failure criteria with one another and with experimental results for 14 challenging test cases for a range of practical laminates made of unidirectional (UD) carbon- or glass-fiber reinforced epoxy layers. The five approaches ranked most highly were the theories of Zinoviev (Zinoviev et al., 1998, 2002), Bogetti (Bogetti et al., 2004a,b), Puck (Puck and Schürmann, 1998; Puck et al., 2002), Cuntze (Cuntze et al., 2004; Cuntze, 2004) and Tsai (Liu and Tsai, 1998; Kuraishi and Tsai, 2002). In the following, the Puck's failure criteria is explained.

1.2.1 Puck's criteria

Puck's failure criteria is based on the Hashin's failure criterion (Hashin, 1980), who distinguished between fiber- and matrix-dominated fracture. Puck et al. (2002) improved Hashin's model by assuming that failure was caused by the normal, σ_n, stresses and tangential, τ_{tn} and τ_{1n}, stresses acting on the failure plane, which forms a fracture angle, θ_{fp}, with the direction shown in Fig. 1.1. The fracture angle was explicitly determined for each combination of normal and shear stresses acting on the lamina. This criteria is divided into two basically independent fracture criteria: Fiber Failure (FF) and Inter Fiber Failure (IFF). In most cases, before the fibers

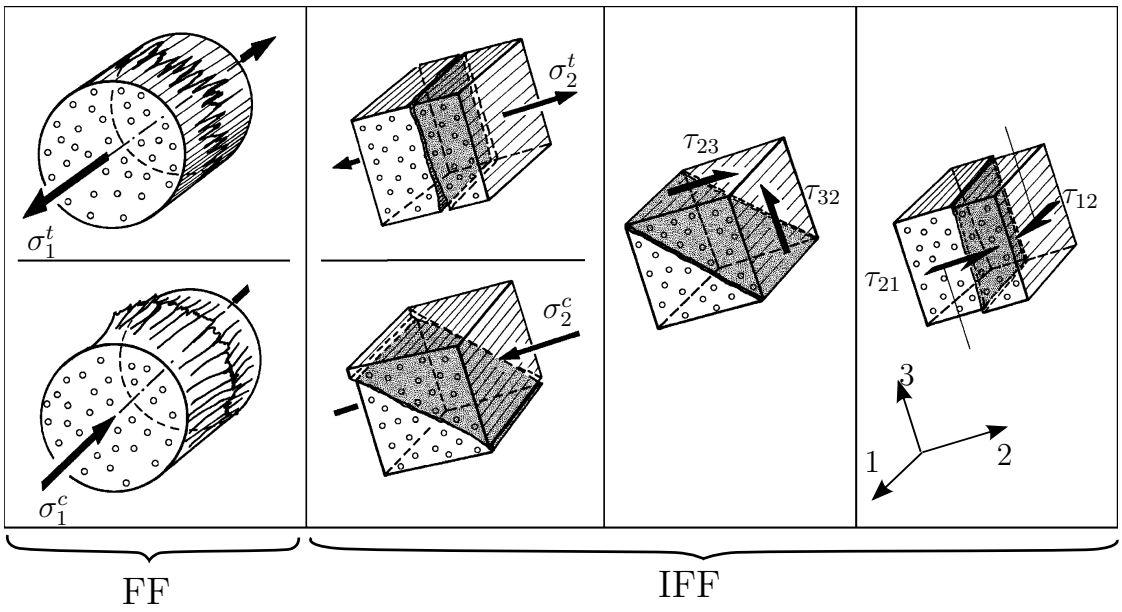

Figure 1.2 Failure in unidirectional composites can be divided into fiber-failure (FF) and inter-fiber failure (IFF) modes. Longitudinal loading, σ_1, leads to FF mode while IFF is due to one or a combination of these loading conditions: transverse normal, σ_2, transverse shear, τ_{23} or τ_{32}, and longitudinal shear, τ_{12} or τ_{21}. Adapted from (Knops, 2008)

can be fully strained, IFF occurs somewhere, which means that locally the integrity of the fiber matrix composite is more or less destroyed (Puck et al., 2002). Fig. 1.2 shows the loading conditions which lead to either FF or IFF mode. FF is not the scope of this study. In this thesis, Puck's IFF criterion for a UD lamina under different combinations of $\sigma_2 - \tau_{12}$ and $\sigma_2 - \tau_{23}$ stress states is used.

Puck's IFF criterion in the $(\sigma_2 - \tau_{12})$ stress-space distinguishes between three different fracture modes namely; Mode-A, -B and -C. As shown in Fig. 1.3, Mode-A is denoted on the failure curve from point a to b. In Mode-A, the composite is under combined transverse tension and in-plane shear which leads to a fracture plane perpendicular to the tensile loading direction, i.e. the fracture angle is $\theta_{fp} = 0°$. With the same fracture angle as Mode-A, Mode-B is determined for the dominant longitudinal shear combined with transverse compression (the path from point b to c). Mode-C is defined for the dominant transverse compression combined with longitudinal shear where inclined fracture planes occur (the path from point c to d). For a given $(\sigma_2 - \tau_{12})$ stress state, the Puck's criterion under Mode-A with $\theta_{fp} = 0°$ is given by (Puck and Schürmann, 1998)

$$\sqrt{\left(\frac{\tau_{12}}{S_{12}}\right)^2 + \left(1 - P_{\perp\parallel}^{(+)}\frac{Y_T}{S_{12}}\right)^2\left(\frac{\sigma_2}{Y_T}\right)^2} + P_{\perp\parallel}^{(+)}\frac{\sigma_2}{S_{12}} = 1 \qquad \text{for } \sigma_2 \geq 0 \tag{1.1}$$

while under Mode-B with $\theta_{fp} = 0°$ is expressed by

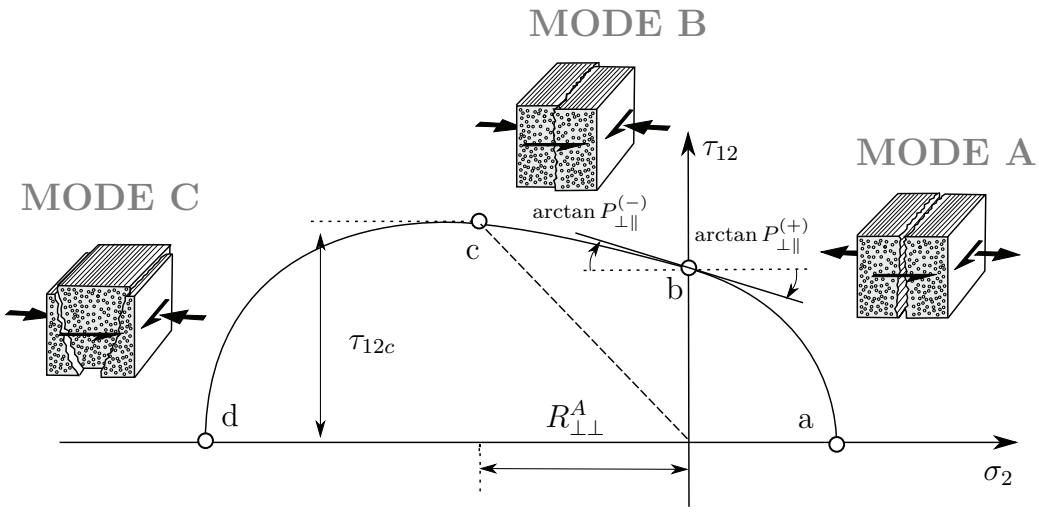

Figure 1.3 Illustration of the analytical $\sigma_2 - \tau_{12}$ fracture envelope for $\sigma_1 = 0$ proposed by Puck and Schürmann (1998). Three different fracture Modes (A, B and C) are shown which are distinguished based on different loading conditions and the fracture angle, θ_{fp}.

$$\frac{1}{S_{12}}\left(\sqrt{\tau_{12}^2 + \left(P_{\perp\parallel}^{(-)}\sigma_2\right)^2} + P_{\perp\parallel}^{(-)}\sigma_2\right) = 1 \qquad \text{for } \sigma_2 < 0 \quad \text{and} \quad 0 \leq |\frac{\sigma_2}{\tau_{12}}| \leq \frac{R_{\perp\perp}^{A}}{|\tau_{12c}|} \tag{1.2}$$

and in Mode-C having $\cos\theta_{fp} = \sqrt{\dfrac{R_{\perp\perp}^{A}}{(-\sigma_2)}}$ is given by

$$\left[\left(\frac{\tau_{12}}{2(1+P_{\perp\perp}^{(-)})S_{12}}\right)^2 + \left(\frac{\sigma_2}{Y_C}\right)^2\right]\frac{Y_C}{(-\sigma_2)} = 1 \qquad \text{for } \sigma_2 < 0 \quad \text{and} \quad 0 \leq |\frac{\tau_{12}}{\sigma_2}| \leq \frac{|\tau_{12c}|}{R_{\perp\perp}^{A}} \tag{1.3}$$

where Y_T, Y_C and S_{12} are the transverse tensile strength, the transverse compressive strength and the longitudinal shear strength of the composite, respectively. The so-called inclination coefficients, $P_{\perp\perp}$ and $P_{\perp\parallel}$, are the slopes of the failure curve in the $\sigma_2 - \tau_{tn}$ and $\sigma_2 - \tau_{12}$ planes, respectively (the latter is shown in Fig. 1.3). The superscripts $(+)$ and $(-)$ stand for tension and compression loading conditions, respectively. While the subscripts $\perp$ and $\parallel$ denote the transverse, x_t, and longitudinal, x_1, directions on the fracture plane. For glass-fiber/epoxy composites $P_{\perp\perp}^{(-)}$ and $P_{\perp\perp}^{(+)}$ are in the range of $0.20 - 0.25$ (Puck et al., 2002). Finally, according to the following relationships the fracture resistance in the fracture plane due to transverse/transverse shear, $R_{\perp\perp}^{A}$, the inclination parameter, $P_{\perp\perp}^{(-)}$, and the shear stress

at the boarder of Mode-B and -C, τ_{12c}, (shown as point c in Fig. 1.3) are defined as (Puck and Schürmann, 1998)

$$\begin{aligned} R^A_{\perp\perp} &= \frac{Y_C}{2(1+P^{(-)}_{\perp\perp})} = \frac{S_{12}}{2P^{(-)}_{\perp\parallel}}\left(\sqrt{1+2P^{(-)}_{\perp\parallel}\frac{Y_C}{S_{12}}}-1\right) \\ P^{(-)}_{\perp\perp} &= P^{(-)}_{\perp\parallel}\frac{R^A_{\perp\perp}}{S_{12}} \\ \tau_{12c} &= S_{12}\sqrt{1+2P^{(-)}_{\perp\perp}} \end{aligned} \tag{1.4}$$

In the $(\sigma_2 - \tau_{23})$ stress-space, the orientation of the fracture plane, θ_{fp}, is always oblique under transverse compression and 0° under transverse tension. Thus, the IFF criterion in the $(\sigma_2 - \tau_{23})$ stress-space has two different conditions given as

$$\begin{aligned} \sqrt{\left[\left(\frac{1}{Y_T}-\frac{2P^{(+)}_{\perp\perp}\left(1+P^{(+)}_{\perp\perp}\right)}{Y_C}\right)\sigma_n(\theta_{fp})\right]^2+\left[\frac{2\left(1+P^{(+)}_{\perp\perp}\right)}{Y_C}\tau_t(\theta_{fp})\right]^2} \\ +\frac{2P^{(+)}_{\perp\perp}\left(1+P^{(+)}_{\perp\perp}\right)}{Y_C}\sigma_n(\theta_{fp}) = 1 \qquad \text{for} \quad \sigma_n \geq 0 \end{aligned} \tag{1.5}$$

$$\begin{aligned} \sqrt{\left[\frac{2\left(1+P^{(-)}_{\perp\perp}\right)}{Y_C}\tau_t(\theta_{fp})\right]^2+\left[\frac{2P^{(-)}_{\perp\perp}\left(1+P^{(-)}_{\perp\perp}\right)}{Y_C}\sigma_n(\theta_{fp})\right]^2} \\ +\frac{2P^{(-)}_{\perp\perp}\left(1+P^{(-)}_{\perp\perp}\right)}{Y_C}\sigma_n(\theta_{fp}) = 1 \qquad \text{for} \quad \sigma_n < 0 \end{aligned} \tag{1.6}$$

with

$$\begin{aligned} \sigma_n(\theta_{fp}) &= \sigma_2\cos^2\theta_{fp} + 2\tau_{23}\sin\theta_{fp}\cos\theta_{fp} \\ \tau_t(\theta_{fp}) &= -\sigma_2\sin\theta_{fp}\cos\theta_{fp} + \tau_{23}\left(\cos^2\theta_{fp}-\sin^2\theta_{fp}\right) \end{aligned} \tag{1.7}$$

According to the WWFE, Puck's theoretical failure envelopes were in very good agreement with the experimental results for the UD laminae. The predicted final failure envelopes and stress-strain curves for the multi-directional laminates were also generally in good agreement with those experimentally measured. However, all the high ranked failure criteria evaluated by Hinton et al. (2004), including Puck's model, have some limitations. For instance in Puck's model, discrepancies between theory and experiment emerged in the test cases where large non-linear deformations were present. In some instances, predictions of final failure strain were much smaller than the observed values and in others the failure envelope was not closed. In addition, none of these five high ranked theories are micromechanics based and

therefore the inclusion of micro defects, e.g. fiber/matrix debonding or voids are not features of these theories. Furthermore, as Puck's model needs some parameters such as Y_T, Y_C, S_{12} and $P_{\perp\parallel}$ to be determined all these theoretical methods are dependent on experimental tests. Experimentally measuring the mechanical properties is sometimes difficult and costly. Alternatively, one can use the numerical modeling considering the micromechanical mechanisms.

1.3 Numerical solutions

By the advancement of computer technology, numerical simulation is becoming a powerful tool to understand the failure processes in composite materials. Numerical modeling has made it possible to predict the mechanical response of composites at different length scales. Fig. 1.4 depicts different length scales of composites used in wind turbine blades. This leads to three main entities (ply, laminate and component) whose mechanical behavior is characterized by three different length scales, namely fiber diameter, ply and laminate thickness, respectively. Fiber diameters are on the order of 5-20 μm, while ply thicknesses are in the range 100-300 μm and standard laminates are several mm in thickness and above. This clear separation of length scales is very useful to carry out multiscale modeling by computing the properties of one entity (e.g. individual plies) at the relevant length scale, homogenizing the results into a constitutive model, and passing this information to the simulations at the next length scale to determine the mechanical behavior of the larger entity (Canal et al., 2011). In the computational micromechanis which is the focus of this study, fiber failure, matrix cracking, fiber/matrix interfacial debonding and porosities can be directly considered as the main features controlling the micro scale failure of composite. To this end, two different strategies have been developed. The first one assumes that the fibers are regularly distributed within the ply, which leads to a simplified unit-cell model including few fibers (normally one or two). The second modeling approach considers a Representative Volume Element (RVE) including several dozens of fibers which are randomly distributed in the matrix. In the first approach, assuming a regular distribution of fibers allows for a much more simple representation of the composite geometry. París et al. (2003) and Correa et al. (2007) modeled a single-fiber unit cell embedded in a polymer matrix. They studied interface debonding by means of the boundary element method. París et al. (2007) and Correa et al. (2008) studied the initiation and propagation of an interface crack which subsequently kinks into the matrix in a single-fiber composite. Romanowicz (2012) computationally predicted the failure locus of a two-fiber unit-cell using a bilinear cohesive zone at the fiber/matrix interface and the Drucker-Prager criterion to consider the pressure-dependent yielding of polymers. Bayat et al. (2012) modeled a unit cell including two fibers using the Differential Quadratic Element Method (DQEM) under generalized plane strain deformation. Similar approach was adopted by Maligno et al. (2009) who studied the effect of thermal residual stress and fiber spacing. An inherent feature of such reduced symmetric unit-cell models is the

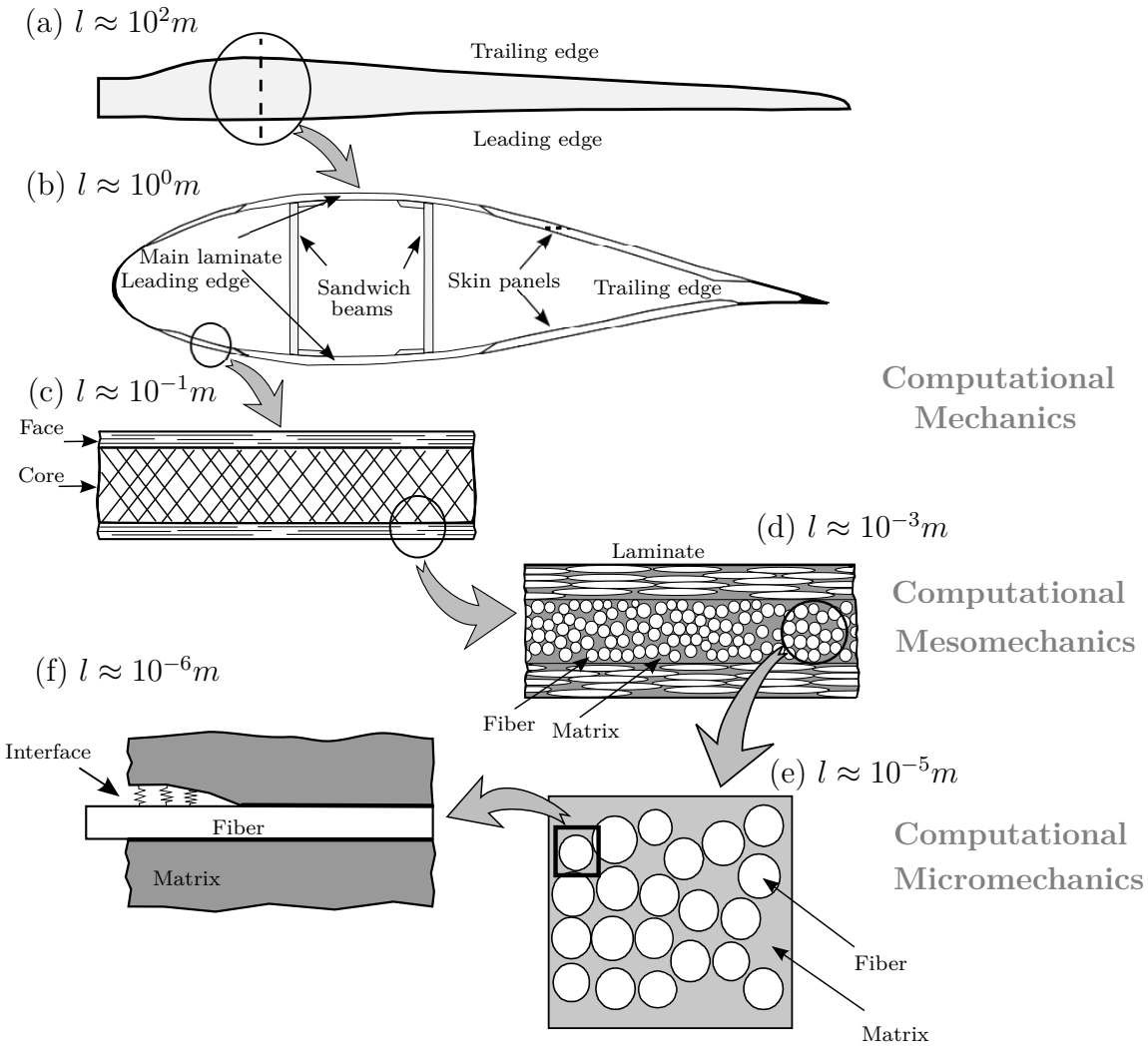

Figure 1.4 Characteristic length scales of composites used in wind turbine blades. a) Structural scale. b) Sub-structural scale. c) Component scale. d) Laminate scale. e) Ply-scale. f) Micro-scale. Inspiration from (Zangenberg, 2013).

repeatability of the stress and strain fields around one or two fibers which results in simultaneously failure of all fiber-matrix interfaces through-out the whole composite.

In the second approach, more complex RVEs can be generated which include dozens of fibers randomly distributed in the matrix. The size of the microstructure included in the RVE is large enough so that the effective properties computed from the RVE are independent of its size and of the position of fibers. In addition, this larger model can simulate the growth of cracks through the ply which are resulting from matrix localized shear bands and interfacial debonding. González and Llorca (2007a,b) and Totry et al. (2008a) validated the multi-fiber RVE modeling strategy with experiments to determine the fracture behavior of a composite under different loading modes. The epoxy matrix in these studies was assumed to behave as an isotropic, elasto-plastic solid using the Coulomb-Mohr yield criterion which takes into account the influence of the triaxiality on the shear yielding of polymers. Interface debonding was modeled by a bi-linear cohesive zone model. Ling et al. (2009) studied fiber-matrix decohesion in combination with matrix cracking by adopting a cohesive zone model together with the Augmented Finite Element Method (A-FEM). The combination of the eXtended Finite Element Method (X-FEM) and the Level Set Method (LSM) was used by Hettich et al. (2008) to model discontinuous failure within composite materials considering several fibers.

1.4 Research overview

The objective of this PhD thesis is to study the effect of micro-scale failure features (e.g. fiber/matrix debonding, matrix deformation and micro-voids) on the damage evolution of UD fiber-reinforced composites. Both the regular fiber distribution approach as well as the random fiber arrangement strategy are used to analyse the overall stress-strain response of composites. Finally, the aim is to use the detailed model with a random distribution of fibers and voids to predict computational failure envelopes based on the micromechanical failure mechanisms and subsequently compare them with Puck's models which are experimentally validated. In order to accurately validate the ability of this numerical model to mimic the micromechanical failure mechanisms, an $in-situ$ experimental observation is carried out.

The thesis is constructed in two parts. The first part serves as a summary and further explanation of the second part. The second part includes five papers written during the author's PhD work. Subsequently these papers are denoted by [P1]-[P5]. The first part comprises five chapters. In the introduction, different failure micromechanisms in a laminae were discussed. In addition, an explanation of Puck's models was given. Chapter two elaborates as the material models used in this study. Chapter three presents the sample manufacturing process and the experimental test. Chapter four includes the summary of results presented in papers [P1]-[P5] and the results of an unpublished work. Finally, chapter five concludes this study.

Chapter 2
Numerical modeling

Based on the material methods used for the matrix, the papers included in this thesis can be divided into two parts. The first part which consists of [P1], [P2] and [P3] is assuming that the matrix is an elasto-plastic material governed by the standard J_2-plasticity theory. In [P1] and [P2] the matrix has the properties of epoxy resin. Normally, using conventional plasticity model which is suitable for ductile materials can not be a proper choice for polymers with brittle and pressure-dependent behaviors. However, in [P1], [P2] the focus is on the early stage of interfacial debonding under transverse tension. As it will be later discussed in the results section, under transverse tension interfacial debonding is the first failure mechanism before damage occurs in the matrix. In [P3], the properties are representing the metal matrix composite where the standard J_2-plasticity is applicable. In the second part including [P4], [P5] and an unpublished work, the standard properties of glass-fiber epoxy composites have been used. In this part, due to different loading conditions the matrix deformation as well as interfacial debonding play significant roles. Thus, in this part the modified Drucker-Prager yield criterion has been used which considers different tensile and compressive yield stresses and the effect of pressure dependency in polymers. In all above studies, fibers are always considered as isotropic purely elastic due to very stiff material properties in comparison with the matrix.

2.1 Material model

2.1.1 Isotropic J_2 plasticity model

Assuming the matrix to be an elasto-plastic isotropic material governed by the standard J_2-plasticity theory, the stress increment is calculated from the total strain increment, $\dot{\epsilon}_{ij}$, which consists of an elastic part, $\dot{\epsilon}^e_{ij}$, and a plastic part, $\dot{\epsilon}^p_{ij}$

$$\begin{aligned} \dot{\epsilon}_{ij} &= \dot{\epsilon}^e_{ij} + \dot{\epsilon}^p_{ij} \\ \dot{\sigma}_{ij} &= L_{ijkl}\dot{\epsilon}_{kl} \end{aligned} \tag{2.1}$$

Here, L_{ijkl} is the fourth order incremental stiffness tensor defined as

$$L_{ijkl} = \frac{E}{1+\nu}\left[\frac{1}{2}\left(\delta_{ik}\delta_{jl}+\delta_{il}\delta_{jk}\right) + \frac{\nu}{1-2\nu}\delta_{ij}\delta_{kl} - \beta\frac{3}{2}\frac{\dfrac{E}{E_t}-1}{\dfrac{E}{E_t}-\dfrac{(1-2\nu)}{3}}\frac{s_{ij}s_{kl}}{\sigma_e^2}\right] \tag{2.2}$$

while,

$$\beta = \begin{cases} 1 & \text{for } \sigma_e = \sigma_f \text{ and } \quad \dot{\sigma}_e \geq 0 \\ 0 & \text{for } \sigma_e < \sigma_f \text{ or } \quad \dot{\sigma}_e < 0 \end{cases} \tag{2.3}$$

where, E is the Young's modulus and ν is the Poisson's ratio. The tangential modulus, E_t, is the slope of the stress-strain curve at the stress level $\sigma_e = \sqrt{\frac{3}{2} s_{ij} s_{ij}}$ and δ_{ij} denotes the Kronecker delta. The stress deviator is defined by $s_{ij} = \sigma_{ij} - \delta_{ij} \frac{\sigma_{kk}}{3}$. In Eq. 2.3, $\dot{\sigma}_e = \frac{3 s_{kl} \dot{\sigma}_{kl}}{2\sigma_e}$ and σ_f is the instantaneous flow stress and during plastic yielding β is unity and the magnitude of L_{ijkl} depends on the stress state and the deformation hardening law whereas in the elastic regime (including elastic unloading) it is governed by Hooke's law where β is zero. The yield surface, f, is taken as the von Mises yield surface

$$f = \sigma_e - \sigma_f(\epsilon_e^p) = 0 \tag{2.4}$$

Where ϵ_e^p is the equivalent plastic strain, work conjugate to σ_e, and it is defined incrementally by the relation $\dot{\epsilon}_e^p = \sqrt{\frac{2}{3} \dot{\epsilon}_{ij}^p \dot{\epsilon}_{ij}^p}$. The hardening behavior determined by the uniaxial stress-strain relation which is represented by the power hardening law

$$\epsilon = \begin{cases} \dfrac{\sigma}{E} & \text{for } \sigma \leq \sigma_y \\ \dfrac{\sigma_y}{E} \left(\dfrac{\sigma}{\sigma_y} \right)^n & \text{for } \sigma > \sigma_y \end{cases} \tag{2.5}$$

where n is the strain-hardening exponent and σ_y denotes the initial yield stress.

2.1.2 Isotropic modified Drucker-Prager model

Epoxy resins are one of the most important thermosets polymers. Thermosets are a class of glassy polymers which are highly cross-linked and have a reputation of being very brittle. Therefore, the matrix which is assumed to have the epoxy resin material properties should fail at very low strains in simple uniaxial tension (Kinloch and Young, 1983). On the other hand, epoxy resins yield and undergo considerable plastic deformation in uniaxial compression or in pure shear, obeying a significant pressure-dependent yield criterion (Quinson, 1997; Puck et al., 2002; Kinloch and Young, 1983). The Drucker-Prager yield criterion has often been used for these type of materials. The Drucker-Prager criterion is a modified von Mises criterion which has different tensile and compressive yield stress (shown with dashed-line in Fig. 2.1a). In addition, the Drucker-Prager yield criterion includes the effect of hydrostatic stresses on the flow stress by including an additional term in the von Mises expression, according to

$$F(I_1, J_2) = \sqrt{3J_2} + \alpha I_1 - c = 0 \tag{2.6}$$

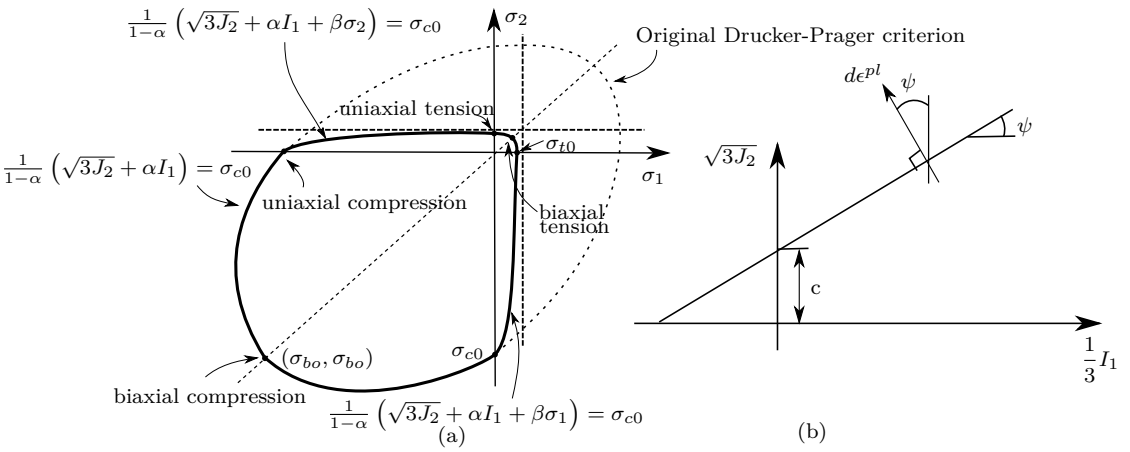

Figure 2.1 Yield surface of the modified Drucker-Prager criterion. The dashed-line denotes the original Drucker-Prager criterion.

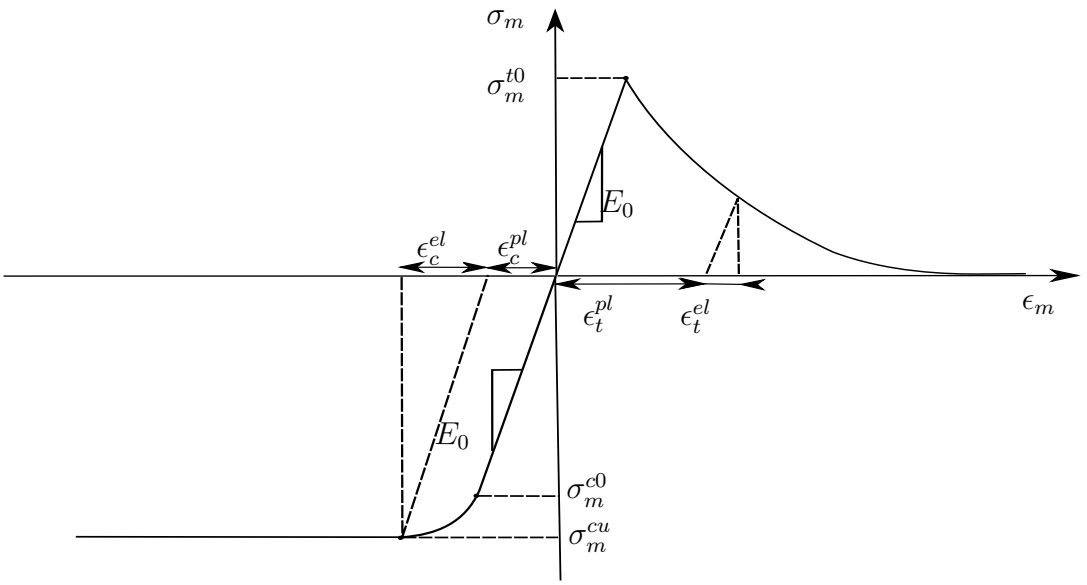

Figure 2.2 Stress-strain behavior of the matrix under uniaxial tension and uniaxial compression.

where I_1 is the first invariant of the stress tensor, J_2 is the second invariant of the deviatoric stress tensor and c is the flow stress under pure shear. The pressure-sensitivity parameter, α, can be determined by (Lubliner, 1989)

$$\alpha = \frac{\frac{\sigma_m^{b0}}{\sigma_m^{c0}} - 1}{2\frac{\sigma_m^{c0}}{\sigma_m^{t0}} - 1} \tag{2.7}$$

Here, σ_m^{c0}, σ_m^{b0} and σ_m^{t0} denote the matrix uniaxial compressive yield stress, the biaxial compressive yield stress and the uniaxial tensile yield stress, respectively, see Fig. 2.1. In order to include the brittle behavior of the epoxy matrix in tension, the modified Drucker-Prager model developed by Lubliner (1989) and Lee (1998) was used in this investigation to simulate the matrix behavior. It is expressed by

$$F(I_1, J_2, \sigma_I, \beta, \alpha) = \frac{1}{1-\alpha}\left(\sqrt{3J_2} + \alpha I_1 + \beta \langle \sigma_I \rangle\right) - \sigma_m^{c0} = 0 \tag{2.8}$$

where σ_I is the maximum principal stress, $\langle\rangle$ denotes the Macaulay brackets (which return the argument if positive and zero otherwise), and β is a function of the tensile, σ_m^{t0}, and compressive, σ_m^{c0}, yield stress according to

$$\beta = \frac{\sigma_m^{c0}}{\sigma_m^{t0}}(1-\alpha) - (1+\alpha) \tag{2.9}$$

The yield surface corresponding to the modified Drucker-Prager criterion is depicted in Fig. 2.1. It follows the standard Drucker-Prager yield criterion with an associated flow rule under compression, which has been experimentally validated for glassy polymers (Puck et al., 2002; Quinson, 1997). However, in tension the matrix is mainly controlled by the maximum principal stress, σ_m^{t0}, which cuts off the yield surface due to very brittle nature of epoxy resin. The tension cut off model is shown with the straight dashed lines in Fig. 2.1a. Furthermore, the extension of the original Drucker-Prager model can include the use of non-circular (anisotropic) yield surface in the deviatoric plane and also the use of non-associated flow rule. In Fig. 2.1b, the Drucker-Prager yield criterion in the meridional plane is shown. In Fig. 2.1b, $\psi = \arctan(3\alpha)$ is the friction angle. Experimental studies show that the value of ψ for polymeric materials ranges between 0° and 23° (Quinson, 1997; Chew et al., 2006). Quinson (1997) and Chew et al. (2006) also discussed that pressure-sensitivity reduces the load-carrying capacity as well as influences the strain for void coalescence, but they also showed that plastic dilatancy effects are relatively milder. Thus, for the sake of simplicity, an associated flow rule is considered to simulate the plastic flow of the matrix.

The stress-strain behavior of the matrix under uniaxial compression and uniaxial tension is shown in Fig. 2.2. Plastic deformation at constant flow stress occurred in compression after yielding, leading to failure by localization of a shear band. In Fig. 2.2, σ_m^{cu} denotes the matrix ultimate compressive strength. Conversely, the behavior in tension was brittle due to micro-cracking and this is accounted for by a softening law (Canal et al., 2012). The energy dissipated by a unit volume during

tensile cracking is G_m which is the area under the tensile stress-strain curve for $\epsilon_m > 0$. The assumed stress-strain behavior shown in Fig. 2.2 for both tension and compression loading is in good agreement with the experimental results reported by Fiedler et al. (2001).

The matrix properties correspond to typical values used in the modified Drucker-Prager model for an epoxy matrix (Canal et al., 2012). The pressure-sensitivity parameter was chosen to be $\alpha = 0.13$ which is within the range reported by Quinson (1997) and Chew et al. (2006).

2.2 Debonding model

When the unit cell is deformed, the interfaces between fibers and matrix tend to separate normally as well as tangentially. In order to capture this fracture behavior, two types of cohesive zone models is used in this thesis. Three-dimensional bilinear cohesive model available in ABAQUS is used in [P5] while the 2D trapezoidal cohesive zone model proposed by Tvergaard and Hutchinson (1993) is implemented in [P1-4]. As illustrated in Fig. 2.3c the failure due to debonding is taken into account by considering a cohesive zone along the interfaces between the fibers and the matrix. The cohesive zone model determines the failure behavior imposing a relation between the separation of two faces of the debonding interface and the tractions which resist against opening. This traction-separation law is regarded as a phenomenological characterization of the separation zone along the interfaces and not the description of atomic separation, see Tvergaard and Hutchinson (1993).

2.2.1 Trapezoidal cohesive zone model

In the trapezoidal cohesive zone model, λ is defined as a non-dimensional parameter describing the separation criterion as

$$\lambda = \sqrt{\left(\frac{u_n}{\delta_n^c}\right)^2 + \left(\frac{u_t}{\delta_t^c}\right)^2} \tag{2.10}$$

such that onset of degradation in traction in the cohesive zone starts at a specified value, $\lambda = \lambda_2$, and fully damage occurs when $\lambda = 1$, see Fig. 2.3. Here, δ_n^c and δ_t^c are the normal and tangential characteristic cohesive lengths, respectively, and u_n and u_t are the normal and tangential separation of the interface, respectively. A traction potential can be defined as

$$\Phi(u_n, u_t) = \delta_n^c \int_0^\lambda \sigma(\acute{\lambda}) d\acute{\lambda} \tag{2.11}$$

where $\sigma(\lambda)$ is defined from the trapezoidal shape of the Fig. 2.3 as

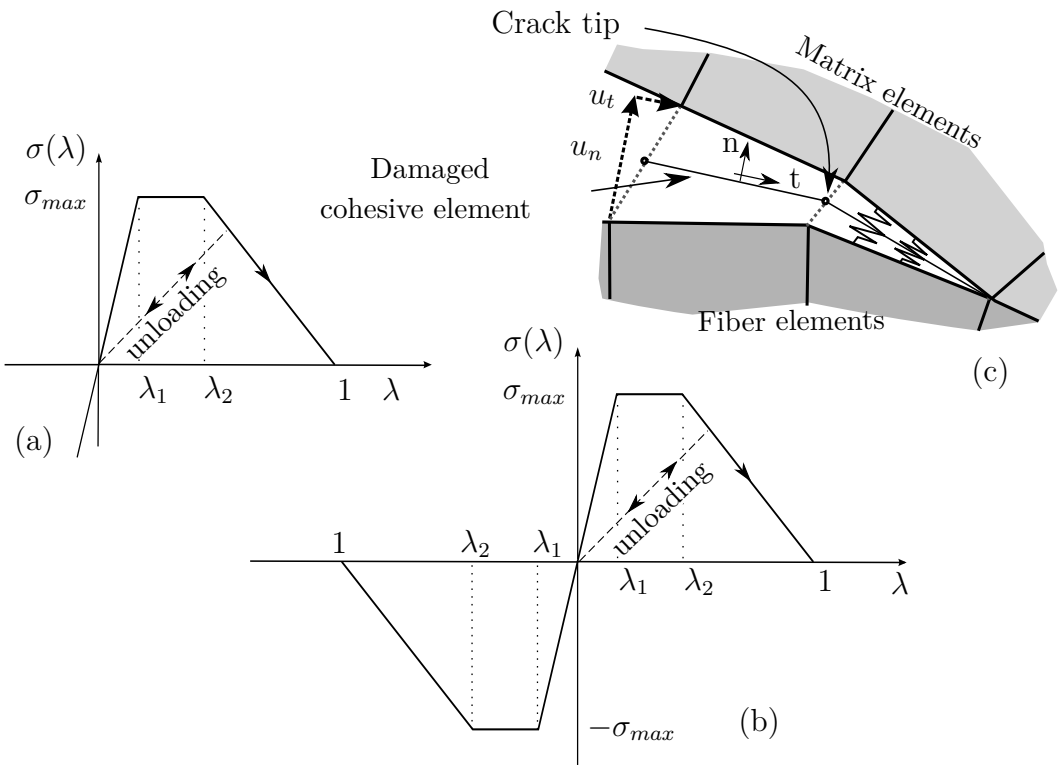

Figure 2.3 a) Normal and b) tangential traction-separation laws used in the trapezoidal cohesive model. c) Schematic illustration of cohesive elements at the fiber/matrix interface. The location of the crack tip is defined as the position of the last damaged cohesive Gauss point.

$$\sigma(\lambda) = \begin{cases} \dfrac{\sigma_{max}}{\lambda_1}\lambda & \text{for } 0 \leq \lambda < \lambda_1 \\ \sigma_{max} & \text{for } \lambda_1 \leq \lambda \leq \lambda_2 \\ \dfrac{\sigma_{max}}{1-\lambda_2}(1-\lambda) & \text{for } \lambda_2 < \lambda \leq 1 \end{cases} \tag{2.12}$$

As long as λ is monotonically increasing the normal, T_n, and tangential, T_t, tractions acting on the interfaces can be derived from the potential function as

$$T_n = \frac{\partial \Phi}{\partial u_n} = \frac{\sigma(\lambda)}{\lambda}\frac{u_n}{\delta_n^c}, \quad T_t = \frac{\partial \Phi}{\partial u_t} = \gamma\frac{\sigma(\lambda)}{\lambda}\frac{u_t}{\delta_t^c} \tag{2.13}$$

where the factor $\gamma = \dfrac{\delta_n^c}{\delta_t^c}$ denotes different failure mechanism in Mode-II than Mode-I such that choosing γ to be smaller than one leads to more ductile failure in Mode-II. However, due to the identical fracture energy for both modes the maximum traction in pure tangential debonding is smaller than the one under pure normal debonding by the magnitude of γ. By assuming $F(\lambda) = \dfrac{\sigma(\lambda)}{\lambda}$, similar to Tvergaard (1990), the incremental expressions of the cohesive tractions are obtained from Eq. 2.13 as

$$\dot{T}_n = \frac{\dot{u}_n}{\delta_n^c}F(\lambda) + \frac{u_n}{\delta_n^c}\frac{\partial F}{\partial \lambda}\dot{\lambda}, \quad \dot{T}_t = \gamma\frac{\dot{u}_t}{\delta_t^c}F(\lambda) + \gamma\frac{u_t}{\delta_t^c}\frac{\partial F}{\partial \lambda}\dot{\lambda} \tag{2.14}$$

Where

$$\dot{\lambda} = \frac{1}{\lambda}\left(\frac{u_n}{\delta_n^c}\frac{\dot{u}_n}{\delta_n^c} + \frac{u_t}{\delta_t^c}\frac{\dot{u}_t}{\delta_t^c}\right) \tag{2.15}$$

As shown in Fig. 2.3a and b, for decreasing λ a type of elastic unloading is used to represent the partly damaged interface:

$$\begin{aligned} T_n &= \frac{u_n}{\delta_n^c}F(\lambda_{max}) \\ & \qquad \text{for } \lambda < \lambda_{max} \text{ or } \dot{\lambda} < 0 \\ T_t &= \gamma\frac{u_t}{\delta_t^c}F(\lambda_{max}) \end{aligned} \tag{2.16}$$

where λ_{max} denotes the maximum reached value of λ. Using Eq. 2.16 denotes that after $\lambda = \lambda_1$ the element is partly damaged, therefore its behavior should be weaker than the undamaged element after unload and subsequent reloading. To represent contact under normal compression, instead of Eq. 2.14a elastic springs with a high stiffness are used by

$$T_n = \frac{u_n}{\delta_n^c}\frac{\sigma_{max}}{\lambda_1} \qquad \text{for } u_n < 0$$
$$\lambda = |\frac{u_t}{\delta_t^c}| \tag{2.17}$$

The incremental traction vector is related to the displacement increments across the interface as

$$\begin{bmatrix} \dot{T}_t \\ \\ \dot{T}_n \end{bmatrix} = \begin{bmatrix} \dfrac{\partial T_t}{\partial u_t} & \dfrac{\partial T_t}{\partial u_n} \\ \\ \dfrac{\partial T_n}{\partial u_t} & \dfrac{\partial T_n}{\partial u_n} \end{bmatrix} \begin{bmatrix} \dot{u}_t \\ \\ \dot{u}_n \end{bmatrix} \tag{2.18}$$

where the matrix on the right hand side is the cohesive tangent matrix. In pure normal separation ($u_t = 0$) the maximum traction is $T_n = \sigma(\lambda)$ where $\lambda = \dfrac{u_n}{\delta_n^c}$, while under pure tangential separation ($u_n = 0$) the maximum traction is $T_t = \gamma\sigma(\lambda)$ where $\lambda = \dfrac{u_t}{\delta_t^c}$. Thus, five interface parameters need to be specified, i.e. δ_n^c, δ_t^c, λ_1, λ_2 and σ_{max}. In addition, a plateau in the maximum traction level in the trapezoidal cohesive zone model simultaneously allows more Gauss points of cohesive elements to be at the maximum stress. This may lead to more stable numerical solutions in comparison with bilinear and exponential models (Chandra et al., 2002). However, Tvergaard and Hutchinson (1993) discussed that under small scale yielding and small scale fracture process zone the shape of the separation law has a secondary importance and the most critical parameters are the maximum cohesive stress and the characteristic cohesive length.

The fiber/matrix interfacial debonding is a mixed mode failure mechanism which involves both normal as well as tangential opening. By assuming Linear Elastic Fracture Mechanics (LEFM) the mode mixity in bimaterials can be defined using a stress intensity factor-based approach as (Rice, 1988; Hutchinson and Suo, 1992)

$$\psi = \tan^{-1}\left(\frac{Im(Kl^{i\varepsilon})}{Re(Kl^{i\varepsilon})}\right) \tag{2.19}$$

where $K = K_I + iK_{II}$ is the complex combination of Mode-I stress intensity factor, K_I, and Mode-II stress intensity factor, K_{II}. The bimaterial mismatch is denoted by ε and l is a reference length scale. Alternatively, the mode mixity can be defined by crack tip opening displacements in terms of tangential and normal displacement components (Liu et al., 1995; Agrawal and Karlsson, 2006; Sørensen and Kirkegaard, 2006).

$$\varphi = \tan^{-1}\left(\frac{u_t}{u_n}\right) \tag{2.20}$$

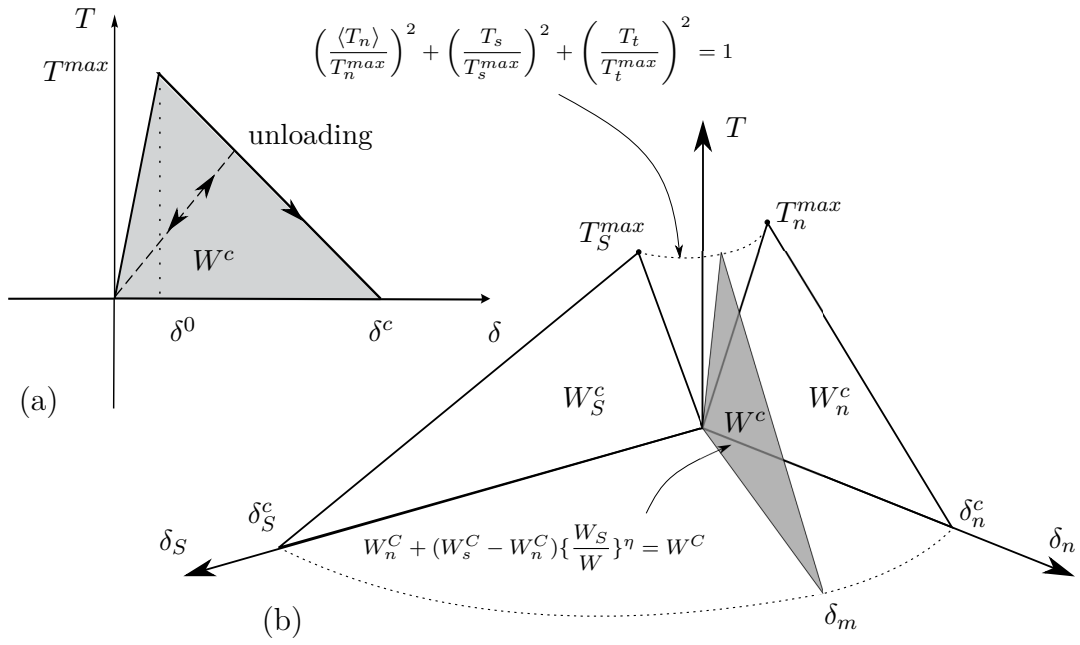

Figure 2.4 a) Bilinear traction-separation law including unload-reloading. b) The mixed mode response of 3D cohesive elements. Damage initiation is specified by quadratic stress criterion while damage evolution uses a mixed-mode energy based criterion proposed by Benzeggagh and Kenane (1996).

whereas the displacement components, u_t and u_n, are obtained at the crack tip. The location of the crack tip is defined as the position of the last damaged cohesive Gauss point, see Fig. 2.3c. The definition of the mode-mixity shown in Eq. 2.20 is used in the current study. The trapezoidal cohesive model assumes the same work of separation for all mode mixities. Experimental studies have shown that the mixed mode fracture energy usually increases significantly with increasing mode mixity (Liechti and Chai, 1992). However, the assumption made in the present study (mode mixity with independent fracture energy) means that in reality, the amount of unstable fiber/matrix debonding will be less than predicted from the present study. So results of this study will be conservative in the sense that the configuration that gives the most stable crack growth in the model, will be even more stable in reality.

2.2.2 3D bilinear cohesive zone model

The cohesive zone model implemented in ABAQUS assumes initially linear elastic behavior followed by the initiation and evolution of damage, see Fig. 2.4a. However, very large initial stiffness may result numerical instability. The elastic behavior can be given as

$$\begin{bmatrix} \dot{T}_n \\ \dot{T}_s \\ \dot{T}_t \end{bmatrix} = \begin{bmatrix} K_{nn} & K_{ns} & K_{nt} \\ K_{ns} & K_{ss} & K_{st} \\ K_{nt} & K_{st} & K_{tt} \end{bmatrix} \begin{bmatrix} \dot{u}_n \\ \dot{u}_s \\ \dot{u}_t \end{bmatrix} \tag{2.21}$$

where $\dot{T}_i$ and $\dot{u}_i$ denotes the incremental traction and displacement components, respectively where the subscript n stands for normal debonding while s and t denote the tangential openings perpendicular and parallel to the fiber direction, respectively. K_{ij} are the stiffness components. Damage in a cohesive element consists of three ingredients: a damage initiation criterion, a damage evolution law and a choice of damage removal upon reaching a completely damaged state (Abaqus, 2012). As shown in Fig. 2.4a, the damage initiation specifies the beginning of degradation in traction-separation law. In [P5] where this cohesive model is used, damage is assumed to initiate based on the quadratic nominal stress criterion defined as

$$\left(\frac{\langle T_n \rangle}{T_n^{max}}\right)^2 + \left(\frac{T_s}{T_s^{max}}\right)^2 + \left(\frac{T_t}{T_t^{max}}\right)^2 = 1 \tag{2.22}$$

where T_n^{max} denotes the maximum normal traction while T_s^{max} and T_t^{max} are the maximum tangential tractions. The Macaulay brackets, $\langle\rangle$, indicate that pure compressive deformation does not lead to damage initiation. This condition is similar to Eq. 2.17 in the trapezoidal cohesive model. Once the damage initiation criterion is met the degradation of cohesive stiffness triggers. In [P5] as shown in Fig. 2.4a, a linear softening behavior is considered. The damage evolution is determined by a mixed-mode fracture criterion proposed by Benzeggagh and Kenane (1996) which is based on the dissipated interfacial fracture energy, W, as

$$W_n^C + (W_s^C - W_n^C)\{\frac{W_S}{W}\}^\eta = W^C \tag{2.23}$$

where the work per unit area of the normal traction is denoted by W_n and by W_s and W_t for shear, respectively. The superscript C denotes the critical energy dissipated due to failure and η is a material parameter. The portion of the total work done by the shear tractions and the corresponding relative displacement components is represented by $W_S = W_s + W_t$. The Benzeggagh-Kenane fracture criterion is particularly useful when the critical fracture energies during deformation purely along the first and the second shear directions are the same; i.e., $W_s^C = W_t^C$ (Abaqus, 2012).

Fig. 2.4b schematically illustrates the mixed-mode traction-separation law in the 3D cohesive elements. The traction on the vertical axis is versus the normal displacement, δ_m, and the portion of the total tangential displacement, δ_S. Two unshaded triangles shown in Fig. 2.4b represent the traction-separation law under pure normal or tangential mode. For any mixed-mode condition, Eq. 2.22 and

2.23 provide the mixed traction-separation law shown by the gray triangle. By determining the mixed critical traction and fracture energy from Eq. 2.22 and 2.23 the corresponding mixed critical cohesive length, δ_m can be obtained.

Finally, as shown in Fig. 2.4a, unloading after the damage initiation is always assumed to occur linearly toward the origin of the traction-separation plane and reloading subsequent to unloading also occurs along the same linear path until it reaches the softening envelope is reached.

2.2.3 The choice of cohesive zone parameters

There are many factors that can influence the parameters of fiber/matrix interfaces, e.g., the material properties of fiber and matrix, the curing process, thermal residual stresses, chemical reactions, fiber sizing and the limitations of the testing method. Consequently, a wide range of values have been used for the cohesive zone parameters in the literature. DiBenedetto (1991) measured the Mode-II fracture energy of an E-glass fiber/epoxy interface using a single fiber fragmentation test method. Depending on the quality of the fiber/matrix bonding, the Mode-II fracture energy was reported in the range 60-230 J/m^2. While Hampe and Marotzke (1995) reported that the Mode-II interface fracture energy is in the range 70-130 J/m^2 using a single fiber pull out test. In addition, it is known that the shear strength of the interface is much higher than its normal strength (Ogihara and Koyanagi, 2010). Varna et al. (1997) and Zhang et al. (1997) linked the numerical predictions and experimental observations of the fiber/matrix interface subjected to a transverse load. Thereby, the interfacial parameters were determined for both, fracture Mode-I and Mode-II. The fracture energies of a glass fiber/matrix interface for Mode-I and Mode-II were found to be 2 J/m^2 and 6 J/m^2, respectively, for fibers without any coupling agent in the sizing. For fibers with coupling agent, the fracture energies for Mode-I and Mode-II were determined to be 10 J/m^2 and 25 J/m^2, respectively. Martyniuk et al. (2013) performed a tensile test on a specimen including a single isolated glass fiber without coupling agent embedded in the epoxy inside the chamber of the Scanning Electron Microscope (SEM). They measured the interface fracture energies for Mode-I and Mode-II to be ~ 0.5 J/m^2 and 2-3 J/m^2, respectively. They also reported the maximum cohesive stress in Mode-I and Mode-II to be 5 MPa and 7 MPa, respectively. Canal et al. (2012) measured the maximum cohesive stress in Mode-I and Mode-II to be 50 MPa and 75 MPa, respectively, by pushing out a fiber in a very thin unidirectional laminate using a nano-indenter.

In this thesis, for the model in [P1] and [P2] with two fibers isolated in a large matrix zone the interfacial properties similar to Martyniuk et al. (2013) has been used. While the interfacial fracture energies for the fibers with coupling agent reported by Varna et al. (1997); Zhang et al. (1997) were used for [P4] and [P5] and the last unpublished study in chapter four. In these papers the maximum cohesive stresses measured by Canal et al. (2012) were considered.

2.3 Numerical methods

2.3.1 The principle of virtual work

For the numerical implementation in [P1-3] the incremental form of the principle of virtual work is adopted. Disregarding body forces, the principle reads

$$\int_V \dot{\sigma}_{ij}\delta\dot{\epsilon}_{ij}dV + \int_{S_I}(\dot{T}_n\delta\dot{u}_n + \dot{T}_t\delta\dot{u}_t)dS = \int_S \dot{T}_i\delta\dot{u}_i dS \tag{2.24}$$

where V denotes the volume of the model having the surface S and S_I is the surface of the fiber-matrix interface.

To control the numerical stability, a discontinuous increment analysis is used, such that when the first Gauss point in the bulk material reaches the plastic regime or when the first Gauss point in the cohesive elements of interface reaches $\lambda = \lambda_2$ the solver turns one step back and continue the solution with reduced increment size. The amount of step reduction is chosen such that a stable and converged solution is achieved. Thus, for further reduced time steps similar results are obtained.

2.3.2 Rayleigh-Ritz method

In a model such as the unit cell studied in [P3], large interfacial cracks compared to the size of the model lead to a severe non-linearity and instability. During debonding neither the load increment nor the displacement are useful as the prescribed quantity, since both change sign along the equilibrium path. To avoid this numerical problem during debonding, a combination of a Rayleigh-Ritz method with the finite element procedure proposed by Tvergaard (1976) was implemented in [P3]. In the case of generalized plane strain applied in [P3], a small number of nodal displacement increments are chosen on the edges, Δ_1, Δ_2 and Δ_3, as well as on the interfaces, δ_i where $i = 4, 5, ..., n$, see Fig. 2.5. Fig. 2.5a shows a schematic drawing of a deformed cell used in [P3]. The force in the x_1-direction applied on the cell side parallel to the x_2-direction, A_1, is F_1, the force in the x_2-direction applied on the cell side parallel to the x_1-direction, A_2 is F_2 and F_3 is the force in the x_3-direction applied on the cell side in the (x_1, x_2)-plane, A_3. Under generalized plain strain condition the unit cell thickness, t, remains constant which is assumed to be unit. The corresponding average stresses are then calculated as

$$\sigma_1 = \frac{F_1}{A_1} = \frac{F_1}{bt} \quad , \quad \sigma_2 = \frac{F_2}{A_2} = \frac{F_2}{at} \quad , \quad \sigma_3 = \frac{F_3}{A_3} = \frac{F_3}{ab} \tag{2.25}$$

then, by assuming $t = 1$ the incremental form of the stresses are given by

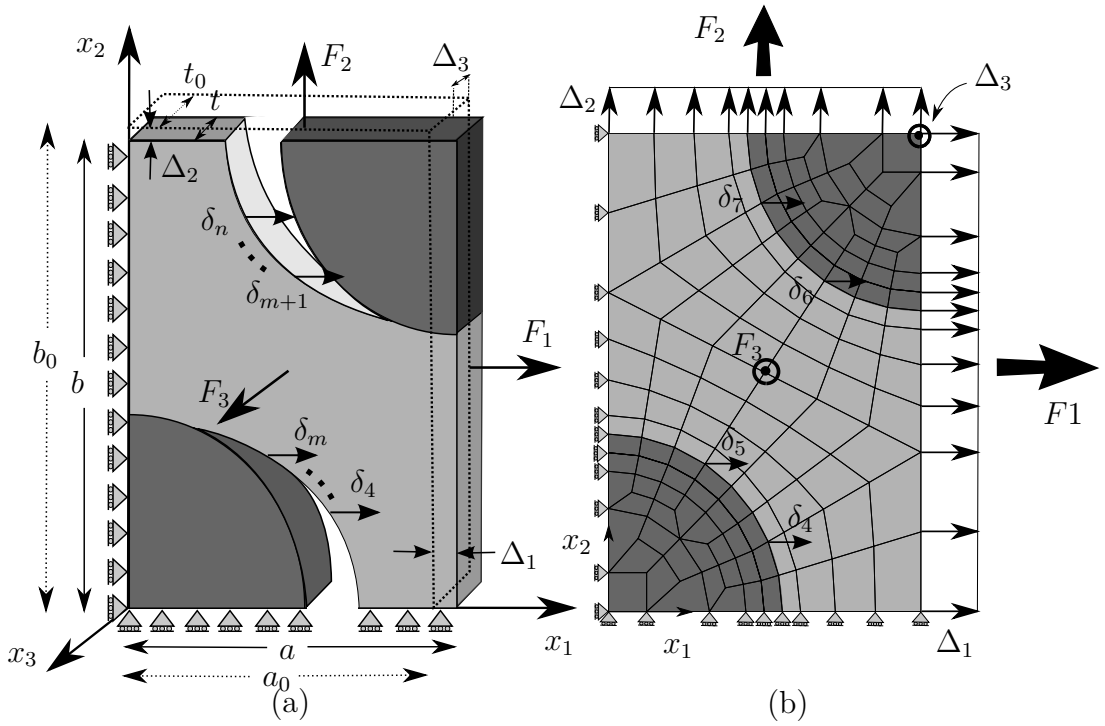

Figure 2.5 a) A chosen set of nodal displacement increments applied on the edges, Δ_1, Δ_2 and Δ_3, as well as on the interfaces, δ_i where $i = 4, 5, ..., n$, in a combination of a Rayleigh-Ritz method with the finite element procedure. b) An example of the set of nodal displacement increments in a finite element model of the unit cell studied in [P3]. This example consists of two incremental displacements on each interface.

$$\begin{aligned}
\dot{\sigma}_1 &= \sigma_1 - \sigma_{10} = \frac{\dot{F}_1}{b} - \frac{F_1}{b^2}\dot{b} = \frac{\dot{F}_1}{b} - \frac{F_1}{b^2}\Delta_2 \\
\dot{\sigma}_2 &= \sigma_2 - \sigma_{20} = \frac{\dot{F}_2}{a} - \frac{F_2}{a^2}\dot{a} = \frac{\dot{F}_2}{a} - \frac{F_2}{a^2}\Delta_1 \\
\dot{\sigma}_3 &= \sigma_3 - \sigma_{30} = \frac{\dot{F}_3}{ab} - \frac{F_3}{a^2 b}\dot{a} - \frac{F_3}{ab^2}\dot{b} = \frac{\dot{F}_3}{b} - \frac{F_2}{a^2}\Delta_1 - \frac{F_3}{ab^2}\Delta_2
\end{aligned} \tag{2.26}$$

where σ_{10}, σ_{20} and σ_{30} are the known values of stresses taken from the previous increment. Subsequently, the incremental forces are given by Eq. 2.26 as

$$\begin{aligned}
\dot{F}_1 &= b(\sigma_1 - \sigma_{10}) + \frac{F_1}{b}\Delta_2 \\
\dot{F}_2 &= a(\sigma_2 - \sigma_{20}) + \frac{F_2}{a}\Delta_1 \\
\dot{F}_3 &= ab(\sigma_2 - \sigma_{20}) + F_3\left(\frac{\Delta_1}{ab} + \frac{\Delta_2}{b}\right)
\end{aligned} \tag{2.27}$$

By a combination of a Rayleigh-Ritz method with the finite element procedure a reduced system of equations can be established as

$$\sum_{j=1}^{n} R_{ij}\delta_j = \dot{F}_i \tag{2.28}$$

where δ_1, δ_2 and δ_3 denote Δ_1, Δ_2 and Δ_3, respectively. The matrix, R_{ij}, and the external incremental load vector, $\dot{F}_i$, given by

$$R_{ij} = \sum_{k=1}^{N}\sum_{l=1}^{N} A_{kl}U_{ki}U_{lj} \quad , \quad \dot{F}_i = \sum_{k=1}^{N} B_k U_{ki} \tag{2.29}$$

where the global stiffness matrix, A_{kl}, and the load vectors, B_k, are known from the previous increment. Each trial function, U_{kj}, is calculated by prescribing the $j\breve{}th$ nodal incremental displacements, δ_j, to one and all other to zero. By this boundary condition and without changing A_{kl} the finite element problem is solved and gives the corresponding trial function, U_{kj}, based on the finite element approximation of Eq. 2.24.

The linear set of equations in Eq. 2.28 can be expanded as

$$\begin{pmatrix} r_{11} \\ r_{21} \\ r_{31} \\ r_{41} \\ \vdots \\ r_{n1} \end{pmatrix} \Delta_1 + \begin{pmatrix} r_{12} \\ r_{22} \\ r_{32} \\ r_{42} \\ \vdots \\ r_{n2} \end{pmatrix} \Delta_2 + \begin{pmatrix} r_{13} \\ r_{23} \\ r_{33} \\ r_{43} \\ \vdots \\ r_{n3} \end{pmatrix} \Delta_3 + \begin{pmatrix} r_{14} \\ r_{24} \\ r_{34} \\ r_{44} \\ \vdots \\ r_{n4} \end{pmatrix} \delta_4 + \cdots + \begin{pmatrix} r_{1n} \\ r_{2n} \\ r_{3n} \\ r_{4n} \\ \vdots \\ r_{nn} \end{pmatrix} \delta_n = \begin{pmatrix} \dot{F}_1 \\ \dot{F}_2 \\ \dot{F}_3 \\ 0 \\ \vdots \\ 0 \end{pmatrix} \tag{2.30}$$

Two ratios are prescribed between the stresses, $\kappa_1 = \dfrac{\sigma_2}{\sigma_1}$ and $\kappa_2 = \dfrac{\sigma_3}{\sigma_1}$. Eq. 2.30 can be rewritten using these stress ratios and two matrix raw operations, $\hat{r}_{2j} = r_{2j} - (\kappa_1 \dfrac{a}{b}) r_{1j}$ and $\hat{r}_{3j} = r_{3j} - (\kappa_2 a) r_{1j}$, resulting in

$$\begin{pmatrix} r_{11} \\ \hat{r}_{21} \\ \hat{r}_{31} \\ r_{41} \\ \vdots \\ r_{n1} \end{pmatrix} \Delta_1 + \begin{pmatrix} r_{12} \\ \hat{r}_{22} \\ \hat{r}_{32} \\ r_{42} \\ \vdots \\ r_{n2} \end{pmatrix} \Delta_2 + \begin{pmatrix} r_{13} \\ \hat{r}_{23} \\ \hat{r}_{33} \\ r_{43} \\ \vdots \\ r_{n3} \end{pmatrix} \Delta_3 + \begin{pmatrix} r_{14} \\ \hat{r}_{24} \\ \hat{r}_{34} \\ r_{44} \\ \vdots \\ r_{n4} \end{pmatrix} \delta_4 + \cdots + \begin{pmatrix} r_{1n} \\ \hat{r}_{2n} \\ \hat{r}_{3n} \\ r_{4n} \\ \vdots \\ r_{nn} \end{pmatrix} \delta_n = \begin{pmatrix} \dot{F}_1 \\ \dot{F}_2 - \dot{F}_1 \\ \dot{F}_3 - \dot{F}_1 \\ 0 \\ \vdots \\ 0 \end{pmatrix} \tag{2.31}$$

By prescribing one of the unknowns (Δ_1,Δ_2,Δ_3,$\delta_4, \cdots \delta_n$), this system of equation can be solved. Initially, Δ_1 is given but afterward the numerically largest amplitude is prescribed. By having Δ_1 and substituting that into Eq. 2.27, Eq. 2.31 reduces to

$$\begin{pmatrix} \hat{r}_{21} - \dfrac{F_2}{a} \\ \hat{r}_{31} - \dfrac{F_3}{a} \\ r_{41} \\ \vdots \\ r_{n1} \end{pmatrix} \Delta_1 + \begin{pmatrix} \hat{r}_{22} + \kappa_1 \dfrac{a}{b}\dfrac{F_1}{b} \\ \hat{r}_{32} - \dfrac{F_3}{b} + \kappa_2 \dfrac{a}{b} F_1 \\ r_{42} \\ \vdots \\ r_{n2} \end{pmatrix} \Delta_2 + \begin{pmatrix} \hat{r}_{23} \\ \hat{r}_{33} \\ r_{43} \\ \vdots \\ r_{n3} \end{pmatrix} \Delta_3 + \tag{2.32}$$

$$\begin{pmatrix} \hat{r}_{24} \\ \hat{r}_{34} \\ r_{44} \\ \vdots \\ r_{n4} \end{pmatrix} \delta_4 + \cdots + \begin{pmatrix} \hat{r}_{2n} \\ \hat{r}_{3n} \\ r_{4n} \\ \vdots \\ r_{nn} \end{pmatrix} \delta_n = \begin{pmatrix} a(\kappa_1\sigma_{10} - \sigma_{20}) \\ ab(\kappa_2\sigma_{10} - \sigma_{30}) \\ 0 \\ \vdots \\ 0 \end{pmatrix}$$

Solving this reduced system of linear equations gives the amplitudes of the trial functions, δ_l. Finally, the complete solution in each increment can be computed as the sum of the trial functions with the corresponding amplitudes as

$$u_k = \sum_{k=1}^{n} U_{kl}\delta_l \quad , \quad k = 1, 2, ...N \tag{2.33}$$

By this approach, a sudden stress-drop of the overall average stress-strain response may be captured. Furthermore, this procedure gives the possibility of controlling the stresses applied to the cell while still using displacement controlled symmetry boundary conditions by prescribing two ratios between the stresses, κ_1 and κ_2.

2.3.3 Mesh sensitivity

In this thesis, all the numerical studies use the cohesive zone models. In addition, in [P4], [P5] and the last unpublished study in chapter four the epoxy matrix is represented by a continuum damage model. It is well-known that both the cohesive zone models as well as the continuum damage models are mesh dependent. Therefore, it is necessary to ensure that the mesh is fine enough such that the mesh sensitivity has the minimum effect on the numerical results. In order to determine the mesh dependency in the cohesive zone model, Tvergaard and Legarth (2007) characterized the length of the fracture process region, ℓ, in the cohesive zone during crack

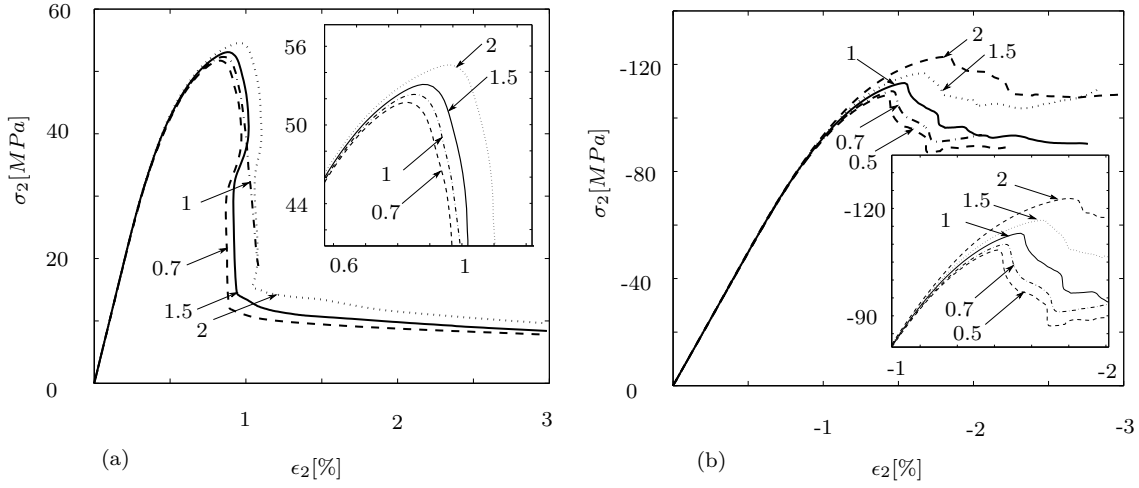

Figure 2.6 The overall stress-strain responses of a microstructral composite model studied in [P4], [P5] with different mesh element sizes under a) uniaxial transverse tension and b) uniaxial transverse compression

growth by the distance from the crack-tip (where in the trapezoidal model is $\lambda = 1$ or in the bilinear model is $\delta = \delta^c$) to the point ahead of the crack-tip (where in the trapezoidal model is $\lambda = \lambda_1$ or in the bilinear model is $\delta = \delta^0$, see Fig. 2.3 and Fig. 2.4). Tvergaard and Legarth (2007) found a good resolution and very little mesh dependence when the value of ℓ is several times larger than the length, Δ_0, of a square element in the uniform mesh region. This requirement is satisfied in the present computations as $\ell \geq 4\Delta_0$.

To analyse the mesh sensitivity of the continuum damage model, the overall stress-strain responses of a microstructural composite model with different mesh element sizes are compared in Fig. 2.6. Here, the model studied in [P4], [P5] is used which includes 70 monosized fibers randomly distributed in the matrix, see Fig. 4.10. Unlike Fig. 4.10, here the cell does not have any porosity. The number referred to each curve denotes the edge element length in a cell with the dimension $100 \times 100 \times 1$. The type of the bulk elements is a 6-node linear triangular element (C3D6) while the cohesive elements are meshed with an 8-node three-dimensional cohesive elements (COH3D8). In addition, the wedge shape and the sweep mesh technique has been used. By choosing this meshing method the nodes on the opposite surfaces of the cell are generated in a way that the constrains of the periodic boundary conditions can be defined. Fig. 2.6a and b show the overall stress-strain response of the cell with different mesh element sizes under uniaxial transverse tension and uniaxial transverse compression, respectively.

The results show that in both loading conditions the mechanical behavior in the elastic regime is not influenced by the size of the mesh. While different mechanical behavior appears with the onset of nonlinearity. Under uniaxial transverse tension the effect of meshing size is negligible. While under uniaxial transverse compression

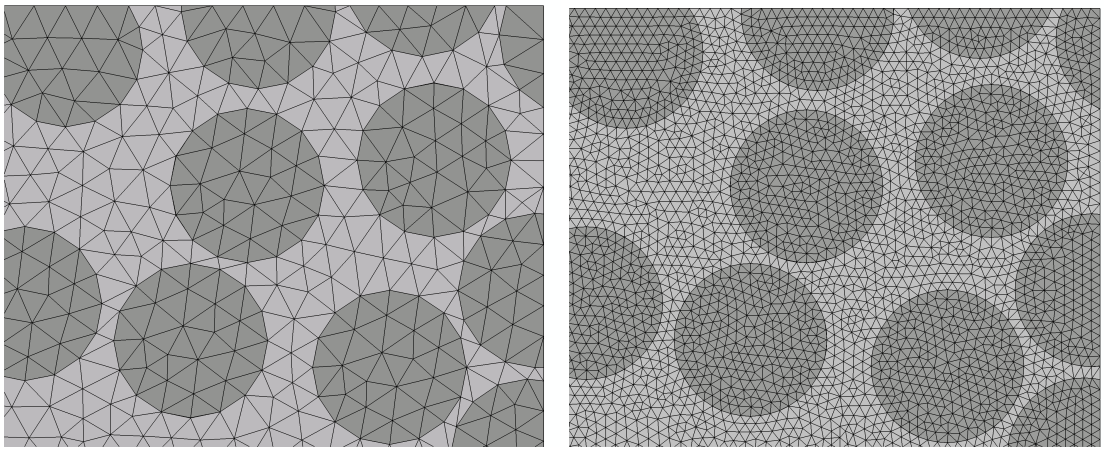

(a) Element size = 2

(b) Element size = 0.7

Figure 2.7 Examples of a model with a) coarse mesh and b) fine mesh.

Elem. Size	Num. Nodes	Num. Elements
2	8,006	6,599
1.5	15,952	13,944
1	26,660	23,940
0.7	55,428	51,431
0.5	95,876	90,512

Table 2.1 The total number of elements and nodes of a cell with different element sizes.

it leads to a significant difference both at the ultimate stress as well as in the softening regime. Under uniaxial transverse tension a sudden interfacial debonding is the dominant failure mechanism while the matrix shear band controls failure under uniaxial transverse compression. Fig. 2.7a and b show the top-right corner of the meshed cell with element size 2 and 0.7, respectively. Fig. 2.7 shows that although a mesh with the element size 2 has similar mechanical behavior as the element size 0.7, the coarse mesh can not produce a circular shape of fibers (voids) which can lead to stress concentration at the sharp corners, specially in the voids. As a conclusion, in this study the element size 0.7 has been used for all loading conditions. Using the element size 0.5 is computationally expensive as it doubles the number of elements in comparison with the element size 0.7 while the results are almost the same.

Chapter 3
Experimental test

This chapter explains the experimental procedure of the last unpublished study in Section 4.4. The material examined in this study is a $[0/90]_s$ glass-fiber/epoxy laminate. A processing method is used to induce micovoids in the laminate. The laminate is subjected to tensile loading perpendicular to 90° ply. During the test, *in-situ* observations are carried out inside the chamber of Scanning Electron Microscope (SEM).

3.1 Sample manufacturing

A set of $[0/90]_s$ glass-fiber/epoxy laminates is manufactured using the vacuum infusion technique. The fabric used in all laminates is a Devold $450g/m^2$ consisting of E-glass fibers with an epoxy compatible size. While the resin is *Hexions Epikote/Epikure MGS RIMR* 135/ *RIMH* 137 epoxy. The type of epoxy has exceptionally slow curing with very low exothermic reactions.

The samples were processed on a glass tool plate which was already treated with a semi-permanent chemical release agent. Peel-ply and perforated release foil and lastly a distribution mesh were added on top of the fabric, see Fig. 3.1a. The distribution mesh ensures that the resin can be transferred throughout the fibers. While the perforated release foil leads the resin to flow easier in the fabric. The peel-ply which is a layer between the laminate and other layers, eases the removal of the mesh from the laminate.

As shown in Fig. 3.1b, three samples were processed at once. Each laminate lay-up has a dimension of $150mm \times 250mm$ and are placed on the glass tool plate. Sealant tape was placed in between the samples such that the samples would not interact with each other, however, it is ensured that they have exactly the same external processing conditions (vacuum level, resin temperature, height difference of resin container, etc). In order to induce defects, a gap was considered between the time when the inlet and outlet were closed off. First sample is connected to the vacuum pump for one hour while the inlet is closed off. Second sample is connected for two hours, and the third sample is left connected overnight with a vacuum reduction of 60%.

After resin infusion, the samples were left at room temperature for 12-16 hours. Afterward, the samples were cured for 5 hours at a moderate temperature, $50°C$, which yields a cure degree around 90% and is enough to demould the samples. Subsequently, the demoulded samples were post-cured for 4 hours at $80°C$. This ply lay-up yields a laminate thickness of $\approx 0.7mm$ which is appropriate for the tensile

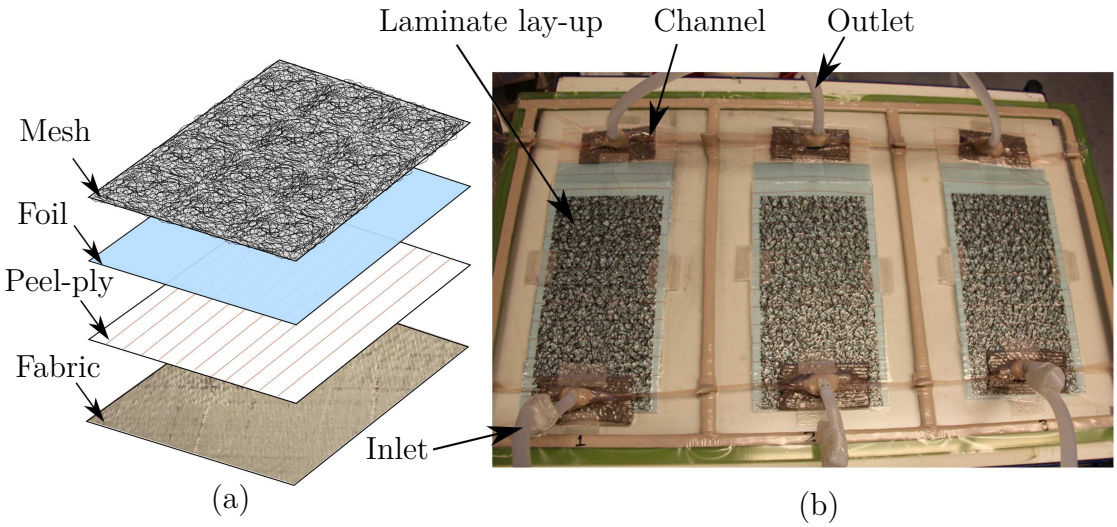

Figure 3.1 a) Schematic lay-up of a laminate consisting of a fabric, peel-ply, perforated release foil and mesh layer. b) Lay-up of three samples on a glass tool plate.

fixture to break the 90° ply. Finally, the laminates were cut into dimensions of $4.2mm \times 60mm \times 0.7mm$.

The sample surfaces of interest were polished, first manually using grinding paper SIC#1200 and SIC#2400, then by automatic polishing using polishing cloths MD-Dac (applied force 40 N, suspensions: DP Blue and Dia Pro Dac 3 μm) and subsequently MD-Nap (40 N, DP Blue and Dia Pro Dac 1 μm). The total automatic polishing time at each step was 5-15 minutes depending on the polished surface quality which is frequently checked using optical microscopy. The final dimension of samples are $4mm \times 60mm \times 0.7mm$, see Fig. 3.2a. Finally, the surface faced towards the microscope is made electrically conducting by a thin coat of gold.

Before *in-situ* SEM observation, an image of the surface of each sample is captured using optical microscopy. As shown in Fig. 3.2b, it is possible to find the location of defects prior to loading.

3.2 *In-situ* experimental test

As shown in Fig. 3.3, the specimen is subjected to the tensile load using a special tensile loading fixture with 1000 N load cell (Sørensen et al., 2002) designed for testing in SEM. The fixture is mounted on the x, y, z stage of the vacuum chamber of SEM (Zeiss, EVO60). The polished and coated surface is oriented towards the microscope electron gun and detectors. By this setting *in-situ* observation of crack initiation under the applied tensile loading can be obtained. During the micro scale experiments, the load is applied to the specimen in increments. After applying the tensile loading, the sample was unloaded by $\approx 30\%$ in order to minimize deformation due to creep and to prevent damage evolution during the scanning. However, since

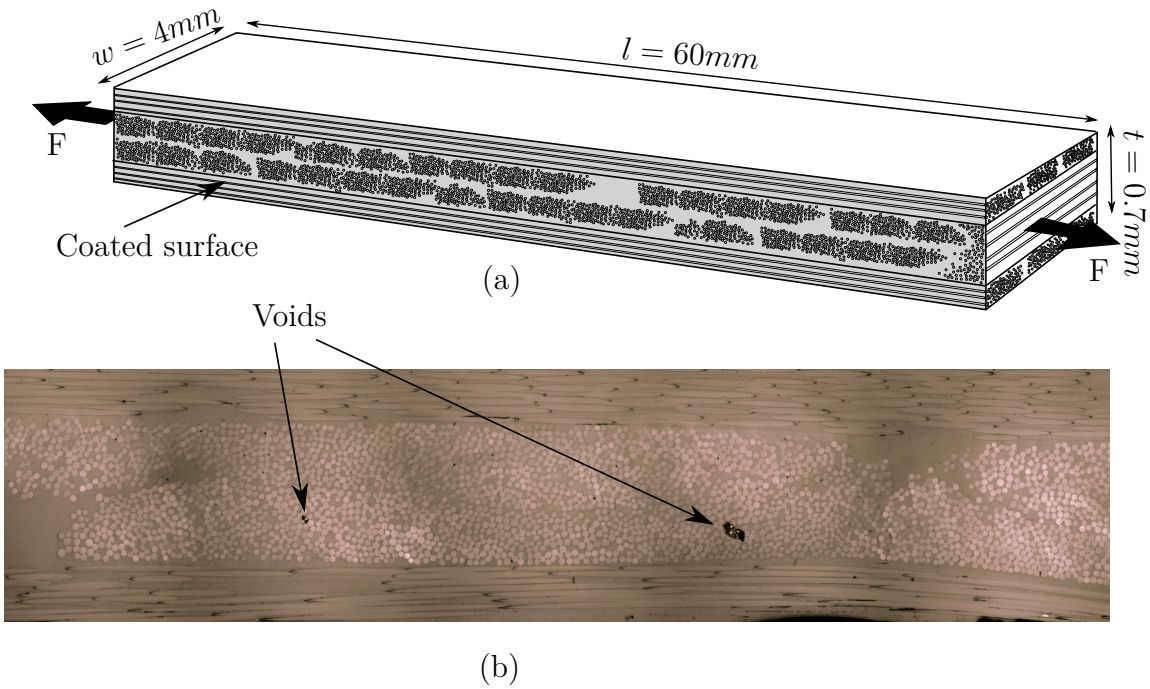

Figure 3.2 a) Schematic drawing of $[0/90]_s$ laminate showing the dimension. b) Preliminary optical microscopy image of the polished surface prior to *in-situ* experiments.

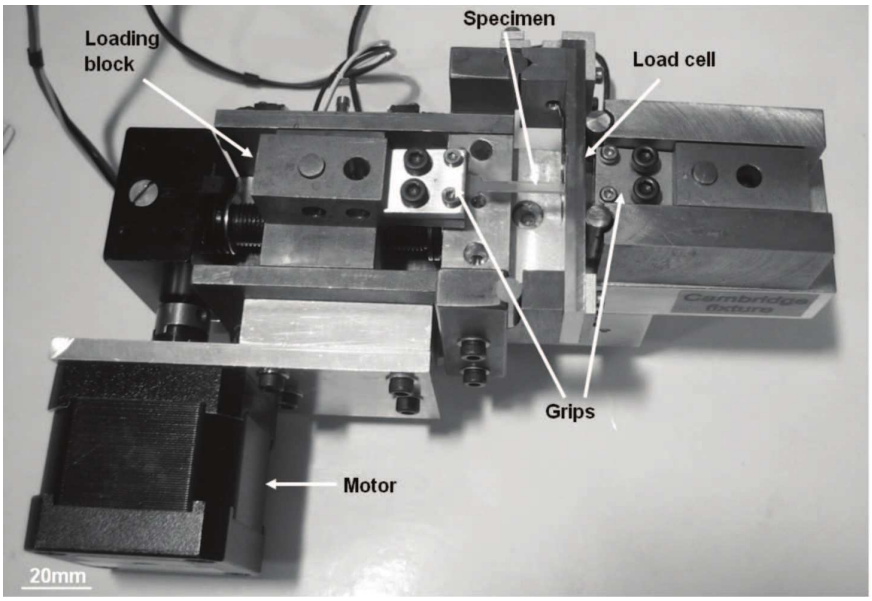

Figure 3.3 Test set-up for tensile testing in SEM. A motor drives a spindle which moves one of the loading blocks and thus one of the grips, resulting in tension of the specimen.

damage normally occurs at the maximum applied load, the maximum load before unloading at each load step is reported. This loading-unloading method may arrest

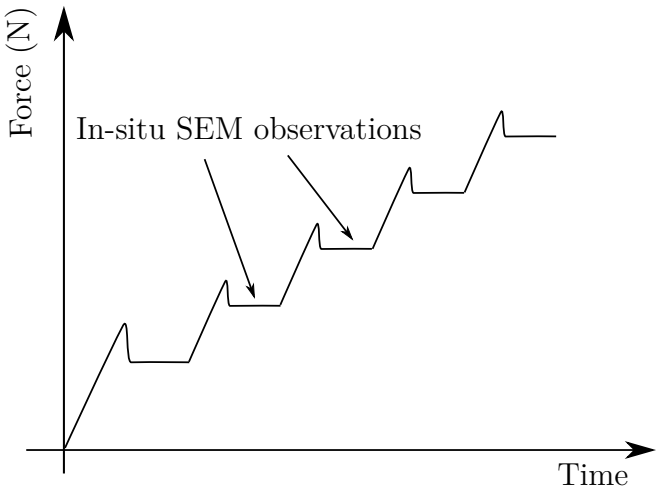

Figure 3.4 Step wise loading in *in-situ* SEM observation. After each loading step, the specimen is unloaded 30% and afterward the specimen scanning is performed.

the initiated and propagated cracks and enable to observe and capture images showing damage evolution using SEM. This step wise loading process is schematically shown in Fig. 3.4. For data analysis, the load was converted to a nominal stress calculated as the applied force divided by the cross sectional area of the specimen gauge section.

SEM images of the free surface of the sample were acquired with a magnification of $\approx 500 \times -2000\times$. This wide range of magnification allowed for both searching for cracks over the laminate surface as well as accurately scanning the initiated cracks. However, the focus of scanning is on the locations of defects which have been already marked by the preliminary optical microscopy images. During SEM observation, the secondary electron signal mixed with the back scattered electron signal were used which allowed for imaging of the charged surface during the scanning period. The results of the experimental test are shown in Fig. 3.5 and Fig. 3.6. Fig. 3.5 demonstrates a cracked $[0/90]_s$ laminate subjected to transverse loading. It is worth to note that there is almost an equal spacing between the cracks developed perpendicular to the loading direction. This phenomena will be elaborated in Section 4.4. Fig. 3.6a and Fig. 3.6c show a microvoid in the resin and the microvoids trapped between the fibers, respectively. Fig. 3.6b and Fig. 3.6d depict the previous images after applying the tensile load. It is shown that cracks initiated from the voids and subsequently propagated along the fiber/matrix interfaces. In Section 4.4, these experimental observation will be utilized to be compared with the results of the numerical modeling.

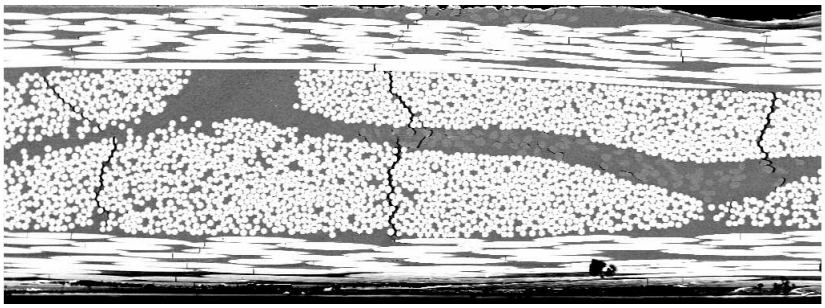

Figure 3.5 The cracked $[0/90]_s$ laminate subjected to transverse loading captured by SEM scanning.

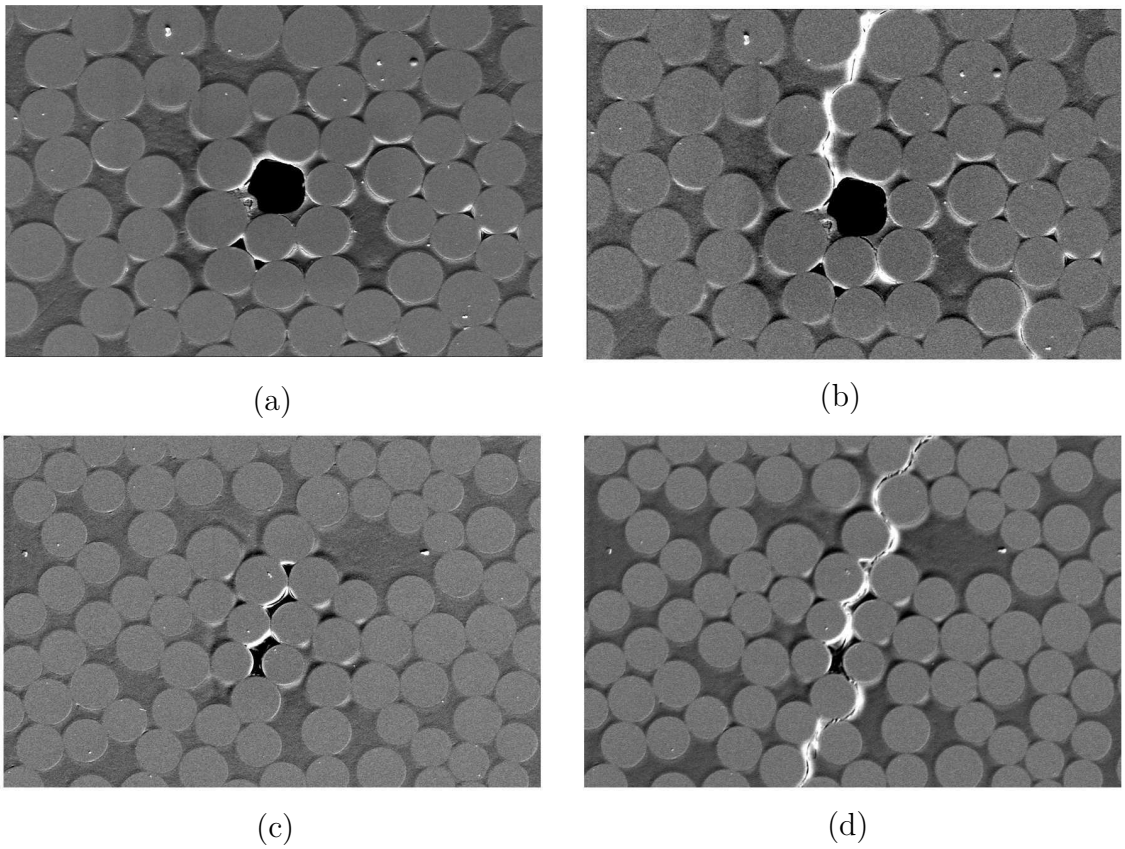

Figure 3.6 a) A micro void in the matrix and c) the voids trapped between the fibers. b) and d) show the cracks initiated from the microvoids.

Chapter 4
Summary of results

This chapter is a summary of the results of the papers included in this thesis.

The first section studies the mixed mode debonding in fiber/matrix interfaces to understand one of the first micromechanical failure mechanisms occurring in composite materials. This study aims at exploring ways to stabilize the early stage of crack debonding in order to determine the interfacial properties for the entire mixed-mode range by *in-situ* observations.

Section 4.2 uses the unit cell approach by assuming a periodic distribution of fibers to predict the macroscopic response of composite under generalized plane strain condition. Finally, the effects of interfacial parameters, fiber positioning and the fiber volume fraction on the overall stress-strain response of composite are discussed.

In section 4.3 different inter-fiber micromechanical failure mechanisms occurring in unidirectional composites have been numerically studied. In this part a larger cell is modeled which includes 70 monosized fibers randomly distributed in the matrix. In addition, two different types of microvoids are randomly generated in the cell, namely; the trapped voids between fibers and circular voids isolated in the matrix. The focus of this section is on the effect of porosity on the macroscopic stress-strain response of composites. Finally, the computational predictions of the failure locus of porous composites in both $(\sigma_2 - \tau_{23})$ and $(\sigma_2 - \tau_{12})$ stress spaces are compared with the Puck's analytical model.

In the last section, the effect of microvoids in the inter-fiber failure of the confined 90° lamina are studied according to the transverse tensile test inside the SEM. The experimental results are compared with the numerical modeling. The methods used in the modeling are similar to the section 4.3.

4.1 Mixed-mode interfacial debonding [P1], [P2]

Debonding in fiber/matrix interfaces occurs in a mixed mode fracture mechanism. Under transverse tension, debonding initiates in Mode-I fracture with very fast crack growth along the interface. Subsequently, the stable crack growth along the interface is due to mixed Mode-I/II fracture. The unstable crack growth in the initial stage of debonding limits the measurement of the normal debonding properties of the interfaces in experimental *in-situ* observations. Martyniuk et al. (2013) reported that the first interfacial crack for a single-fiber embedded in a polymer matrix was observed at the angle 40°- 60°.

In this section, two configurations have been considered. The first model consists of two fibers while the second case considers a fiber in the vicinity of a hole both cases isolated in a large zone of the matrix. By means of the finite element modeling, the effect of positioning of one fiber in the vicinity of another fiber (or a hole) on stabilizing interfacial debonding is studied. Fig. 4.1a shows a 2D cell with two circular fibers (or one fiber and a hole) which are embedded in the matrix. The cell is under uniaxial tension by imposing a uniform normal displacement, Δ_1, in the x_1-direction. The dimension of the cell is determined by the length, b, the width, a, and the radii of fibers which are assumed to be identical $R^{\#1}$=$R^{\#2}$ = R. The cell is under plane stress condition to numerically model the specimen surface at which the debonding is monitored by the SEM in the experimental *in-situ* test.
The boundary conditions are implemented incrementally as follows

$$\begin{aligned} &\dot{T}_2 = 0 \quad \text{and} \quad \dot{u}_1 = 0, \quad \text{on} \quad x_1 = 0 \\ &\dot{T}_1 = 0 \quad \text{and} \quad \dot{u}_2 = 0, \quad \text{on} \quad x_2 = 0 \\ &\dot{T}_2 = 0 \quad \text{and} \quad \dot{u}_1 = \dot{\Delta}_1, \quad \text{on} \quad x_1 = a \\ &\dot{T}_1 = 0, \quad \text{on} \quad x_2 = b \end{aligned} \tag{4.1}$$

Here, the focus is on the interfaces close to the ligament where the interaction of fiber-fiber or fiber-hole is dominant. Therefore, as shown in Fig. 4.1b, it is assumed that only half of the interface of each fiber which is in the ligament can debond while the other half is fully bonded. As shown in Fig. 4.1b, the debonding angle in each fiber is divided into two parts; The positive angle which denotes the crack starting from the zero-angle until the crack tip in the ligament and the negative angle which shows the crack initiating from the zero-angle to the crack tip away from the ligament. The material and interfacial properties are given in Table 4.1. The cohesive zone parameters are chosen according to the experimental measurements reported by Martyniuk et al. (2013).

Fig. 4.2 shows the effect of two positioning parameters; The ligament thickness, d, and the positioning angle, α, on the interfacial debonding behavior. The plots are given as the debonding angle as a function of the normalized remote stress. Fig. 4.2a and b are the results of the two-fiber configuration while Fig. 4.2c and d show the results of the fiber-hole model. The results are compared with a single fiber model

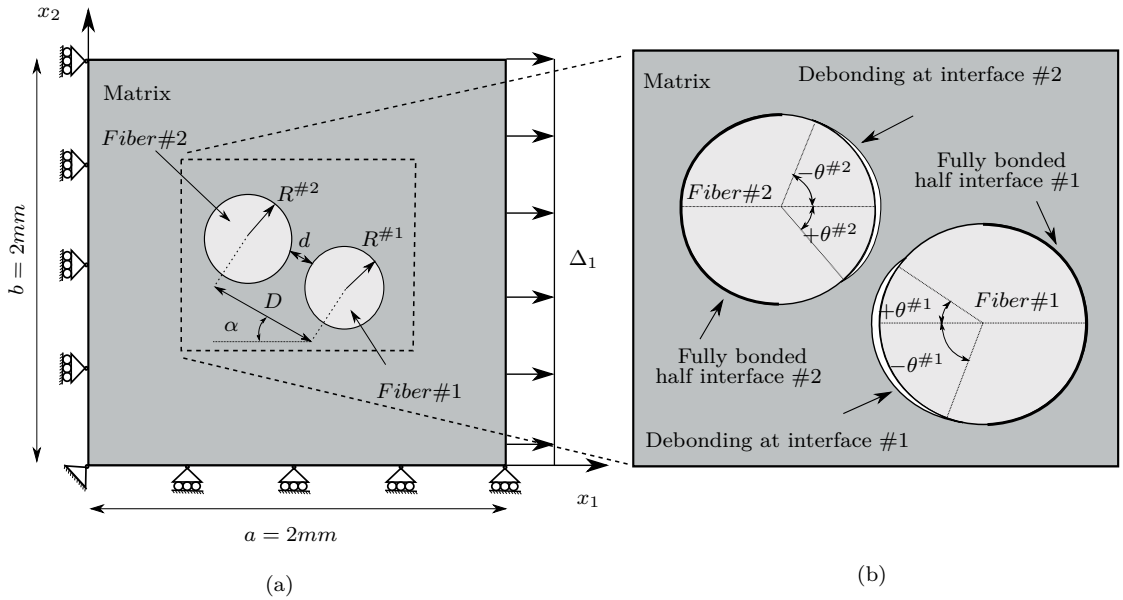

Figure 4.1 a) The 2D model including two circular fibers (or one fiber and a hole) embedded in the matrix. The dimensions, loads and the coordinate system are shown. The position of fibers with respect to each other is specified by the position angle of the fibers, α, and the thickness of the ligament, d. b) A deformed cell with partly debonded interfaces. The bold half circles around the fibers denote the fully bonded area of each fiber.

Fiber		Matrix			Interface				
E_f $[GPa]$	ν_f	E_m $[GPa]$	ν_m	σ_y $[MPa]$	Φ $[\frac{J}{m^2}]$	σ_{max} $[MPa]$	$\delta_n^c = \frac{1}{5}\delta_t^c$ $[\mu m]$	λ_1	λ_2
72	0.21	3	0.3	15	1	6	0.16	0.01	0.1

Table 4.1 Constants of the constitutive models of the fibers, the matrix and the interface.

as a reference case. The plots of both configurations indicate that decrease of α significantly reduces the slope of the curves with positive debonding angles which denotes a slower (more stable) crack propagation. In addition, this reduction starts in earlier stage of debonding (more dominant Mode-I fracture) for smaller α values. Comparing Fig. 4.2a with b and Fig. 4.2c with d shows that this crack stabilization effect is more pronounced in smaller ligament thicknesses. Furthermore, in the fiber-hole model decrease of α also postpones interfacial debonding.

The effect of the positioning parameters; d and α are shown in Fig. 4.3. The plots show the mode mixity angle, φ, defined in Eq. 2.20 as a function of the debonding angle. Fig. 4.3a and b show the results of the two-fiber configuration and Fig. 4.3c and d belong to the fiber-hole model. The corresponding results for a single fiber model is also given as a reference case. The results show that smaller α leads to steeper slopes of the curves in positive debonding angles. Higher slopes of the curves denote larger rate of increase in the mode mixity. Therefore, smaller α reduces the interval of debonding angle at which Mode-I fracture is dominant. On the other hand, increase of mode mixity stabilize the crack propagation as it was shown in Fig. 4.2. Comparing the results of Fig. 4.3a and Fig. 4.3c shows that in the two-fiber model the effect of positioning parameters can lead to a stable crack growth in more dominant Mode-I failure whereas in the fiber-hole configuration the stable crack initiates under a mixed mode failure. Consequently, this study suggests that the two-fiber configuration can stabilize the crack initiation under dominant mode-I which is of interest for the experimental measurements of the normal debonding properties of the interfaces.

Contour plots of the accumulated equivalent plastic strain, ϵ_e^p, of the two-fiber model (Fig. 4.4a and b) and the fiber-hole model (Fig. 4.4c and d) are depicted. All plots are captured at $\epsilon_{11} = 1\%$ and ($\Sigma_{11}/\sigma_{max} = 3.2$) for the position angle, $\alpha = 15^\circ$. The figures show that smaller d value leads to more plastic deformation of the matrix in the ligament. Fig. 4.3 shows that for small d values the interfacial crack opening in the ligament grows very slowly when the crack tips meet each other. Similar to Fig. 4.3, Fig. 4.4 shows that the crack tips unload due to the other opened interface. Further loading leads to severe plastic deformations in the ligament instead of further interfacial crack growth. This phenomena has been explained in detail in [P2].

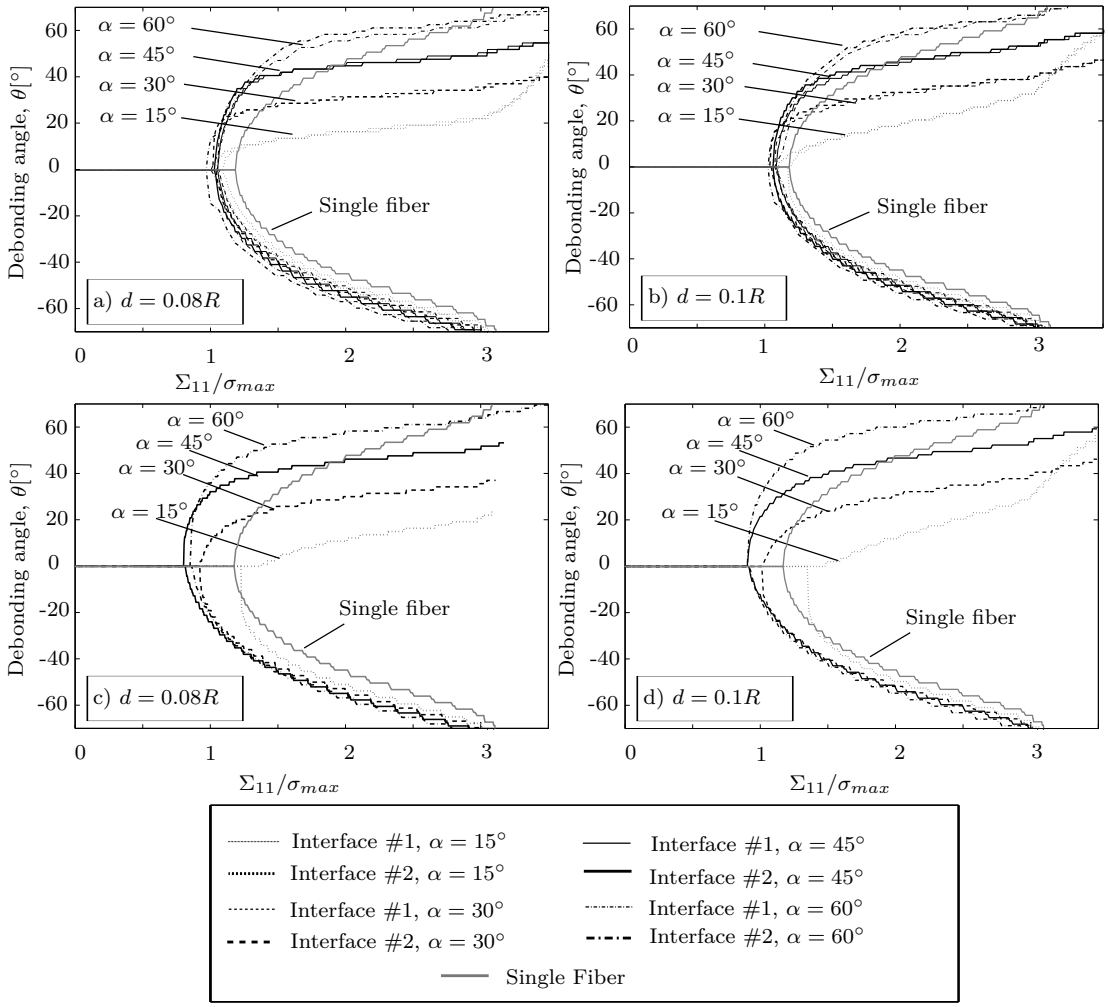

Figure 4.2 The effect of the positioning parameters. The plots show the debonding angle as a function of the normalized remote stress. The results of two different ligament thicknesses for two-fiber configuration are shown in a and b while for fiber-hole model are given in c and d.

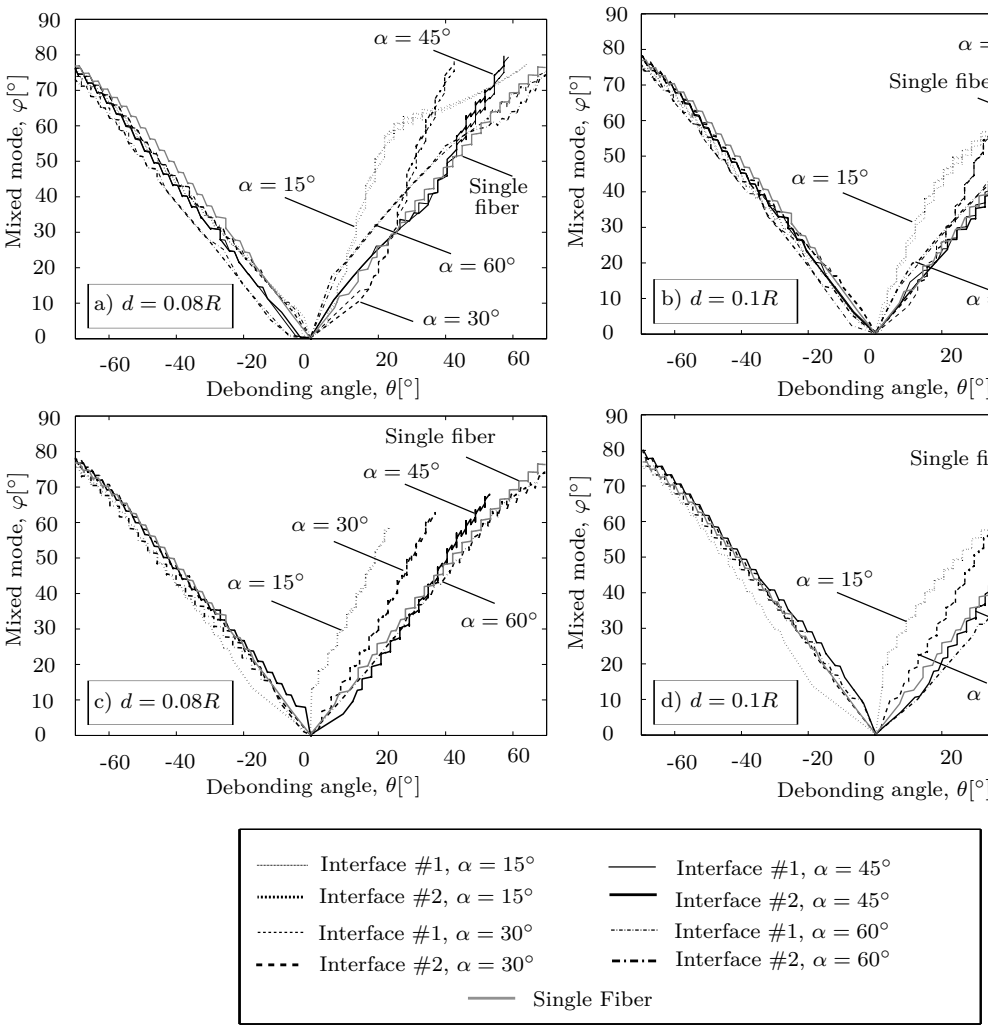

Figure 4.3 The effect of the positioning parameters. The plots show the mode mixity angle, φ, as a function of the debonding angle. The results of two different ligament thicknesses for the two-fiber configuration are shown in a and b while for the fiber-hole configuration are given in c and d.

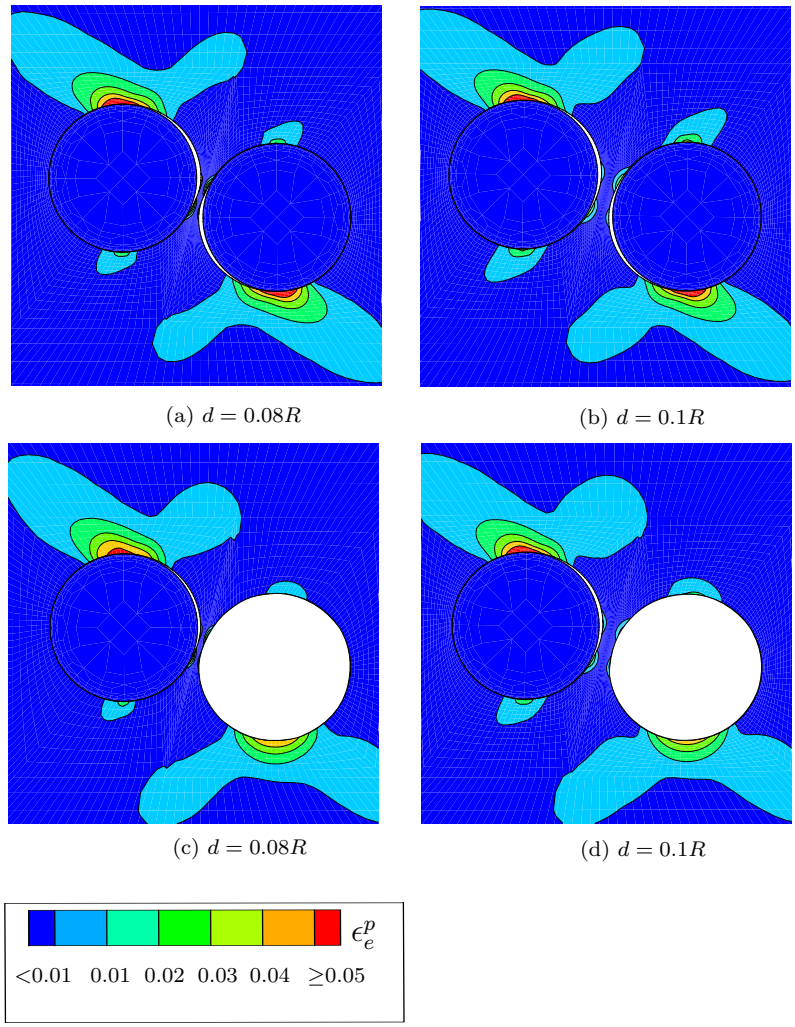

(a) $d = 0.08R$ (b) $d = 0.1R$

(c) $d = 0.08R$ (d) $d = 0.1R$

Figure 4.4 Contours of the accumulated equivalent plastic strain, ϵ_e^p, of two-fiber and fiber-hole models. The results are shown at $\epsilon_{11} = 1\%$ and $\Sigma_{11}/\sigma_{max} = 3.2$ for the position angle, $\alpha = 15^\circ$ and two different ligament thicknesses; a) and c) $d = 0.08R$, b) and d) $d = 0.1R$.

4.2 Uniformly fiber distribution approach [P3]

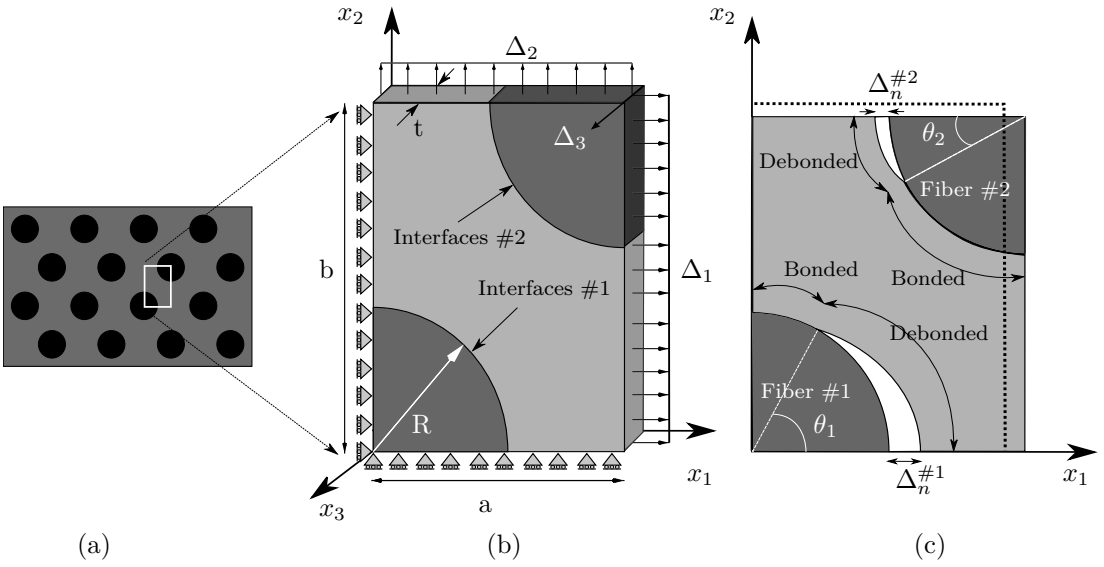

Figure 4.5 a) The periodic hexagonal fiber distribution in the matrix. b) The unit cell including two quarter circular fibers showing the dimensions, loads and the coordinate system. c) A deformed and partly debonded unit cell under an x_1-direction tensile load dominated. The dash line denotes the undeformed shape of the unit cell.

The overall response of unidirectional composites is studied by considering a simplified unit cell including two quarter circular fibers. This unit cell represents a periodically hexagonal distribution of fibers, see Fig. 4.5a. This idealized fiber arrangement results computations in which are less time consuming. Furthermore, by using this unit cell approach the possibility of having different fiber-matrix strengths exists which is not the case of standard unit cell analyses containing a single fiber. The dimension of the unit cell is determined by the thickness, t, the length, b, the width, a, and the radius of the fibers, R, which yields the fiber volume fraction $V_f = \frac{\pi R^2}{2ab}$. The cell is subjected to normal load in the three directions only; i.e. $(\Sigma_{11}, \Sigma_{22}, \Sigma_{33}) \neq 0$ whereas $\Sigma_{12} = \Sigma_{13} = \Sigma_{23} = 0$. Due to the symmetries in geometry and loads, the cell edges remain straight during the deformations. It is emphasized that this generalized plane strain problem formulation only includes a single uniform in-plane deformation imposed by the displacement Δ_3. The boundary conditions are implemented incrementally as follows

$$
\begin{array}{llllll}
\dot{u}_1 = 0 & \text{and} & \dot{T}_2 = 0, & \text{on} & & x_1 = 0 \\
\dot{u}_1 = \dot{\Delta}_1 & \text{and} & \dot{T}_2 = 0, & \text{on} & & x_1 = a \\
\dot{u}_2 = 0 & \text{and} & \dot{T}_1 = 0, & \text{on} & & x_2 = 0 \\
\dot{u}_2 = \dot{\Delta}_2 & \text{and} & \dot{T}_1 = 0, & \text{on} & & x_2 = b \\
\dot{u}_3 = 0, & & & \text{on} & & x_3 = 0 \\
\dot{u}_3 = \dot{\Delta}_3, & & & \text{on} & & x_3 = t \\
\dot{T}_1 = 0 & \text{and} & \dot{T}_2 = 0, & \text{on} & x_1 \in]0, a[\quad \text{and} \quad x_2 \in]0, b[&
\end{array}
\tag{4.2}
$$

where $\dot{\Delta}_1$ and $\dot{\Delta}_2$ describe incremental displacement quantities on the two edges of the unit cell and $\dot{\Delta}_3$ is the incremental displacement quantity in the fiber direction, and T_i are surface tractions. Two constant stress-ratios, $\kappa_1 = \frac{\Sigma_{22}}{\Sigma_{11}}$ and $\kappa_2 = \frac{\Sigma_{33}}{\Sigma_{11}}$, are defined to impose the triaxial normal loading under generalized plane strain condition. The matrix material properties are $\nu_m = 0.35$, $\frac{\sigma_0}{E_m} = 0.004$ and the strain-hardening exponent, $n = 5$ and the material properties of the fibers are $\nu_f = 0.3$ and $\frac{E_f}{E_m} = 6.0$. The interfacial parameters are $\delta^c = \delta_n^c = \delta_t^c = 0.02R$, (both interfaces), while interface #1 has $\sigma_{max}^{\#1} = 1.5\sigma_y$, $\lambda_1^{\#1} = 0.2$ and $\lambda_2^{\#1} = 0.4$, and for interface #2, $\sigma_{max}^{\#2} = 2\sigma_y$, $\lambda_1^{\#2} = 0.3$ and $\lambda_2^{\#2} = 0.5$. These parameters are unchanged in the following calculations unless otherwise stated.

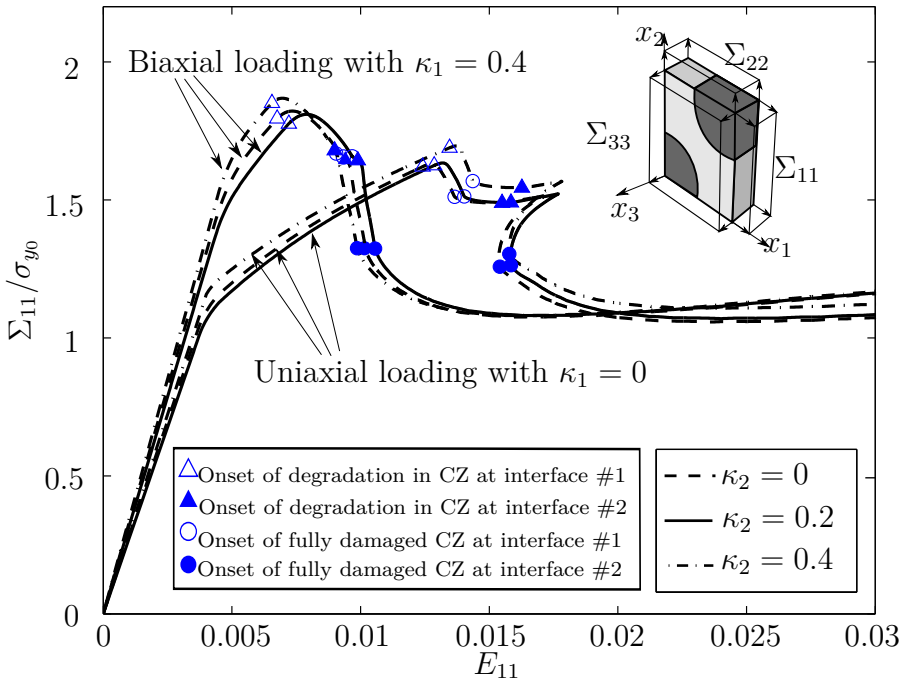

Figure 4.6 Effect of different loading conditions, $\kappa_1 = \frac{\Sigma_{22}}{\Sigma_{11}}$ and $\kappa_2 = \frac{\Sigma_{33}}{\Sigma_{11}}$ on the stress-strain curve.

Fig. 4.6 shows the effect of different loading conditions imposed by different stress ratios, κ_1 and κ_2 on the overall stress-strain response of the unit cell. A larger κ_1 value increases the loading in the x_2-direction which tends to open the interfaces. On the other hand, increase of κ_2 contracts the unit cell because of loading in the x_3-direction which has closing effect. Therefore, as shown in Fig. 4.6, onset of degradation in cohesive zone starts at a lower overall strain under biaxial loading and a larger κ_2 enhances the overall stress response.

The effect of the maximum cohesive stress, σ_{max}, on the macroscopic stress-strain response of unit cell is shown in Fig. 4.7. The results indicate that generally increase of σ_{max} rises the maximum ultimate stress of the composite. However, Fig. 4.7a shows that larger σ_{max} at both interfaces leads to a more sudden stress drop. In addition, numerical instability increases during debonding of interface #2 when the interfaces are stronger. Fig. 4.7b shows that increase of interfacial strength in interface #2 interacts the debonding behavior of the other interface although the parameters of interface #1 are kept unchanged.

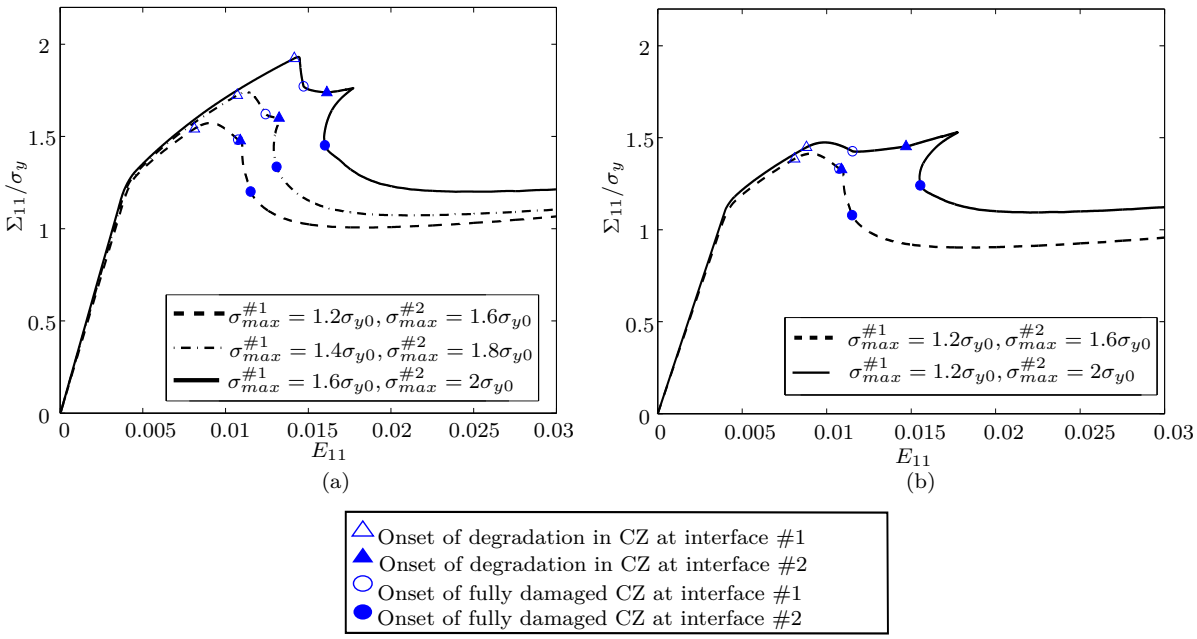

Figure 4.7 Effect of the maximum cohesive stress, σ_{max}, on the stress-strain curve where a) shows the effect of increasing σ_{max} in both interfaces while keeping the difference between σ_{max} of the two interfaces constant, b) illustrates the interaction between two interfaces when the maximum cohesive stress at interface #1 is constant while interface #2 increases.

The effect of fiber volume fraction, V_f, on the overall stress-strain response is shown in Fig. 4.8. The results of unit cells with debonding interfaces are compared with those corresponding to fully bonded interfaces. In both cases larger V_f leads

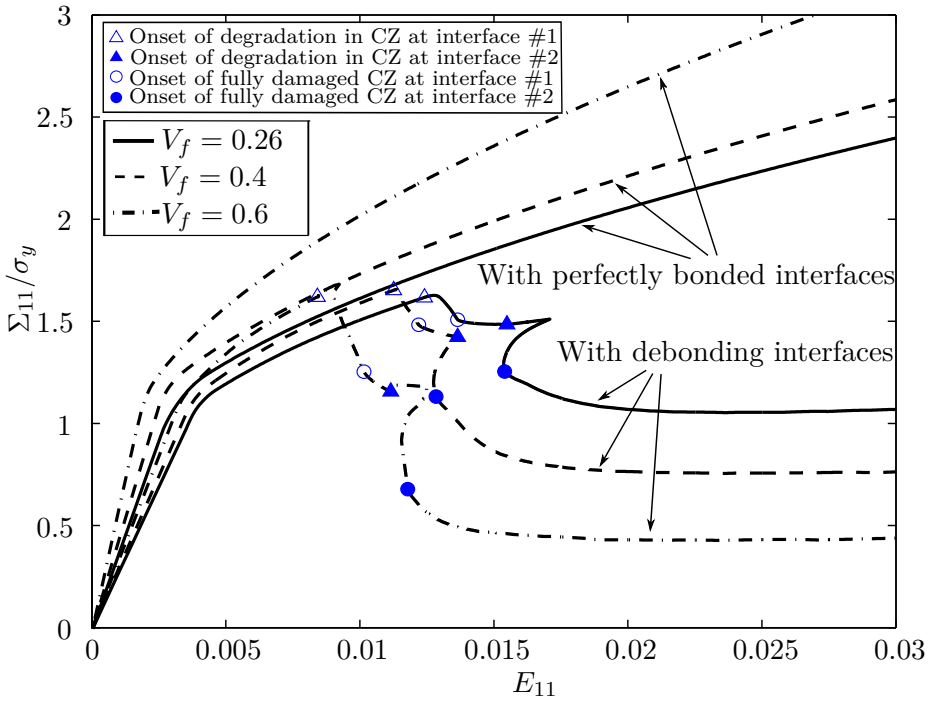

Figure 4.8 Effect of the fiber volume fraction, V_f, on the stress-strain curve.

to higher overall stress response. However, due to interfacial debonding each unit cell with weak interfaces results in a lower stress response compared with its corresponding unit cell with perfectly bonded interfaces. Increase of V_f also leads to larger debonding cracks in a cell which cause earlier onset of interfacial debonding and lower load-carrying capacity after the stress drops.

Fig. 4.9 demonstrates the effect of fiber volume fraction, V_f, on the damage evolution of the unit cell. The contour plots show change of the von Mises stress distribution influenced by the fiber volume fraction. Larger V_f concentrates the matrix plastic deformation in the ligament between two fibers while in the fully bonded case the highest stress can be observed at the two opposite corner of the cells. In addition, Fig. 4.9 indicates that larger V_f leads to increase of crack length along the interface and also larger normal crack end opening, Δ_n, at a certain overall strain.

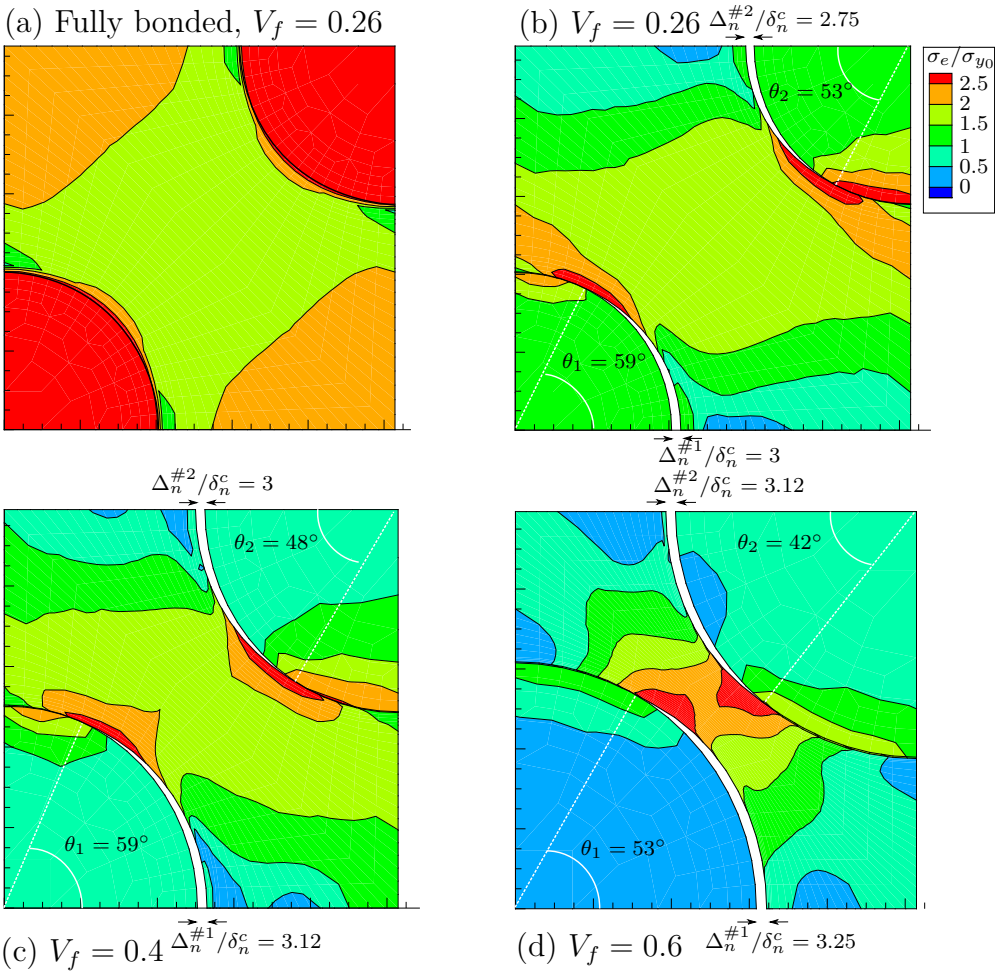

Figure 4.9 The effect of fiber volume fraction, V_f, on the contour plots of the normalized von Mises stress, $\frac{\sigma_e}{\sigma_y}$, at $E_{11} = 0.029$, see Fig. 4.8.

4.3 Randomly fiber distribution approach [P4], [P5]

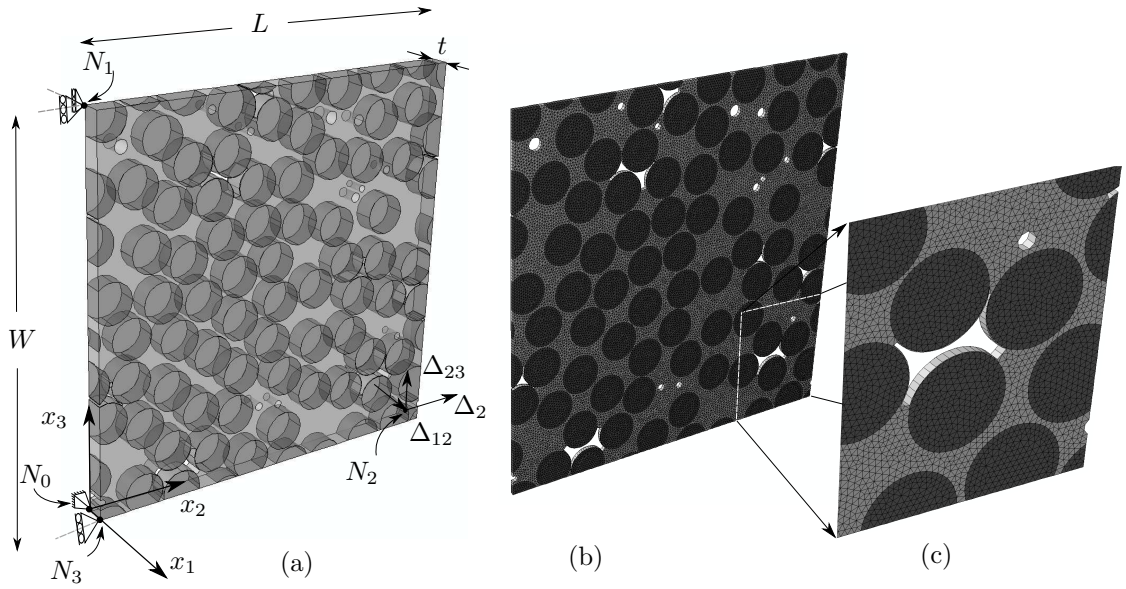

Figure 4.10 a) Illustration of the fiber and void distribution in a cross-section of a fiber-reinforced composite. The dimensions, loads and the coordinate system are shown. The cell can be subjected to transverse tension/compression by applying $\dot{\Delta}_2$, out-of-plane shear by applying $\dot{\Delta}_{23}$, out-of-plane shear by imposing $\dot{\Delta}_{23}$ and in-plane shear by applying $\dot{\Delta}_{12}$. b) Finite element mesh of the cell. The mesh includes around 48,000 solid elements, 3,350 cohesive elements and 56,000 nodes. c) A close view of the mesh is shown.

In unidirectional composites, several inter-fiber failure mechanisms happen under different transverse normal and/or shear loading conditions. These physical failures generate different failure planes. Fiber/matrix debonding and localized matrix deformation occur along these fracture planes whereas other zones of composite may remain undamaged. This micromechanical phenomena can not be captured by the unit cell approach which assumes a regular distribution of fibers. The regular fiber arrangement results that the entire matrix as well as fiber/matrix interfaces deform simultaneously and similarly to the unit cell with few fibers(normally one or two).

Significant advancements in the power of computers and the computational tools have made it possible to compute a larger volume element including dozens of fibers. Assuming a randomly arrangement of several fibers the composite material is modeled more realistically. Using the randomly fiber distribution approach, this section aims at numerically capturing different inter-fiber failure mechanisms by taking into account the micromechanical damage processes. The focus of this section is on the effect of microvoids on the microscopic and macroscopic behavior of composites.

A schematic of the microstructure of unidirectional composites including fibers, matrix and microvoids is depicted in Fig. 4.10a. The chosen cell includes a random

distribution of circular fibers, circular microvoids and microvoids isolated between the fibers. This model considers that all voids and fibers are cylindrical. The dimension of the cell is determined by the length, L , the width, W, the thickness, t, and the radius of the N_f monosized fibers, R_f, which yields the fiber volume fraction $V_f = N_f \pi R_f^2 / WL$. The total void volume fraction, V_v, is the sum of the void volume fraction of the N_v circular voids of radius R_v^i, $\sum_{i=1}^{N_v} \pi {R_v^i}^2 / WL$, plus the void volume fraction due to the trapped voids isolated between the fibers. The cell in these analyses is always a square cell with $L = W = L_0$.

The cell contains a random distribution of 70 monosized fibers of radius $R_f = 0.1L_0$ leading to the fiber volume fraction of $\sim 60\%$ and void volume fraction of $1 - 5\%$, which are realistic values for composites of good quality. The majority of this porosity is found in voids trapped between fibers while some isolated voids are also dispersed in the matrix. Fibers and voids intersecting the cell edges were split and copied to the opposite sides of the square cell to create a periodic microstructure.

Fig. 4.10a shows a master node, N_0, and three slave nodes, N_1, N_2 and N_3. Different loading conditions can be defined by specifying proper boundary conditions at these nodes. The boundary condition in the $(\sigma_2 - \tau_{23})$ stress space is imposed by

$$\begin{array}{ll} u_1 = u_2 = u_3 = 0 & \text{at } N_0 = (0,0,0) \\ u_1 = u_2 = 0 & \text{at } N_1 = (0,0,L_0) \\ u_2 = \Delta_2, u_3 = \Delta_{23} & \text{at } N_2 = (0,L_0,0) \\ u_1 = 0 & \text{at } N_3 = (t,0,0) \end{array} \tag{4.3}$$

while the boundary condition for the $(\sigma_2 - \tau_{12})$ stress space is specified by

$$\begin{array}{ll} u_1 = u_2 = u_3 = 0 & \text{at } N_0 = (0,0,0) \\ u_1 = u_2 = 0 & \text{at } N_1 = (0,0,L_0) \\ u_1 = \Delta_{12}, u_2 = \Delta_2 & \text{at } N_2 = (0,L_0,0) \\ u_2 = 0 & \text{at } N_3 = (t,0,0) \end{array} \tag{4.4}$$

where $\vec{u} = (u_1, u_2, u_3)$ is the displacement vector, Δ_2 denotes the compression or tension imposed displacement depending on the sign of Δ_2, Δ_{23} specifies the transverse shear deformation and Δ_{12} defines the in-plane shear deformation. In Eq. 4.3, the constrain at N_3 denotes the plane strain condition. Periodic boundary conditions are applied to the edges of the cell to ensure the continuity between neighboring cells. The periodic boundary conditions can be expressed in terms of the prescribed displacement vectors $\vec{U}_1$, $\vec{U}_2$ and $\vec{U}_3$ which relate the displacements, $\vec{u}$, between opposite edges according to

$$\begin{aligned} \vec{U}_1 &= \vec{u}(0,x_2,x_3) - \vec{u}(t,x_2,x_3) \\ \vec{U}_2 &= \vec{u}(x_1,0,x_3) - \vec{u}(x_1,L_0,x_3) \\ \vec{U}_3 &= \vec{u}(x_1,x_2,0) - \vec{u}(x_1,x_2,L_0) \end{aligned} \tag{4.5}$$

In the $(\sigma_2 - \tau_{23})$ stress space, combined uniaxial tension/compression along the x_2-axis and transverse shear deformation are imposed with $\vec{U_2} = (0, \Delta_2, \Delta_{23})$. While in the $(\sigma_2 - \tau_{23})$ stress space, combined uniaxial tension/compression and in-plane shear deformation are imposed with $\vec{U_2} = (\Delta_{12}, \Delta_2, 0)$. In both above loading conditions, the component of U_1 and U_3 are chosen so that the average normal and shear forces acting on the cell surfaces are zero (besides those corresponding to transverse tension/compression, transverse shear and longitudinal shear).

The overall mechanical behavior of composite materials can be studied by the finite element simulation of a representative microstructure of composites. This approach is known as the Representative Volume Element (RVE). The RVE can be defined as the smallest material volume element of an heterogeneous material for which the average stress and strain microfields converge to an asymptotically constant value which is size independent and represents the effective macroscopic constitutive response (Drugan and Willis, 1996). Therefore, the RVE should contain enough information on the microsructure yet be sufficiently smaller than the macroscopic structural dimension. The existence and size of an RVE of a heterogeneous materials were analysed by Gitman et al. (2007). They discussed that an RVE can be found in both linear-elastic and hardening regimes. However, in the case of hardening the value of the standard deviation relative to the expectation is much larger than in linear-elasticity, which indicates that the size of the RVE in hardening is significantly larger than in linear-elasticity. They also conclude that once in softening, material loses the representative properties, in other words an RVE cannot be found. Fig. 4.11 shows the overall stress-strain response of four cells with different randomly distribution of 2% void volume fraction under a) pure transverse tension, b) pure transverse compression and c) pure longitudinal shear loading. All cells contain 70 monosized fibers with the same fiber distribution giving 60% fiber volume fraction. The difference between the cells is the arrangement of 2% void volume fraction which are randomly distributed in the matrix. Some simulations are stopped due to numerical instabilities after the stress drop was attained. Regardless of different void distribution, Fig. 4.11 shows that the elastic response of the cells are almost the same while the nonlinear response differs which leads also to different ultimate stress. Totry et al. (2008a) discussed that different arrangement of fibers in an RVE including 30 fibers with interface debonding under uniaxial compression shows up to 7% deviation in the ultimate failure stress. This scatter can be even larger when the same RVE includes voids. Fig. 4.11 shows that with the same distribution of 70 fibers, different arrangement of voids with $V_v = 2\%$ can lead to around 17%, 12% and 15% deviation in the ultimate stress response of unidirectional composite under transverse uniaxial tension, transverse uniaxial compression and longitudinal shear, respectively. However, this part does not aim at studying an RVE which represents the whole macroscopic behavior of the lamina but focuses on the effect of different micromechanical failure mechanisms on a specific configuration of a lamina which contains several fibers and voids randomly distributed in the matrix.

The following studies in this section consider volume elements which are gener-

ated by 70 monosized fibers with the same fiber distribution giving 60% fiber volume fraction. While the void distribution varies in the cells with different void volume fractions. The results are discussed in two parts based on the imposed loading conditions. The first part which belongs to [P4] studies a cell subjected to combined transverse normal and shear loadings in the $(\sigma_2 - \tau_{23})$ stress space. The combination of transverse normal and longitudinal shear loading condition in the $(\sigma_2 - \tau_{12})$ stress space is discussed in the second part. A detailed study of the second part can be found in [P5].

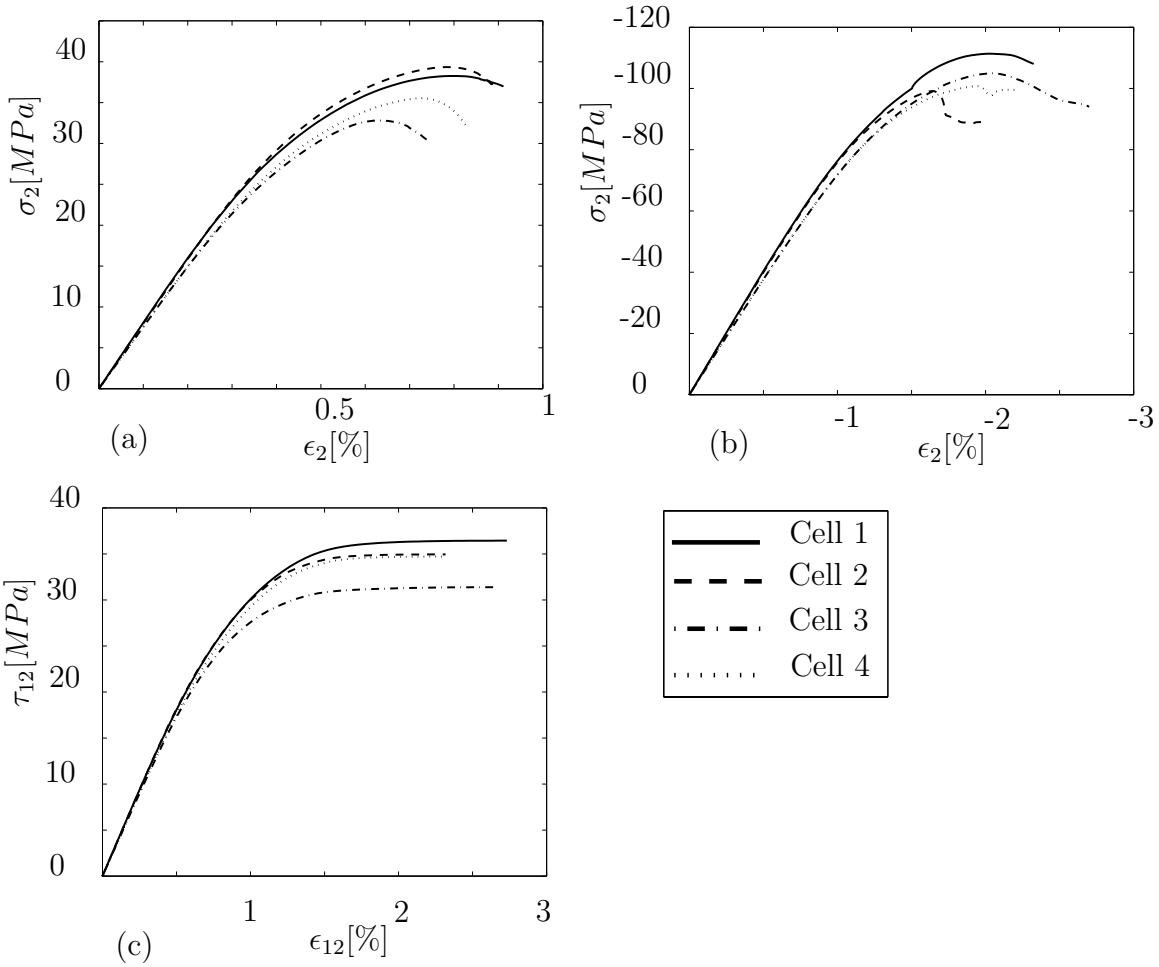

Figure 4.11 a) The overall stress-strain response of four cells with different randomly distribution of 2% void volume fraction, V_v, under a) pure transverse tension, b) pure transverse compression and c) pure longitudinal shear loading. The fiber distribution in all cases is the same and is generated by 70 monosized fibers giving 60% fiber volume fraction, V_f.

Before showing the results of mechanical response of composite under different loading conditions, it is worth to discuss two main micromechanical mechanisms occurring in unidirectional composites, namely; fiber/matrix interfacial debonding

and localized matrix deformation. Depends on the loading condition or the material properties one or both of these mechanisms controls failure of the material. Fig. 4.12 shows the macroscopic strength of unidirectional composites as a function of the interfacial fracture energies for different void volume fractions. The results of the cells subjected to uniaxial transverse tension, uniaxial transverse compression and pure longitudinal shear are shown in Fig. 4.12a, b and c, respectively. Both the normal and tangential fracture energies of the interfaces change such that the ratio $W_t^C/W_n^C = 2.5$ holds for all cases. The results show that with respect to the material parameters chosen in [P5] the overall composite strength under uniaxial tension and compression rises with increase of the interfacial toughness up to $W_n^C/G_m = 0.5$ and $W_t^C/G_m = 1.25$. While further increase of interfacial fracture energies does not affact the macroscopic strength of composite. This is due to the fact that with weak interfaces the fiber/matrix debonding mainly controlls failure of composites while the matrix deformation is the dominant failure mechanism if the interfaces are too strong. However, under pure longitudinal shear the interfacial toughness does not influence the overall longitudinal shear strength of composites. This can be explained by the pure tangential debonding along the fibers which is the only interfacial failure mechanism under pure longitudinal shear. In this case the initiation of tangential damage of interface along the fibers is prevented due to very strong tangential cohesive stress, $T_t^{max} = 75MPa$, which is chosen to be larger than the matrix ultimate tensile strength, $\sigma_m^{t0} = 50MPa$. It is also worth to notice that the behavior of composite strength versus the interfacial toughness keeps unchanged under different void volume fractions. This means that microvoids can not switch the dominant failure mechanism from interfacial debonding to matrix deformation or vice versa although they may trigger the onset of damage in smaller load carrying capacity.

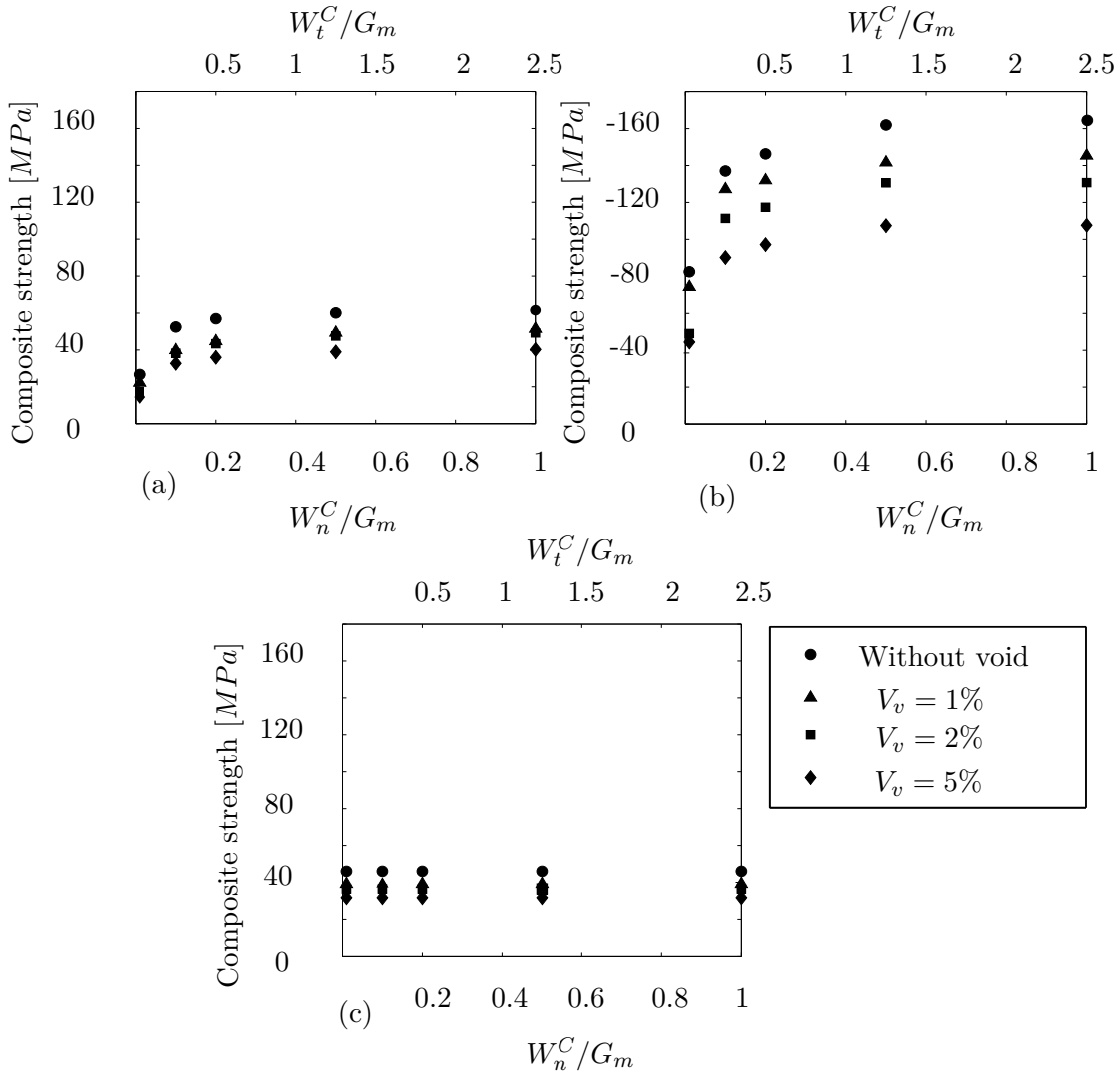

Figure 4.12 Effect of interfacial fracture energy on the macroscopic strength of unidirectional fiber-reinforced composites under a) pure transverse tension, b) pure transverse compression and c) pure longitudinal shear.

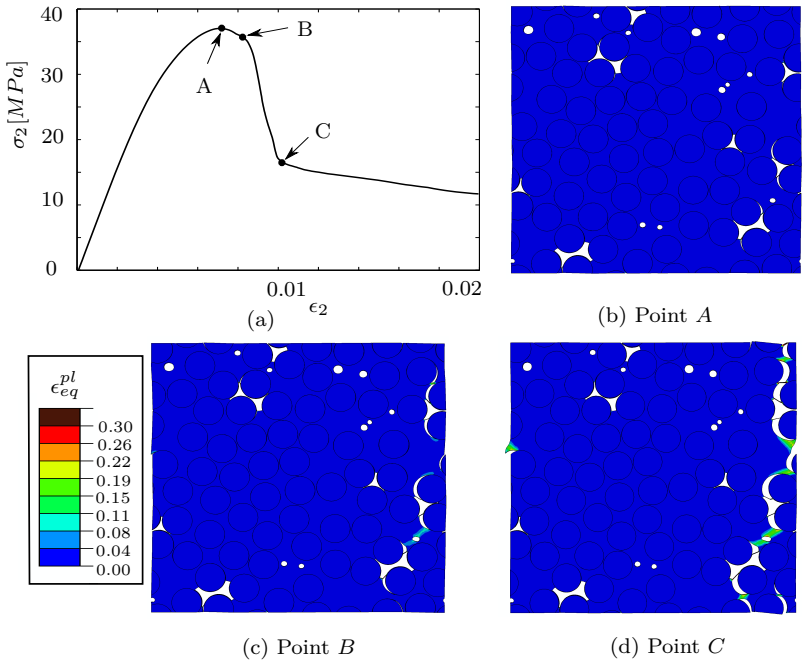

Figure 4.13 (a) Stress-strain response under transverse tension of a cell containing 60% fibers and 2% of pores. Contour plot of the equivalent plastic strain within the cell for: (b) Point A in the stress-strain curve. (c) Point B in the stress-strain curve. (d) Point C in the stress-strain curve. The displacements are magnified by a factor of 3 in the contour plots. The loading axis was horizontal.

4.3.1 *Inter-fiber failure in the* $(\sigma_2 - \tau_{23})$ *stress space [P4]*

Here, the mechanical behavior of unidirectional composites subjected to transverse normal and shear loadings is studied. Fig. 4.13a shows the overall stress-strain response of a cell containing $V_f = 60\%$ and $V_v = 2\%$ under uniaxial transverse tension. Three situations correspond to the ultimate stress, initial stage of softening and after the complete stress drop are marked on the curve with points A, B and C, respectively. The corresponding contour plots of the equivalent plastic strain for the points A, B and C are shown in Fig. 4.13b, c and d. Fig. 4.13b shows that stress concentration around the trapped voids leads to crack initiation at the neighboring fiber/matrix interfaces. The interfacial crack initiation results a nonlinear stress-strain behavior up to ultimate stress (point A). The ultimate stress occurs in a smaller value than the matrix tensile strength, $\sigma_m^{t0} = 65MPa$, and the maximum cohesive normal stress, $\sigma_{max} = 50MPa$ which is due to the presence of voids. Subsequently, the crack propagates through the interfaces perpendicular to the transverse tension, point B. The crack propagation leads to a sudden stress drop which significantly reduces the load carrying capacity until point C reaches where the further loading is tolerated by the matrix in the ligaments between the debonded interfaces.

This microstructural modeling can be used to computationally predict the failure

locus of unidiractional composites in the $\sigma_2 - \tau_{23}$ stress space. Fig. 4.14 shows the numerical prediction of the cells with three different void volume fractions which are compared with a cell without porosity. To cover the entire failure locus each cell is subjected to 11 different loading conditions produced by different ratios of the shear displacement, Δ_{23}, to the normal displacement, Δ_2. The strength under biaxial loading (transverse tension or compression and transverse shear) was determined by the point at which one (or often both) normal and shear stresses began to decrease as the normal and shear displacements increase. The Puck's analytical prediction is also calculated from Eqs. 1.5 and 1.6 by using the ultimate compressive and tensile strengths of composite obtained from the numerical simulations. The results show a good agreement between the computational and the analytical predictions for all void volume fractions. However, in the combined transverse compression and shear there are small scatters between the numerical prediction and the analytical solution. These scatters can be due to the fact that the Puck's model does not consider the micromechanical effect of microvoids which can triggers interfacial debonding at a smaller stress. Fig. 4.14 shows that porosity can significantly shrinks the macroscopic failure locus of composites such that this reduction for $V_v = 5\%$ is nearly 40% of the entire $\sigma_2 - \tau_{23}$ stress space.

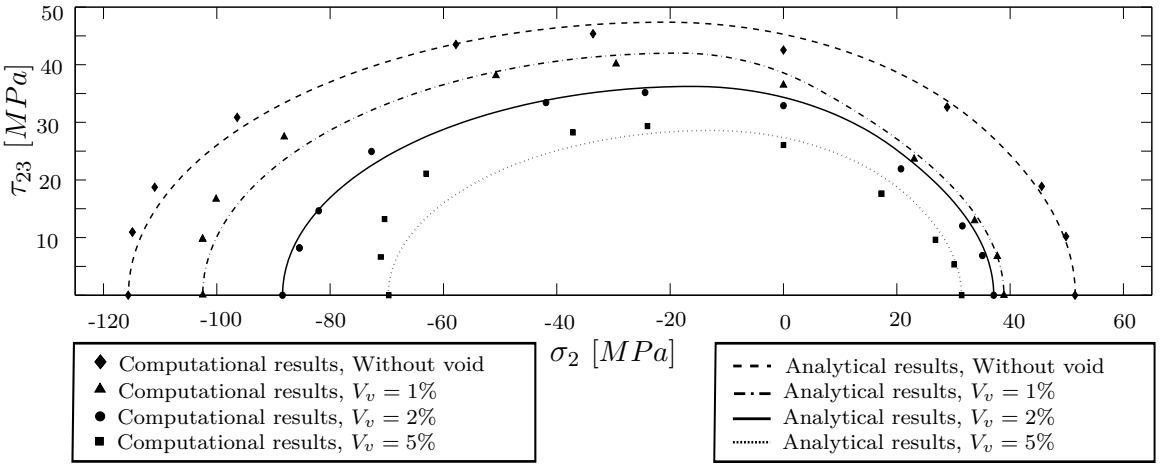

Figure 4.14 Failure locus of a unidirectional fiber-reinforced composite in the $\sigma_2 - \tau_{23}$ stress space as function of porosity. The lines correspond to the predictions of the Puck's model (Puck et al., 2002). The solid symbols stand for the numerical predictions obtained from the numerical simulation of an RVE of the microstructure.

4.3.2 Inter-fiber failure in the $(\sigma_2 - \tau_{12})$ stress space [P5]

In this part, the mechanical behavior of porous unidirectional composite in the $(\sigma_2 - \tau_{12})$ stress space is studied. Fig. 4.15 shows the effect of void volume fraction on the overall stress-strain response of unidirectional composites under combined transverse tension and longitudinal shear, $\Delta_{12}/\Delta_2 = 1$, dominant longitudinal shear combined with transverse compression, $\Delta_{12}/\Delta_2 = -10$ and dominant transverse compression combined with longitudinal shear, $\Delta_{12}/\Delta_2 = -0.5$ in Fig. 4.15a, b and c, respectively. In all cases, larger void volume fraction reduces the elastic response of composite. This reduction is more pronounced in the hardening regime which results a significant decrease in the composite ultimate stresses. Fig. 4.15 shows that even 1% void volume fraction can reduce 25%, 10% and 15% of the ultimate stress in Fig. 4.15a, b and c, respectively. Different reduction values in Fig. 4.15a, b and c is due to various failure mechanisms occurring under different loading conditions. The details of different micromechanical failure mechanisms provoked by porosity are discussed in [P5].

Similar to the strategy discussed in Fig. 4.14, in Fig. 4.16 the failure locus of unidirectional composites as function of porosity is computationally predicted in the $\sigma_2 - \tau_{12}$ stress space. Having the ultimate compressive, tensile and shear stresses of composite obtained from the numerical simulations the analytical predictions of the Puck's model is also calculated using Eqs. 1.1, 1.2, 1.3. The results show a very good agreement between the computational and analytical predictions. It is worth to notice that the computational model has been also able to predict different physically-based failure modes defined by Puck et al. (2002). Similar to Fig. 4.14, Fig. 4.16 also shows the enormous effect of porosity on the reduction of mechanical response of composites in the $\sigma_2 - \tau_{12}$ stress space. This reduction effect from a non-voided composite to a composite with $V_v = 5\%$ is up to 48% in Mode-A, 33% in Mode-B and up to 44% in Mode-C.

Fig. 4.17 shows the ability of the microstructural model to predict different physically based failure modes, namely; mode A, mode B and mode C. Fig. 4.17 illustrates the contour plots of the accumulated plastic strain of a cell with $V_f = 60\%$ and $V_v = 2\%$. Fig. 4.17a and b denote the mode A where the fracture plane is perpendicular to the transverse tension. The model also shows that under mode A the dominant failure mechanism is the fiber/matrix interfacial debonding which is initiates from the trapped voids. The mode B is shown in Fig. 4.17c and d where the deformation is mainly due to the longitudinal shear loading. In agreement with the Puck's model, the model shows a fracture plane with zero fracture angle, $\theta_f = 0$. Due to choosing a large cohesive tangential strength, $T_t^{max} = 75MPa$, the failure mechanism, here, is mainly controlled by matrix deformation. However, in the case of weaker tangential properties of the interfaces the failure would be controlled by the interface tangential debonding although the angle of fracture plane was the same. In Fig. 4.17e and d the severe transverse compression leads to an oblique fracture plane. This oblique failure plane is attributed to the pressure sensitivity

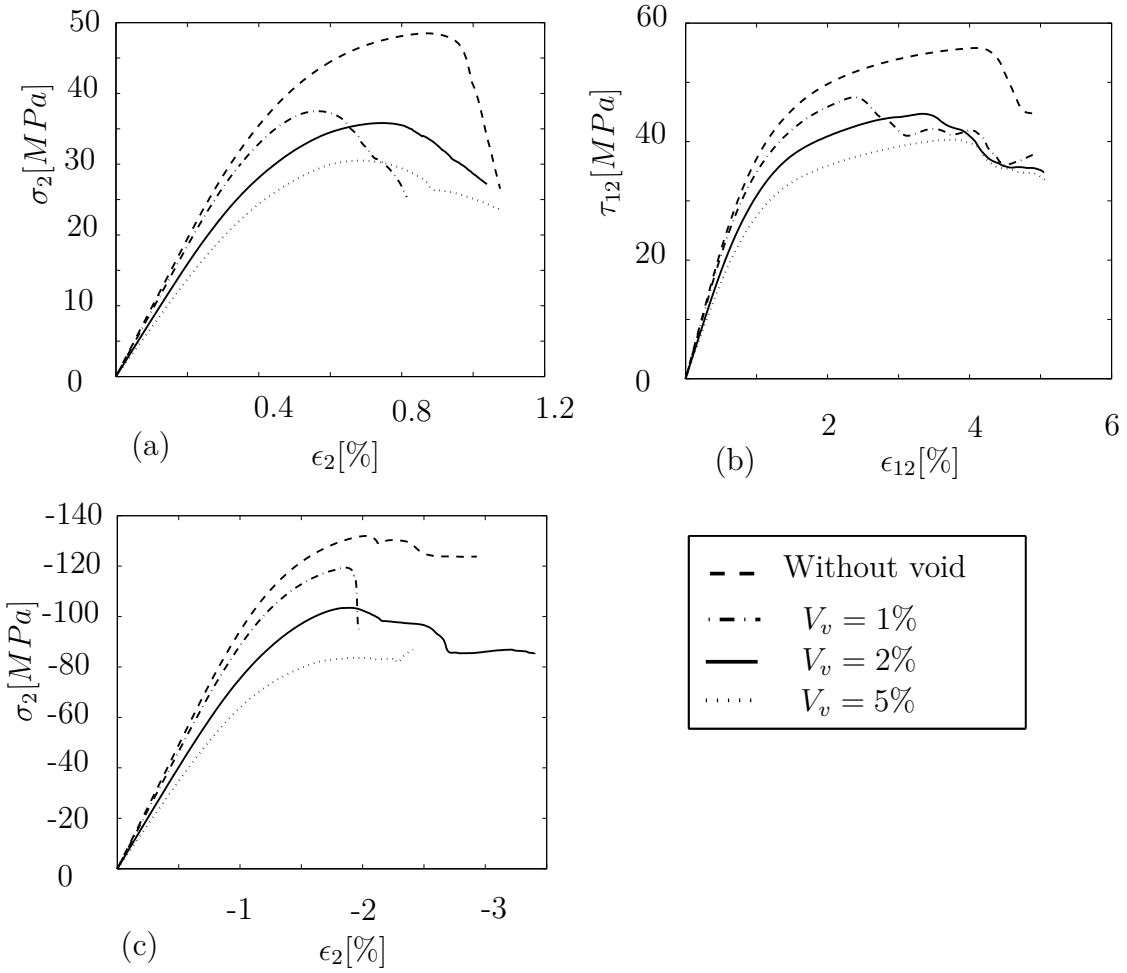

Figure 4.15 Effect of void volume fraction on the overall stress-strain response of unidirectional fiber-reinforced composites under a) combined transverse tension and longitudinal shear, $\Delta_{12}/\Delta_2 = 1$, b) dominant longitudinal shear combined with transverse compression, $\Delta_{12}/\Delta_2 = -10$ and c) dominant transverse compression combined with longitudinal shear, $\Delta_{12}/\Delta_2 = -0.5$. The curves are plotted in the corresponding dominant loading stress.

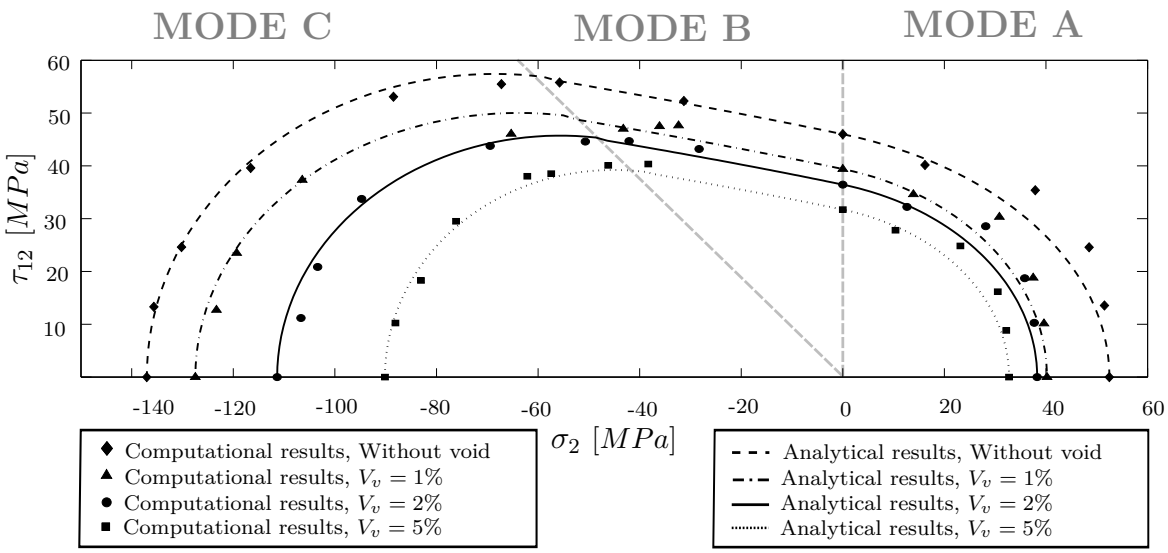

Figure 4.16 Failure locus of a unidirectional fiber-reinforced composite in the $\sigma_2 - \tau_{12}$ stress space as function of porosity. The lines correspond to the predictions of the Puck's model (Puck et al., 2002). The solid symbols stand for the numerical predictions obtained from the numerical simulation of an RVE of the microstructure.

of matrix yield strength (González and Llorca, 2007a) and the predictions are in the range reported by (Puck et al., 2002). Furthermore, the simulation predicts a wedge shaped fracture under Mode-C which is due to the sliding of composite along the shear bands and the debonded interfaces under large compressive deformation. This failure which is known as the ˝explosive effect˝can cause delamination and local buckling which is dangerous compared to the fairly harmless crack forming due to transverse tensile stress (Puck and Schürmann, 1998).

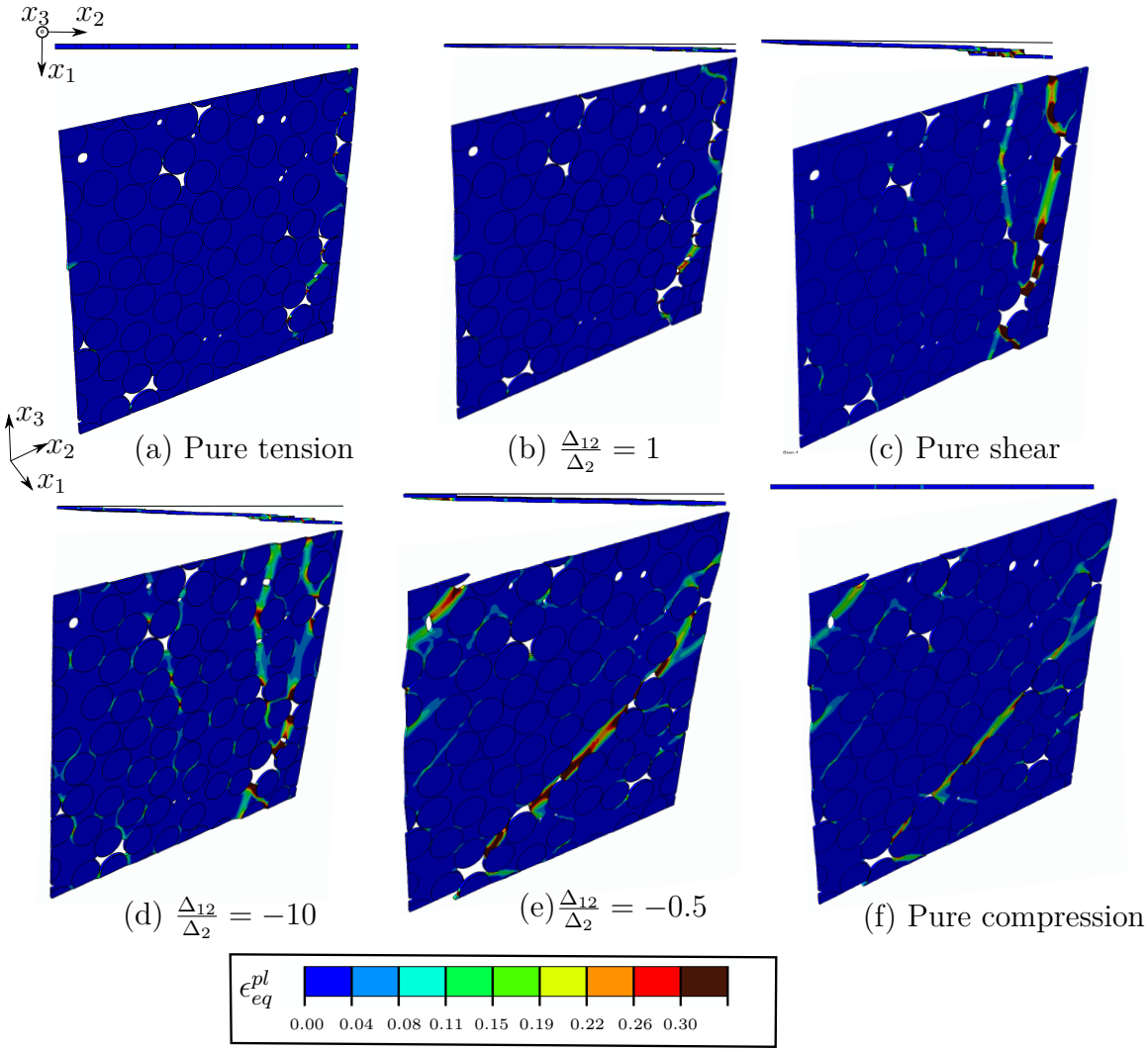

Figure 4.17 Contour plots of the accumulated plastic strain of a cell with $V_v = 2\%$ subjected to a) pure transverse tension, b) combined transverse tension and longitudinal shear with $\Delta_{12}/\Delta_2 = 1$, c) combined transverse compression and longitudinal shear with $\Delta_{12}/\Delta_2 = -10$, d) pure compression, e) combined transverse compression and longitudinal shear with $\Delta_{12}/\Delta_2 = -0.5$ and f) pure shear. Figures (a) and (b) are at $\epsilon_2 = 1.5\%$ while the rest are at the dominant strain, ϵ_2 or $\epsilon_{12} = 2.5\%$. All the figures are magnified by factor 2.

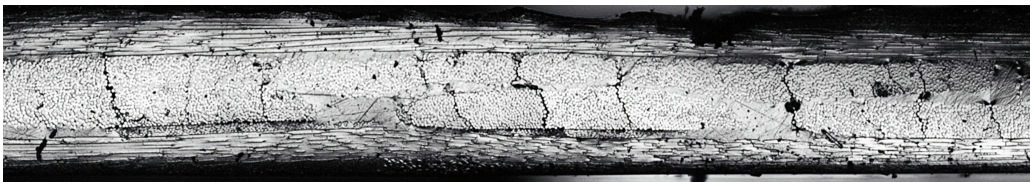

Figure 4.18 Intra-laminate cracks with a spacing from each other developed across the 90° ply in a $[0/90]_s$ specimen. The image also show that cracks emanated from voids.

4.4 Intra-ply failure in $[0/90]_s$ laminate under transverse tension

As discussed in the previous part, under transverse tension a lamina may suddenly and completely fail due to development of a single crack orthogonal to the loading direction. Unlike a lamina, in laminate composites made of individual plies stacked with various in-plane orientations, the failure is gradually rather than a sudden phenomena. In a $[0/90]_s$ laminate, for example, first the inter-fiber failure occurs along the 90° ply generating large numbers of cracks perpendicular to the loading direction. The macroscopic effect of these cracks is reduction of the laminate stiffness. Finally, fiber breakage in the 0° plies leads to complete failure. This study focuses on the first failure mechanism occurring in 90° ply. Fig. 4.18 which is the result of the author's experimental study discussed in section 4.3, shows the transverse multiple cracks in the 90° ply. In the failure of the 90° ply, at a certain stage of loading , the cracks of spacing L develop across the ply, and the tensile stress in the 90° ply is therefore partially relieved. With further increase of the loading, a new set of cracks are nucleated and grow half-way between the existing cracks (Hutchinson and Suo, 1992). These new set of cracks are propagated due to transferring the shear load through the interfaces of 0/90 plies into the 90° ply between the existing cracks.

Hashin (1987); McCartney (1992); Abdelrahman and Nayfeh (1999) analytically analysed the stiffness reduction of cracked laminates with cross-ply laminates, i.e., $[0/90]_s$ configuration. All these methods give results which are in good agreement with the experimental data. However, all these studies assume that plies are elastically homogeneous materials. Therefore, they are not able to reveal the micromechanical features in the plies. Here, the attempt is to understand the micromechanisms occurring in the laminate which lead to the development of the cracks and consequently stiffness reduction.

In this part, the micromechanical failure of a glass/epoxy $[0/90]_s$ laminate is studied experimentally as well as numerically. The process of sample manufacturing and the method of experimental testing were explained in Chapter 3. The numerical methods used for the modeling are the same as Section 4.3. In the event of the transverse cracks with spacing, L, a representative element can be considered at which the stresses and strains are repeated along the laminate, see the dashed-line in Fig. 4.19a. By choosing a proper boundary and interface conditions this element

can be modeled by means of the finite element method. In Fig. 4.19b, a model of $[0/90]_s$ laminate is depicted. The 0° plies are assumed to be homogenized and behave as a linear elastic, isotropic solid whose elastic constants are computed from the matrix and fiber elastic properties using Voigt model. While in the 90° ply the actual microstructure is represented, where all the fracture processes occur. In the modeling of 90°, similar to Section 4.3, the fibers are assumed to be isotropic elastic material while the matrix behaves elasto-plastically by following the modified Drucker-Prager model. Interfacial debonding is modeled by using the trapezoidal cohesive zone model. The position and diameter of fibers and voids are extracted from the image of the corresponding specimen captured by SEM scanning. A Cartesian reference coordinate system, x_i, is placed at the bottom-left corner of the cell and aligned with its edges. The positive direction of the first axis, x_1, points in the out-of-plane normal direction to the (x_2, x_3)-plane. Periodic boundary conditions are applied to the left and right edges of the model denoted in Fig. 4.19b by S_L and S_R, respectively. The periodic boundary conditions can be expressed in terms of the prescribed incremental displacement vector $\dot{\vec{U}}_2$ which relate the incremental displacements, $\vec{u}$, between opposite edges (S_L and S_R) according to

$$\vec{u}(0, x_3) - \vec{u}(L_0, x_3) \quad = \quad \dot{\vec{U}}_2 \tag{4.6}$$

Uniaxial transverse tension along the x_2-axis is imposed with $\dot{\vec{U}}_2 = (\dot{\Delta}_2, 0)$ where $\dot{\Delta}_2$ denotes the tensile incremental displacement.

Fig. 4.20 compares the numerical predictions with the experimental results. Fig. 4.20 shows that the numerical simulation precisely capture the evolution of the crack propagation with the load. In both the experimental observation and the numerical simulation, the crack initiates from the larger microvoid at the remote stress, $\sigma_2 \approx 30$ MPa. A closer view of the numerical prediction of crack initiation around the void is given in Fig. 4.20b. The experimental and numerical results show that damage triggers by interface decohesion around the void. It is also shown that the crack growth is controlled by the fiber/matrix debonding. Consequently, Fig. 4.20 denotes that the numerical simulation strategy is able to predict the crack path accurately.

Fig. 4.21 illustrates the contour plots of the maximum principal stress of the microstructrual modelling. Fig. 4.21 shows the sequence of the crack initiating from the microvoid and propagating along the fiber/matrix interfaces. The numerical results give a detailed information of the stress distribution around the crack.

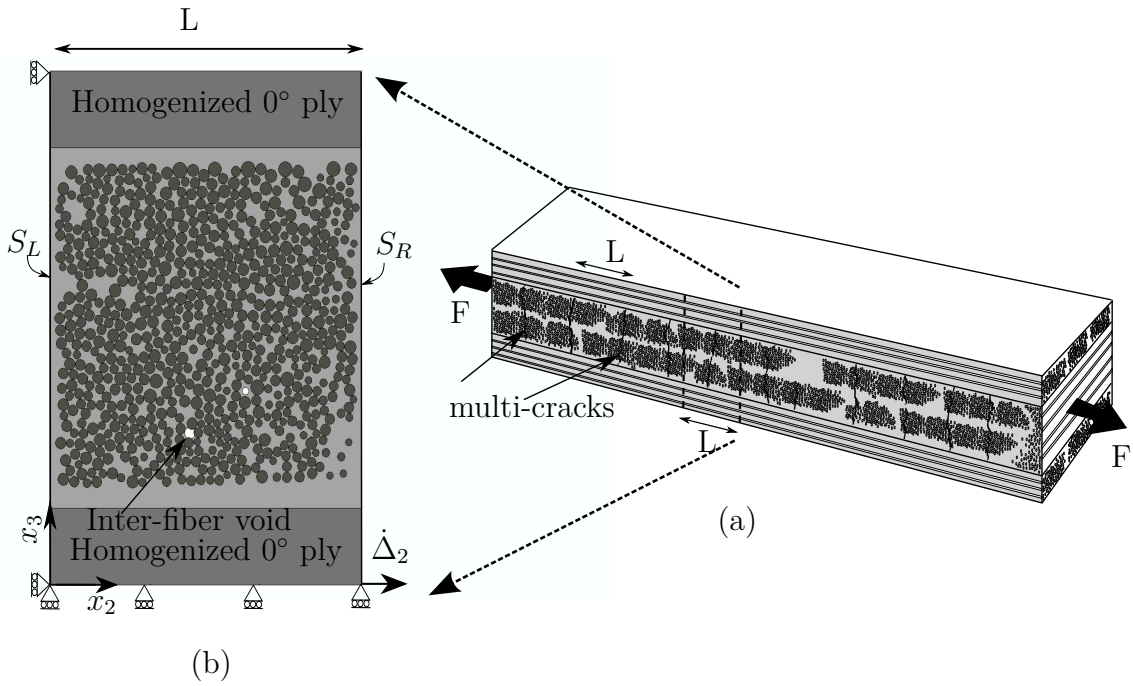

Figure 4.19 a) Schematic of the $[0/90]_s$ laminate with an array of multiple transverse cracks under uni-axial transverse tensile loading. b) The numerical model which consists of two homogenized elastic 0° plies and a ply including the details of the actual microstructure of 90° lamina. The length of the model is chosen to be the average of the distance between the cracks, L.

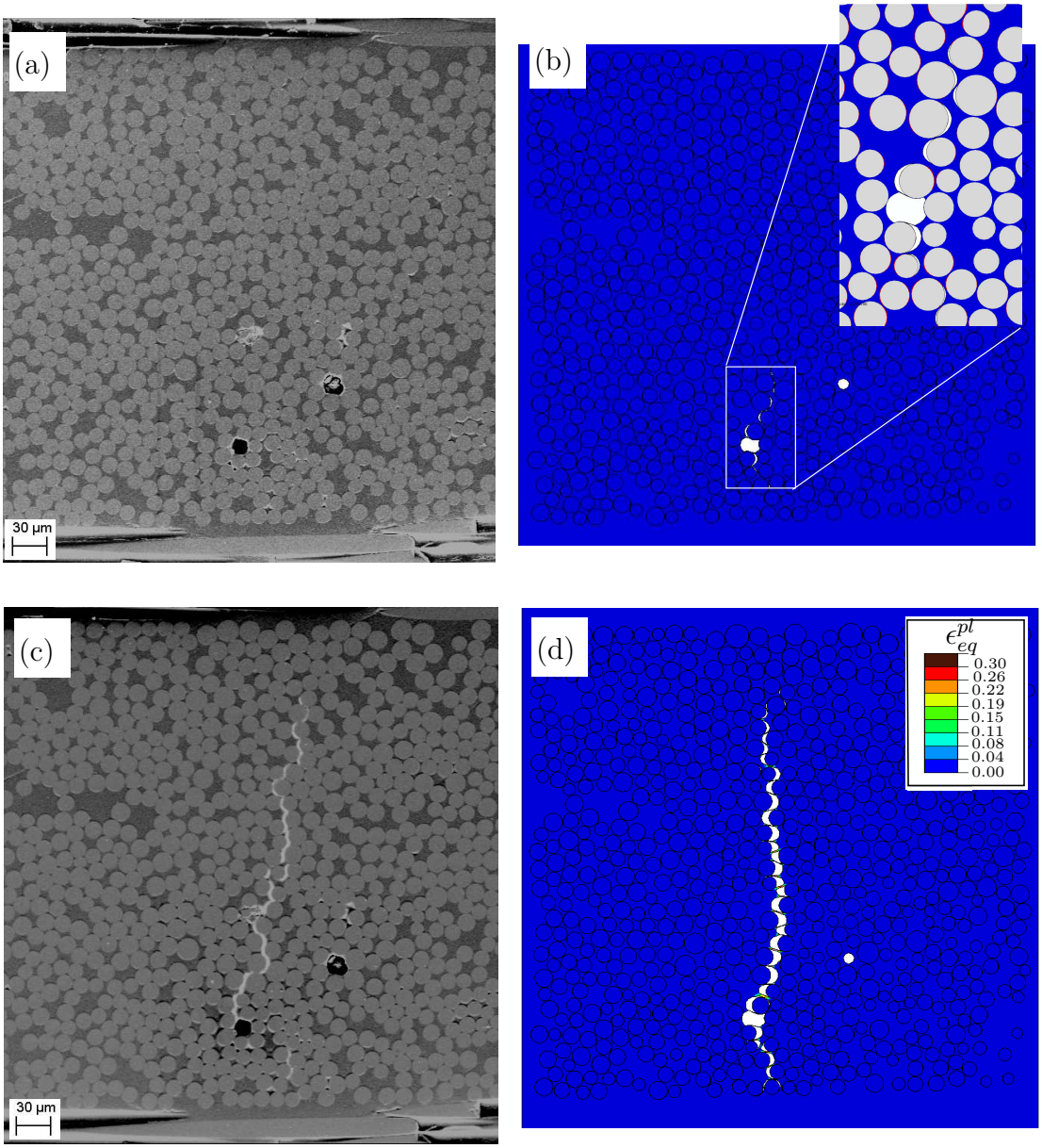

Figure 4.20 Crack initiates from the larger microvoid and propagates along the fiber/ matrix interfaces perpendicular to the loading direction. The left images correspond to the scanning electron micrographs during *In-situ* experimental testing while the right images are the simulation results showing the contour plots of the equivalent plastic strain.

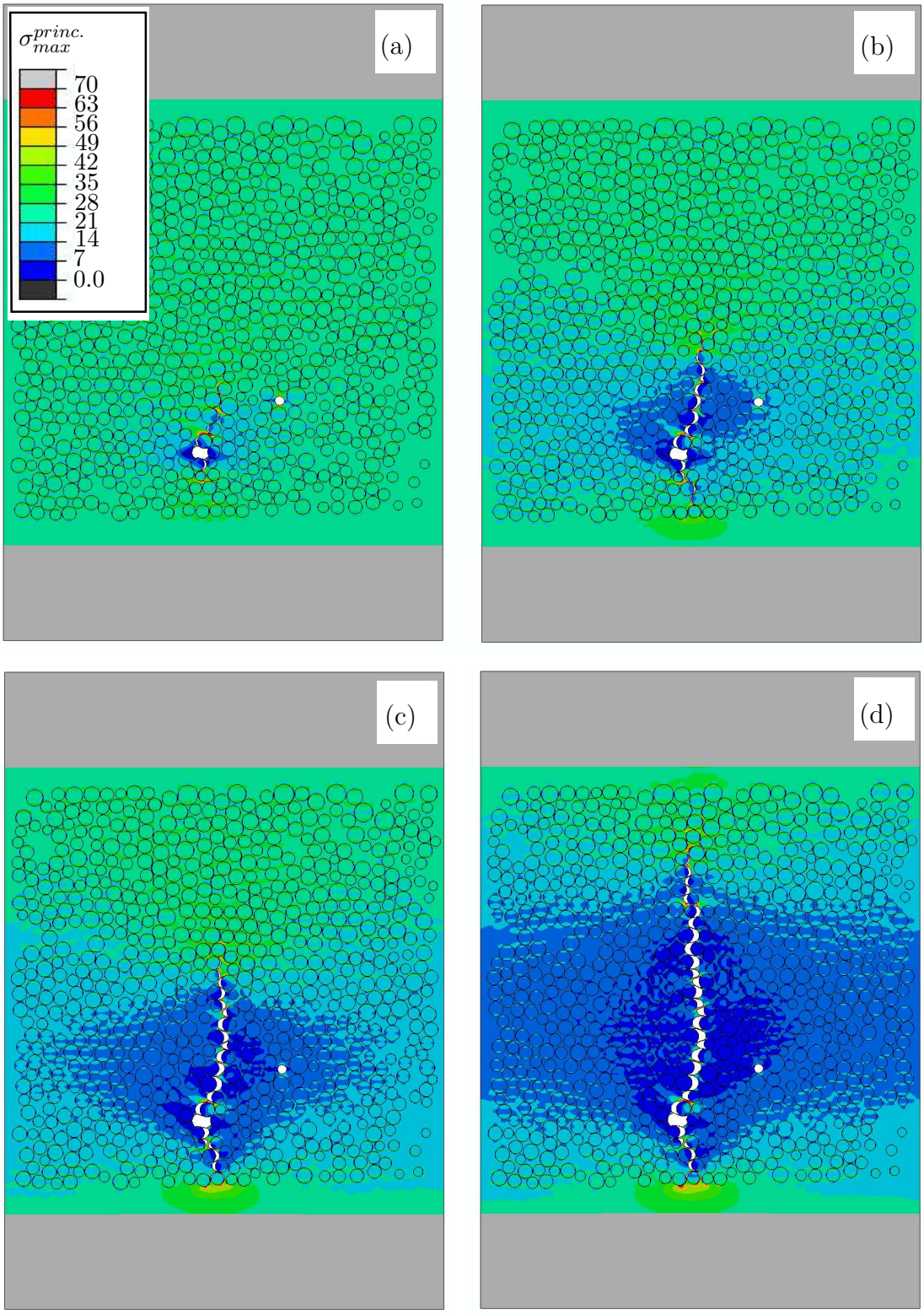

Figure 4.21 Contour plots of the maximum principal stress of the numerical modelling showing the sequence of the crack initiating from the microvoid and propagating along the fiber/matrix interfaces.

Chapter 5
Conclusions

In this thesis the effect of micro-scale features such as fiber/matrix interfacial debonding, matrix deformation and microvoids on the microscopic as well as macroscopic mechanical response of UD composites was studied. This study tried to understand accurately the critical micromechanical failure mechanisms in composites due to these micro-scale features. To this end, microstructural composites were simulated by means of finite element method. The cohesive zone methods were used to model debonding at the fiber/matrix interfaces. For the matrix, both the standard J_2-plasticity theory suitable for ductile materials as well as the modified Drucker-Prager plasticity model appropriate for the brittle-like materials such as epoxies were used. Two types of microvoids were also modeled in a cell containing a random distribution of dozens of fibers.

Firstly, the mixed mode interfacial debonding was numerically studied using the cohesive zone model. The detailed information is given in [P1] and [P2]. In this study, two configurations were considered. The first model consists of two glass-fibers embedded in a large zone of the matrix while the other case includes one glass-fiber close to a hole. The aim was to develop a way such that it becomes possible to measure interfacial properties for smaller values of $\psi(\theta)$ (dominant mode-I fracture region). In both configurations, decrease of the position angle stabilized the crack growth at the interface in the ligaments. This effect was more significant in the cases with small ligament thickness. This study concluded that the fiber-fiber configuration leads to capture stable cracks under dominant mode-I fracture. Consequently, this study suggested that the two-fiber configuration can stabilize the crack initiation under dominant mode-I which is of interest for the experimental measurements of the normal debonding properties of the interfaces.

Afterward, two different approaches were utilized to obtain the overall mechanical response of UD composites from the microstructural modeling. The first approach was used in [P3] where the UD composite was simplified by considering a regular distribution of fibers. Then, the composite was represented by a hexagonal unit-cell including two quarter-circular fibers. This study aimed at considering a more realistic model for composites than a single-fiber unit cell by including two different fiber-matrix strengths to capture different initiation and propagation of interfacial microcracks and consequently their effects on the overall response of the structure. It was shown that uneven interfacial strength has a significant influence on the nonlinear behavior of the overall response of the unit cell. It was also found that crack growth along the interface is stabilized by decreasing the maximum cohesive stress, σ_{max}, increase of the characteristic cohesive distance, $\delta^c = \delta_n^c = \delta_t^c$, and larger dimensional ratio, b/a. Furthermore, it was shown that larger maximum cohe-

sive stress, smaller dimensional ratio, increase of the characteristic cohesive distance or decrease of the fiber volume fraction postpone onset of interfacial debonding.

As the second approach, in [P4] and [P5] a cell was modeled including 70 monosized fibers and two types of microvoids which were randomly distributed in the matrix. Periodic boundary conditions were applied to the edges of the cell to ensure the continuity between neighboring cells. In this model the modified Drucker-Prager plasticity model was used to represent the brittle-like and pressure-dependent behavior of epoxy matrix. The cohesive zone model was considered at the fiber/matrix interfaces. The cell was subjected to different loading conditions such as the transverse tension, the transverse compression, the transverse shear and the longitudinal shear. By applying these loading conditions, all the inter-fiber failure mechanisms of UD composites were analyzed numerically. The focus of these studies was to determine the influence of the porosity on the mechanical response of UD fiber-reinforced composites. The results showed that porosity reduces markedly the strength of the composite under transverse tension and compression although it does not modify the dominant failure micromechanisms. Failure under tension was controlled by interface decohesion while in compression it was dominated by the localization of a plastic shear band through the matrix. In both cases, interfiber voids acted as stress concentrators which triggered the onset of failure at lower stresses. Circular voids within the matrix influenced the localization path throughout the microstructure. The model was also used to determine numerically the failure envelope in the σ_2 - τ_{23} and σ_2 - τ_{12} stress spaces of composite containing V_v =0, 1, 2 and 5%. The numerical results were in good agreement with the predictions of Puck's model (based on the transverse tensile, transverse compressive and longitudinal shear strengths provided by the computational micromechanics). This supported the validity of the computational model to predict different failure mechanisms based on the microstructural features. Finally, an experimental study was carried out to be compared with the numerical modeling strategy used in the randomly fiber distributed approach. The experimental and numerical results showed that damage triggers by interface decohesion around the void. It was also observed that the crack growth is controlled by the fiber/matrix debonding. Consequently, the results showed that the numerical simulation strategy is able to predict the initiation of cracks and also the path of the propagation cracks accurately.

References

Abaqus. Analysis user's manual, version 6.12. Simulia. 2012.

Abdelrahman W.G., Nayfeh A.H., 1999. Stress transfer and stiffness reduction in orthogonally cracked laminates. Mech Mater 31, 303-316.

Agrawal A.,Karlsson A.M., 2006. Obtaining mode mixity for a bimaterial interface crack using the virtual crack closure technique. International Journal of Fracture 141, 75-98.

Azizi R., 2012. Micromechanical modeling of damage in periodic composites using strain gradient plasticity. Engineering Fracture Mechanics 92, 101-113.

Bayat M., Aghdam M.M., 2012. A micromechanics-based analysis of effects of square and hexagonal fiber arrays in fibrous composites using DQEM. Eur J Mech A-Solid 32, 32-40.

Benzeggagh M.L., Kenane M., 1996. Measurement of mixed-mode delamination fracture toughness of unidirectional glass/epoxy composites with mixed-mode bending apparatus. Composites Science and Technology 56, 439-449.

Bogetti T.A., Hoppel C.P.R., Harik V.M., Newill J.F., Burns B.P., 2004. Predicting the nonlinear response and progressive failure of composite laminates, Compos Sci Technol 64, 329-342.

Bogetti T.A., Hoppel C.P.R., Harik V.M., Newill J.F., Burns B.P., 2004. Predicting the nonlinear response and failure of composite laminates: correlation with experimental results. Compos Sci Technol 64, 477-485.

Canal L.P., Segurado J., Llorca J., 2009. Failure surface of epoxy-modified fiber-reinforced composites under transverse tension and shear. Int J Solids Struct 46, 2265-2274.

Canal L.P., 2011. Experimental and computational micromechanical study of fiber-reinforced polymers. PhD thesis.

Canal L.P., González C., Segurado J., Llorca J., 2012. Intraply fracture of fiber-reinforced composites: Microscopic mechanisms and modeling. Compos Sci Technol 72, 1223-1232.

Chandra N., Li H., Shet C., Ghonem H., 2002. Some issues in the application of cohesive zone models for metal-ceramic interfaces. International Journal of Solids and Structures 39, 2827-2855.

Chew H.B., Guo T.F., Cheng L., 2006. Effects of pressure-sensitivity and plastic dilatancy on void growth and interaction. Int J Solids Struct 43, 6380-6397.

Correa E., Gamstedt E.K., París F., Mantič V., 2007. Effects of the presence of compression in transverse cyclic loading on fibre–matrix debonding in unidirectional composite plies. Composites Part A 38, 2260-2269.

Correa E., Mantič V., París F., 2008. A micromechanical view of inter-fibre failure of composite materials under compression transverse to the fibres. Compos Sci Technol 68, 2010-2021.

Cuntze R.G., Freund A., 2004a. The predictive capability of failure mode concept – based strength criteria for multidirectional laminates. Compos Sci Techno 64, 343-377.

Cuntze R.G., 2004b. The predictive capability of failure mode concept-based strength criteria for multidirectional laminates: Part B. Compos Sci Technol 64, 487-516.

DiBenedetto A.T., 1991. Measurement of the Thermomechanieal Stability of Interphases by the Embedded Single Fiber Test. Composites Science and Technology 42, 103-123.

Drugan W.J., Willis J.R., 1996. A micromechanics-based nonlocal constitutive equation and minimum RVE size estimates for random elastic composites containing aligned spheroidal heterogeneities. Journal of the Mechanics and Physics of Solids 57, 1578-1595.

Fiedler B., Hojo M., Ochiai S., Schulte K., Ando. M., 2001. Failure behavior of an epoxy matrix under different kinds of static loading. Composites Science and Technology 61, 1615-1624.

Gitman I., Askes H., Sluys L., 2007. Representative volume: Existence and size determination. Engineering Fracture Mechanics 74, 2518-2534.

González C., Llorca J., 2007. Mechanical behavior of unidirectional fiber-reinforced polymers under transverse compression: Microscopic mechanisms and modeling. Composites Science and Technology 67, 2795-2806.

Ghiorse S.R., 1993. Effect of void content on the mechanical properties of carbon/epoxy laminates. SAMPE Quarterly 1, 54-9.

González C., Llorca J., 2007a. Mechanical behavior of unidirectional fiber-reinforced polymers under transverse compression: Microscopic mechanisms and modeling. Compos Sci Technol 67, 2795-2806.

González C., Llorca J., 2007b. Numerical simulation of the fracture behavior of Ti/SiC composites between 20 $°C$ and 400 $°C$. Metall Mater Trans A 38, 169-79.

Hampe A., Kalinka G., Meretz S., Schulz E., 1994. An advanced equipment for single-fibre pull-out test designed to monitor the fracture process. Composites: Part A 26, 40-46.

Hampe A., Marotzke C., 1995. The energy release rate of the fiber/polymer matrix interface: measurement and theoretical analysis, Journal of Reinforced Plastics and Composites 16, 341-352.

Hashin Z., 1980. Failure criteria for unidirectional fiber composites. J Appl Mech 47, 329-334.

Hashin Z., 1987. Analysis of orthogonally cracked laminates under tension. J Appl Mech 54, 872-879.

Herakovich C.T., 1998. Mechanics of Fibrous Composites. John Wiley & Sons.

Hettich T., Hund A., Ramm E., 2008. Modeling of failure in composites by X-FEM and level sets within a multiscale framework. Comput. Methods Appl. Mech. Engrg. 197, 414-424.

Hinton M.J., Soden P.D., 1998. Predicting failure in composite laminates: the background of the exercise. Compos Sci Technol 58, 1001-1010.

Hinton M.J., Soden P.D., Kaddour A.S., 2004. Failure criteria in fiber reinforced polymer composites: the world wide failure exercise. Elsevier.

Hutchinson J.W., Suo Z., 1992. Mixed mode cracking in layered materials. Advances in Applied Mechanics 29, 63-191.

Jones, Robbert M. Mechanics of composite materials, 2nd ed, 1999. Taylor & Francis Ltd.

Kinloch A.J., Young R.J., 1983. Fracture behaviour of polymers. Elsevier Applied Science Publishers.

Knops M., 2008. Analysis of Failure in Fiber Polymer Laminates. Springer.

Kuraishi A., Tsai S.W., Liu K., 2002. A progressive quadratic failure criterion, Part B. Compos Sci Technol 62, 1682–1696.

Lee J., Fenves G.L., 1998. Plastic-damage for cyclic loading of concrete structures. J Eng Mech 124, 892-900.

Legarth B.N., 2004. Unit cell debonding analyses for arbitrary orientation of plastic anisotropy. International Journal of Solids and Structures 41, 7267-7285.

Legarth B.N., 2005. Effects of geometrical anisotropy on failure in a plastically anisotropic metal. Engineering Fracture Mechanics 72, 2792-2807.

Ling D., Yang Q., Cox B., 2009. An augmented finite element method for modeling arbitrary discontinuities in composite materials. International Journal of Fracture 156, 53-73.

Liu S., Mei Y., Wu T.Y., 1995. Bimaterial interfacial crack growth as a function of mode-mixity. EEE Transactions on Components, Packaging, and Manufacturing Technology: Part A 18, 618-626.

Liu K.S., Tsai S.W., 1998. A progressive quadratic failure criterion of a laminate. Compos Sci Technol 58, 1023–1032.

Liechti K.M., Chai Y.S., 1992. Asymmetric shielding in interfacial fracture under in-plane shear. J Appl Mech 59, 295–304.

Llorca J., González C., Molina-Aldareguía J.M., Segurado J., Seltzer R., Sket F., Rodríguez M., Sádaba S., Muñoz R., Canal L.P., 2011. Multiscale modeling of composite materials: a roadmap towards virtual testing. Adv Mater 23, 5130-5147.

Lubliner J., Oliver J., Oller S., Oñate E., 1989. A plastic-damage model for concrete. Int J Solids Struct 25, 299-329.

Maligno A.R., Warrior N.A., Long A.C., 2009. Effects of inter-fibre spacing on damage evolution in unidirectional (UD) fibre-reinforced composites. EUR J MECH A-SOLID 28, 768-776.

Martyniuk K., Sørensen B.F., Modregger P., Lauridsen E.M., 2013. 3D in situ observations of glass fibre/matrix interfacial debonding. Composites: Part A 55 63-73.

McCartney L.N., 1992. Theory of stress transfer in a $0^\circ - 90^\circ - 0^\circ$ cross-ply laminate containing a parallel array of transverse cracks. J Mech Phys Solids 400, 27-68.

Needleman A., Borders T., Brinson L., Flores V., Schadler L., 2010. Effect of an interphase region on debonding of a CNT reinforced polymer composite. Compos Sci Technol 70, 2207-2215.

Ogihara S., Koyanagi J., 2010. Investigation of combined stress state failure criterion for glass fiber/epoxy interface by the cruciform specimen method. Composites Science and Technology 70, 143-150.

París F., Correa E., Cañas J., 2003. Micromechanical view of failure of the matrix in fibrous composite materials. Composites Science and Technology 63, 1041-1052.

París F., Correa E., Cañas J., Mantič V., 2007. Kinking of Transversal Interface Cracks Between Fiber and Matrix. Journal of Applied Mechanics 74, 703-716.

Puck A., Schürmann H., 1998. Failure analysis of FRP laminates by means of physically based phenomenological models. Compos Sci Technol 58, 1045-1067.

Puck A., Kopp J., Knops M., 2002. Guidelines for the determination of the parameters in Puck's action plane strength criterion. Compos Sci Technol 62, 371-378.

Quinson R., Perez J., Rink M., Pavan A., 1997. Yield criteria for amorphous glassy polymers. J Mater Sci 32, 1371-9.

Rice J.R., 1988. Elastic Fracture Mechanics Concepts for Interfacial Cracks, Journal of Applied Mechanics 110, 98-103.

Romanowicz M., 2012. A numerical approach for predicting the failure locus of fiber reinforced composites under combined transverse compression and axial tension. Comput Mater Sci 51, 7-12.

Sørensen B.F., 2006. Determination of mixed mode cohesive laws. Engineering Fracture Mechanics 73, 2642-2661.

Sørensen B.F., Horsewell A., Skov-Hansen P., 2002. In- situ observation of crack formation Bi-2223 HTS tapes. Physica C: Superconductivity 372-376, 1032-1035.

Sørensen B.F., Goutianos S., 2014. Mixed Mode cohesive law with interface dilatation. Mech Mater 70, 76-93.

Totry E., González C., Llorca J., 2008. Failure locus of fiber-reinforced composites under transverse compression and out-of-plane shear. Compos Sci Technol 68, 829-839.

Tvergaard V., 1976. Effect of thickness inhomogeneities in internally pressurized elasticplastic spherical shells. Journal of the Mechanics and Physics of Solids 24, 291-304.

Tvergaard V., 1990. Effect of fibre debonding in a whisker-reinforced metal. Material Science and Engineering A125, 203-213.

Tvergaard V., Hutchinson J.W., 1992. The relation between crack growth resistance and fracture process parameters in elastic-plastic solids. J Mech Phys Solids 40, 1377-1397.

Tvergaard V., Hutchinson J.W., 1993. The influence of plasticity on mixed mode interface toughness. J Mech Phys Solids 41, 1119-1135.

Tvergaard V., Legarth B.N., 2007. Effect of anisotropic plasticity on mixed mode interface crack growth. Engineering Fracture Mechanics 74, 2603-2614.

Varna J., Berglund L.A., Ericson M.L., 1997. Transverse single-fibre test for interfacial debonding in composites:2. Modelling, Composites Part A 28A, 317-326.

Yang Q.D., Thouless M.D., 2001. Mixed-mode fracture analyses of plastically-deforming adhesive joints. International Journal of Fracture 110, 175-187.

Zangenberg J., 2013. The effects of fibre architecture on fatigue life-time of composite materials. PhD thesis. ISBN:978-87-92896-48-3.

Zhang H., Ericson M.L., Varna J., Berglund L.A., 1997. Transverse single-fibre test for interfacial debonding in composites: 1. Experimental observations, Composites Part A 28, 309–315.

Zinoviev P., Grigoriev S.V., Labedeva O.V., Tairova L.R., 1998. Strength of multi-layered composites under plane stress state. Compos Sci Technol 58, 1209-1224.

Zinoviev P.A., Lebedeva O.V., Tairova L.P., 2002. Coupled analysis of experimental and theoretical results on the deformation and failure of laminated composites under a plane state of stress. Compos Sci Technol 62, 11711-1724.

Publication [P1]

Experimental and numerical studies of the micro-mechanical failure in composites

EXPERIMENTAL AND NUMERICAL STUDIES OF THE MICRO-MECHANICAL FAILURE IN COMPOSITES

D. A. Vajari[1*], K. Martyniuk[2], B. F. Sørensen[2], B. N. Legarth[1]

[1] Department of Mechanical Engineering, Solid Mechanics, Technical University of Denmark, 2800 Kgs. Lyngby, Denmark,
[2] Department of Wind Energy, Section of Composites and Materials Mechanics, Technical University of Denmark, Risø Campus, 4000 Roskilde, Denmark
[*] Corresponding author (dvaj@mek.dtu.dk)

Abstract

The fibre/matrix interfacial debonding is found to be the first microscale failure mechanism leading to subsequent macroscale transverse cracks in composite materials under tensile load. In this paper, the micromechanical interface failure in fiber-reinforced composites is studied experimentally and by numerical modeling by means of the finite element analysis. Two fibers embedded in the matrix are subjected to a remote transverse tensile load (see Fig. 1a). The trapezoidal cohesive zone model proposed by Tvergaard and Hutchinson [14] is used to model the fracture of the fiber-matrix interfaces. This study is based on the comparison between the results of numerical modeling and those corresponding to the experimental tests by employing two parameters: The angle from the load direction to the crack tip and the crack normal opening. This comparison aims to investigate the interfacial properties and also assess the progressive fiber-matrix debonding by focusing on the interaction of two fibers with dissimilar interfacial strengths.

1 Introduction

Depending on the material properties and loading conditions, interface debonding, matrix failure and/or fiber breakage are the main failure mechanisms in composites. In many cases, interfacial debonding is the first mechanisms which leads to crack initiation and propagation. Therefore, it is important to investigate the interface parameters accurately. The interface fracture energy, ϕ, and the maximum cohesive stress, σ_{max}, are the most critical parameters playing significant roles in failure of interfaces. The experimental part of the present research aims at determining the interface parameters. Furthermore, the effects of fiber dimension and fiber spacing on the damage evolution in glass-epoxy composites are studied by means of the numerical simulation. Therefore, as the first step it is necessary to find out a proper experimental test method in order to measure the interface fracture energy and the maximum cohesive stress. The lack of a standard two-dimensional test and its corresponding device is the first problem in selecting the method of experimental test. Different methods have been used to characterize the fiber/matrix interface parameters such as the fragmentation test, the pull-out test, the push-in test and the push-out test. Each of these methods has some advantages and disadvantages which should be

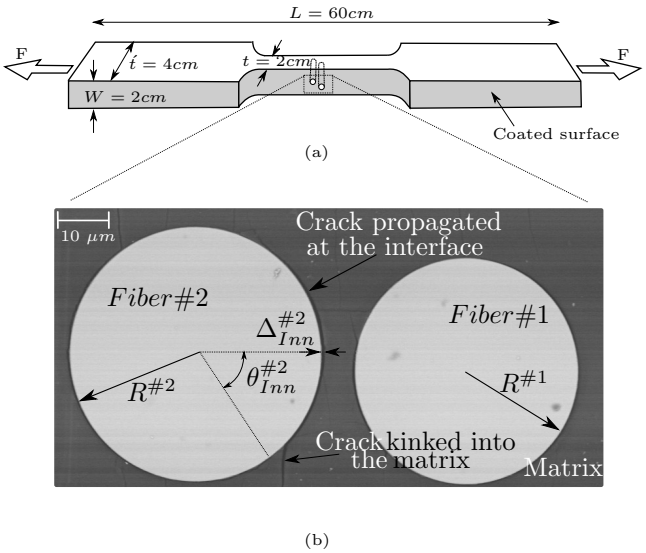

Figure 1: a) Schematic drawing of specimen with a dog-bone shaped epoxy resin including two glass fibers in the middel of specimen. b) Example of debonding obseved in SEM under tensile test.

considered for a specific purpose under investigation. The fragmentation test was proposed by Kelly and Tyson[5] to study the interface properties in metal matrix composites. This method was appropriate for composites with ductile matrices and brittle fibers. While, the pull-out test is usually performed for the tough fibers surrounded by brittle matrix. Although the fragmentation test as well as the pull-out test lead to durable results but their testing conditions can be difficult to fulfill. In the push-in technique a single fiber is pushed by means of a nanoindentor on a cross-section of a bulk specimen of the laminate until interface decohesion occurs. On the other hand, the push-in test does not require any laborious sample preparation. However, the interpretation of this method is somehow difficult because the length of the debonded interface below the surface is not known. Thus, the results should be analyzed in terms of a shear lag model or FE simulations of the test [8]. The push-out test is very similar to the push-in test but is carried out on a very thin specimen. Although the push-out test requires more difficult specimen preparation, but leads to a more direct measurement of the interface strength [2]. However, both the push-in as well as push-out methods involve frictional sliding while the friction law or shear stress is unknown. Thus it is difficult to separate debonding and frictional sliding which happen simultaneously. Furthermore, all above interface measuring techniques try to investigate the tangential properties of the interface. While for the cases subjected to a tensile load normal to the fiber orientation, like the preset study, the dominant debonding is due to normal opening of the interfaces. Thus, in this research another method has been used which approaches to a more direct measurement of the normal properties of fiber/matrix interfaces in uni-directional composites. In this method, a specimen including a single or double fibers embedded in the matrix is subjected to tensile load inside the chamber of the Scanning Electron Microscope (SEM). The cross-section normal to the fiber orientation will be monitored while the load is being applied. By this technique, more precise data with respect to the normal properties of interface such as the cohesive maximum normal stress and cohesive fracture energy can be determined.

This paper comprises five sections. After the introduction the proposed experimental method is presented in detail in the next section. Then, the numerical methods used in the simulation is given in section 3. In the fourth section, the results are shown and discussed. Finally, this study is concluded in section 5.

2 Experimental Study

The fiber/matrix interface properties of fiber-reinforced composites are determined according to the transverse tensile test inside the SEM. The glass-fibers used in this experimental study are provided by Ahlstorm. The diameters of fibers are $\sim$ 45-55 μm. The fibers with large diameter are chosen to measure the interface debonding since this is easier by the SEM. The experimental samples are manufactured by positioning two glass-fibers in a rubber mold. Then, the mold is filled up with a fast-curing epoxy resin named *RIMR 135* (from Momentive company) which surrounds the fibers. The fibers Young's modulus and Poisson's ratio are $E_f = 72GPa$ and $\nu_f = 0.21$, respectively and for the matrix the properties are $E_m = 3GPa$ and $\nu_m = 0.3$. The yield stress of the matrix material is $\sigma_y = 16MPa$. To find the yield stress of the matrix, a parameter study is carried out to fit the numerical debonding angle-remote stress curve as well as the numerical crack normal opening-remote stress cuve with those corresponding to the experimental data. Thermal compressive residual stresses in the fiber along the longitudinal axis as well as in the radial direction arise due to the thermal expansion mismatch between constituent phases, chemical shrinkage of the resin and non-uniform curing [6]. Radial residual stresses in glass fibers embedded in epoxy resin have rather significant contribution to the general process-induced stress state [16]. However, the residual stresses in the longitudinal direction along the fibers are significantly influencing the stresses in the fibers surrounded by a large volume of resin. It has been shown by single-fiber fragmentation tests that fibers without any pre-loading while curing are under compressive residual stresses [16].

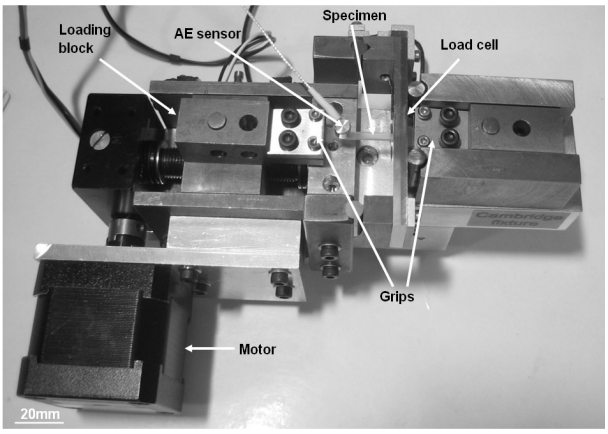

Figure 2: Test set-up for tensile testing in SEM. A motor drives a spindle that moves one of the loading blocks and thus one grip, resulting in tension or compression of the specimen.

Residual stresses could also influence interface properties and cause debonding prior to loading which would prevent studying of interface properties. Therefore, the fibers are pre-loaded before curing. The amount of pre-load can be estimated by calculating the expected compressive residual thermal stress in the fiber. Residual compressive stress of the fibers due to the thermal expansion mismatch between constituent phases are given by [3] and [4]

$$\sigma_f^{th} = (\alpha_m - \alpha_f)(T - T_{ref})\frac{E_f}{1 + (\frac{V_f}{V_m})(\frac{E_f}{E_m})} \quad (1)$$

where, α_m and α_f stands for the thermal expansion coefficient of the matrix and the fibers, respectively. The room temperature is denoted by T and T_{ref} is the reference temperature at which the material solidifies upon cooling. The fiber volume fraction is V_f while the matrix volume fraction is V_m. Finally, E_m and E_f denote the Young's modulus of the matrix and the fibers, respectively. The value of the aforementioned parameters are given in Table. 1. During post-curing the samples including two fibers embedded in a large volume of resin are heated at $60°C$. In this temperature the fibers are under a thermal compressive stress of $\sigma_f^{th} = -130MPa$ which corresponds to a strain level of $\varepsilon^{th} = -0.18\%$. However, the above calculation of residual stresses does not include the chemical reactions. Therefore, during manufacturing process the fibers were pre-strained a little more, i.e. $+0.25\%$. This pre-straining fulfills by applying a weight of $20g$ at each fibers ends. After positioning and pre-straining, the mold is filled up with previously degassed resin. Specimen was cured at $23°C$ for 24 hours and subsequently post-curing at $60°C$ for 10 hours. The surface of interest was polished in order to remove any cracks from the surfaces as well as fulfilling microscopy requirements. Once smooth surface is obtained, samples are reshaped to the dog-bone shape in order to facilitate mechanical testing. The final geometry of the sample is shown in Fig. 1a. Then, the surface faced to the microscope is electrically conducted by a thin coating of a carbon layer.

Material properties	Value
$\alpha_m\ [\frac{1}{°C}]$	65×10^{-6}
$\alpha_f\ [\frac{1}{°C}]$	5.1×10^{-6}
$T\ [°C]$	20
$T_{ref}\ [°C]$	50
$\frac{V_f}{V_m}\ [-]$	≈ 0 (for two-fiber composite)

Table 1: The thermal parameters of the epoxy resin used for the residual compressive stress calculation.

As shown in Fig. 2, the specimen is subjected to the tensile load using a special tensile loading fixture [11] designed for testing in SEM. The fixture was mounted on the x, y, z stage of the vacuum chamber of SEM (Zeiss, EVO60). The polished surface was oriented towards the microscope electron gun and detectors. By this setting in situ observation of crack initiation under the tensile loading can be obtained. During the micro scale experiments, the load was applied to the specimen in increments. The tensile test was interrupted at various load steps until ultimate failure. This enabled observing and capturing of images of the crack propagation using SEM facilities. The fiber/matrix debonding as well as matrix failure near the fibers is shown in Fig. 1b where a crack is seen to initiate at the interfaces between the fibers and the matrix. It propagates along the fiber/matrix interface until a certain angle is reached, at which the crack kinked into the matrix. This study considers the failure be-

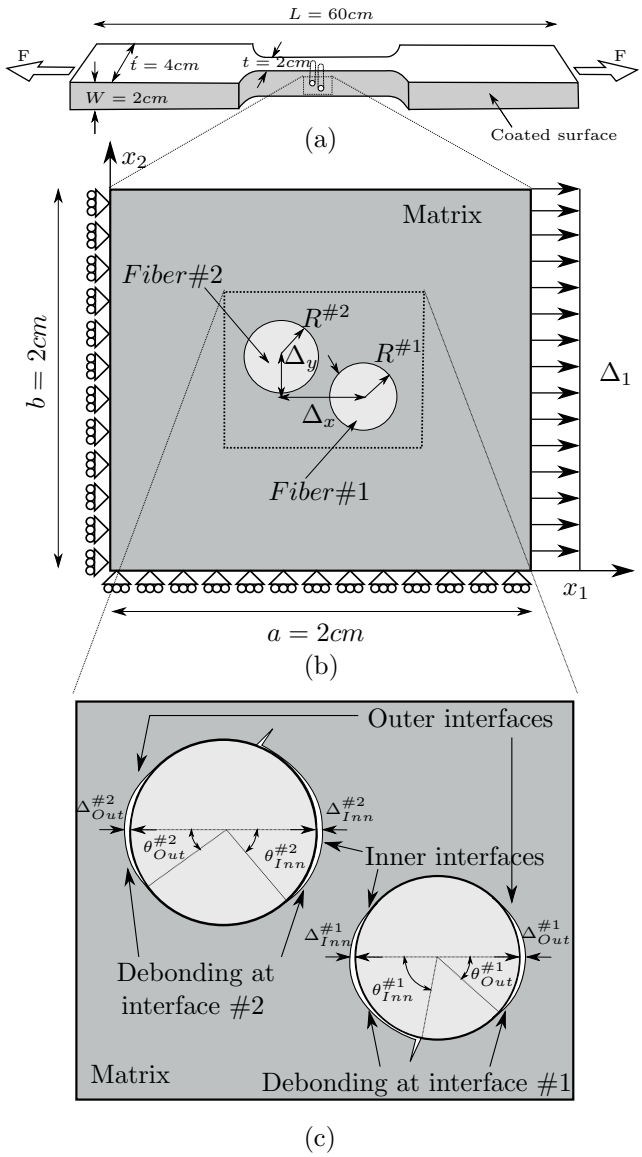

Figure 3: a) Schematic drawing of specimen with a dog-done shaped epoxy resin including two glass fibers in the middle of specimen. b) The chosen 2D-cell from the middle of specimen including two circular fibers. The dimensions, loads and the coordinate system are shown. c) A deformed and partly debonded cell under an x_1-direction tensile load.

fore interfacial crack kinks to the matrix. In the results section, it will be shown that the interface at which debonding initiates depends on the strength of the interfaces as well as the size of the fibers.

3 Numerical Modeling

To simulate the observed fiber/matrix debonding, two circular fibers are embedded in a large zone of matrix (see Fig. 3b). A Cartesian reference coordinate system, x_i, is placed at the bottom-left corner of the cell and aligned with the unit cell edges. The dimension of the cell is determined by the length, b, the width, a, and the radius of the fibers, $R^{\#1}$ and $R^{\#2}$. The cell is subjected to a normal load in x_1-direction. The boundary conditions are implemented incrementally as follows

$$\begin{aligned} &\dot{T}_2 = 0 \quad \text{and} \quad \dot{u}_1 = 0, \quad \text{on} \quad x_1 = 0 \\ &\dot{T}_1 = 0 \quad \text{and} \quad \dot{u}_2 = 0, \quad \text{on} \quad x_2 = 0 \\ &\dot{T}_2 = 0 \quad \text{and} \quad \dot{u}_1 = \dot{\Delta}_1, \quad \text{on} \quad x_1 = a \\ &\dot{T}_1 = 0, \quad \text{on} \quad x_2 = b \end{aligned} \tag{2}$$

where $\dot{\Delta}_1$ and $\dot{\Delta}_2$ describe incremental displacement quantities on the two edges of the cell, and T_i are surface tractions. The overall macroscopic stress increment, $\dot{\Sigma}_{ij}$, are computed as

$$\begin{aligned} \dot{\Sigma}_{11} &= \frac{1}{tb}\int_0^b \dot{T}_1 t dx_2, \qquad \text{at} \quad x_1 = a \\ \dot{\Sigma}_{22} &= \frac{1}{ta}\int_0^a \dot{T}_2 t dx_1, \qquad \text{at} \quad x_2 = b \end{aligned} \tag{3}$$

and the corresponding macroscopic incremental strains are defined as

$$\dot{E}_{11} = \frac{\dot{\Delta}_1}{a}, \quad \dot{E}_{22} = \frac{\dot{\Delta}_2}{b} \tag{4}$$

Assuming $\Sigma_{33} = 0$, the composite is assumed to deform by uniaxial normal loading under plane stress condition. It means, the modeling simulates the specimen surface at which the debonding is monitored by the SEM. In Fig. 3c, the schematic drawing of the specimen with the debonded interfaces are shown after applying tensile load. In each fiber two parameters are measured; The crack opening distance of the inner and outer interface of the fibers which are denoted by Δ_{Inn} and Δ_{Out}, respectively and also the debonding angle being called here as the debonding angle. As shown in Fig. 3c, two angles have been measured in each fiber with debonded interfaces. The crack angle at the inner interface of the fiber #1 is denoted with $\theta^{\#1}_{Inn}$ and the crack angle at the outer interface of the fiber #1 is shown with $\theta^{\#1}_{Out}$. The same notation is used for fiber #2.

3.1 Isotropic Plasticity Model

The matrix is assumed to be an elasto-plastic material governed by the standard J_2-plasticity theory, while the fibers are considered as purely elastic. Both the matrix as well as the fibers are modelled as isotropic materials. In the matrix, the stress increment is calculated from the total strain increment, $\dot{\epsilon}_{ij}$, which consists of an elastic part, $\dot{\epsilon}^e_{ij}$, and a plastic part, $\dot{\epsilon}^p_{ij}$

$$\begin{aligned} \dot{\epsilon}_{ij} &= \dot{\epsilon}^e_{ij} + \dot{\epsilon}^p_{ij} \\ \dot{\sigma}_{ij} &= L_{ijkl}\dot{\epsilon}_{kl} \end{aligned} \tag{5}$$

Here, L_{ijkl} is the fourth order incremental stiffness tensor defined as

$$L_{ijkl} = \frac{E_m}{1+\nu_m}[\frac{1}{2}\left(\delta_{ik}\delta_{jl}+\delta_{il}\delta_{jk}\right) + \frac{\nu_m}{1-2\nu_m}\delta_{ij}\delta_{kl} - \beta\frac{3}{2}\frac{\frac{E_m}{E_t}-1}{\frac{E_m}{E_t}-\frac{(1-2\nu_m)}{3}}\frac{s_{ij}s_{kl}}{\sigma_e^2}] \tag{6}$$

while,

$$\beta = \begin{cases} 1 & \text{for } \sigma_e = \sigma_f \text{ and } \quad \dot{\sigma}_e \geq 0 \\ 0 & \text{for } \sigma_e < \sigma_f \text{ or } \quad \dot{\sigma}_e < 0 \end{cases} \tag{7}$$

where, E_m is the Young's modulus and ν_m is the Poisson's ratio of the matrix. The tangential modulus, E_t, is the slope of the stress-strain curve at the stress level $\sigma_e = \sqrt{\frac{3}{2}s_{ij}s_{ij}}$ and δ_{ij} denotes the Kronecker delta. The stress deviator is defined by $s_{ij} = \sigma_{ij} - \delta_{ij}\frac{\sigma_{kk}}{3}$. In Eq. 7, $\dot{\sigma}_e = \frac{3s_{kl}\dot{\sigma}_{kl}}{2\sigma_e}$ and σ_f is the instantaneous flow stress. During plastic yielding β is unity and the magnitude of L_{ijkl} depends on the stress state and the deformation hardening law whereas in the elastic regime (including elastic unloading) it is governed by Hooke's law where β is zero. The yield surface, f, is taken as the von Mises yield surface

$$f = \sigma_e - \sigma_f(\epsilon^p_e) = 0 \tag{8}$$

Here, $\sigma_f = \sigma_f(\epsilon^p_e)$, where and ϵ^p_e is the equivalent plastic strain, work conjugate to σ_e, and it is defined incrementally by the relation $\dot{\epsilon}^p_e = \sqrt{\frac{2}{3}\dot{\epsilon}^p_{ij}\dot{\epsilon}^p_{ij}}$. The hardening behavior determined by the uniaxial stress-strain relation which is represented by the power hardening law

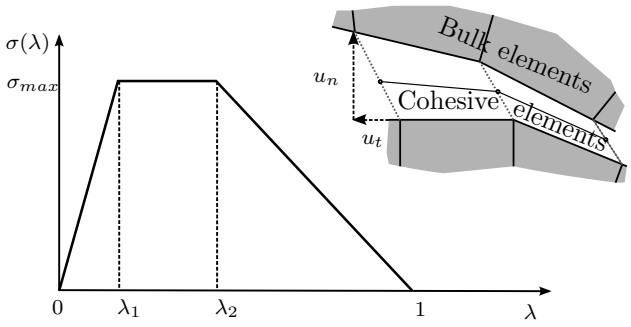

Figure 4: Traction-separation law used to characterize interface separation.

$$\epsilon = \begin{cases} \frac{\sigma}{E} & \text{for } \sigma \leq \sigma_y \\ \frac{\sigma_y}{E}\left(\frac{\sigma}{\sigma_y}\right)^n & \text{for } \sigma > \sigma_y \end{cases} \tag{9}$$

where n is the strain-hardening exponent and σ_y denotes the initial yield stress.

3.2 Cohesive Zone Model

When the cell is deformed, the interfaces between fibers and matrix tend to separate normally as well as tangentially. In order to capture this fracture behavior, a trapezoidal cohesive zone model proposed by Tvergaard and Hutchinson [14] is used (see Fig. 4). As illustrated in Fig. 3c the failure by debonding is taken into account by considering two generally uneven cohesive zones along the two reinforcement interfaces. The cohesive zone model determines the failure behavior imposing a relation between tractions and separations. This traction-separation law is regarded as a phenomenological characterization of the separation zone along the interfaces and not the description of atomic separation, see [14]. In this model, λ is defined as a non-dimensional parameter describing the separation as

$$\lambda = \sqrt{\left(\frac{u_n}{\delta^c_n}\right)^2 + \left(\frac{u_t}{\delta^c_t}\right)^2} \tag{10}$$

such that onset of degradation in the cohesive zone starts at a specified value, $\lambda = \lambda_2$, and fully damage occurs when $\lambda = 1$. Here, δ^c_n and δ^c_t are the normal and tangential characteristic cohesive lengths, respectively, and u_n and u_t are the normal and tangential separation of the interface,

respectively. A traction potential can be defined as

$$\Phi(u_n, u_t) = \delta_n^c \int_0^\lambda \sigma(\acute{\lambda}) d\acute{\lambda} \qquad (11)$$

from which the normal, T_n, and tangential, T_t, tractions acting on the interfaces can be devided according to

$$T_n = \frac{\partial \Phi}{\partial u_n} = \frac{\sigma(\lambda)}{\lambda} \frac{u_n}{\delta_n^c}, \quad T_t = \frac{\partial \Phi}{\partial u_t} = \frac{\sigma(\lambda)}{\lambda} \frac{\delta_n^c}{\delta_t^c} \frac{u_t}{\delta_t^c} \qquad (12)$$

The incremental traction vector is related to the displacement increments across the interface as

$$\begin{bmatrix} \dot{T}_t \\ \\ \dot{T}_n \end{bmatrix} = \begin{bmatrix} \frac{\partial T_t}{\partial u_t} & \frac{\partial T_t}{\partial u_n} \\ \\ \frac{\partial T_n}{\partial u_t} & \frac{\partial T_n}{\partial u_n} \end{bmatrix} \begin{bmatrix} \dot{u}_t \\ \\ \dot{u}_n \end{bmatrix} \qquad (13)$$

where the matrix on the right hand side is the cohesive tangent matrix. In pure normal separation ($u_t = 0$) the maximum traction is $T_n = \sigma(\lambda)$ where $\lambda = \frac{u_n}{\delta_n^c}$, while under pure tangential separation ($u_n = 0$) the maximum traction is $T_t = \frac{\delta_n^c}{\delta_t^c}\sigma(\lambda)$ where $\lambda = \frac{u_t}{\delta_t^c}$. Thus, for both the interfaces considered here, five interface parameters need to be specified, i.e. δ_n^c, δ_t^c, λ_1, λ_2 and σ_{max}. In addition, a plateau in the maximum traction level in the trapezoidal cohesive zone model simutaneously allows more Gauss points of cohesive elements to be at the maximum stress. This may lead to more stable numerical solutions in comparison with bilinear and exponential models [1]. However, Tvergaard and Hutchinson [14] discussed that under small scale yielding and small scale fracture process zone the shape of the separation law has a secondary importance and the most critical parameters are the maximum cohesive stress and the characteristic cohesive length. Finally, it should emphesized that this model takes the same fracture energy for all mode mixities although the tangential cohesive length, δ_t^c, is considered to be larger than the normal cohesive length, δ_n^c.

3.3 Numerical Methods

For the numerical implementation the incremental form of the principle of virtual work is adopted. Disregarding body forces, the principle reads

$$\int_V \dot{\sigma}_{ij} \delta \dot{\epsilon}_{ij} dV + \int_{S_I} (\dot{T}_n \delta \dot{u}_n + \dot{T}_t \delta \dot{u}_t) dS = \int_S \dot{T}_i \delta \dot{u}_i dS \qquad (14)$$

where V denotes the volume of the unit cell having the surface S and S_I is the surface of the fiber-matrix interface. In Fig. 5 an example of finite element mesh is shown. The mesh consists of 4420 elements including 286 cohesive elements. Eight-node quadrilateral elements with nine Gauss points are used for the bulk materials while six-node quadrilateral elements with three Gauss points are considered for the cohesive zones. As shown in Fig. 5, the mesh is refined near the interfaces. Tvergaard and Legarth [15] characterized the length of the fracture process region, ℓ, in the cohesive zone during crack growth by the distance from the crack-tip, where $\lambda = 1$, to the point ahead of the crack-tip where $\lambda = \lambda_1$. They found a good resolution and very little mesh dependence when the value of ℓ is several times the length, Δ_0, of a square element in the uniform mesh region (here, around the interfaces in Fig. 5). This requirement is satisfied in the present computations as $\ell \geq 10\Delta_0$ corresponding to 10 elements in the active cohesive zone. In each incremental step, Δt, for

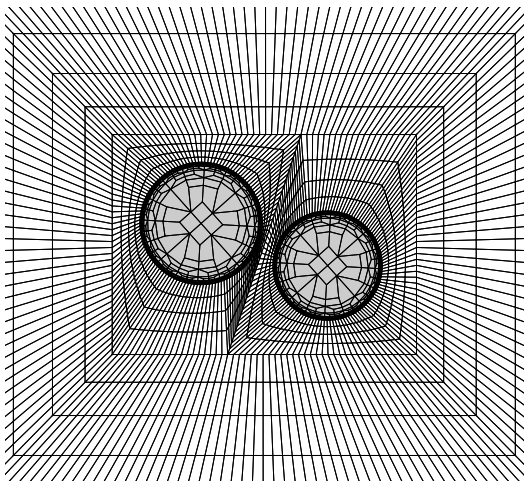

Figure 5: An example of mesh used for the computations. The fiber are positioned in the matrix with the distance of $\Delta_x = 60\mu m$ and $\Delta_y = 20\mu m$ from each other. The fibers radiuses are $R^{\#1} = 25\mu m$ and $R^{\#2} = 28\mu m$.

the next increment is corrected according to $(\dot{\epsilon}^p)_{max} \cdot \Delta t \leq c_1$ and $\left(\dot{\lambda}\right)_{max} \cdot \Delta t \leq c_2$, where the label max refers to the maximum effective plastic strain rate in any Gauss point, or the maximum rate of debonding separation measure at the current increment. Since a forward Euler integration scheme is adopted, it has been investigated if the results are affected by c_1 and c_2. Thus, the values of the constants c_1 and c_2 are in several computations chosen as $c_1 = 0.01$ and $c_2 = 0.004$. In addition, discontinuous increment analysis is used, such that when the first Gauss point in the bulk material reaches the plastic regime or when the first Gauss point in the cohesive elements of each interface reaches $\lambda = \lambda_2$ the solver turns one step back and continue the solution with reduced increment size. The amount of step reduction as well as c_1 and c_2 parameters are chosen such that a stable and converged solution is achieved. Thus, for further reduced time steps similar results are obtained.

4. Results and discussion

The in situ observations from the tensile tests conducted inside SEM reveal that debonding at the fiber/matrix interfaces is the first failure mechanism occurring in the two-fiber composite tested here. The results show that the crack initiates at 0° and 180° with respect to the tensile load orientation at $\sim 7MPa$. The applied remote stress is defined by $\sigma_{exp} = \dfrac{F}{A}$ where F and A are the applied tensile load and the area under the load, respectively. Subsequently, the crack propagates at the fiber/matrix interface until a point at which further load leads to crack kinking into the matrix. The applied remote stress at kinking has been measured to be $\sigma_{exp} \sim 14MPa$. In addition, as shown in Fig. 1 the orientation of crack propagating into the matrix is perpendicular to the load orientation indicating mode-I fracture in the matrix. In order to characterize the cohesive parameters used in the numerical modeling, a parameter study has been carried out by fitting the numerical results with the experimental findings. Beside the amount of remote stress at which debonding initiates, the angle of the propagating crack as well as the amount of crack normal opening distance at the

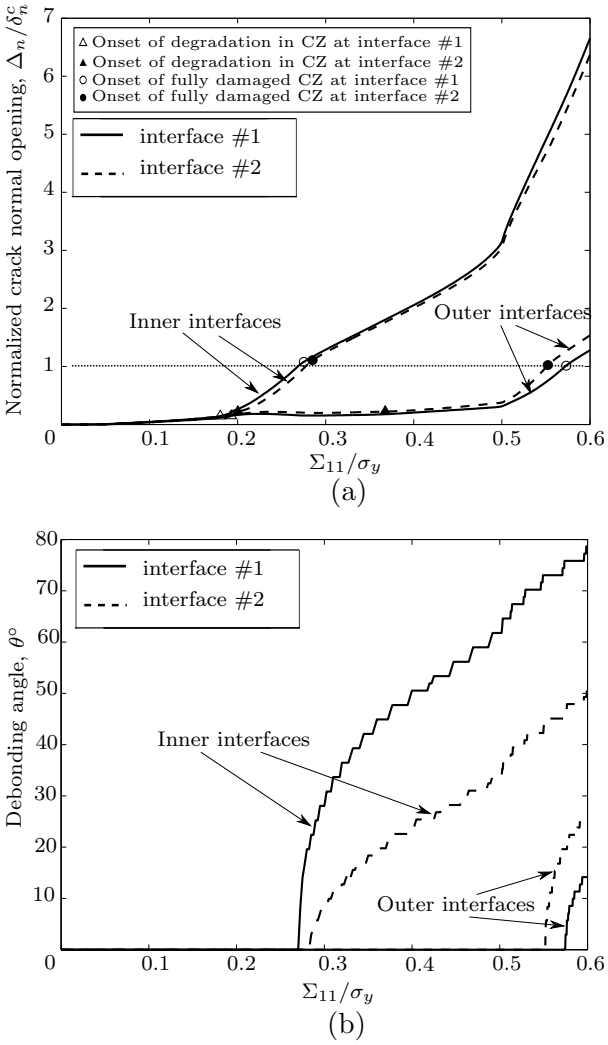

Figure 6: a) The normalized crack normal opening-remote stress and b) the debonding angle-remote stress for the reference case, $R^{\#1} = R^{\#2} = 25\mu m$, $\delta_n^c = 0.006R^{\#1}$, $\delta_t^c = 5\delta_n^c$, $\sigma_{max}^{\#1} = \sigma_{max}^{\#2} = 0.5\sigma_y$, $\lambda_1 = 10^{-4}$, $\lambda_2^{\#1} = 0.1$ and $\lambda_2^{\#2} = 0.2$. The figure illustrates the onset of degradation in the cohesive zone and fully damaged cohesive zone of the two interfaces on the curve.

fiber/matrix interfaces have been measured. This comparison indicates that the maximum cohesive stress is $\sigma_{max} \simeq 8MPa$ and the characteristic cohesive length is $\delta_n^c \lesssim 0.15\mu m$. Calculating the interface normal fracture energy, ϕ, by $\phi = \dfrac{\sigma_{max}(1 + \lambda_2 - \lambda_1)\delta_n^c}{2}$, the above characterization denotes that the interface normal fracture energy is relative small ($\lesssim 0.5\dfrac{J}{m^2}$) in comparison with the epoxy fracture energy which is normally above $100\dfrac{J}{m^2}$. Furthermore, the very small char-

acteristic cohesive length indicates that failure of glass-fiber/epoxy interfaces are very brittle.

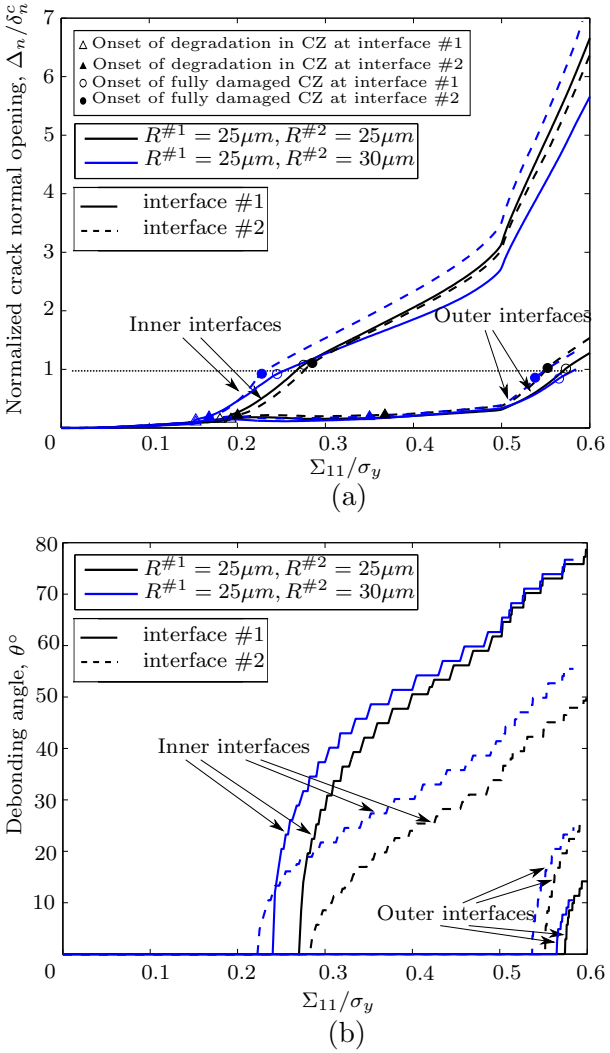

Figure 7: Effect of the fiber radius, R, on a) the normalized crack normal opening, Δ_n/δ_n^c, and b) the debonding angle, θ. The interfaces parameters, the geometry (except the radius of fibers) and loading conditions are identical to the reference case, see Fig. 6.

Using the above characterized cohesive parameters, a parameter study is carried out to assess the effect of fiber positioning and the maximum cohesive stress on the damage evolution of two-fiber composite. In Fig. 6, the behavior of the two-fiber cell for a reference case is shown. The reference case denotes when $R^{\#1} = R^{\#2} = 25\mu m$ and the interfacial parameters for both interfaces are $\delta_n^c = 0.006R^{\#1}$, $\delta_t^c = 5\delta_n^c$, $\sigma_{max}^{\#1} = \sigma_{max}^{\#2} = 0.5\sigma_y$ and $\lambda_1 = 10^{-4}$, while interface #1 has $\lambda_2^{\#1} = 0.1$, and for interface #2, $\lambda_2^{\#2} = 0.2$. Different λ_2 values which also yield slightly different fracture energies (i.e. $\phi^{\#1} = 0.48\frac{J}{m^2}$ and $\phi^{\#2} = 0.54\frac{J}{m^2}$) lead to uneven interfacial strengths at the two interfaces. Many experiments (e.g. [9] [12]) have shown that the the interfacial fracture energy increases with mode mixity. However, in the current study a cohesive law with the same fracture energy for all mode mixities is used. Fig. 6a and Fig. 6b illustrates the normalized crack normal opening, Δ_n/δ_n^c, and the debonding angle, θ, respectively. The inner interfaces denote

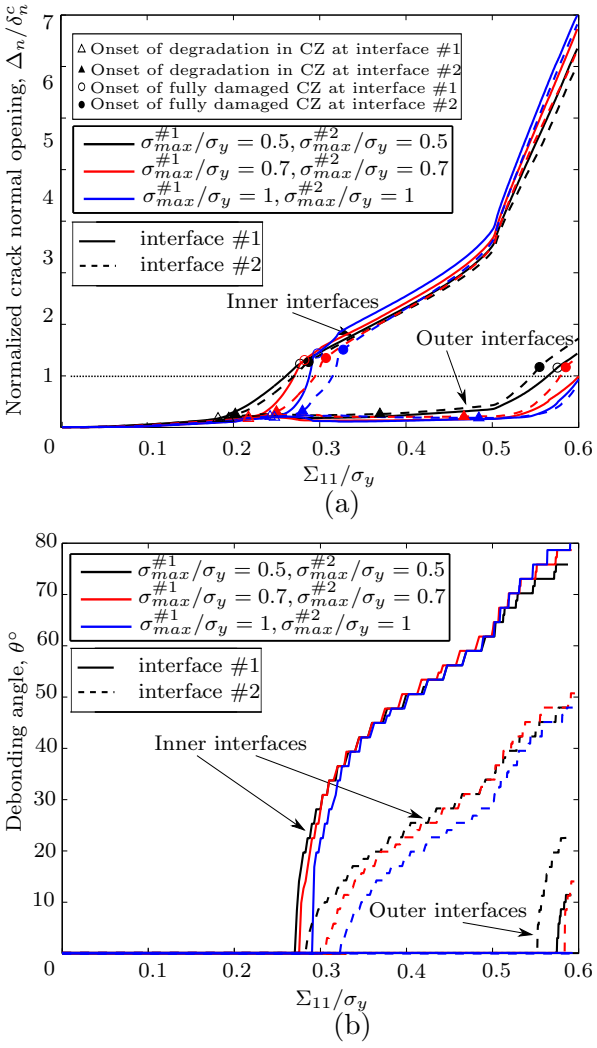

Figure 8: Effect of the maximum cohesive stress, σ_{max}, on a) the normalized crack normal opening distance, Δ_n/δ_n^c, and b) the debonding angle, θ. The interfaces parameters (except the maximum cohesive stresses), the geometry and loading conditions are identical to the reference case, see Fig. 6.

the interfaces in the ligament between the two fibers while the outer interfaces are those at the outer side of the fiber far away from the other fiber (see Fig. 2). As shown in Fig. 6a, the initial crack opening occurs at $\frac{\Sigma_{11}}{\sigma_y} \simeq 0.27$ at the inner interfaces and $\frac{\Sigma_{11}}{\sigma_y} \simeq 0.57$ at the outer interfaces which shows that debonding at the interfaces close to the ligaments initiates earlier than those on the outer sides. This clearly shows that the presence of the second fiber strongly affect the debonding of the first fiber. These numerical values of stress at the crack initiation match to the experimental findings reported in the beginning of the result section. At the inner interfaces, by increasing the loading the normalized crack normal opening, Δ_n/δ_n^c, grows up slightly with a linear slope until the point where debonding leads to nonlinear behavior on the curve. This nonlinearity is due to the degradation of traction-separation in the cohesive low when $\lambda = \lambda_2$ at each cohesive Gauss points. The first Gauss point which reaches $\lambda = \lambda_2$ is depicted by ($\triangle$). Afterwards, subsequent Gauss points at the same cohesive interface also pass $\lambda = \lambda_2$ and therefore the interface gets weaker which leads to nonlinearity on the curve until the first Gauss point at $\Sigma_{11} \simeq 0.28\sigma_y$ gets fully damaged, i.e. $\lambda^{\#1} = 1$, ($\bigcirc$). By continuing loading the crack propagates along interface #1. When interface #1 is being debonded, the normalized crack normal opening versus normalized remote stress shows again a linear behavior until interface #2 starts debonding at $\Sigma_{11} \simeq 0.55\sigma_y$. As for interface #1, the same points are marked but with the filled symbols ($\blacktriangle$ and $\bullet$). The slope of the curves in Fig. 6b represents the crack growth rates. For all cases in the beginning of the crack growth the slope is very sharp denoting that the crack propagates very fast and unstable. But subsequently the slope decreases and the crack propagates at almost a constant growth rate. París et al. ([10] and [9]) studied the mechanisms of failure in a single fiber surrounded by the matrix under transverse tension. Their observation shows that a crack starts running at the interfaces and after a certain angle (between 60° to 70°) the crack kinks into the matrix. The same interval of kinking angle is confirmed in the present experimental obsevations. However, this research focuses on the failure mechanisms before kinking occurs. Therefore, in Fig. 6b, the curves are shown until maximum $\theta = 80°$.

Fig. 7 shows the effect of fiber radius size on the crack initiation at the interfaces. In this figure, fiber #1 has $R^{\#1} = 25\mu m$ while the radius of fiber #2 is $R^{\#2} = 30\mu m$. As depicted in Fig. 7a (see $\bigcirc$-marks and $\bullet$-marks) and in Fig. 7b earlier debonding occurs at the both interfaces when the radius of fiber #2 increases. This earlier debonding can be due to the decrease of the ligament between the two fibers. However, the behavior of the curves remain almost unchanged.

The effect of the maximum cohesive stress is shown in Fig. 8. As illustrated in Fig. 8b, increase of the maximum cohesive stress postpones debonding. But as shown in Fig. 8a, increasing the maximum cohesive stress leads to larger normal crack opening. In addition, Fig. 8b depictes that the cracks of the inner interfaces after $\sim 40°$ grow exactly on the same curve regardless of the maximum cohesive changes.

Lastly, Fig. 9 illustrates the corresponding contours of the accumulated equivalent plastic strain, ϵ_e^p, for the reference case when the remote stress in x_1-direction is $\frac{\Sigma_{11}}{\sigma_y} = 0.6$ (see Fig. 6). Some plastic deformation can be seen in the ligament between two fibers but most plastic deformations are in front of the crack tips in the top and bottom of the fibers. This plasticity in the vicinity of the crack tips is due to the tensile stress in x_1-direction which eventually leads to shear debonding at the interfaces in the top and bottom of the fibers. Fig. 9 also shows the same crack normal opening in the inner interfaces as well as at the outer interfaces. Although the outer interfaces have smaller crack openings than the inner interfaces. In addition, the debonding at the inner interface in the ligament between the fibers, $\theta_{Inn}^{\#2} = 51°$, shows smaller crack angle than the inner interface away from the ligament, $\theta_{Inn}^{\#1} = 79°$.

5. Conclusion

The interfacial parameters are characterized by comparing the experimental results with those from the finite element analysis using the cohe-

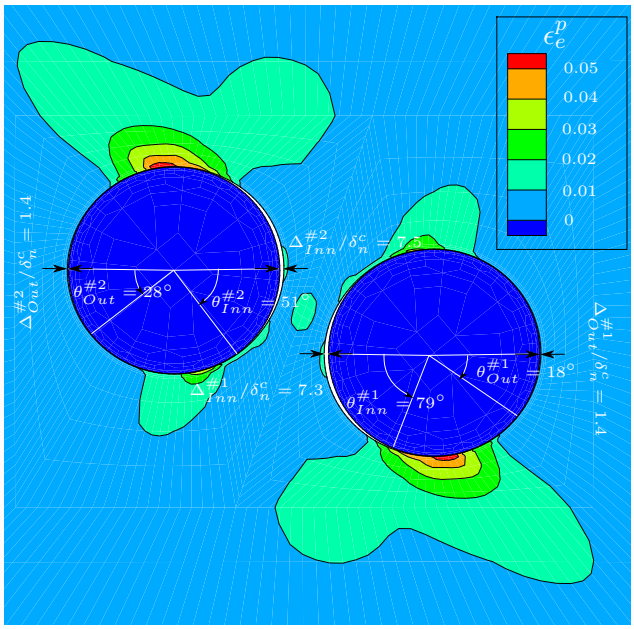

Figure 9: Contours of the accumulated equivalent plastic strain, ϵ_e^p, at $\Sigma_{11}/\sigma_y = 0.6$, see Fig. 6.

sive zone model. The experimental results are determined by performing the in situ tensile tests on a two-fiber composite inside the chamber of SEM. The characterization showes that the maximum cohesive stress is $\sigma_{max} \simeq 8MPa$ while the characteristic cohesive length is $\delta_n^c \lesssim 0.15\mu m$. These two parameters result that the interface normal fracture energy, ϕ, to be $(\lesssim 0.5\frac{J}{m^2})$. Then, knowing the actual interface properties, different positioning of fibers is studied to investigate the progressive interfacial damage evolution by focusing on the interaction between two fibers with uneven interfacial strengths. It was found that the interfacial normal fracture energy is significantly small compared to the epoxy fracture energy. The results show that debonding initiates at the inner interfaces followed by the outer interfaces. In addition, debonding triggers earlier if the radius of one of the fibers increases. Finally, larger maximum cohesive stress leads to stronger interfaces and subsequently postpones debonding of the interfaces.

Acknowledgement

The authors would like to thank the research technicians: Steen J. Bang, Christian H. Madsen and Jonas Heininge for their assistance with specimen preparation. This work is supported by the Danish Council for Strategic Research (grant no.:09-067212) under the Danish Center for Composite Structures and Materials for Wind Turbines.

References

[1] N. Chandra, H. Li, C. Shet, H. Ghonem "Some issues in the application of cohesive zone models for metal?ceramic interfaces". *International Journal of Solids and Structures*, Vol.39, pp 2827-2855, 2002.

[2] A. Godara, L. Gorbatikh, G. Kalinka, A. Warrier, O. Rochez, L. Mezzo, F. Luizi, A.W. van Vuure, S.V. Lomov, I. Verpoest "Interfacial shear strength of a glass fiber/epoxy bonding in composites modified with carbon nanotubes". *Composites Science and Technology*, Vol.70, pp 1346-1352, 2010.

[3] J.W. Hutchinson and Z. Suo "Mixed Mode Cracking in Layered Materials". *Advances in Applied Mechanics*, Vol.29, pp 63-191, 1992.

[4] J.W. Hutchinson "Mixed mode fracture mechanics of interfaces". *Metal-Ceramics, Acta-Scripta Metallurgica Proceedings Series* Vol.4, pp 295-306, 1990.

[5] A. Kelly, W.R. Tyson "Tensile properties of fiber-reinforced metals: cop- per/tungsten and copper/molybdenum". *Journal of the Mechanics and Physics of Solids* Vol.13, pp 329-350, 1965.

[6] B.K. Larson, L.T. Drzal "Glass fibre sizing/matrix interphase formation in liquid composite moulding: effects on fibre/matrix adhesion and mechanical properties". *Composites* Vol.25, pp711-21, 1994.

[7] B.N. Legarth and C.F. Niordson "Debonding failure and size effects in micro-reinforced composites". *International Journal of Plasticity* Vol.26, pp 149-165, 2010.

[8] J.M. Molina-Aldareguía, M. Rodríguez, C. González, J. LLorca "An experimental and numerical study of the influence of local effects on the application of the fibre push-in test.". *Philosophical Magazine* Vol.91, pp 1293-1307. 2011.

[9] F. París, E. Correa, J. Cañas "Micromechanical view of failure of the matrix in fibrous composite materials". *Composites Science and Technology* Vol.63, pp 1041-1052, 2003.

[10] F. París, E. Correa, J. Cañas, V. Mantič "Kinking of Transversal Interface Cracks Between Fiber and Matrix". *Journal of Applied Mechanics* Vol.74, pp 703-716, 2007.

[11] B.F. Sørensen, A. Horsewell, P. Skov-Hansen "In- situ observation of crack formation Bi-2223 HTS tapes". *Physica C: Superconductivity* Vol.372-376, pp. 1032-1035, 2002.

[12] B.F. Sørensen, T.K. Jacobsen "Characterizing delamination of fibre composites by mixed mode cohesive laws". *Composites Science and Technology* Vol.69, pp. 445-456, 2009.

[13] V. Tvergaard "Effect of thickness inhomogeneities in internally pressurized elastic-plastic spherical shells". *Journal of the Mechanics and Physics of Solids* Vol.24, pp 291-304, 1976

[14] V. Tvergaard, J.W. Hutchinson "The influence of plasticity on mixed mode interface toughness". *Journal of the Mechanics and Physics of Solids* Vol.41, pp 1119-1135, 1993.

[15] V. Tvergaard, B.N. Legarth "Effect of anisotropic plasticity on mixed mode interface crack growth". *Engineering Fracture Mechanics* Vol.74, pp 2603-2614, 2007.

[16] S.F. Zhandarov, E.V. Pisanovab "The local bond strength and its determination by fragmentation and pull-out test". *Composites Science and Technology* Vol.57, pp 957-64, 1997.

Publication [P2]

Effect of fiber positioning on mixed-mode fracture of interfacial debonding in composites

Effect of Fiber Positioning on Mixed-mode Fracture of Interfacial Debonding in Composites

Danial Ashouri Vajari[a,*], Bent F. Sørensen[b], Brian Nyvang Legarth[a]

[a] *Department of Mechanical Engineering, Solid Mechanics, Technical University of Denmark, DK-2800 Kgs. Lyngby, Denmark*
[b] *Department of Wind Energy, Section of Composites and Materials Mechanics, Technical University of Denmark, Risø Campus, 4000 Roskilde, Denmark*

Abstract

Under transverse tensile loading, fibers oriented prependicular to the tensile direction can undergo fiber/matrix debonding. Experiments show that the first stage of fiber/matrix interface debonding is mode-I dominated fracture with very fast crack growth rate. Subsequent stable crack propagation along the interface is due to mixed mode I/II fracture. The aim of this study is to explore ways to stabilize the early stage of debonding so that it becomes possible to determine the mixed mode interfacial fracture properties for the entire mode-mixity range by *in-situ* observations. Therefore, the objective of this study is to stabilize crack initiation in the dominant mode-I fracture by changing the position of one fiber with its neighboring fiber or hole using the finite element analysis. The progressive fiber/matrix debonding is studied by focusing on the interaction of one fiber with its neighboring fiber or hole. The results show that decrease of the position angle stabilize the crack growth at the interface in the ligaments. This effect is more significant in the cases with small ligament thickness. In the two-fiber model and at very small ligaments the results show that the crack growth stops when the crack tips meet each other in the ligament and further crack growth is under dominant mode-II fracture. In the fiber-hole model, both the crack initiation and propagation are stabilized by decrease of the position angles at very thin ligaments. This paper suggests that an experimental set-up may lead to ease the characterization of interfacial properties due to more stable crack growth.

*Corresponding author
Email address: dvaj@mek.dtu.dk (Danial Ashouri Vajari)

Keywords: Micromechanics, Composites, Interfacial debonding, Mode-mixity, Finite element

1. Introduction

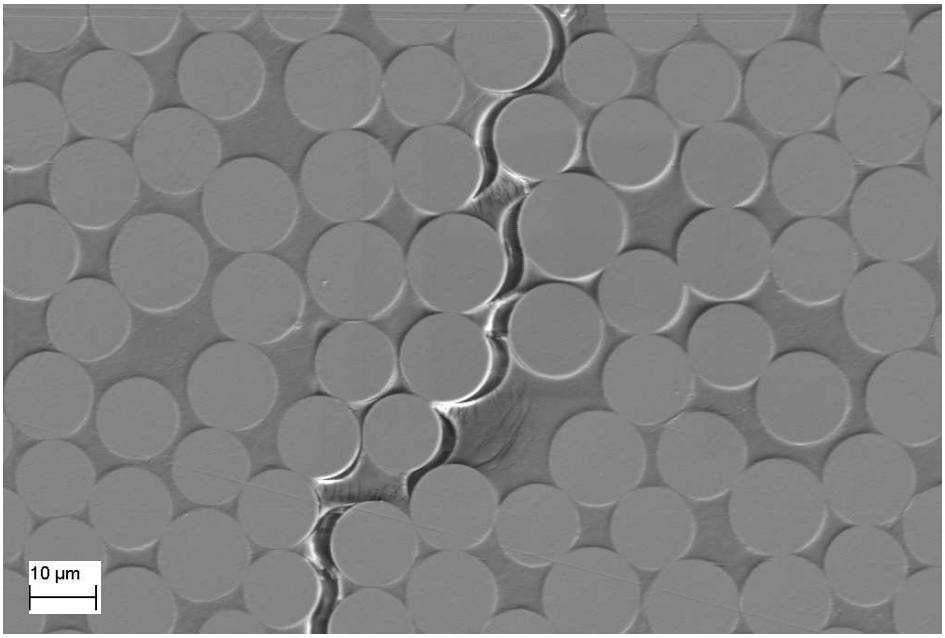

Figure 1: The *in-situ* SEM observation of crack growth in 90° glass-epoxy lamina under transverse tensile loading.

Fiber/matrix interfacial debonding is one of the main micromechanical failure mechanisms in composites. As shown in Fig. 1, the author's experimental observations show that in glass-polymer composites under transverse tensile loading cracks often initiate and propagate at the fiber/matrix interfaces due to weaker strength of interfaces in comparison with the matrix and fibers. Thus, in these loading conditions the interfacial failure mechanisms often controls the macroscopic strength of unidirectional composites (Moraleda et al., 2009). As a result, it is essential to accurately understand the failure mechanisms occurring at the fiber/matrix interfaces.

Contrary to homogenous and isotropic materials where crack propagates in pure mode-I under mode-I tension, mode-mixity is an important factor

in bimaterials such as fiber-reinforced composites as interfacial debonding occurs always under mixed mode (Williams, 1959; Rice, 1988; Agrawal and Karlsson, 2006). The existence of mode-mixity is due to the elastic mismatch between two different materials along an interface which leads to a non-symmetric stress field at the crack tip (Rice, 1988; Hutchinson, 1990). As a result, for a single fiber oriented perpendicular to the tensile direction, crack initiation will be mode-I dominant for angle of the crack tip position at 0° or 180° with respect to the loading direction. The amount of shear (mode-II) increases as the crack tip propagates along the interface and the debonding angle increases. It is found that the interfacial fracture toughness, G_c, depends on the mode-mixity (Liechti and Chai, 1992) and the mode-mixity, itself, varies with respect to the debonding angle (París et al., 2003). París et al. (2003, 2007) reported that the mode-II is dominant at debonding angle of $60^\circ - 70^\circ$ which leads to a stable crack growth or crack kinking into the matrix. Different analytical methods have been used to calculate the mode-mixity at the interfacial crack tips. Mode mixity can be determined using a stress intensity factor-based approach by assuming linear elastic fracture mechanics (LEFM) or can be based on the components of the energy release rate (Rice, 1988; Hutchinson, 1990). It can also be determined by crack tip opening displacements in terms of tangential and normal displacement components (Liu et al., 1995; Agrawal and Karlsson, 2006; Sørensen and Kirkegaard, 2006).

For complicated geometries or loading conditions the numerical methods are often preferred rather than the analytical approaches. Among different numerical methods, cohesive zone models have been widely used in numerical studies as a powerful tool to model fracture of the bimaterial interfaces and especially when LEFM is not applicable. Several cohesive zone models with different traction-separation laws have been proposed. Yang and Thouless (2001) used a mode-dependent cohesive law. This model allowed them to consider different work of separation (fracture energy) under mode-II than mode-I and subsequently used a mode mixity defined from the work of separations of shear and normal tranctions. However, they implemented an uncoupled cohesive stiffness (i.e. the normal traction depends only on the normal opening displacement and is independent of the tangential opening and visa versa for the shear traction). In the present study, the trapezoidal cohesive model proposed by Tvergaard and Hutchinson (1993) is used. In the trapezoidal cohesive model the normal and tangential tractions are derived from the same work of separation but they depend on both the normal as

well as the tangential displacement components. Here, the interfacial mode-mixity is calculated based on the crack tip opening displacement.

In order to approach to realistic numerical results, experimental tests has to be conducted to determine the cohesive parameters. Different experimental techniques have been performed to characterize the fiber/matrix interface parameters such as the fragmentation test (Kelly and Tyson, 1965), the pull-out test (Hampe et al., 1994), the push-in test and the push-out test (Kerans and Parthasarathy, 1991). Each of these methods has some advantages and disadvantages which should be considered for a specific purpose under investigation. However, all above interface measuring techniques try to investigate the tangential properties of the interface. While for the cases subjected to a tensile load normal to the fiber orientation, like the preset study, the dominant debonding is due to normal opening of the interfaces. Martyniuk et al. (2013) used another method which approaches to a more direct measurement of the normal properties of fiber/matrix interfaces in uni-directional composites. In this method, a specimen including a single isolated fiber embedded in the matrix was subjected to tensile load inside the chamber of the Scanning Electron Microscope (SEM). The cross-section normal to the fiber orientation was monitored while the load was being applied. By this technique, more precise data with respect to the normal properties of interface such as the maximum normal stress of adhesion and the normal fracture energy of interface can be determined. However, their debonding angle measurements were limited by unstable debonding crack growth in the early stages of debonding such that the first arrested debond crack tip angle was captured at the angle $40^\circ - 60^\circ$, which corresponds to the mode mixity of $\psi(\theta) > 60^\circ$. It means that no interface measurement for the dominant mode-I fracture could be determined. Therefore, it is of high interest to develop this method such that it becomes possible to measure interfacial properties for smaller values of $\psi(\theta)$ (dominant mode-I fracture region). To this end, the present study has one fiber positioned in the neighbor of another fiber or a hole to study the effect of the interaction between the interfacial debonding at the fiber with respect to its neighboring fiber or hole. The idea is to clarify if this interaction can lead to stabilize the interfacial crack growth at the smaller mode mixity values.

2. Problem formulation

A numerical model is established to study the possibility of stabilizing interfacial debonding at a fiber by positioning another fiber or hole in its vicinity. A 2D cell is chosen such that two circular fibers (or one fiber and a hole) are embedded in a large zone of the matrix (see Fig. 2a). A Cartesian reference coordinate system, x_i, is placed at the bottom-left corner of the cell and aligned with the cell edges. The dimension of the cell is determined by the length, b, the width, a, and the radii of the fibers, $R^{\#1}$ and $R^{\#2}$. The cell is subjected to a uniform normal displacement, Δ_1, in the x_1-direction.

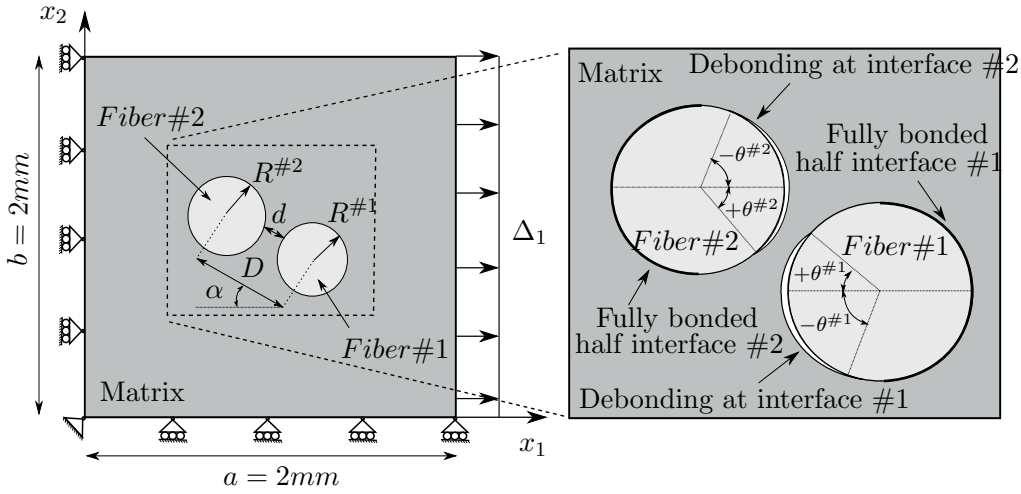

Figure 2: a) The 2D model including two circular fibers embedded in the matrix. The dimensions, loads and the coordinate system are shown. c) A deformed cell with partly debonded interfaces. The bold half circles around the fibers denote the fully bonded area of each fiber.

The boundary conditions are implemented incrementally as follows

$$\begin{aligned} &\dot{T}_2 = 0 \quad \text{and} \quad \dot{u}_1 = 0, \quad \text{on} \quad x_1 = 0 \\ &\dot{T}_1 = 0 \quad \text{and} \quad \dot{u}_2 = 0, \quad \text{on} \quad x_2 = 0 \\ &\dot{T}_2 = 0 \quad \text{and} \quad \dot{u}_1 = \dot{\Delta}_1, \quad \text{on} \quad x_1 = a \\ &\dot{T}_1 = 0, \quad \text{on} \quad x_2 = b \end{aligned} \tag{1}$$

and the corresponding macroscopic incremental strains are defined as

$$\begin{aligned} \dot{E}_{11} &= \frac{\dot{u}_1}{a}, \quad \text{at} \qquad x_1 = a \\ \dot{E}_{22} &= \frac{\dot{u}_2}{b}, \quad \text{at} \qquad x_2 = b \end{aligned} \tag{2}$$

where $\dot{u}_1$ and $\dot{u}_2$ are the incremental displacement components in x_1- and x_2-direction, respectively, while $\dot{\Delta}_1$ describes the prescribed incremental displacement quantity applied on the edge of the cell at $x_1 = a$, and T_i are surface tractions. The overall macroscopic stress increment, $\dot{\Sigma}_{ij}$, are computed as

$$\begin{aligned} \dot{\Sigma}_{11} &= \frac{1}{b}\int_0^b \dot{T}_1 dx_2, \qquad \text{at} \quad x_1 = 0 \\ \dot{\Sigma}_{22} &= \frac{1}{a}\int_0^a \dot{T}_2 dx_1, \qquad \text{at} \quad x_2 = 0 \end{aligned} \tag{3}$$

Considering $\Sigma_{33} = 0$, the cell is assumed to deform by uniaxial normal loading under plane stress condition. It means, the modeling simulates the specimen surface at which the debonding is monitored by the SEM. In Fig. 2b, the schematic drawing of the deformed cell with the debonded interfaces are shown after applying the tensile load. In each fiber the debonding angle, $\theta^{\#i}$, is measured where i denotes the fiber number. As shown in Fig. 2b, the debonding angle in each fiber is divided to two parts; The positive angle which denotes the crack starting from the zero-angle until the crack tip in the ligament and the negative angle which shows the crack initiating from the zero-angle to the crack tip away from the ligament. The position of fibers with respect to each other is specified by the position angle of the centers of the fibers, α, and the distance between the center of the two fibers, D. The thickness of the ligament is $d = D - R^{\#1} - R^{\#2}$.

In the present study it is assumed that only half of the interface of each fiber which is in the ligament can debond while the other half is fully bonded, see Fig. 2b. In Fig. 2b, the bold solid curves around the fibers denote the fully bonded half interfaces. This assumption allows us to focus on the cracks growing in the ligament where the interaction of fiber-fiber or fiber-hole is dominant. Although this study considers two isolated fiber (fiber and hole) embedded in the matrix but in the real structure of composites interfacial debonding also normally occurs in the ligaments of two of more close fibers. As it can be seen from Fig. 1, in a glass-epoxy composite cracks initiate and

propagate from the interfaces in the ligaments of two fibers and subsequently link up with other debonded interfaces in their vicinity.

2.1. Isotropic Plasticity Model

The matrix is assumed to be an elasto-plastic material governed by the standard J_2-plasticity theory, while the fibers are considered as purely elastic. Both the matrix as well as the fibers are modeled as isotropic materials. The hole is modeled to be an elastic material with very small Young's modulus and Poisson's ratio tending to zero. In the matrix, the stress increment is calculated from the total strain increment, $\dot{\epsilon}_{ij}$, which consists of an elastic part, $\dot{\epsilon}^e_{ij}$, and a plastic part, $\dot{\epsilon}^p_{ij}$

$$\begin{aligned} \dot{\epsilon}_{ij} &= \dot{\epsilon}^e_{ij} + \dot{\epsilon}^p_{ij} \\ \dot{\sigma}_{ij} &= L_{ijkl}\dot{\epsilon}_{kl} \end{aligned} \tag{4}$$

Here, L_{ijkl} is the fourth order incremental stiffness tensor defined as (Tvergaard and Hutchinson, 1992)

$$L_{ijkl} = \frac{E_m}{1+\nu_m}[\frac{1}{2}\left(\delta_{ik}\delta_{jl}+\delta_{il}\delta_{jk}\right) + \frac{\nu_m}{1-2\nu_m}\delta_{ij}\delta_{kl} - \beta\frac{3}{2}\frac{\frac{E_m}{E_t}-1}{\frac{E_m}{E_t}-\frac{(1-2\nu_m)}{3}}\frac{s_{ij}s_{kl}}{\sigma_e^2}] \tag{5}$$

while,

$$\beta = \begin{cases} 1 & \text{for } \sigma_e = \sigma_f \text{ and } \quad \dot{\sigma}_e \geq 0 \\ 0 & \text{for } \sigma_e < \sigma_f \text{ or } \quad \dot{\sigma}_e < 0 \end{cases} \tag{6}$$

where, E_m is the Young's modulus and ν_m is the Poisson's ratio of the matrix. The tangential modulus, E_t, is the slope of the uniaxial stress-strain curve at the stress level $\sigma_e = \sqrt{\frac{3}{2}s_{ij}s_{ij}}$ and δ_{ij} denotes the Kronecker delta. The stress deviator is defined by $s_{ij} = \sigma_{ij} - \delta_{ij}\frac{\sigma_{kk}}{3}$. In Eq. 6, $\dot{\sigma}_e = \frac{3s_{kl}\dot{\sigma}_{kl}}{2\sigma_e}$ and σ_f is the instantaneous flow stress. During plastic yielding β is unity and the magnitude of L_{ijkl} depends on the stress state and the deformation hardening law whereas in the elastic regime (including elastic unloading) it is governed by Hooke's law where β is zero. The yield condition, f, is taken as the von Mises yield surface

$$f = \sigma_e - \sigma_f(\epsilon^p_e) = 0 \tag{7}$$

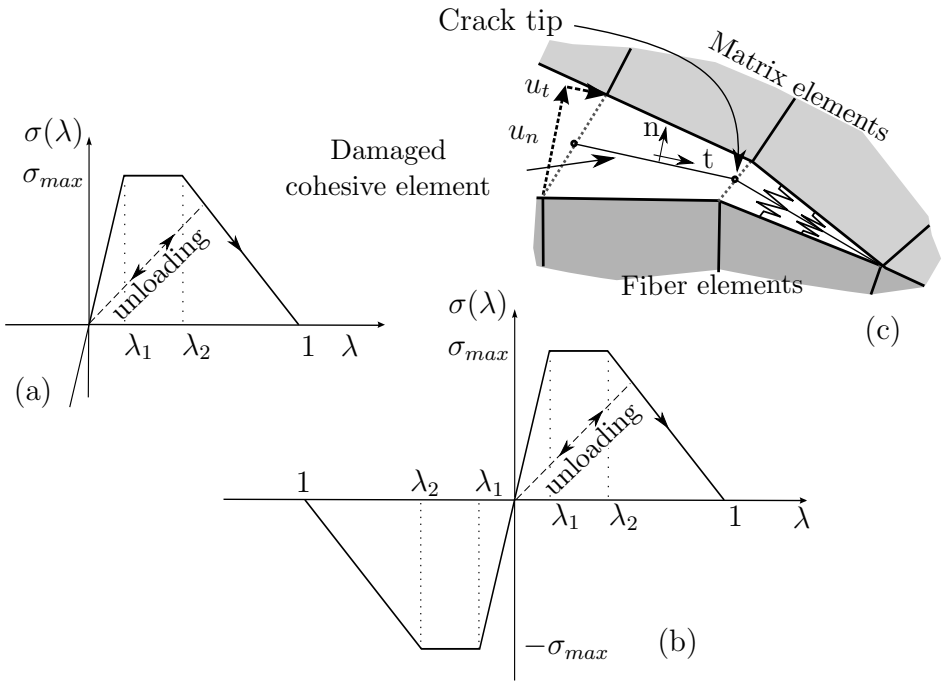

Figure 3: Traction-separation law used to characterize interface separation.

Here, $\sigma_f = \sigma_f(\epsilon_e^p)$, where and ϵ_e^p is the equivalent plastic strain, work conjugate to σ_e, and it is defined incrementally by the relation $\dot{\epsilon}_e^p = \sqrt{\frac{2}{3}\dot{\epsilon}_{ij}^p \dot{\epsilon}_{ij}^p}$. The hardening behavior determined by the uniaxial stress-strain relation which is represented by the power hardening law

$$\epsilon = \begin{cases} \dfrac{\sigma}{E_m} & \text{for } \sigma \leq \sigma_y \\ \dfrac{\sigma_y}{E_m}\left(\dfrac{\sigma}{\sigma_y}\right)^n & \text{for } \sigma > \sigma_y \end{cases} \tag{8}$$

where n is the strain-hardening exponent and σ_y denotes the initial yield stress.

2.2. Cohesive Zone Model

The fiber/matrix interfacial debonding is a mixed mode failure mechanism which involves both normal as well as tangential opening. The present

numerical study uses the trapezoidal cohesive zone model proposed by Tvergaard and Hutchinson (1993) to model this failure phenomena. The cohesive zone model is based on a relation between the separation of two faces of the debonding interface and the tractions which resist against opening. This traction-separation law is regarded as a phenomenological characterization of the separation zone along the interfaces and not the description of atomic separation. The failure criterion at the interface is based on a non-dimensional parameter, λ, which is defined as

$$\lambda = \sqrt{\left(\frac{u_n}{\delta_n^c}\right)^2 + \left(\frac{u_t}{\delta_t^c}\right)^2} \tag{9}$$

such that onset of degradation in traction in the cohesive zone starts at a specified value, $\lambda = \lambda_2$, and fully damage occurs when $\lambda = 1$, see Fig. 3. Here, δ_n^c and δ_t^c are the normal and tangential characteristic cohesive lengths, respectively, and u_n and u_t are the normal and tangential separation of the interface, respectively. A traction potential can be defined as

$$\Phi(u_n, u_t) = \delta_n^c \int_0^\lambda \sigma(\acute{\lambda}) d\acute{\lambda} \tag{10}$$

where $\sigma(\lambda)$ is defined from the trapezoidal shape of the Fig. 3 as

$$\sigma(\lambda) = \begin{cases} \dfrac{\sigma_{max}}{\lambda_1}\lambda & \text{for } 0 \leq \lambda < \lambda_1 \\ \sigma_{max} & \text{for } \lambda_1 \leq \lambda \leq \lambda_2 \\ \dfrac{\sigma_{max}}{1-\lambda_2}(1-\lambda) & \text{for } \lambda_2 < \lambda \leq 1 \end{cases} \tag{11}$$

As long as λ is monotonically increasing the normal, T_n, and tangential, T_t, tractions acting on the interfaces can be derived from the potential function as

$$T_n = \frac{\partial \Phi}{\partial u_n} = \frac{\sigma(\lambda)}{\lambda}\frac{u_n}{\delta_n^c}, \quad T_t = \frac{\partial \Phi}{\partial u_t} = \gamma\frac{\sigma(\lambda)}{\lambda}\frac{u_t}{\delta_t^c} \tag{12}$$

where the factor $\gamma = \dfrac{\delta_n^c}{\delta_t^c}$ denotes different failure mechanism in mode-II than mode-I such that choosing γ to be smaller than one leads to more ductile

failure in mode-II. However, due to the indentical fracture energy for both modes the maximum traction in pure tangential debonding is smaller than the one under pure normal debonding by the magnitude of γ. By assuming $F(\lambda) = \dfrac{\sigma(\lambda)}{\lambda}$, similar to Tvergaard (1990), the incremental expressions of the cohesive tractions are obtained from Eq. 12 as

$$\dot{T}_n = \frac{\dot{u}_n}{\delta_n^c} F(\lambda) + \frac{u_n}{\delta_n^c} \frac{\partial F}{\partial \lambda} \dot{\lambda}, \quad \dot{T}_t = \gamma \frac{\dot{u}_t}{\delta_t^c} F(\lambda) + \gamma \frac{u_t}{\delta_t^c} \frac{\partial F}{\partial \lambda} \dot{\lambda} \tag{13}$$

where

$$\dot{\lambda} = \frac{1}{\lambda} \left(\frac{u_n}{\delta_n^c} \frac{\dot{u}_n}{\delta_n^c} + \frac{u_t}{\delta_t^c} \frac{\dot{u}_t}{\delta_t^c} \right) \tag{14}$$

As shown in Fig. 3a and b, for decreasing λ a type of elastic unloading is used to represent the partly damaged interface

$$\begin{aligned} T_n &= \frac{u_n}{\delta_n^c} F(\lambda_{max}) \\ & \qquad\qquad \text{for } \lambda < \lambda_{max} \text{ or } \dot{\lambda} < 0 \\ T_t &= \gamma \frac{u_t}{\delta_t^c} F(\lambda_{max}) \end{aligned} \tag{15}$$

where λ_{max} denotes the maximum reached value of λ. Using Eq. 15 dictates that after $\lambda = \lambda_1$ the element is partly damaged, therefore its behavior should be weaker than the undamaged element after unloading and subsequent reloading. Contact under normal compression, is presented by elastic springs with a high stiffness. Then, instead of Eq. 12

$$\begin{aligned} T_n &= \frac{u_n}{\delta_n^c} \frac{\sigma_{max}}{\lambda_1} \\ & \qquad\qquad \text{for } u_n < 0 \\ \lambda &= |\frac{u_t}{\delta_t^c}| \end{aligned} \tag{16}$$

As mentioned, the model assumes the same work of separation for all mode mixities. Experimental studies have shown that the mixed mode fracture energy usually increases significantly with increasing mode mixity (Liechti and Chai, 1992). However, the assumption made in the present study (fracture energy independent of mode mixity) means that in reality, the amount of

unstable fiber/matrix debonding will be less than predicted from the present study. So our results will be conservative in the sense that the configuration that gives the most stable crack growth in the model, is expected to be even more stable in the experiments. In pure normal separation ($u_t = 0$) the maximum traction is $T_n = \sigma(\lambda)$ where $\lambda = \dfrac{u_n}{\delta_n^c}$, while under pure tangential separation ($u_n = 0$) the maximum traction is $T_t = \dfrac{\delta_n^c}{\delta_t^c}\sigma(\lambda)$ where $\lambda = \dfrac{u_t}{\delta_t^c}$. Thus, five interface parameters need to be specified, i.e. δ_n^c, δ_t^c, λ_1, λ_2 and σ_{max}. In addition, a plateau in the maximum traction level in the trapezoidal cohesive zone model simultaneously allows more Gauss points of cohesive elements to be at the maximum stress. This may lead to more stable numerical solutions in comparison with bilinear and exponential models Chandra et al. (2002). However, Tvergaard and Hutchinson (1993) discussed that under small scale yielding and small scale fracture process zone the shape of the separation law has a secondary importance and the most critical parameters are the maximum cohesive stress and the characteristic cohesive length.

Assuming LEFM the mode mixity in bimaterials can be defined using a stress intensity factor-based approach as (Rice, 1988; Hutchinson and Suo, 1992)

$$\psi = \tan^{-1}\left(\frac{Im(Kl^{i\varepsilon})}{Re(Kl^{i\varepsilon})}\right) \tag{17}$$

where $K = K_I + iK_{II}$ is the complex combination of mode-I, K_I, and mode-II, K_{II}. The bimaterial mismatch is denoted by ε and l is a reference length scale. Alternatively, the mode mixity can be defined by crack tip opening displacements in terms of tangential and normal displacement components (Liu et al., 1995; Agrawal and Karlsson, 2006; Sørensen and Kirkegaard, 2006).

$$\varphi = \tan^{-1}\left(\frac{u_t}{u_n}\right) \tag{18}$$

whereas the displacement components, u_t and u_n, are obtained at the crack tip. The location of the crack tip is defined as the position of the last damaged cohesive Gauss point, see Fig. 3c. The definition of the mode-mixity shown in Eq. 18 is used in the current study, due to easy implementation in a finite element code.

2.3. Numerical Methods

For the numerical implementation the incremental form of the principle of virtual work is adopted. Disregarding body forces, the principle reads

$$\int_V \dot{\sigma}_{ij}\delta\dot{\epsilon}_{ij}dV + \int_{S_I}(\dot{T}_n\delta\dot{u}_n + \dot{T}_t\delta\dot{u}_t)dS = \int_S \dot{T}_i\delta\dot{u}_i dS \tag{19}$$

where V denotes the volume of the unit cell having the surface S and S_I is the surface of the fiber-matrix interfaces. An example of a finite element mesh is shown in Fig. 4. The mesh consists of almost 27,500 nodes and 9,200 elements including 256 cohesive elements. Eight-node quadrilateral elements with nine Gauss points are used for the bulk materials while six-node quadrilateral elements with three Gauss points are considered for the cohesive zones. As shown in Fig. 4, the mesh is highly refined near the interfaces. Tvergaard and Legarth (2007) characterized the length of the fracture process region, ℓ, in the cohesive zone during crack growth by the thickness from the crack-tip, where $\lambda = 1$, to the point ahead of the crack-tip where $\lambda = \lambda_1$. They found a good resolution and very little mesh dependence when the value of ℓ is several times the length, Δ_0, of a square element in the uniform mesh region (here, around the interfaces in Fig. 4). This requirement is satisfied in the present computations as $\ell \geq 4\Delta_0$ corresponding to at least 4 elements each having 3 Gauss points resolves the fracture process zone.

3. Results and Discussion

The results are presented by the interfacial debonding angle, θ, and the value of mode-mixity, φ, in the crack tip for the specified tensile loading displacement. The fibers are assumed to be purely elastic with Young's modulus, $E_f = 72GPa$, and Poisson's ratio, $\nu_f = 0.21$. While the matrix behaves as elasto-plastic material with Young's modulus, $E_m = 3GPa$, Poisson's ratio, $\nu_m = 0.3$, and the initial yield stress, $\sigma_y^0 = 0.005E_m$. The cohesive zone parameters are chosen according to the experimental measurements of glass/epoxy (Epoxydharz HT 2) reported by Martyniuk et al. (2013). Table 1 shows the value of the parameters used in the current study. In order to study the effect of interaction of one fiber with its neighboring fiber (hole) on the fiber/matrix debonding, two cases are considered: A two-fiber composite model and a model consisting of a fiber and a hole both embedded in a large matrix zone, see Fig. 2.

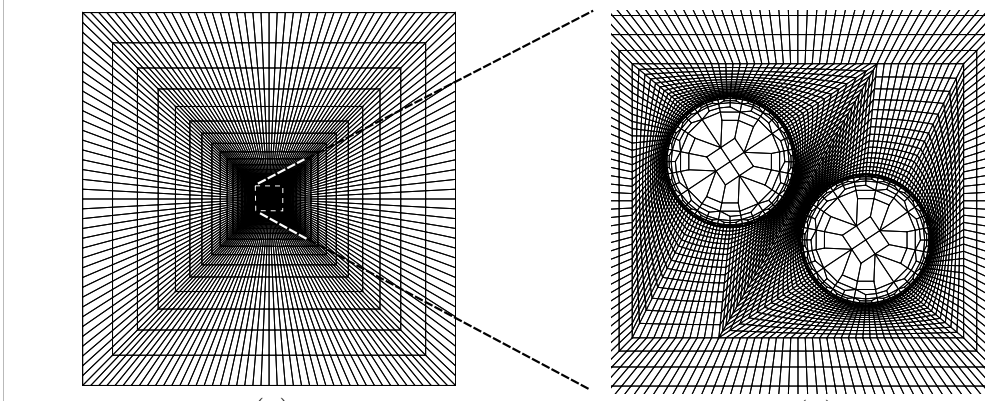

Figure 4: An example of mesh used for the computations. The fibers are placed in the matrix with the thickness of $d = 10\mu m$ and the relative position angle, $\alpha = 30^\circ$ from each other. The fibers radii are $R^{\#1} = R^{\#2} = 25\mu m$.

Fiber		Matrix			Interface				
E_f $[GPa]$	ν_f	E_m $[GPa]$	ν_m	σ_y $[MPa]$	Φ $[\frac{J}{m^2}]$	σ_{max} $[MPa]$	$\delta_n^c = \frac{1}{5}\delta_t^c$ $[\mu m]$	λ_1	λ_2
72	0.21	3	0.3	15	1	6	0.16	0.01	0.1

Table 1: Constants for the constitutive models of the fibers, the epoxy matrix and the interfaces.

3.1. Case1: Two-fiber composite model

In the two-fiber composite model, two fibers embedded in an epoxy matrix are considered which include cohesive zones at fiber/matrix interfaces. In this model, interface #1 (see Fig. 2b) is chosen to be slightly stronger than the other interface such that it has $\sigma_{max}^{\#1} = 7MPa$ and $\delta_n^{c\#1} = \frac{1}{5}\delta_t^{c\#1} = 0.17\mu m$ which leads to the cohesive fracture energy, $\Phi^{\#1} = 1.15J/m^2$. The cohesive parameters at interface #2 are the same as Table. 1. The uneven interfacial properties are more realistic as the real fiber-reinforced composites generally have imperfect interfacial strengths. Fig. 5 illustrates the effect of the positioning parameters; The ligament thickness, d, and the position angle, α, on the fiber/matrix debonding behavior of two-fiber composite model. All the results are compared with the single fiber case. The interfacial debonding angle, θ, is shown as a function of the normalized remote stress,

Σ_{11}/σ_{max}. París et al. (2003, 2007) reported that in a single-fiber model the mode-II is dominant at debonding angle of $60^\circ - 70^\circ$ which leads to a stable crack growth or crack kinking into the matrix. Since this study is focusing on the initial debonding angles where the mode-I is dominant and does not consider the crack kinking into the matrix, the axis of the interfacial debonding angle is plotted in the interval $[-70^\circ, 70^\circ]$. At each interfacial debonding angle, the slope of the curves reflects the crack growth rate such that a steeper slope means a faster crack growth while a lower slope denotes more stable crack propagation. Results for four different ligament thicknesses: $d = 0.08R$, $d = 0.1R$, $d = 0.4R$ and $d = 0.8R$ are shown in Fig. 5a, b, c and d, respectively. As shown in Fig. 2b, the positive θ is for the crack growing at the interface in the ligament between the two fibers while negative θ denotes the crack propagating in the other direction. Fig. 5 shows that the cracks which are growing away from the ligament (shown with negative θ) are not affected by the neighboring fiber and have almost the same behavior in all positions. Thus, the focus of the discussion in this section is on the behavior of the cracks which are initiating and propagating in the ligament (shown with positive θ). In the ligament between two fibers, the interfacial debonding is influenced by both the ligament thickness parameter, d, and the fiber position angle, α. Fig. 5 shows that for a specific d value, decrease of α stabilizes the crack growth indicated by a lower slope of the curve. When the value of d is very small (in Fig. 5a and b) the effect of α is more pronounced. In Fig. 5a and b, the cracks with both signs of debonding at the interfaces initiate at almost the same remote stress and with the same initial crack growth rate. However, the subsequent positive debonding angles follow a plateau on the curves. A schematic drawing is given in Fig. 6 to explain this mechanism more clearly. Fig. 6c represents a typical curve shown in Fig. 5a and b. Two points are marked on this curve, A and B, whose corresponding deformed geometries are schematically shown in Fig. 6a and b, respectively. At point A, the cracks are propagating along the interface with a large crack growth rate and barely interact with each other. The crack growth rate then decreases when two crack tips are approaching each other. The crack tips meet each other almost at the position where the center of two fibers are aligned with each other (the gray dashed line in Fig. 6b). In the other words, the crack tips reaches each other when their debonding angles tend to $\theta = \alpha$. At this debonding angle, as shown in Fig. 6b, the front of each crack tip is under unloading (and crack faces may even get into contact) by the other opened interface. Consequently, further debonding at each crack

tip is more due to tangential debonding rather than normal opening. This phenomena can be seen specially in Fig. 5a where the curves follow a plateau at $\theta \geq \alpha$. By increase of d value this effect reduces and the interfaces behave more symmetrically for all debonding angles. For the cases with $\alpha = 15^\circ$, at $\Sigma_{11}/\sigma_{max} = 3$ where the remote stress reaches the matrix yield stress, σ_y, a slightly increase of the crack growth rate occurs which is due to the plastic deformation around the crack tips in the small ligament zone which will be discussed in detail later.

The amount of mode-mixity in the crack tip at each debonding angle is given in Fig. 7. Similar to Fig. 5, the interfacial debonding in the negative debonding angles are almost independent of the positioning parameters. The steeper slope in each debonding angle indicates that the rate of the mode mixity is larger. Larger rate of the mode mixity denotes that the portion of mode-II fracture increases over mode-I fracture. In agreement with the discussion of Fig. 5, Fig. 7a and b shows that for small d values, the rate of changes in mode-mixity significantly rises when θ reaches the value of the position angle, α. However, an increase of the ligament thickness makes this effect smaller. As shown in Fig. 7d, at large d values the behavior of the interfacial debonding is almost symmetrical for both positive and negative debonding angles.

Fig. 8 represents the mixed mode angle, φ, as a function of the normalized remote stress. This figure shows that in the crack initiation stage the mode mixity significantly increases. This sudden increase stops at a certain value of mode mixity and the subsequent loading leads to a more flat curve which denotes a more stable crack growth. Comparing different α values shows that $\alpha = 15^\circ$ gives the best behavior in terms of more dominant mode-I fracture specially for small values of d. All other cases behave similar to the single fiber case. Fig. 8a shows that for $\alpha = 15^\circ$ the sudden increase of the mode mixity stops around $\theta \simeq 15^\circ$. This indicates that for $\alpha = 15^\circ$ the first arrested crack can be captured at earlier loading steps. Consequently, the results of this figure in addition to Fig. 5 and Fig. 7 suggest that for the two-fiber configuration with very small ligament thickness, a position angle of $\alpha \leq 15^\circ$ lead to a more stable interfacial debonding situation interfacial debonding situation.

Fig. 9 shows the contour plots of the equivalent plastic strain, ϵ_e^p, of the two-fiber models with different ligament thickness with the same position angle, $\alpha = 15^\circ$. Fig. 9 depicts that smaller d values lead to larger plastic deformation in front of the crack tips in the matrix. As also discussed in

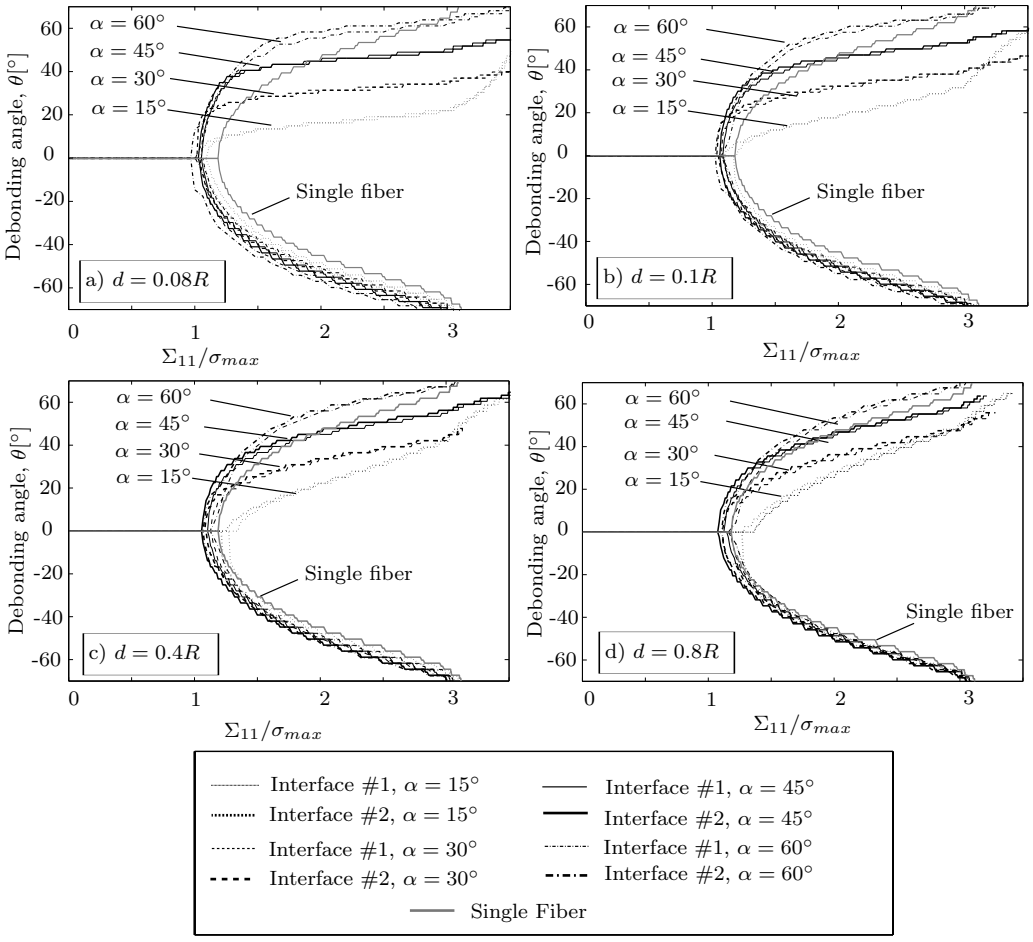

Figure 5: The effect of the positioning parameters. The ligament thickness, d, and the position angle, α, on the fiber/matrix debonding behavior of two-fiber composite model. The results are shown by the interfacial debonding angle, θ, versus the normalized remote stress. The single fiber is shown as a reference case. The single fiber is shown as a reference case. The results are shown for four different ligament thicknesses: a) $d = 0.08R$, b) $d = 0.1R$, c) $d = 0.4R$ and d) $d = 0.8R$.

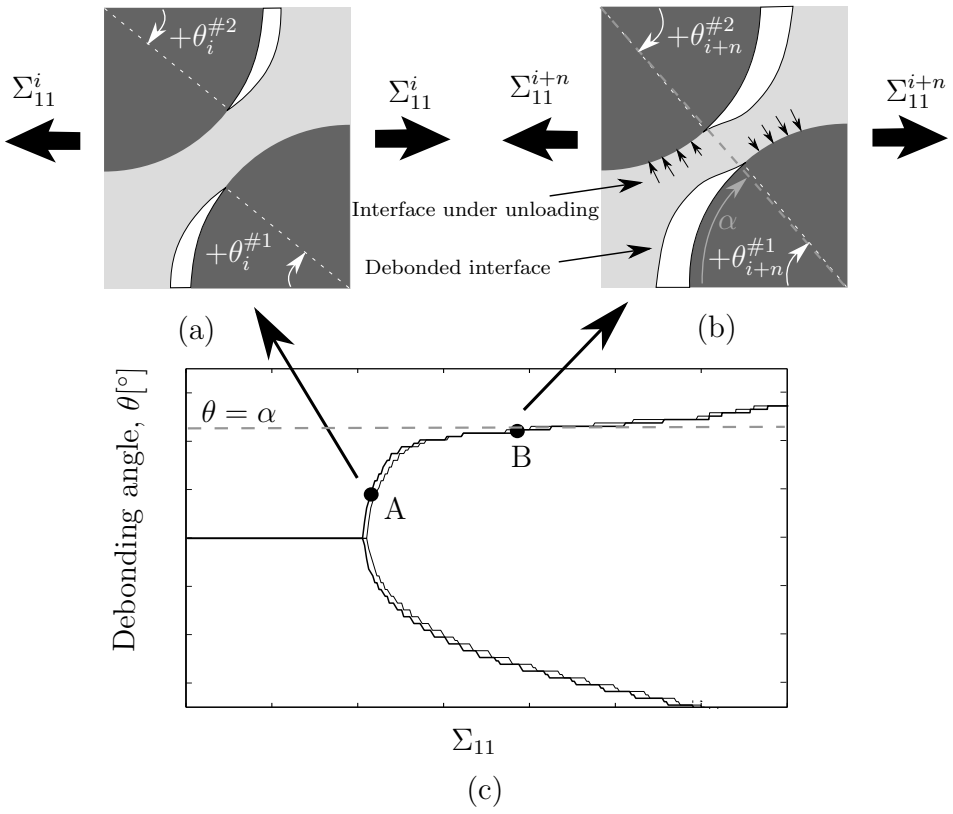

Figure 6: Schematic drawing of the sequence of interfacial debonding in the ligament of two fibers under transverse tension where i and $i+n$ stand for two different number of increments, corresponding to point A and B.

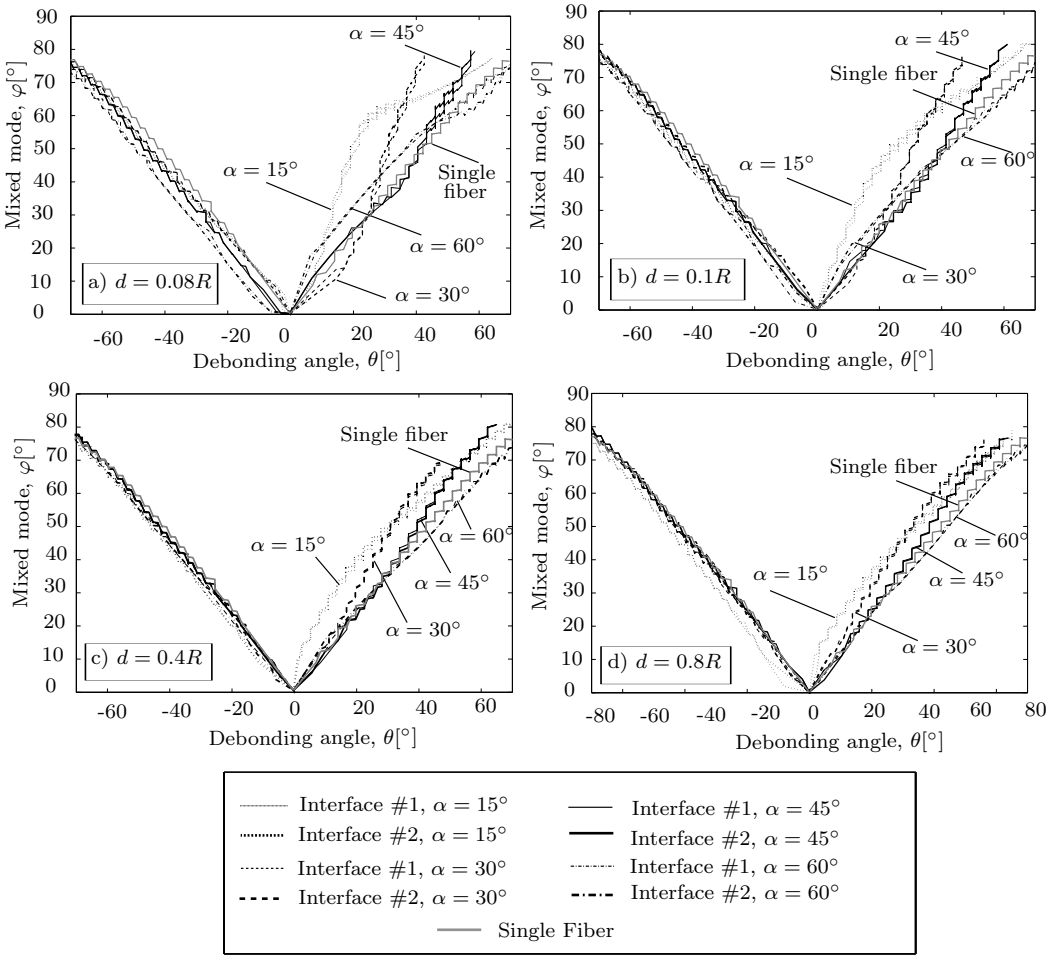

Figure 7: The effect of the positioning parameters. The ligament thickness, d, and the position angle, α, on the fiber/matrix debonding behavior of two-fiber composite model. The results are shown by the interfacial debonding angle, θ, versus the mixed mode angle, φ. The single fiber is shown as a reference case. The results are shown for four different ligament thicknesses: a) $d = 0.08R$, b) $d = 0.1R$, c) $d = 0.4R$ and d) $d = 0.8R$.

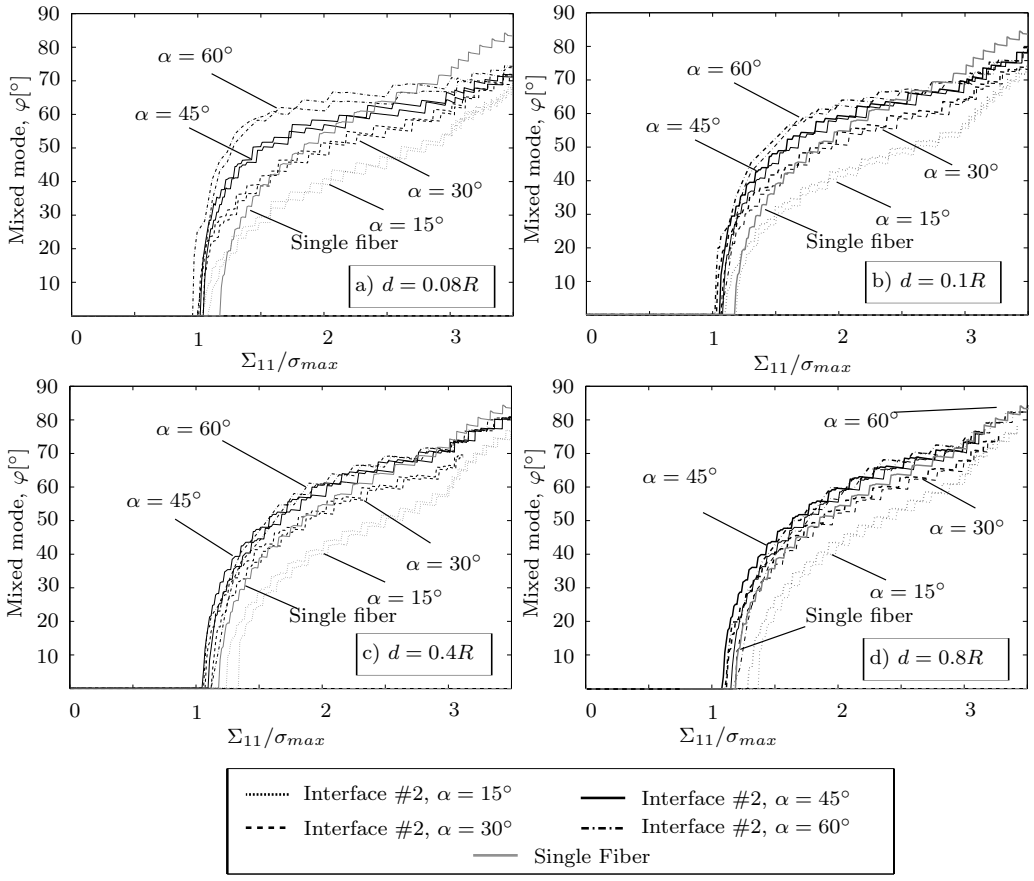

Figure 8: The effect of ligament thickness, d, and the position angle, α, on the fiber/matrix debonding behavior of two-fiber composite model. The results are shown by the mixed mode angle, φ, versus the normalized remote stress. The single fiber is shown as a reference case. The results are shown for four different ligament thicknesses: a) $d = 0.08R$, b) $d = 0.1R$, c) $d = 0.4R$ and d) $d = 0.8R$.

Fig. 6, Fig. 9a and b shows that for small d values the interfacial crack opening in the ligament grows very slowly when the crack tips meet each other. Similar to Fig. 6b, Fig. 9 shows that the crack tips unload due to the other opened interface. Further loading leads to severe plastic deformations in the ligament instead of further interfacial crack growth.

3.2. Case2: Fiber-hole composite model

In the second case, fiber #1 is substituted with a hole by assuming almost zero Young's modulus and Poisson's ratio. In this section, the same types of plots as in the previous case are discussed. Fig. 10 shows the effect of the position angle, α, and the ligament thickness, d, on the fiber/matrix debonding. The results are given by plots of the normalized remote stress, Σ_{11}/σ_{max}, versus the interfacial debonding angle, θ. The figure includes four different ligament thickness: $d = 0.08R$, $d = 0.1R$, $d = 0.4R$ and $d = 0.8R$ as shown in Fig. 10a, b, c and d, respectively. Fig. 10 shows that the interfacial debonding in the ligament is affected by change of the position angle in all ligament thicknesses. The effect of the positioning parameters on the interfacial debonding at the crack with negative value of θ is milder. For the cracks growing in the ligament, smaller α leads to reduced slope which indicates a smaller crack propagation. This stabilized crack growth occurs even from the initiation which can be utilized in the experimental investigations. Regardless of d values, smaller α postpones the crack initiation when $\alpha < 45^\circ$. Specially at $\alpha = 15^\circ$, smaller d value significantly postpones the crack initiation and also reduce the crack growth rate in the ligament. Furthermore, at $\alpha = 15^\circ$ decrease of the ligament thickness leads to postpone the crack initiation in the ligament in comparison with the other crack end with negative θ. This effect is due to the presence of the hole, which is easily deformed, enabling unloading of the interface in a narrow ligament thickness.

Fig. 11 shows the value of the mode mixity at the crack tip as a function of the interfacial debonding angle. The slopes of the curves are almost constant. Fig. 11 shows that in the positive θ axis the slope of the curves increases by decrease of the position angle, α. The sharper slope indicates that in each debonding angle the rate of change in the mode mixity is larger which denotes that the portion of mode-II fracture increases. Fig. 11 depicts that for $\alpha = 15^\circ$ for a certain debonding angle smaller d value leads to larger mode mixity. This can be seen in Fig. 11a where $d = 0.08R$ the value of the mode mixity at $\theta = 10^\circ$ is $\varphi \simeq 50^\circ$ while at $d = 0.1R$ shown in Fig. 11b the mode mixity at $\theta = 10^\circ$ is $\varphi \simeq 30^\circ$. This phenomena explains the stable

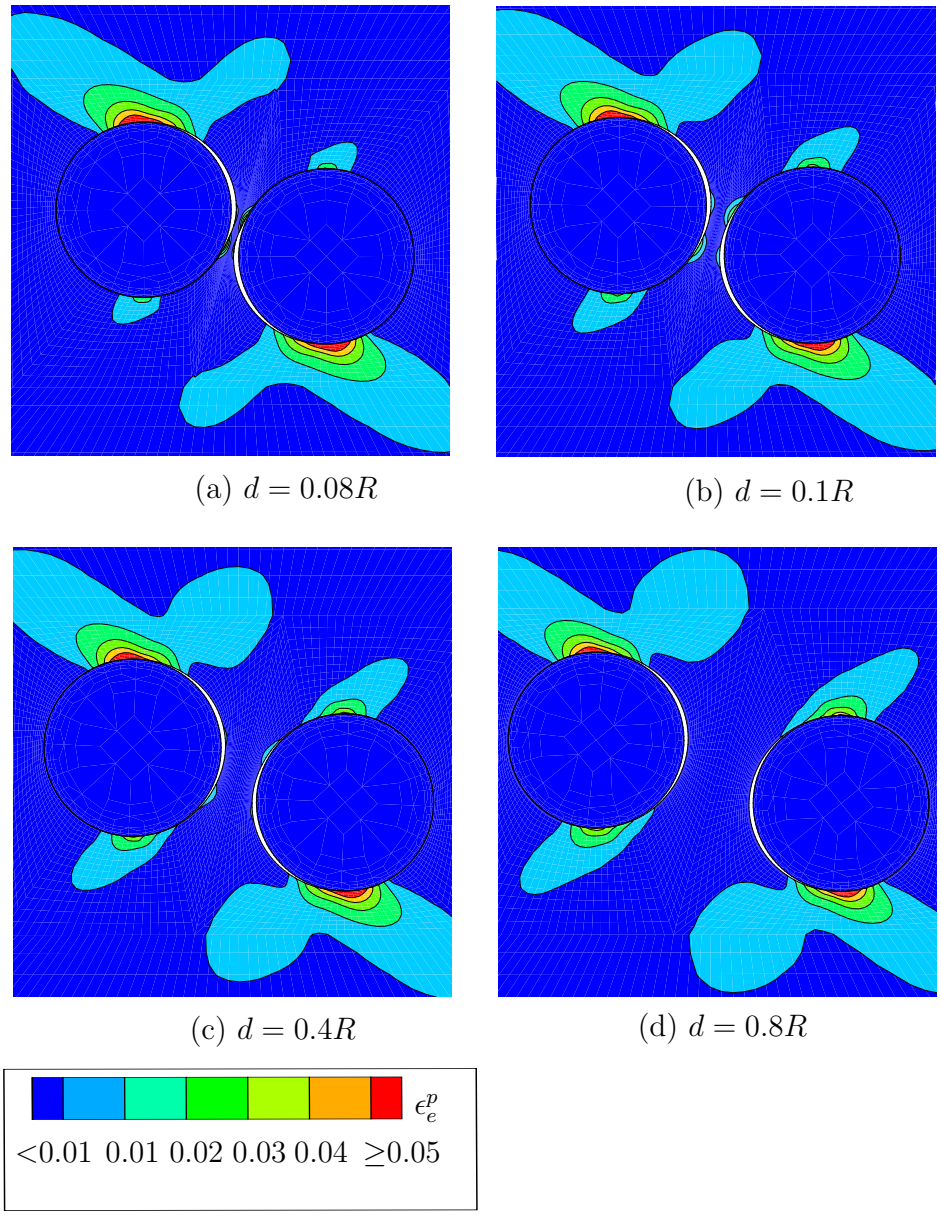

Figure 9: Contours of the accumulated equivalent plastic strain, ϵ_e^p, of two-fiber composite model. The results are shown at $\epsilon_{11} = 1\%$ ($\Sigma_{11}/\sigma_{max} = 3.2$) for the position angle, $\alpha = 15^\circ$ and four different ligament thicknesses: a) $d = 0.08R$, b) $d = 0.1R$, c) $d = 0.4R$ and d) $d = 0.8R$.

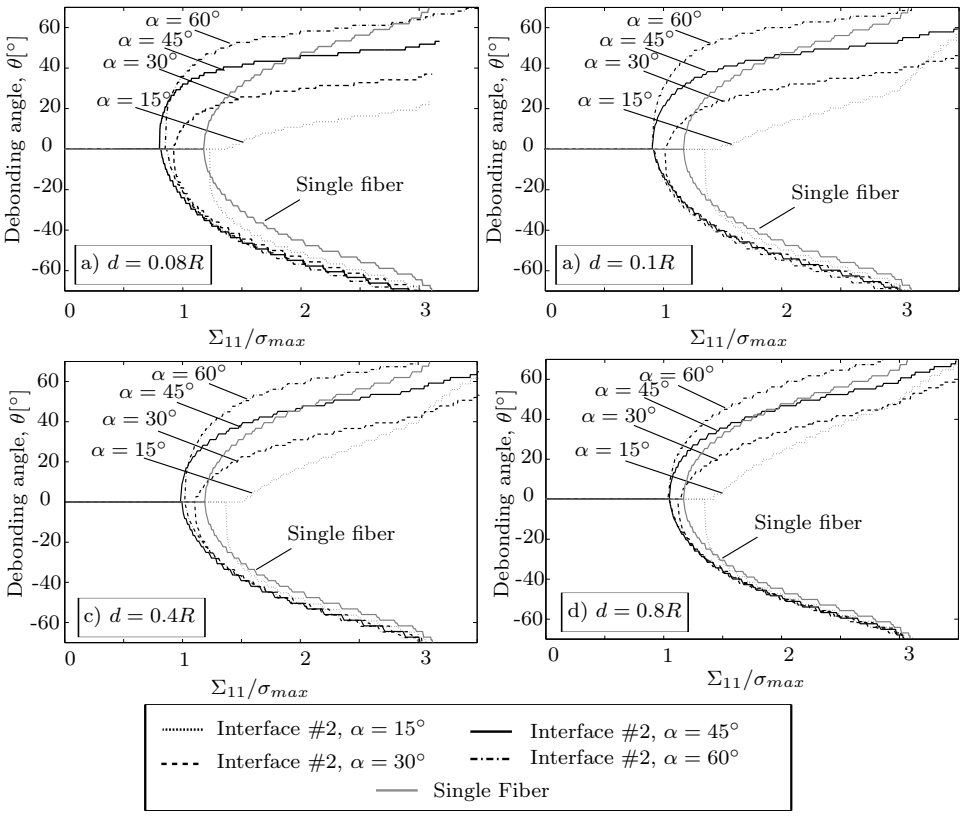

Figure 10: The effect of ligament thickness, d, and the position angle, α, on the fiber/matrix debonding behavior of fiber-hole composite model. The results are shown by the interfacial debonding angle, θ, versus the normalized remote stress. The single fiber is shown as a reference case. The results are shown for four different ligament thicknesses: a) $d = 0.08R$, b) $d = 0.1R$, c) $d = 0.4R$ and d) $d = 0.8R$.

crack growth rate at smaller d values in Fig. 10. Furthermore, comparing the results of Fig. 11a and Fig. 7a shows that in the two-fiber model the effect of the positioning parameters can lead to a stable crack growth in larger dominant mode-I failure whereas in the fiber-hole configuration the stable crack initiates under a mixed mode failure.

Fig. 12 represents the mixed mode angle, φ, as a function of the normalized remote stress. This figure shows that smaller d postpones debonding while decrease of α stabilize crack propagation. However, the crack initiation occurs in a larger mode mixity angle when α is small. Comparing Fig. 12 with Fig. 8 shows that in both cases a decrease of α stabilize the crack propagation while in the two-fiber configuration the crack initiates in a more dominant mode-I.

4. Summary and conclusions

The effect of fiber positioning on the interfacial debonding in composites was studied numerically. Two different configurations were analysed. The first model included two fibers embedded in a large zone of the matrix while the other case had one fiber close to a hole. The position of the fibers and hole were specified by two position parameters, namely: The ligament thickness and the position angle. The matrix was assumed to behave elasto-plastically while the fibers were purely elastic and much stiffer than the matrix. The debonding at the fiber/matrix interfaces was modeled using the trapezoidal cohesive zone.

In both configurations, decrease of the position angle stabilized the crack growth at the interface in the ligaments. This effect was more significant in the cases with small ligament thickness. It was found that the stabilization of crack growth has a direct relationship with increase of mode mixity which leads to contribute more mode-II fracture at the interface. In the two-fiber model and at very small ligaments the results showed that the interfacial crack propagates very slowly when the crack tips meet each other in the ligament and further crack growth is under dominant mode-II fracture. This was found to be due to unloading by the opened crack at the other interface. It was shown that further loading primarily develops the plastic zone in front of the crack tips in the ligament.

As a conclusion, for further experimental investigations the numerical results of this paper shows that similar experimental set-up as the two considered configurations will lead to ease the characterization of interfacial prop-

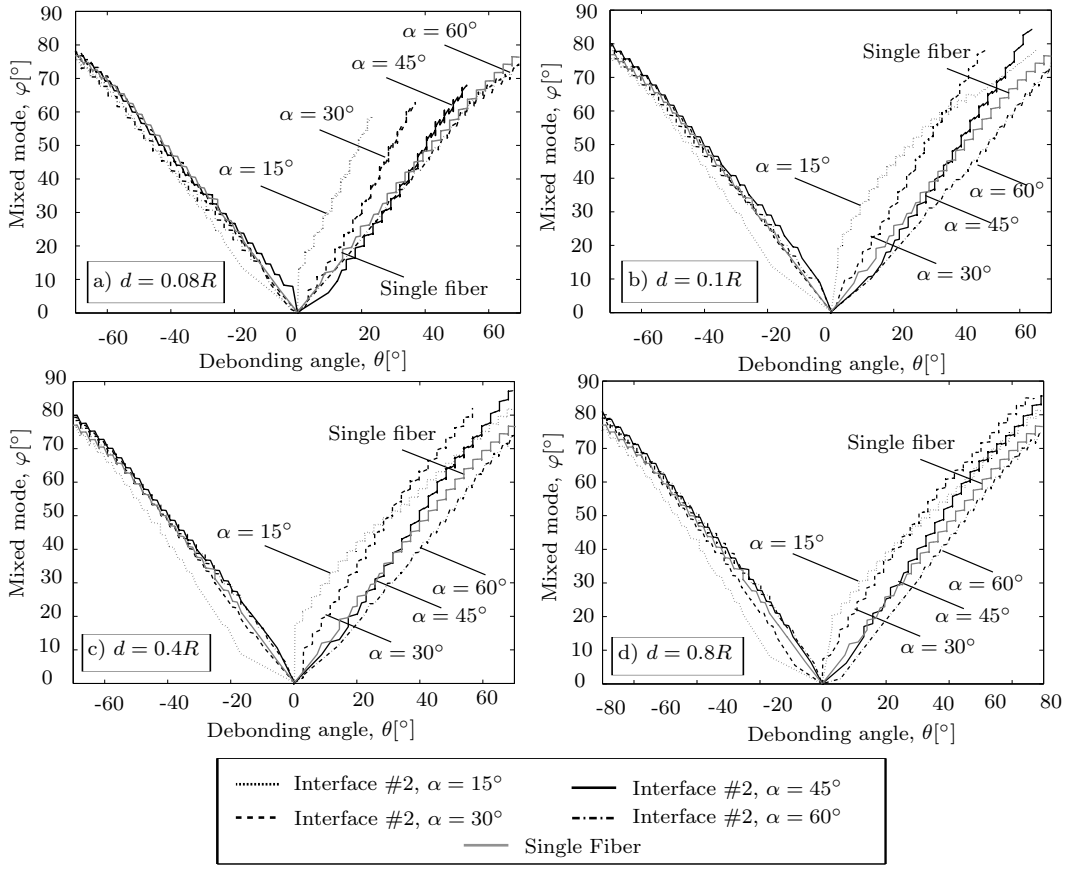

Figure 11: The effect of ligament thickness, d, and the position angle, α, on the fiber/matrix debonding behavior of fiber-hole composite model. The results are shown by the interfacial debonding angle, θ, versus the mixed mode angle, φ. The single fiber is shown as a reference case. The results are shown for four different ligament thicknesses: a) $d = 0.08R$, b) $d = 0.1R$, c) $d = 0.4R$ and d) $d = 0.8R$.

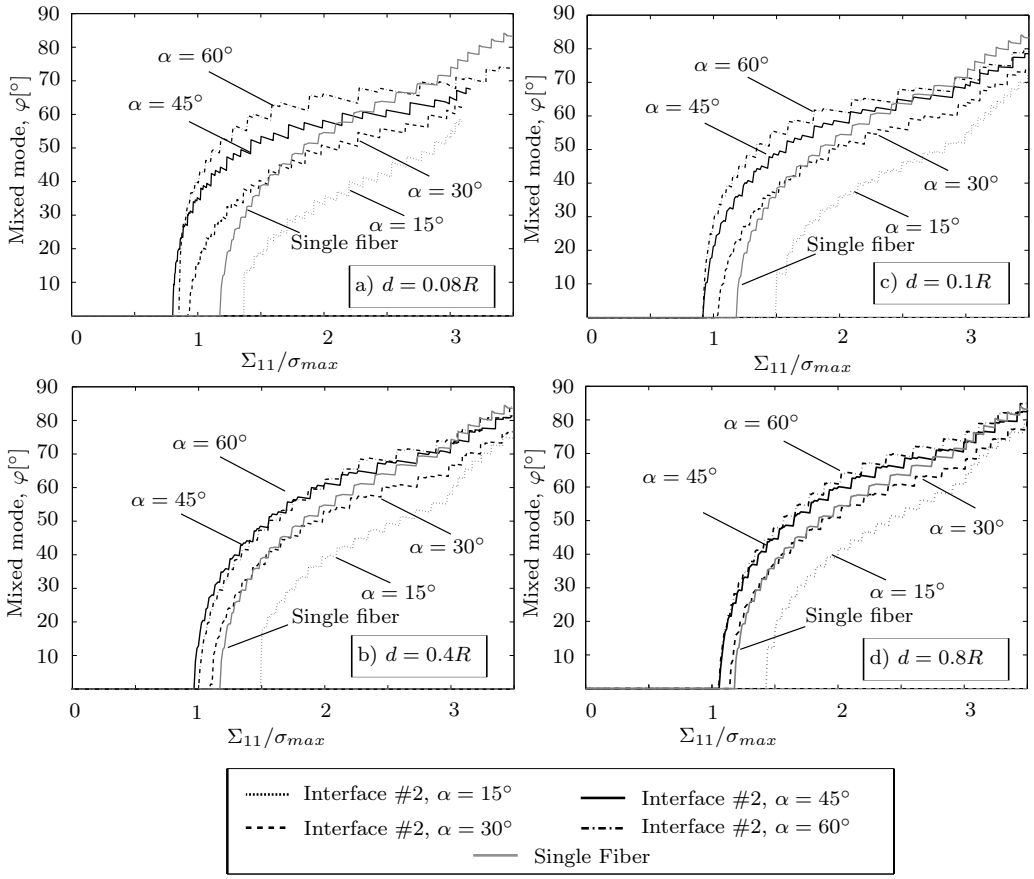

Figure 12: The effect of ligament thickness, d, and the position angle, α, on the fiber/matrix debonding behavior of fiber-hole composite model. The results are shown by the mixed mode angle, φ, versus the normalized remote stress plots, φ. The single fiber is shown as a reference case. The results are shown for four different ligament thicknesses: a) $d = 0.08R$, b) $d = 0.1R$, c) $d = 0.4R$ and d) $d = 0.8R$.

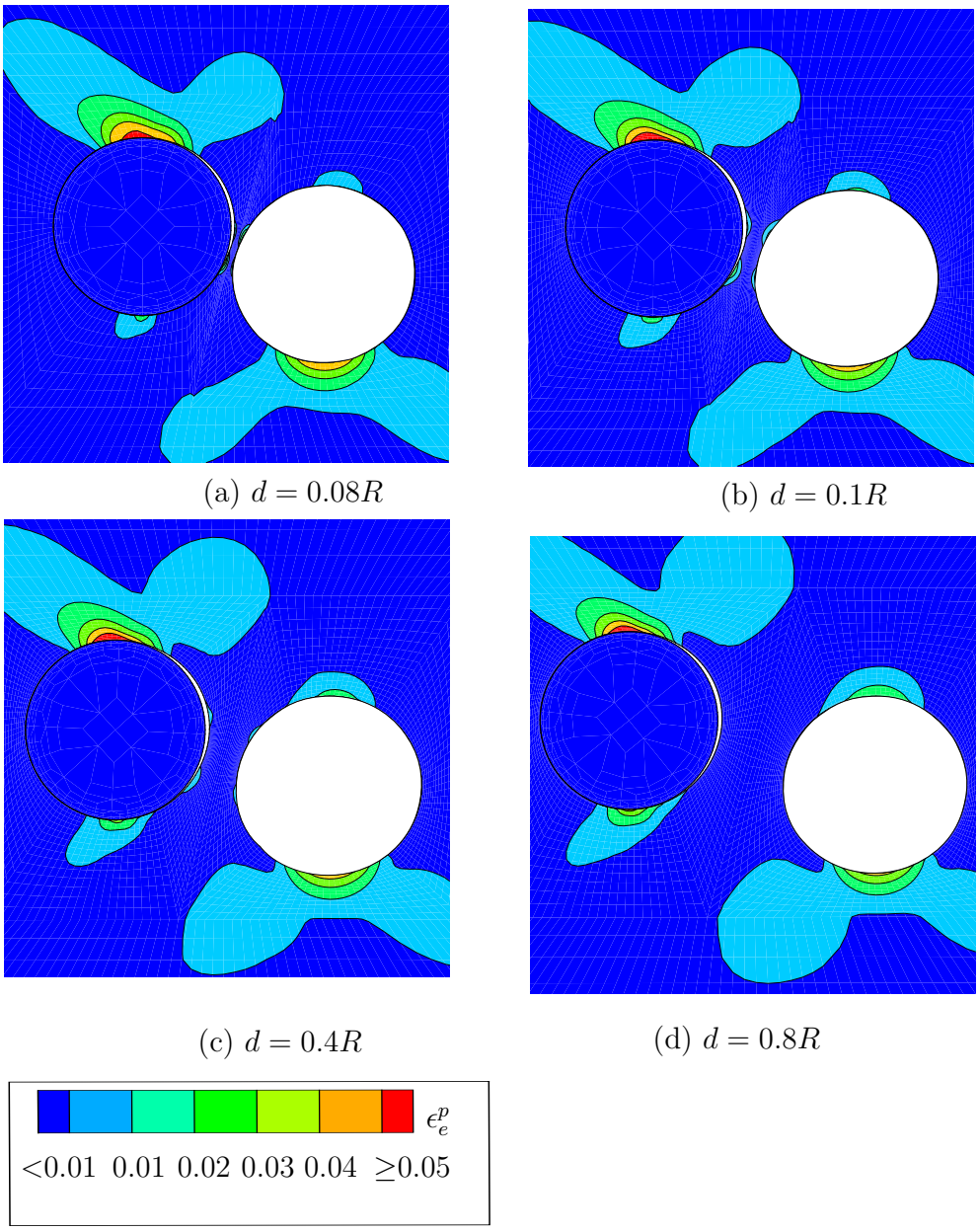

Figure 13: Contours of the accumulated equivalent plastic strain, ϵ_e^p, of fiber-hole composite model. The results are shown at $\epsilon_{11} = 1\%$ ($\Sigma_{11}/\sigma_{max} = 3.2$) for the position angle, $\alpha = 15^\circ$ and four different ligament thicknesses: a) $d = 0.08R$, b) $d = 0.1R$, c) $d = 0.4R$ and d) $d = 0.8R$.

erties compared to the single fiber model. This study predicts that in the case of small ligament thickness and position angle the first arrested cracks will be captured in an earlier and more stable stage of interfacial debonding. The numerical results of $\alpha = 15^\circ$ and $d = 0.08R$ for both considered models were promising. However, the initial crack in the fiber-hole model is in a mixed mode failure while the fiber-fiber configuration leads a stable cracks under dominant mode-I fracture. Additionally, from an experimental point of view the two-fiber configuration is also preferable because it is easier to manufacture the specimens. Consequently, this study suggests that the two-fiber configuration can stabilize the crack initiation under dominant mode-I which is of interest for the experimental measurements of the normal debonding properties of the interfaces.

5. Acknowledgment

This work is supported by the Danish Council for Strategic Research (grant no.: 09-067212) under the Danish Center for Composite Structures and Materials for Wind Turbines.

References

Agrawal, A.,Karlsson, A.M., 2006. Obtaining mode mixity for a bimaterial interface crack using the virtual crack closure technique. Int. J. Fracture 141, 75-98.

Chandra, N., Li, H., Shet, C., Ghonem, H., 2002. Some issues in the application of cohesive zone models for metal-ceramic interfaces. Int. J. Solids Struct 39, 2827-2855.

Gamstedt, E.K., Sjögren, B.A., 1999. Micromechanisms in tension-compression fatigue of composite laminates containing transverse plies, Comp. Sci. Technology 59, 167-178.

Hampe, A., Kalinka, G., Meretz, S., Schulz, E., 1994. An advanced equipment for single-fibre pull-out test designed to monitor the fracture process, Composites: Part A. 26, 40-46.

Hutchinson, J.W., 1990. Mixed mode fracture mechanics of interfaces. Metal-Ceramics, Acta-Scripta Metallurgica Proceedings Series 4, 295-306.

Hutchinson, J.W., Suo, Z., 1992. Mixed mode cracking in layered materials. Advances in Applied Mechanics 29, 63-191.

Kelly, A., Tyson , W.R., 1965. Tensile properties of fiber-reinforced metals: copper/tungsten and copper/molybdenum. J. Mech. Phys. Solids 13,329-350.

Kerans, R.J., Parthasarathy, T.A., 1991. Theoretical analysis of the fiber pullout and pushout tests, J. Am. Ceram. Soc. 74, 1585-1596.

Liechti, K.M., Chai Y.S., 1992. Asymmetric shielding in interfacial fracture under in-plane shear. J. Appl. Mech 59, 295304.

Liu, S., Mei, Y., Wu, T.Y., 1995. Bimaterial interfacial crack growth as a function of mode-mixity. EEE Transactions on Components, Packaging, and Manufacturing Technology: Part A 18, 618-626.

Martyniuk, K., Sørensen, B.F., Modregger, P., Lauridsen, E.M., 2013. 3D in situ observations of glass fibre/matrix interfacial debonding. Composites: Part A 55, 63-73.

Moraleda, J., Segurado, J., Llorca, J., 2009. Effect of interface fracture on the tensile deformation of fiber-reinforced elastomers. International Journal of Solids and Structures 46, 4287-4297.

París, F., Correa, E., Cañas, J., 2003. Micromechanical view of failure of the matrix in fibrous composite materials. Composites Science and Technology 63, 1041-1052.

París, F., Correa, E., Cañas, J., Mantič, V., 2007. Kinking of transversal interface cracks between fiber and matrix. J. Appl. Mech 74, 703-716.

Rice, J.R., 1988. Elastic fracture mechanics concepts for interfacial cracks, J. Appl. Mech. 110 98-103.

Sørensen, B.F., Kirkegaard, P., 2006. Determination of mixed mode cohesive laws. Eng. Frac. Mechanics 73, 2642-2661.

Tvergaard, V., 1976. Effect of thickness inhomogeneities in internally pressurized elasticplastic spherical shells. J. Mech. Phys. of Solids 24, 291-304.

Tvergaard, V., 1990. Effect of fibre debonding in a whisker-reinforced metal. Mater. Sci. Engineering A125, 203-213.

Tvergaard, V., Hutchinson, J.W., 1992. The relation between crack growth resistance and fracture process parameters in elastic-plastic solids. J. Mech. Phys. Solids 40, 1377-1397.

Tvergaard, V., Hutchinson, J.W., 1993. The influence of plasticity on mixed mode interface toughness. J. Mech. Phys. Solids 41, 1119-1135.

Tvergaard, V., Legarth, B.N., 2007. Effect of anisotropic plasticity on mixed mode interface crack growth. Eng. Frac. Mechanics 74, 2603-2614.

Williams, M.L., 1959. The stress around a fault or crack in dissimilar media. Bull. Seismol. Soc. Am. 49, 199-204.

Yang, Q.D., Thouless., M.D., 2001. Mixed-mode fracture analyses of plastically-deforming adhesive joints. Int. J. of Fracture 110, 175-187.

Publication [P3]

Micromechanical modeling of unidirectional composites with uneven interfacial strengths

European Journal of Mechanics A/Solids 42 (2013) 241–250

Contents lists available at SciVerse ScienceDirect

European Journal of Mechanics A/Solids

journal homepage: www.elsevier.com/locate/ejmsol

Micromechanical modeling of unidirectional composites with uneven interfacial strengths

Danial Ashouri Vajari*, Brian Nyvang Legarth, Christian F. Niordson

Department of Mechanical Engineering, Solid Mechanics, Technical University of Denmark, DK-2800 Kgs. Lyngby, Denmark

ARTICLE INFO

Article history:
Received 2 January 2013
Accepted 16 June 2013
Available online 2 July 2013

Keywords:
Micromechanics
Cohesive zone model
Generalized plane strain

ABSTRACT

Composite materials under loads normal to the fiber orientation often fail due to debonding between fibers and matrix. In this paper a micromechanical model is developed to study the interfacial and geometrical effects in fiber-reinforced composites using generalized plane strain by means of the finite element method. Assuming a periodic distribution of fibers in the matrix, a unit cell is chosen including two quarter-circular fibers. By using this unit cell approach the composite material is modeled rather realistically as the possibility of having different fiber–matrix strength exists. In the present study two different cases are considered: I) Two perfectly bonded interfaces. II) Two debonding interfaces of uneven strength. The fibers are purely elastic while the matrix is considered as isotropic with an elasto-plastic behavior. To model the fracture of the fiber–matrix interfaces, a trapezoidal cohesive zone model is used. A parametric study is carried out to evaluate the influence of the interfacial properties, fiber position and fiber volume fraction on the overall stress–strain response as well as the end-crack opening displacement and the opening crack angle. All the results presented are compared with corresponding perfectly bonded interfaces. Generally, different crack initiations and propagations at the two interfaces are seen, which result in an overall stress–strain response of the material that often first depict a rather smooth stress drop followed by a second sudden stress drop. This behavior is shown to be very sensitive to interface parameters as well as geometrical parameters. The interfacial dissimilarity shows for all the investigations, that decreasing the maximum cohesive strength leads to more stable interfacial crack growth, whereas increasing the critical interfacial separation causes a less distinct debonding at one interface before debonding at the other.

1. Introduction

Failure mechanisms of fiber-reinforced composites still is a challenging topic as the anisotropic nature of composites complicates the numerical modeling as well as the experimental testing. Unidirectional fiber-composites subjected to transverse tensile loads often fail by two different failure mechanisms. One is associated with matrix damage and the other is caused by micro-cracks growing at the interfaces between the fibers and the matrix. For longitudinal loading matrix and fiber cracking are the most often seen failure modes. The present study focuses on micro-cracks growing at the fiber–matrix interfaces as load cases where the transverse loading dominates over the longitudinal loading are considered.

A real composite material is a complex mixture of fibers, matrix and porosities. However, the porosity of high quality composite materials is normally less than 2% and porosities are therefore in most modeling situations ignored. González and Llorca (2007) used a Representative Volume Element (RVE) with random distribution of multiple fibers embedded in the matrix. They performed a parameter study to assess the influence of matrix and interface properties on the stress–strain curve, the compressive strength, the ductility and the corresponding failure modes. They found that the composite properties under transverse compression were mainly controlled by interface strength and the matrix yield strength in uniaxial compression. Moraleda et al. (2009) studied the influence of interface properties (strength and toughness) on the tensile behavior of fiber-reinforced elastomers and they observed that the onset of damage and tensile strength are controlled by interface strength while the evolution of damage depends on the interface toughness. Totry et al. (2008a,b) predicted the failure locus of a unidirectional C/PEEK composite subjected to transverse compression and longitudinal shear. They computed the failure locus of a fiber-reinforced composite under transverse compression and out-of-plane shear and pointed out the need to

* Corresponding author. Tel.: +45 50363658; fax: +45 45931475.
E-mail address: dvaj@mek.dtu.dk (D. Ashouri Vajari).

0997-7538/$ – see front matter © 2013 Elsevier Masson SAS. All rights reserved.
http://dx.doi.org/10.1016/j.euromechsol.2013.06.008

include interface fracture in the failure criteria for composites. Fang et al. (2011) investigated multiple cracking in a ceramic matrix composite also using a multi-fiber RVE. Here, fiber–matrix decohesion was analyzed in combination with matrix cracking by adopting a cohesive zone model together with the Augmented Finite Element Method (A-FEM), see Ling et al. (2009). The combination of the eXtended Finite Element Method (X-FEM) and the Level Set Method (LSM) was used by Hettich et al. (2008) to model discontinuous failure within composite materials considering several fibers. In their work, the principal stress criterion for matrix cracking and the criterion suggested by Brewer and Lagace (1988) was adopted for fiber–matrix debonding. These complicated multiple fiber RVE studies assume a linear elastic matrix behavior until failure.

Assuming a regular distribution of the fibers allows for a much more simple representation of the composite geometry. Bayat and Aghdam (2012) modeled a unit cell including only two fibers using the Differential Quadratic Element Method (DQEM) under generalized plane strain deformations. Similar approach was adopted by Maligno et al. (2009) who studied the effect of thermal residual stress and fiber spacing. They used maximum principal stress failure and stiffness degradation for damage analysis. Neither Bayat and Aghdam (2012) nor Maligno et al. (2009) considered debonding at the fiber–matrix interface. Even more simplified models where only a single fiber is taken into account have been used for analyses of advanced non-linear matrix behavior. Different types of plasticity models have been implemented to study failure. Tvergaard (1990) used the classical J_2 flow theory, while Needleman et al. (2010) assumed a visco-plastic polymer material model for the matrix and Legarth (2004) implemented different yield criteria to investigate the effect of different orientations of plastic anisotropy. Micro-scale plasticity has also been used by Legarth and Niordson (2010) and Azizi (2012) in a viscous and time-independent formulation, respectively. Creep behavior was investigated by Bao et al. (1991). An inherent feature of such reduced fully symmetric single-fiber RVE models is the repeatability of the stress and strain fields around the fibers which results in simultaneously failure of all fiber–matrix interfaces through-out the whole composite. Hinz et al. (2007) studied an RVE similar to what was used in Bayat and Aghdam (2012) with hexagonal fiber alignment assuming matrix plasticity. Assuming identical cohesive interfaces strength, Hinz et al. included interfacial debonding using the bi-linear cohesive zone of Xu and Needleman (1993).

All of the above discussed multi-fiber studies who considered interface debonding assumed identical interfacial properties. Thus, once interfacial debonding failure has been initiated, the basic assumption is that all other fibers experience similar simultaneous failure. Zhou and Molinari (2004) simulated a three-dimensional model to investigate the dynamic tensile properties of homogeneous ceramics without any reinforcement. Their study implements a modified Weibull theory to distribute cohesive elements with different strengths between the bulk elements. Similarly, by having different cohesive properties the present study aims at considering a slightly more realistic model by including two different fiber–matrix interfaces of uneven strengths. This will capture different initiation locations and propagations of the interfacial micro-cracks and consequences on the overall response of the material. Uniaxially transverse tension is considered by imposing generalized plane strain conditions. The geometrical model used is similar to the models used by Hinz et al. (2007) and Bayat and Aghdam (2012) but here the trapezoidal cohesive zone model proposed by Tvergaard and Hutchinson (1993) is used to simulate the fracture process. Having more than one active cohesive zone often causes complications in terms of numerical instabilities. Therefore, a combination of the finite element and the Rayleigh–Ritz method is implemented as proposed by Tvergaard (1976). To summarize, the novelty of present study is considering non-uniform interfacial strengths in an elasto-plastic unit-cell subjected to various 3D macroscopic normal loads and the main focus of this study is on the interaction between two fibers and their effects on the progressive fiber–matrix debonding. Particularly when they have dissimilar interfacial properties and the distance between two fibers changes. Finally, the resulting overall stress–strain curve as well as the equivalent plastic strain and stress distributions are shown. In these results the effect of fiber position, volume fraction and interfacial parameters are discussed. In addition, the normal opening of the crack end as well as the angle between the loading direction and the progressive crack front will be discussed.

2. Problem formulation

Generally fiber-reinforced composites are analyzed in a full 3D setting to represent the geometry, loads and boundaries as fibers can be distributed in a variety of different ways during manufacturing and the loading can be arbitrarily. Analyses accounting for such behavior would make the computations complicated and time consuming. Thus, here simplified studies are performed as a periodic distribution is analyzed (see Fig. 1a) and a generalized plane strain unit cell is extracted which includes two

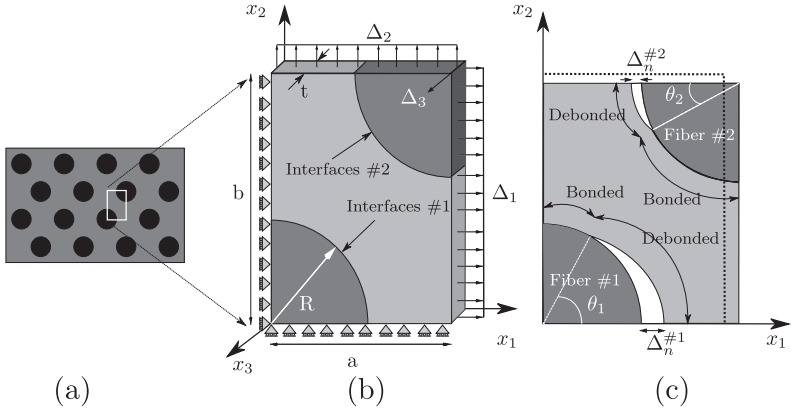

Fig. 1. a) The fiber distribution in the matrix. b) The unit cell including two quarter circular fibers showing the dimensions, loads and the coordinate system. c) A deformed and partly debonded unit cell under an x_1-direction tensile load dominated. The dash line denotes the undeformed shape of the unit cell.

quarter-circular fibers as shown in Fig. 1b. By using this unit cell approach the possibility of having different fiber–matrix strengths exists which is not the case of standard unit cell analyses containing a single fiber. A Cartesian reference coordinate system, x_i, is placed at the center of the lower fiber and aligned with the unit cell edges (see Fig. 1b). The positive direction of the third axis, x_3, points in the out-of-plane direction normal to the (x_1,x_2)-plane. The dimension of the unit cell is determined by the thickness, t, the length, b, the width, a, and the radius of the fibers, R, which yields the fiber volume fraction $V_f = \pi R^2/2ab$. The cell is subjected to normal load in the three directions only; i.e. $(\Sigma_{11}, \Sigma_{22}, \Sigma_{33}) \neq 0$ whereas $\Sigma_{12} = \Sigma_{13} = \Sigma_{23} = 0$. Due to the symmetries in geometry and loads, the cell edges remain straight during the deformations. It is emphasized that this generalized plane strain problem formulation only includes a single uniform out-of-plane deformation imposed by the displacement Δ_3. The boundary conditions are implemented incrementally as follows

$$\begin{array}{llllll} \dot{u}_1 = 0 & \text{and} & \dot{T}_2 = 0, & \text{on} & x_1 = 0 \\ \dot{u}_1 = \dot{\Delta}_1 & \text{and} & \dot{T}_2 = 0, & \text{on} & x_1 = a \\ \dot{u}_2 = 0 & \text{and} & \dot{T}_1 = 0, & \text{on} & x_2 = 0 \\ \dot{u}_2 = \dot{\Delta}_2 & \text{and} & \dot{T}_1 = 0, & \text{on} & x_2 = b \\ \dot{u}_3 = 0, & & & \text{on} & x_3 = 0 \\ \dot{u}_3 = \dot{\Delta}_3, & & & \text{on} & x_3 = t \\ \dot{T}_1 = 0 & \text{and} & \dot{T}_2 = 0, & \text{on} & x_1 \in]0,a[\quad \text{and} \quad x_2 \in]0,b[\end{array} \tag{1}$$

where $\dot{\Delta}_1$ and $\dot{\Delta}_2$ describe incremental displacement quantities on the two edges of the unit cell and $\dot{\Delta}_3$ is the incremental displacement quantity in the out-of-plane direction, and T_i are surface tractions. Two constant stress-ratios, $\kappa_1 = \Sigma_{22}/\Sigma_{11}$ and $\kappa_2 = \Sigma_{33}/\Sigma_{11}$, are enforced where the overall macroscopic stress increment, $\dot{\Sigma}_{ij}$, are computed as

$$\begin{aligned} \dot{\Sigma}_{11} &= \tfrac{1}{tb}\int_0^b \dot{T}_1 t \mathrm{d}x_2, \quad \text{at} \quad x_1 = a \\ \dot{\Sigma}_{22} &= \tfrac{1}{ta}\int_0^a \dot{T}_2 t \mathrm{d}x_1, \quad \text{at} \quad x_2 = b \\ \dot{\Sigma}_{33} &= \tfrac{1}{ab}\int_0^a\int_0^b \dot{T}_3 \mathrm{d}x_2 \mathrm{d}x_1, \quad \text{on}(x_1,x_2) - \text{plane} \end{aligned} \tag{2}$$

and the corresponding macroscopic incremental strains are defined as

$$\dot{E}_{11} = \frac{\dot{\Delta}_1}{a}, \quad \dot{E}_{22} = \frac{\dot{\Delta}_2}{b} \quad \text{and} \quad \dot{E}_{33} = \frac{\dot{\Delta}_3}{t} \tag{3}$$

Hence, the composite is assumed to deform by triaxial normal loading under generalized plane strain condition. This reduces the problem to only specifying one out-of-plane displacement (Δ_3) as well as in-plane displacements (Δ_1 and Δ_2).

3. Material model

3.1. Isotropic plasticity model

The matrix is assumed to be an elasto-plastic material governed by the standard J_2-plasticity theory, while the fibers are considered as purely elastic. Both the matrix as well as the fibers are modeled as isotropic materials. In the matrix, the stress increment is calculated from the total strain increment, $\dot{\epsilon}_{ij}$, which consists of an elastic part, $\dot{\epsilon}^e_{ij}$, and a plastic part, $\dot{\epsilon}^p_{ij}$

$$\begin{aligned} \dot{\epsilon}_{ij} &= \dot{\epsilon}^e_{ij} + \dot{\epsilon}^p_{ij} \\ \dot{\sigma}_{ij} &= L_{ijkl}\dot{\epsilon}_{kl} \end{aligned} \tag{4}$$

Here, L_{ijkl} is the fourth order incremental stiffness tensor defined as

$$L_{ijkl} = \frac{E}{1+\nu}\left[\frac{1}{2}\left(\delta_{ik}\delta_{jl}+\delta_{il}\delta_{jk}\right) + \frac{\nu}{1-2\nu}\delta_{ij}\delta_{kl} - \beta\frac{3}{2}\frac{\frac{E}{E_t}-1}{\frac{E}{E_t}-\frac{(1-2\nu)}{3}}\frac{s_{ij}s_{kl}}{\sigma_e^2}\right] \tag{5}$$

while,

$$\beta = \begin{cases} 1 & \text{for } \sigma_e = \sigma_f \text{ and } \dot{\sigma}_e \geq 0 \\ 0 & \text{for } \sigma_e < \sigma_f \text{ or } \dot{\sigma}_e < 0 \end{cases} \tag{6}$$

where, E is the Young's modulus and ν is the Poisson's ratio. The tangential modulus, E_t, is the slope of the stress–strain curve at the stress level $\sigma_e = \sqrt{(3/2)s_{ij}s_{ij}}$ and δ_{ij} denotes the Kronecker delta. The stress deviator is defined by $s_{ij} = \sigma_{ij} - \delta_{ij}(\sigma_{kk}/3)$. In Eq. (6), $\dot{\sigma}_e = (3s_{kl}\dot{\sigma}_{kl})/2\sigma_e$ and σ_f is the instantaneous flow stress and during plastic yielding β is unity and the magnitude of L_{ijkl} depends on the stress state and the deformation hardening law whereas in the elastic regime (including elastic unloading) it is governed by Hooke's law where β is zero. The yield surface, f, is taken as the von Mises yield surface

$$f = \sigma_e - \sigma_f(\epsilon^p_e) = 0 \tag{7}$$

Here, $\sigma_f = \sigma_f(\epsilon^p_e)$, where and ϵ^p_e is the equivalent plastic strain, work conjugate to σ_e, and it is defined incrementally by the relation $\dot{\epsilon}^p_e = \sqrt{(2/3)\dot{\epsilon}^p_{ij}\dot{\epsilon}^p_{ij}}$. The hardening behavior determined by the uniaxial stress–strain relation which is represented by the power hardening law

$$\epsilon = \begin{cases} \frac{\sigma}{E} & \text{for } \sigma \leq \sigma_y \\ \frac{\sigma_y}{E}\left(\frac{\sigma}{\sigma_y}\right)^n & \text{for } \sigma > \sigma_y \end{cases} \tag{8}$$

where n is the strain-hardening exponent and σ_y denotes the initial yield stress.

3.2. Cohesive zone model

When the unit cell is deformed, the interfaces between fibers and matrix tend to separate normally as well as tangentially. In order to capture this fracture behavior, a trapezoidal cohesive zone model proposed by Tvergaard and Hutchinson (1993) is used. As illustrated in Fig. 1c the failure by debonding is taken into account by considering two generally uneven cohesive zones along the two reinforcement interfaces. The cohesive zone model determines the failure behavior imposing a relation between tractions and separations. This traction-separation law is regarded as a phenomenological characterization of the separation zone along the interfaces and not the description of atomic separation, see Tvergaard and Hutchinson (1993). In this model, λ is defined as a non-dimensional parameter describing the separation as

$$\lambda = \sqrt{\left(\frac{u_n}{\delta_n^c}\right)^2 + \left(\frac{u_t}{\delta_t^c}\right)^2} \tag{9}$$

such that onset of degradation in cohesive zone starts at a specified value, $\lambda = \lambda_2$, and fully damage occurs when $\lambda = 1$. Here, δ_n^c and δ_t^c are the normal and tangential characteristic cohesive lengths, respectively, and u_n and u_t are the normal and tangential separation of the interface, respectively. A traction potential can be defined as

$$\Phi(u_n, u_t) = \delta_n^c \int_0^{\lambda} \sigma\left(\lambda'\right) \mathrm{d}\lambda' \tag{10}$$

from which the normal, T_n, and tangential, T_t, tractions acting on the interfaces can be divided according to

$$T_n = \frac{\partial \Phi}{\partial u_n} = \frac{\sigma(\lambda)}{\lambda}\frac{u_n}{\delta_n^c}, \quad T_t = \frac{\partial \Phi}{\partial u_t} = \frac{\sigma(\lambda)}{\lambda}\frac{\delta_n^c}{\delta_t^c}\frac{u_t}{\delta_t^c} \tag{11}$$

The incremental traction vector is related to the displacement increments across the interface as

$$\begin{bmatrix} \dot{T}_t \\ \dot{T}_n \end{bmatrix} = \begin{bmatrix} \frac{\partial T_n}{\partial u_t} & \frac{\partial T_n}{\partial u_n} \\ \frac{\partial T_n}{\partial u_t} & \frac{\partial T_n}{\partial u_n} \end{bmatrix} \begin{bmatrix} \dot{u}_t \\ \dot{u}_n \end{bmatrix} \tag{12}$$

where the matrix on the right hand side is the cohesive tangent matrix. In pure normal separation ($u_t = 0$) the maximum traction is $T_n = \sigma(\lambda)$ where $\lambda = u_n/\delta_n^c$, while under pure tangential separation ($u_n = 0$) the maximum traction is $T_t = (\delta_n^c/\delta_t^c)\sigma(\lambda)$ where $\lambda = u_t/\delta_t^c$. Thus, for both the interfaces considered here, five interface parameters need to be specified, i.e. δ_n^c, δ_t^c, λ_1, λ_2 and $\sigma_{\max}$. In addition, a plateau in the maximum traction level in the trapezoidal cohesive zone model simultaneously allows more Gauss points of cohesive elements to be at the maximum stress. This may lead to more stable solutions compared to the bilinear and exponential models. However, Tvergaard and Hutchinson (1993) discussed that the shape of the separation law has a secondary importance and the most critical parameters are the maximum cohesive stress and the characteristic cohesive length.

4. Numerical methods

For the numerical implementation the incremental form of the principle of virtual work is adopted. Disregarding body forces, the principle reads

$$\int_V \dot{\sigma}_{ij}\delta\dot{\epsilon}_{ij}\mathrm{d}V + \int_{S_l} \left(\dot{T}_n\delta\dot{u}_n + \dot{T}_t\delta\dot{u}_t\right)\mathrm{d}S = \int_S \dot{T}_i\delta\dot{u}_i\mathrm{d}S \tag{13}$$

where V denotes the volume of the unit cell having the surface S and S_l is the surface of the fiber–matrix interface.

In Fig. 3 three different examples of finite element meshes are shown for different unit cell dimensions. All the meshes include 1590 bulk elements and 64 cohesive elements. Eight-node quadrilateral elements with nine Gauss points are used for the bulk materials while six-node quadrilateral elements with three Gauss points are considered for the cohesive zones. As shown in Fig. 3, the mesh is refined near the interfaces. Tvergaard and Legarth (2007) characterized the length of the fracture process region, ℓ, in the cohesive zone during crack growth by the distance from the crack-tip, where $\lambda = 1$, to the point ahead of the crack-tip where $\lambda = \lambda_1$. They found a good resolution and very little mesh dependence when the value of ℓ is several times the length, Δ_0, of a square element in the uniform mesh region (here, around the interfaces in Fig. 3). This requirement is satisfied in the present computations as $\ell \geq 6\Delta_0$.

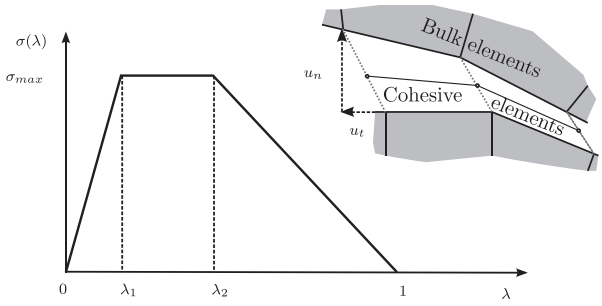

Fig. 2. Traction-separation law used to characterize interface separation.

During debonding neither the load increment nor the displacement is useful as the prescribed quantity, since both change sign along the equilibrium path. To avoid this numerical problem during debonding, a combination of a Rayleigh–Ritz method with the finite element procedure proposed by Tvergaard (1976) is implemented. The approach is to choose a small number of nodal displacements as trial displacements on the edges as well as on the interfaces. Then, the finite element problem is solved by prescribing one of these nodal displacements to one and all other to zero. This gives a set of trial functions based on the finite element approximation of Eq. (13) and a reduced system of equations can be established. Solving this reduced system of linear equations gives the amplitudes of the trial functions. Finally, the complete solution in each increment can be computed as the sum of the trial functions with the corresponding amplitudes (Tvergaard, 1976). By this approach, a sudden stress-drop of the overall average stress–strain response may be captured. Furthermore, this procedure gives the possibility to control the stresses applied to the cell while still using displacement controlled symmetry boundary conditions by prescribing two ratios between the macroscopic stresses, $\kappa_1 = \Sigma_{22}/\Sigma_{11}$ and $\kappa_2 = \Sigma_{33}/\Sigma_{11}$.

In each incremental step, Δt, for the next increment is corrected according to $(\dot{\epsilon}^p)_{\max}\cdot\Delta t \leq c_1$ and $(\dot{\lambda})_{\max}\cdot\Delta t \leq c_2$, where the label max refers to the maximum effective plastic strain rate in any Gauss point, or the maximum rate of debonding separation measure at the current increment. Since a forward Euler integration scheme is adopted, it has been investigated if the results are affected by c_1 and c_2. Thus, the values of the constants c_1 and c_2 are in several computations chosen as $c_1 = 0.01$ and $c_2 = 0.004$. In addition, discontinuous increment analysis is used, such that when the first Gauss point in the bulk material reaches the plastic regime or when the

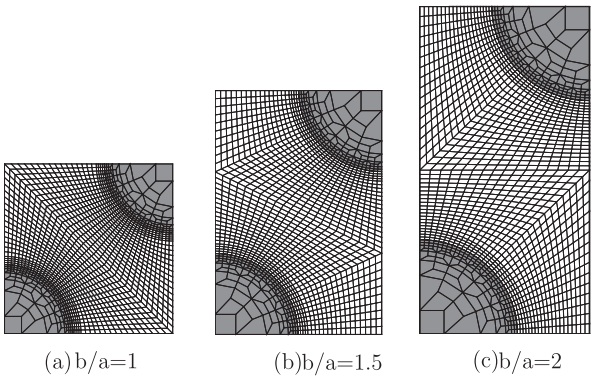

Fig. 3. Examples of mesh used for the computations. The fiber volume fraction is $V_f = (\pi R^2)/(2ab) = 0.26$ where in a) $b = a$, b) $b = 1.5a$ and c) $b = 2a$.

first Gauss point in the cohesive elements of each interface reaches $\lambda = \lambda_2$ the solver turns one step back and continue the solution with reduced increment size. The amount of step reduction as well as c_1 and c_2 parameters are chosen such that a stable and converged solution is achieved. Thus, for further reduced time steps similar results are obtained.

5. Results and discussion

The matrix material properties are considered to be $\nu_m = 0.35$, $\sigma_0/E_m = 0.004$ and $n = 5$ and the material properties of the fibers are $\nu_f = 0.3$ and $E_f/E_m = 6.0$. A parameter study is performed on the interfacial parameters: The characteristic cohesive length, $\delta^c = \delta_n^c = \delta_t^c$ (Eq. (9)), and the maximum cohesive strength, $\sigma_{\max}$, as well as on the dimensional ratio, b/a, and the fiber volume fraction, V_f, under different loading conditions defined by $\kappa_1 = \Sigma_{22}/\Sigma_{11}$ and $\kappa_2 = \Sigma_{33}/\Sigma_{11}$. The results will highlight the influence of these parameters on the macroscopic stress–strain response (Σ_{11},E_{11}) of the overall inhomogeneous material as well as the normal crack end opening and the crack opening angle of the two interfaces.

Initially, the behavior of the unit cell for a reference case is discussed. The reference case denotes when the fiber volume fraction is $V_f = 0.26$ and the interfacial parameters are $\delta^c = \delta_n^c = \delta_t^c = 0.02R$ (both interfaces), while interface #1 has $\sigma_{max}^{\#1} = 1.5\sigma_y$, $\lambda_1^{\#1} = 0.2$ and $\lambda_2^{\#1} = 0.4$, and for interface #2, $\sigma_{max}^{\#2} = 2\sigma_y$, $\lambda_1^{\#2} = 0.3$ and $\lambda_2^{\#2} = 0.5$, and the loading is specified by $\kappa_1 = 0$, $\kappa_2 = 0.2$. Fig. 4 illustrates the overall stress–strain response for the reference case as well as a unit cell with perfectly bonded interfaces. At first, both curves follow the elastic modulus. Because of the cohesive zone specified on the interfaces, the reference case shows lower elastic modulus. After reaching the macroscopic yield stress, plasticity leads to a nonlinear behavior in both cases but the onset of yielding in the perfectly bonded case is slightly earlier than in the reference case. Unlike the perfectly bonded case, another nonlinearity happens due to debonding at the interfaces. Onset of degradation in cohesive zone occurs when the coupled cohesive parameter reaches $\lambda = \lambda_2$ and debonding initiates at the weakest interface at fiber #1. In Fig. 4, at $\Sigma_{11} = 1.62\sigma_y$ the

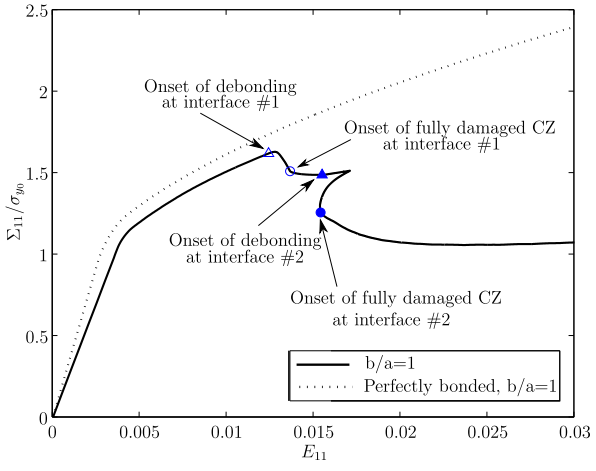

Fig. 4. The overall stress–strain response for the reference case, $V_f = 0.26$, $\delta^c = \delta_n^c = \delta_t^c = 0.02R$, for interface #1, $\sigma_{\max}^{\#1} = 1.5\sigma_y$, $\lambda_1^{\#1} = 0.2$ and $\lambda_2^{\#1} = 0.4$, and for interface #2, $\sigma_{\max}^{\#2} = 2\sigma_y$, $\lambda_1^{\#2} = 0.3$ and $\lambda_2^{\#2} = 0.5$, under loading condition with $\kappa_1 = \Sigma_{22}/\Sigma_{11} = 0$, $\kappa_2 = \Sigma_{33}/\Sigma_{11} = 0.2$. The case with perfectly bonded interfaces is also shown by the dashed line. The figure illustrates the onset of degradation in cohesive zone (CZ) and fully damaged cohesive zone of the two interfaces on the curve.

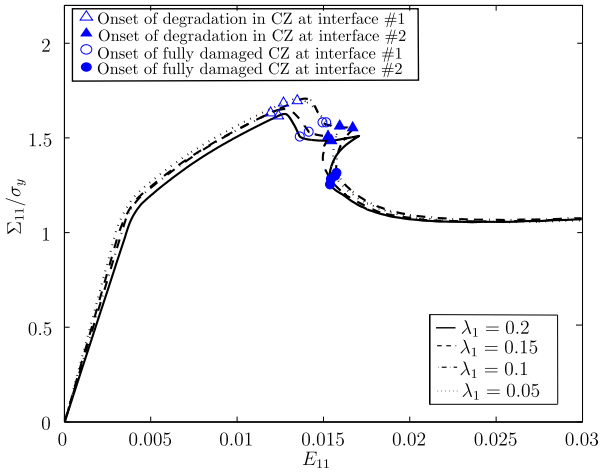

Fig. 5. Effect of different λ_1 on the overall stress–strain curve.

first Gauss point in the cohesive elements reaches $\lambda = \lambda_2$, see Fig. 2, near fiber #1 which is depicted by (△) on the curve. Afterward, subsequent Gauss points at the same cohesive interface also pass $\lambda = \lambda_2$ and therefore the interface gets weaker which leads to a stress-drop until the first Gauss point at $\Sigma_{11} = 1.5\sigma_y$ gets fully damaged, i.e. $\lambda^{\#1} = 1$ (see ○-mark on the curve). By continuing loading the crack propagates through interface #1. When interface #1 is still partly debonded, again the load carrying capacity increases slightly until interface #2 starts debonding at $\Sigma_{11} = 1.48\sigma_y$. As for interface #1, the same points are marked but with the filled color (▲). The sudden stress-drop with negative macroscopic strain observed during debonding at interface #2 has the physical meaning of a mechanical unstable situation where the load drops instantaneously as the overall displacement increases due to dynamic debonding. From the modeling point of view, this implies that there is no unique relation between force and displacement in this quasi-static analysis, where dynamic effects are neglected. In order to satisfy equilibrium and resolve the unstable solution the combined finite element and Rayleigh–Ritz method has been used. Further loading leads to an increase in overall stress with a

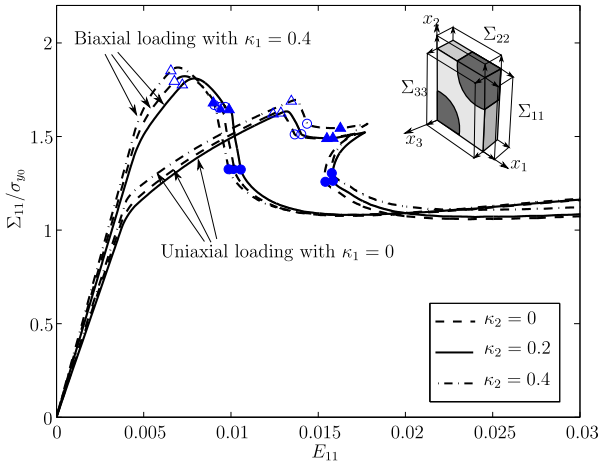

Fig. 6. Effect of different loading conditions, $\kappa_1 = \Sigma_{22}/\Sigma_{11}$ and $\kappa_2 = \Sigma_{33}/\Sigma_{11}$ on the stress–strain curve.

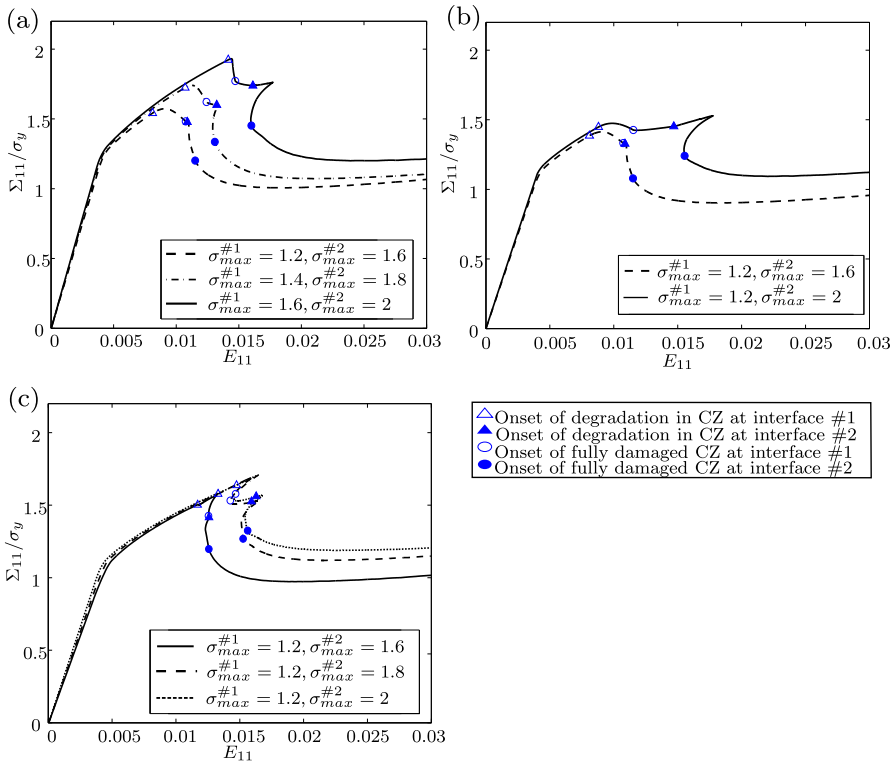

Fig. 7. Effect of the maximum cohesive stress, $\sigma_{\max}$, on the stress–strain curve where a) shows the effect of increasing $\sigma_{\max}$ in both interfaces while keeping the difference between $\sigma_{\max}$ of the two interfaces constant, b) illustrates the interaction between two interfaces when the maximum cohesive stress at interface #1 is constant while interface #2 increases and c) depicts the results of the same work of fracture, Φ, at both interfaces although the interfacial strengths are different. The loading is specified by $\kappa_1 = 0$ and $\kappa_2 = 0.2$.

significantly reduced slope compared to the part when debonding has not initiated yet. This difference in slope can be related to the microcracks growing at the interfaces and matrix yielding. The load carrying capacity at the end of the simulation saturates approximately at the same level as the initial macroscopic yield strength.

Cohesive zone models can be categorized into two types, the intrinsic and extrinsic cohesive models (Ortiz and Pandol, 1999). Extrinsic models avoid artificial softening effects which are present in intrinsic models. Extrinsic models usually require complicated updating schemes for the modified mesh by adding nodes and elements. Intrinsic models allow easier implementation. However, intrinsic models introduce artificial compliance depending on the area of cohesive element surfaces introduced and the cohesive element property. This problem can be dealt with by approaching an initially rigid cohesive model making $\lambda_1 \to 0$. In Fig. 5 the effect of different λ_1 on the overall stress–strain response of unit cell is shown. A larger value of λ_1 may slightly reduce the elastic response of the unit-cell and the maximum failure stress (the deviation of the maximum failure stress between $\lambda_1 = 0.05$ and $\lambda_1 = 0.2$ is around 5%). By considering that the elastic part is not the main focus of this study and noting the similar stress–strain behaviors, $\lambda_1 = 0.2$ is chosen for subsequent calculations.

Different loading conditions can be simulated by changing the stress ratios, $\kappa_1 = \Sigma_{22}/\Sigma_{11}$ and $\kappa_2 = \Sigma_{33}/\Sigma_{11}$. When κ_2 is zero, the unit cell is under overall plane stress condition while its nonzero value denotes the generalized plane strain condition. When κ_1 is also zero the unit cell is subjected to uniaxial transverse loading in the x_1-direction. Increase of κ_1 leads to biaxial loading until it reaches a very large value mimicking uniaxial loading in the x_2-direction. Fig. 6 depicts different stress–strain responses for different stress ratios, κ_1 and κ_2, where the situation $\kappa_1 = 0$ and $\kappa_2 = 0.2$ denotes the reference case discussed in Fig. 4. A larger κ_1 value increases the loading in the x_2-direction which tends to open the interfaces. On the other hand, increase of κ_2 contracts the unit cell because of loading in the x_3-direction which has closing effect.

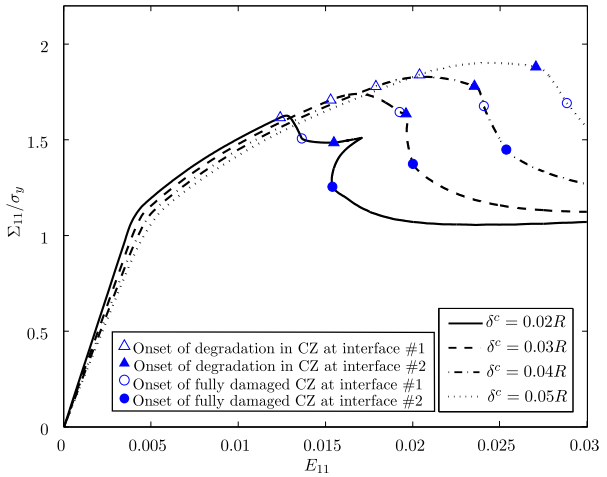

Fig. 8. Effect of critical cohesive distance, $\delta^c = \delta^c_n = \delta^c_t$ (the same for both interfaces), on the overall stress–strain curve. The remaining parameters are the same as reference case, $V_f = 0.26$, $(\sigma^{\#1}_{\max}, \sigma^{\#2}_{\max}) = (1.5\sigma_y, 2\sigma_y)$, $(\lambda^{\#1}_1, \lambda^{\#1}_2) = (0.2, 0.4)$ and $(\lambda^{\#2}_1, \lambda^{\#2}_2) = (0.3, 0.5)$. The loading is specified by $\kappa_1 = 0$, $\kappa_2 = 0.2$.

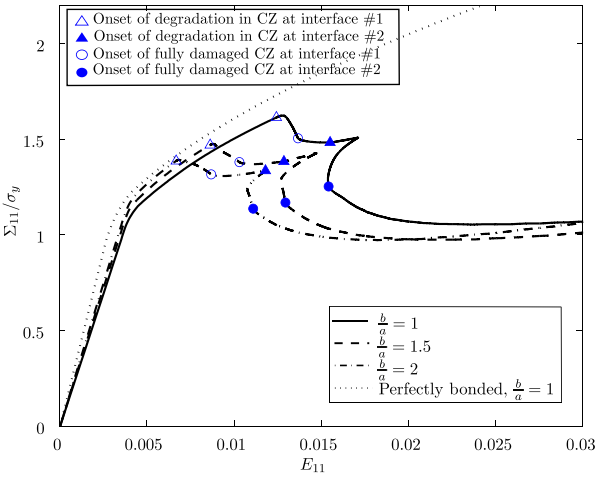

Fig. 9. Effect of the dimensional ratio, b/a, on the stress–strain curve with the constant volume fraction, $V_f = 0.26$. The interfaces and loading conditions are identical to the reference case, see Fig. 4.

Therefore, as shown in Fig. 6, onset of degradation in cohesive zone starts at a lower overall strain under biaxial loading and a larger κ_2 enhances the overall stress response. Subsequently, all the investigations throughout the paper will be subjected to the loading condition with $\kappa_1 = 0$ and $\kappa_2 = 0.2$ (as in the reference case).

Fig. 7 shows the effect of the maximum cohesive stress, $\sigma_{\max}$, on the overall stress–strain curve. Fig. 7a shows the effect of increasing $\sigma_{\max}$ in both interfaces keeping the difference between $\sigma_{\max}$ of two interfaces constant and Fig. 7b illustrates the interaction between two interfaces when the maximum cohesive stress in interface #1 is constant while interface #2 increases. Considering the case with $(\sigma^{\#1}_{max}, \sigma^{\#2}_{max}) = (1.2\sigma_y, 1.6\sigma_y)$ and comparing to the curves with $(\sigma^{\#1}_{\max}, \sigma^{\#2}_{\max}) = (1.4\sigma_y, 1.8\sigma_y)$ and $(\sigma^{\#1}_{\max}, \sigma^{\#2}_{\max}) = (1.6\sigma_y, 2\sigma_y)$ shows that the increase of $\sigma_{\max}$ leads to a stronger interface and therefore delaying due to debonding (see Fig. 7b). It can also be seen that an increase of $\sigma_{\max}$ leads to less stable crack growth at both interfaces (less smooth curve) and furthermore it enhances the load carrying capacity between two interfacial debondings (the open and filled symbols are moving apart). In Fig. 7b, the case with $(\sigma^{\#1}_{\max}, \sigma^{\#2}_{\max}) = (1.2\sigma_y, 1.6\sigma_y)$ shows earlier onset of degradation in cohesive zone and stress-drop at interface #1 compared to the one with $(\sigma^{\#1}_{\max}, \sigma^{\#2}_{\max}) = (1.2\sigma_y, 2\sigma_y)$ although the maximum cohesive stress at interface #1, $\sigma^{\#1}_{\max}$, for both of them is identical. This can be explained by the larger $\sigma^{\#2}_{\max}$ which postpones onset of degradation in cohesive zone in interface #2 and therefore debonding of interface #2 does not interact much with the first debonding. This leads to a more stable crack growth and furthermore allows the load carrying capacity to enhance before the onset of degradation in cohesive zone at interface #2 initiates. Unlike Fig. 7a and b, the work of fracture, Φ, for the cases discussed in Fig. 7c is identical at both interfaces although the interfacial strengths are different. Fig. 7c shows that a larger $\sigma_{\max}$ causes later debonding but less stable crack growth at both interfaces which is similar to Fig. 7a. It should be noted that the curve of $(\sigma^{\#1}_{\max}, \sigma^{\#2}_{\max}) = (1.2\sigma_y, 1.6\sigma_y)$ in Fig. 7c differs with Fig. 7a and b due to the fact that λ_1 and λ_2 has changed in Fig. 7c to satisfy the condition of similar work of fracture at the two interfaces for various $\sigma_{\max}$ values.

The effect of the characteristic cohesive length, $\delta^c = \delta^c_n = \delta^c_t$, of both interfaces on the overall stress–strain response is shown in Fig. 8 where the values of $\sigma_{\max}$, λ_1 and λ_2 are chosen as in the reference case. Hence, δ^c is identical for both interfaces and similar to the reference case, the uneven strength is specified by different maximum cohesive stress, $\sigma_{\max}$, and also different λ_1 and λ_2 for each interface. The curve with $\delta^c = 0.02R$ refers to the reference case shown in Fig. 4. Increase of δ^c shows a slightly smaller elastic modulus but gives a significant delay of debonding due to the stronger interfaces and leads to more stable crack growth in both interfaces. In addition, larger δ^c causes earlier onset of degradation in cohesive zone in interface #2 (▲) than the point where the cohesive zone at interface #1 gets fully damaged (○) such that no enhanced load carrying capacity is reached between debonding of two interfaces for large δ^c values.

The dimensional ratio defined as the length over the width of unit cell, b/a, is a non-interfacial parameter. In fact, this ratio specifies the distance between the center of two fibers. By keeping

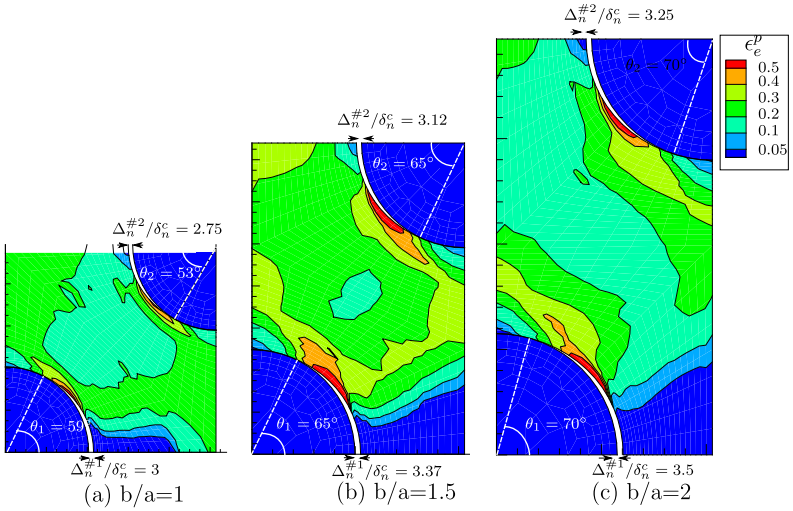

Fig. 10. The effect of fiber position specified by the dimensional ratio, b/a, on the damage evolution of the unit cell. Contours of the equivalent plastic strain, ϵ^p_e, is shown at $E_{11} = 0.029$, see Fig. 9.

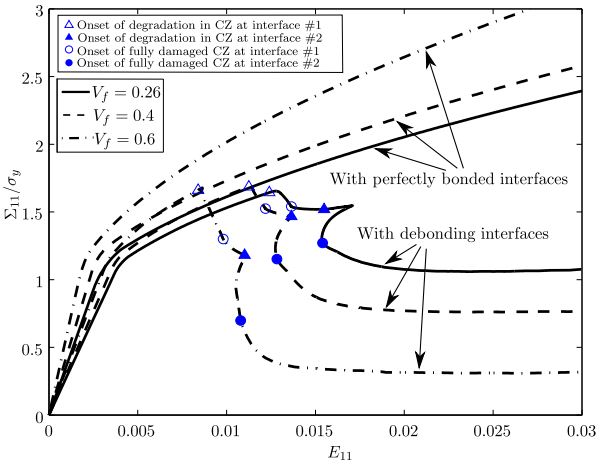

Fig. 11. Effect of the fiber volume fraction, V_f, on the stress–strain curve. The interfaces and loading conditions are identical to the reference case, see Fig. 4.

the fiber volume fraction constant, smaller b means closer fibers in a unit cell. Fig. 9 shows the effect of the dimensional ratio on the overall stress–strain response when the fiber volume fraction is constant. Like previous cases, due to the existence of cohesive zone the elastic modulus is smaller than the perfectly bonded case. Debonding initiates earlier due to an increase of b/a and the smoother slope during the stress drop indicates more stable crack growth. This is due to the fact that the larger b/a gives a smaller interfacial zone where potential debonding failure can occur compared to the total length of cell, b. The load carrying capacity well after debonding of both interfaces is seen to be practically independent of b/a-ratio and has a level similar to the initial yield strength. Fig. 10 illustrates the corresponding contours of the accumulated equivalent plastic strain, ϵ_e^p, for the different dimensional ratios, b/a, of the unit cell. All the data shown in Fig. 10 are captured at the overall strain in x_1-direction $E_{11} = 0.029$ in Fig. 9. Furthermore, in Fig. 10 larger normal crack end opening and opening angle are observed in both interfaces when b/a increases. This will be discussed further in relation to Fig. 13.

Fig. 11 shows the effect of the fiber volume fraction, V_f, on the overall stress–strain response when the interfaces have uneven strength, $(\sigma_{\max}^{\#1}, \sigma_{\max}^{\#2}) = (1.5\sigma_y, 2\sigma_y)$. Similar to the discussion of the dimensional ratio, b/a, Fig. 9, all the characteristic cohesive lengths

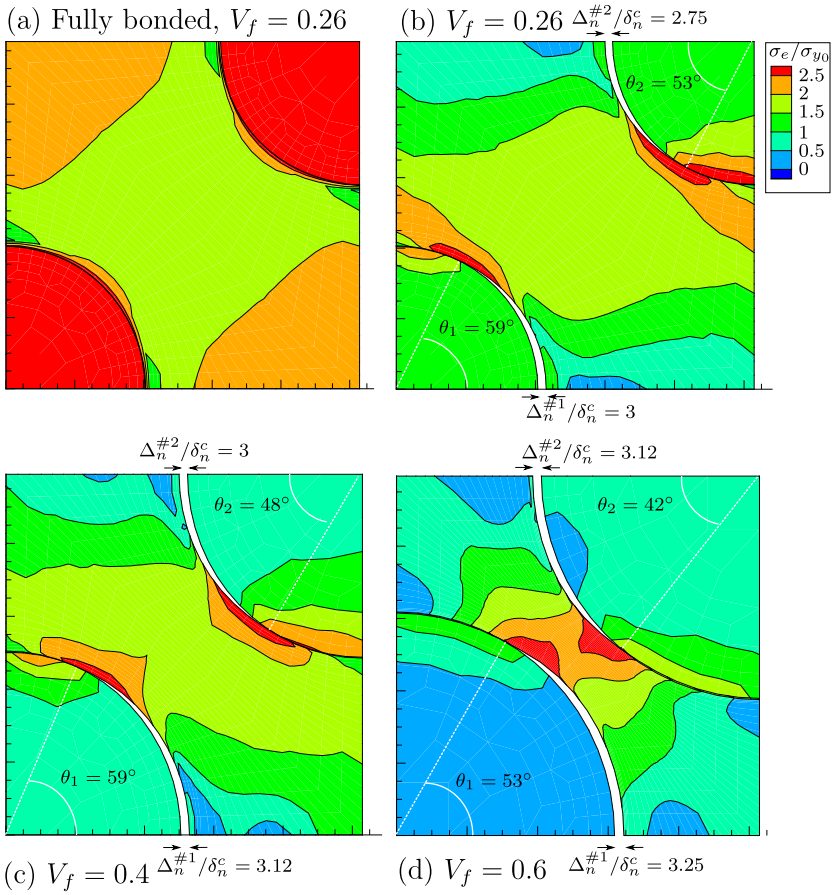

Fig. 12. The effect of fiber volume fraction, V_f, on the damage evolution of the unit cell. Contours of normalized von Mises stress, σ_e/σ_y, is shown at $E_{11} = 0.029$, see Fig. 11.

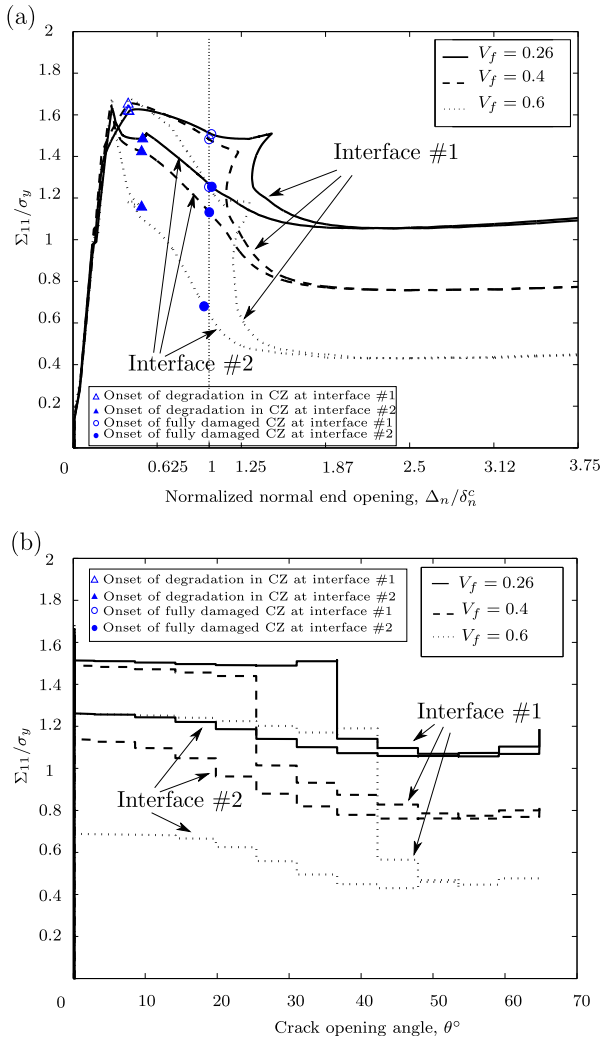

Fig. 13. Effect of the volume fraction, V_f, on a) the normalized normal crack end opening, Δ_n/δ_n^c, and b) the crack opening angle, θ. The interfaces and loading conditions are identical to the reference case, see Fig. 4.

are considered to be the same as the reference case where $V_f = 0.26$. Here, two different cases are considered, one with two perfectly bonded interfaces and another one with two active cohesive zones along the interfaces. As expected, a larger V_f gives stiffer overall response in both cases before debonding. An increase of V_f leads to earlier onset of degradation in cohesive zone and also significantly larger stress-drop is observed. On the other hand, a smaller volume fraction leads to smaller cohesive zones postponing debonding at interface #2 and allows the load carrying capacity to enhance.

Fig. 12 depicts the contours of the normalized von Mises stress, σ_e/σ_y, at different fiber volume fractions, V_f. By increasing V_f the stress is intensified in the region where two crack tips are in the ligament between the fibers (Fig. 12b–c) while in the perfectly bonded case high stresses can be observed at the two opposite corners of the cell (see Fig. 12a). As shown in Fig. 1c, the normal crack end opening, Δ_n, denotes the maximum normal opening of the crack at the interface and the crack opening angle, θ, is the angle from the crack tip to the x_1-direction. Fig. 12 shows that a larger normalized normal crack end opening, Δ_n/δ_n^c, at both interfaces is another effect of increasing the fiber volume fraction. For $V_f = 0.26$ the normalized normal crack end opening is $\Delta_n/\delta_n^c \leq 3$ (Fig. 12b) whereas Δ_n/δ_n^c is ≥ 3 for $V_f = 0.26$ (Fig. 12c–d). On the other hand, the larger crack end opening seen for increasing V_f has the effect of less crack extensions as shown by the crack opening angle, θ. Thus, for $V_f = 0.6$ θ_1 is 53° compared to $\theta_1 = 59°$ for $V_f = 0.26$ and $V_f = 0.4$ and $\theta_2 = 42°$ for $V_f = 0.6$ but 48° and 53° for $V_f = 0.26$ and $V_f = 0.4$, respectively. When the crack tips are in a narrow ligament region of the matrix, as shown in Fig. 12d, the further loading leads to plastic deformation in that region instead of progressive crack growing. This can be seen as weak crack blunting initiation close to the crack tips. Thus, a larger volume fraction in a perfectly bonded case leads to a stronger material. In cases with interface debonding a large volume fraction increases slightly the macroscopic failure stress of the cell but causes larger stress drop during failure which leads to a lower load carrying capacity in the post-failure regime. This is related to the larger interfaces where potential debonding failure can occur.

The effects of fiber volume fraction, V_f, on the normalized normal crack end opening, Δ_n/δ_n^c, and the crack opening angle, θ, are shown in Fig. 13a and b, respectively. As shown in Fig. 13a, the initial crack opening occurs at $\Sigma_{11}/\sigma_y \simeq 0.2$ for all cases. By increasing the loading, the normalized normal crack end opening, Δ_n/δ_n^c, grows up with a linear slope until the point where debonding and plasticity lead to nonlinear behavior on the curve. It is noticeable that for all volume fractions at both interfaces the onset of fully damage occurs at the same normal crack end opening, $\Delta_n/\delta_n^c = 1$, specifying the characteristic cohesive zone opening. After $\Delta_n/\delta_n^c = 2.25$ for $V_f = 0.26$, $\Delta_n/\delta_n^c = 2$ for $V_f = 0.4$ and $\Delta_n/\delta_n^c = 1.75$ for $V_f = 0.6$ in Fig. 13a both interfaces follow the same curve with constant load carrying capacity. In Fig. 13b, after $\theta = 65°$ for all cases the curves no longer progress implying that the cracks no longer propagate which is in agreement with experimental failure observations and numerical studies (París et al., 2007, 2003). París et al. (2007, 2003) studied the mechanisms of failure in a single fiber surrounded by the matrix under transverse tension. Their observation shows that a crack starts running at the interfaces and after a certain angle (between 60° to 70°) the crack kinks into the matrix. The present research focuses on the failure mechanisms before kinking occurs. Fig. 13b shows how the increase of V_f leads to crack initiation at a lower stress level which denotes earlier debonding. In addition, the difference in stresses at crack initiation points between two interfaces increases when V_f is larger. In the case with $V_f = 0.4$, at $\theta = 25°$, in the cases with $V_f = 0.26$ and $V_f = 0.6$ at $\theta = 37°$ a stress drop can be seen at interface #1 denoting the situation, $\lambda = \lambda_2$, until crack initiation, $\lambda = 1$. Fig. 13b also shows that in this period the crack propagation at interface #1 stops. Furthermore, it can be observed that increase of V_f leads to a larger (negative) slope at both interfaces which denotes faster crack growth during debonding.

6. Conclusion

The failure mechanism caused by interfacial debonding in composites has been studied. In the present work, a unit cell including two quarter-circular fibers has been modeled to represent a periodic distribution of fibers embedded in the matrix using generalized plane strain. The matrix was assumed to be an isotropic elasto-plastic material governed by the standard isotropic J_2-plasticity theory, while the fibers were considered as purely elastic. To model the fracture of the fiber–matrix interfaces, a trapezoidal cohesive zone model was used. This study has aimed at considering a more realistic model for composites by including two different fiber–matrix strengths to capture different initiation and propagation of interfacial microcracks and consequently their effects on

the overall response of the structure. It was shown that uneven interfacial strength has a significant influence on the nonlinear behavior of the overall response of the unit cell.

The present study has assumed that the adopted unit cell represents the composite. This has been shown to hold true in linear-elastic and hardening regimes by Gitman et al. (2007), based on a statistical analysis of numerical experiments of random heterogeneous materials. However, in the case of softening materials, they discussed that the RVE may not exist, due to the fact that the material in softening may show localized deformation. Once localization takes place, the deformations inside the localized band become very large without contributing much to the overall deformation of the body (Tvergaard, 1982). This observation indicates, that first the unit cell approach can in general be representative until the maximum load carrying capacity is reached. After onset of failure when softening begins, the unit cell may not be fully representative of the material. However, the unit cell may still be representative of the deformation regions with severe localized deformations.

Generally, the current study shows different crack initiations and propagations at the two interfaces, which result in an overall stress–strain response of the material that often first depict a rather smooth stress drop followed by a second sudden stress drop. Throughout the paper, identical characteristic cohesive distance was considered for both interfaces. It is found that upon decreasing the maximum cohesive stress, $\sigma_{\max}$, increase of the characteristic cohesive distance, $\delta^c = \delta_n^c = \delta_t^c$, and larger dimensional ratio, b/a, lead to more stable crack growth at the interfaces during debonding (see Fig. 9). It was also shown that a delay in onset of degradation in cohesive zone of the interfaces and consequently stronger interfaces can be caused by larger maximum cohesive stress, smaller dimensional ratio, increase of the characteristic cohesive distance or decrease of the fiber volume fraction (see Figs. 7–9 and 11). Furthermore, having identical work of fracture, Φ, in two interfaces with uneven strengths, larger maximum cohesive stress at the stronger interface gives less stable crack growth during debonding and also leads to larger load carrying capacity after debonding. By keeping the fiber volume fraction constant, an increase of the dimensional ratio led to larger normal crack end opening, Δ_n, and opening angle, θ, at both interfaces.

Acknowledgment

This work is supported by the Danish Council for Strategic Research (grant no.: 09-067212) under the Danish Center for Composite Structures and Materials for Wind Turbines.

References

Azizi, R., 2012. Micromechanical modeling of damage in periodic composites using strain gradient plasticity. Engineering Fracture Mechanics 92, 101–113.
Bao, G., Hutchinson, J.W., McMeeking, R.M., 1991. Particle reinforcement of ductile matrices against plastic flow and creep. Acta Metallurgica et Materialia 8, 1871–1882.
Bayat, M., Aghdam, M.M., 2012. A micromechanics-based analysis of effects of square and hexagonal fiber arrays in fibrous composites using DQEM. European Journal of Mechanics – A: Solids 32, 32–40.
Brewer, J., Lagace, P., 1988. Quadratic stress criterion for initiation of delamination. Journal of Composite Materials 22, 1141–1155.
Fang, X.J., Yang, Q.D., Cox, B.N., Zhou, Z.Q., 2011. An augmented cohesive zone element for arbitrary crack coalescence and bifurcation in heterogeneous materials. International Journal for Numerical Methods in Engineering 88, 841–861.
Gitman, I., Askes, H., Sluys, L., 2007. Representative volume: existence and size determination. Engineering Fracture Mechanics 74, 2518–2534.
González, C., Llorca, J., 2007. Mechanical behavior of unidirectional fiber-reinforced polymers under transverse compression: microscopic mechanisms and modeling. Composites Science and Technology 67, 2795–2806.
Hettich, T., Andrea, Hund, Ekkehard, Ramm, 2008. Modeling of failure in composites by X-FEM and level sets within a multiscale framework. Computer Methods in Applied Mechanics and Engineering 197, 414–424.
Hinz, S., Jones, F.R., Schulte, K., 2007. Micromechanical modelling of shear deformation of a 90°-ply in Glare at elevated temperatures. Computational Materials Science 39, 142–148.
Legarth, B.N., 2004. Unit cell debonding analyses for arbitrary orientation of plastic anisotropy. International Journal of Solids and Structures 41, 7267–7285.
Legarth, B.N., Niordson, C.F., 2010. Debonding failure and size effects in micro-reinforced composites. International Journal of Plasticity 26, 149–165.
Ling, D., Yang, Q., Cox, B., 2009. An augmented finite element method for modeling arbitrary discontinuities in composite materials. International Journal of Fracture 156, 53–73.
Maligno, A.R., Warrior, N.A., Long, A.C., 2009. Effects of inter-fibre spacing on damage evolution in unidirectional (UD) fibre-reinforced composites. European Journal of Mechanics – A: Solids 28, 768–776.
Moraleda, J., Segurado, J., Llorca, J., 2009. Effect of interface fracture on the tensile deformation of fiber-reinforced elastomers. International Journal of Solids and Structures 46, 4287–4297.
Needleman, A., Borders, T., Brinson, L., Flores, V., Schadler, L., 2010. Effect of an interphase region on debonding of a CNT reinforced polymer composite. Composites Science and Technology 70, 2207–2215.
Ortiz, M., Pandol, A., 1999. Finite-deformation irreversible cohesive elements for three-dimensional crack-propagation analysis. International Journal for Numerical Methods in Engineering 44, 1267–1282.
París, F., Correa, E., Cañas, J., 2003. Micromechanical view of failure of the matrix in fibrous composite materials. Composites Science and Technology 63, 1041–1052.
París, F., Correa, E., Mantič, V., 2007. Kinking of transversal interface cracks between fiber and matrix. Journal of Applied Mechanics 74, 703–716.
Totry, E., González, C., Llorca, J., 2008a. Prediction of the failure locus of C/PEEK composites under transverse compression and longitudinal shear through computational micromechanics. Composites Science and Technology 68, 3128–3136.
Totry, E., González, C., Llorca, J., 2008b. Failure locus of fiber-reinforced composites under transverse compression and out-of-plane shear. Composites Science and Technology 68, 829–839.
Tvergaard, V., 1976. Effect of thickness inhomogeneities in internally pressurized elastic–plastic spherical shells. Journal of the Mechanics and Physics of Solids 24, 291–304.
Tvergaard, V., 1982. Material failure by void coalescence in localized shear bands. International Journal of Solids and Structures 18, 659–672.
Tvergaard, V., 1990. Effect of fibre debonding in a whisker-reinforced metal. Material Science and Engineering A125, 203–213.
Tvergaard, V., Hutchinson, J.W., 1993. The influence of plasticity on mixed mode interface toughness. Journal of the Mechanics and Physics of Solids 41, 1119–1135.
Tvergaard, V., Legarth, B.N., 2007. Effect of anisotropic plasticity on mixed mode interface crack growth. Engineering Fracture Mechanics 74, 2603–2614.
Xu, X.P., Needleman, A., 1993. Void nucleation by inclusion debonding in a crystal matrix. Modelling and Simulation in Materials Science and Engineering 1, 111–132.
Zhou, F., Molinari, J.F., 2004. Stochastic fracture of ceramics under dynamic tensile loading. International Journal of Solids and Structures 41, 6573–6596.

Publication [P4]

A numerical study of the influence of microvoids in the transverse mechanical response of unidirectional composites

Composites Science and Technology 97 (2014) 46–54

Contents lists available at ScienceDirect

Composites Science and Technology

journal homepage: www.elsevier.com/locate/compscitech

A numerical study of the influence of microvoids in the transverse mechanical response of unidirectional composites

Danial Ashouri Vajari [a,*], Carlos González [b,c], Javier Llorca [b,c], Brian Nyvang Legarth [a]

[a] Department of Mechanical Engineering, Solid Mechanics, Technical University of Denmark, DK-2800 Kgs. Lyngby, Denmark
[b] IMDEA Materials Institute, C/Eric Kandel 2, 28906 Getafe, Madrid, Spain
[c] Department of Materials Science, Polytechnic University of Madrid, 28040 Madrid, Spain

ARTICLE INFO

Article history:
Received 25 March 2014
Received in revised form 31 March 2014
Accepted 5 April 2014
Available online 19 April 2014

Keywords:
C. Computational mechanics
A. Polymer–matrix composites (PMCs)
B. Porosity/Voids
C. Failure criterion

ABSTRACT

The effect of porosity on the transverse mechanical properties of unidirectional fiber-reinforced composites is studied by means of computational micromechanics. The composite behavior is simulated by the finite element analysis of a representative volume element of the composite microstructure in which the random distribution of fibers and the voids are explicitly included. Two types of voids – interfiber voids and matrix voids – were included in the microstructure and the actual damage mechanisms in the composite, namely matrix and interface failure, were accounted for. It was found that porosity (in the range 1–5%) led to a large reduction in the transverse strength and the influence of both types of voids in the onset and propagation of damage throughout the microstructure was studied under transverse tension and compression. Finally, the failure locus of the composite lamina under transverse tension/compression and out-of-plane shear was obtained by means of computational micromechanics and compared with the predictions of Puck's model and with experimental data available in the literature. The results show that the strength of composites is significantly reduced by the presence of voids.

1. Introduction

The combination of stiff glass-fibers embedded in low density polymers leads to a lightweight material with outstanding stiffness, strength and creep resistance. However, composite materials present different physical failure mechanisms as a function of loading conditions. At the microscopic level, failure is controlled by the brittle nature of epoxy matrix, the decohesion of the fiber/matrix interface and the presence of defects (voids, delaminations).

Numerical simulation is becoming a powerful tool to understand the failure processes and subsequently design of composite materials. Within the realm of the micromechanical simulation of the deformation and failure processes, two different strategies have been developed. The first one assumes that the fibers are regularly distributed within the ply, which leads to a simplified unit-cell model including few fibers (normally one or two). For instance, París et al. [1] studied interface debonding by modeling a single-fiber unit cell embedded in polymer matrix. In a similar model, Correa et al. [2] studied the initiation and propagation of an interface crack which subsequently kinks into the matrix. Romanowicz [3] computationally predicted the failure locus of a two-fiber unit-cell using a bi-linear cohesive zone at the fiber/matrix interface and the Drucker–Prager criterion to consider the pressure-dependent yielding of polymers. Although these unit-cell studies provided valuable insights into the micromechanisms of deformation and fracture, their results cannot be extrapolated to predict the behavior of actual composite plies because the regular fiber distribution is not realistic.

The second modeling approach considers an RVE including several dozens of fibers which are randomly distributed in the matrix. The size of the microstructure included in the RVE is large enough so that the effective properties are independent of the RVE size and of the position of fibers. Gonzàlez and Llorca [4] and Totry et al. [5] validated the multi-fiber RVE modeling strategy with experiments to determine the fracture behavior of composite under different loading modes. The matrix in these studies was assumed to follow the Coulomb–Mohr yield criterion. Interface debonding was modeled by a bi-linear cohesive zone model.

Special attention must be given to the role of defects and, in particular, of voids due to their influence on the mechanical performance of composite materials. Voids can be found in different shapes and sizes and there are two principal sources. The first one is air entrapment in the composite (particularly between plies)

* Corresponding author. Tel.: +45 50107641; fax: +45 45931475.
E-mail address: dvaj@mek.dtu.dk (D. Ashouri Vajari).

http://dx.doi.org/10.1016/j.compscitech.2014.04.004
0266-3538/

during lay-up. In addition, voids may be formed by volatile components or contaminants which vaporize during the high-temperature part of the composite cure cycle [6]. Typical voids found in glass-fiber polymer composites used in wind turbines are found in Fig. 1. Fig. 1a shows large voids as compared to the fiber diameter, while Fig. 1b provides a closer view of microvoids whose size is comparable or smaller than the fiber diameter. These microvoids appear normally between the fibers where the matrix cannot easily flow in during manufacturing or they can also be originated due to very small air bubbles being trapped in the matrix. It is well established that porosity reduces the mechanical properties of fiber-reinforced composites controlled by the matrix (interlaminar shear strength, transverse strength as well as modulus, fatigue resistance, etc., see Thomason [6]). Experimental work has been also carried out to assess the effect of voids on the mechanical behavior of composites. Hernández et al. [7] studied the effect of temperature cycle on the void volume fraction, shape and spatial distribution in composites using X-ray microtomography. Regardless of the final porosity, voids were elongated and oriented parallel to the fibers. Detailed studies of the effect of porosity on the transverse mechanical properties of UD laminates are limited. Olivier et al. [8] analyzed the effect of porosity on the transverse tensile strength while several investigations [8–11] studied the influence of void volume fraction on the interlaminar shear strength. Porosity always reduced significantly the shear strength but there were large differences among different materials. This was attributed to the influence of void size, shape and spatial distribution.

Several numerical studies have also been conducted to evaluate the effect of voids in epoxies. Chew et al. [12] and Cheng and Guo [13] studied the void interaction and coalescence in polymers. They showed that microvoid cavitation, enhanced by strain softening, accelerates the process of void coalescence resulting in brittle-like failure at lowered stresses and strains. Moraleda et al. [14] studied the finite deformation of porous elastomers by selecting an RVE containing a random distribution of circular voids. Nevertheless, to the authors' knowledge, the effect of microvoids on the mechanical response of composites has not been simulated within the framework of multi-void/fiber RVEs in which both are randomly distributed in the matrix and this is the main objective of this investigation. The geometrical model provides a realistic representation of the composite microstructure, which explicitly considers the spatial distribution of fibers, matrix, interfaces and voids. This work focuses on the microvoids shown in Fig. 1b whose diameters are small and are found between fibers. The effect of volume fraction, size and position of voids on the overall stress–strain response of UD composites will be analyzed. As a result of these analyses, the failure locus including the effect of porosity will be obtained for UD composites subjected to transverse tension/compression and out-of-plane shear.

2. Problem formulation

Microvoids may be arbitrarily shaped, which requires an expensive full 3D simulation. However, experiments by Little et al. [15] and Hernández et al. [7] have shown that micron-sized voids within composite plies were elongated and oriented along the fiber direction. They found that the void aspect ratio (length/average diameter) was in the range 10–40 and the void aspect ratio increased with the void volume. They have also shown that $\sim 45\%$ of the voids have a diameter less than 50 μm and $\sim 20\%$ of the voids have a diameter below 20 μm [15]. These observations indicate the presence of cylindrical microvoids, which can be modeled in 2D in a similar way as the fibers.

A schematic of the microstructure of UD composites including fibers, matrix and microvoids is depicted in Fig. 2a. The corresponding square cell is shown in Fig. 2b, which includes the distribution of dozens of circular fibers, circular microvoids and microvoids isolated between the fibers. Obviously, this 2D representation considers that all voids and fibers are cylindrical. A Cartesian reference coordinate system, x_i, is placed at the bottom-left corner of the cell and aligned with its edges (Fig. 2b). The positive direction of the first axis, x_1, points in the out-of-plane normal direction to the (x_2, x_3)-plane. The dimension of the cell is determined by the length, L , the width, W, the radius of the N_f monosized fibers, R_f, which yields the fiber volume fraction $V_f = N_f \pi R_f^2 / WL$. The total void volume fraction, V_v, is the sum of the void volume fraction of the N_v circular voids of radius R_v^i, $\sum_{i=1}^{N_v} \pi {R_v^i}^2 / WL$, plus the void volume fraction due to the trapped voids isolated between the fibers (four shown in Fig. 2b). The cell in these analyses is always a square cell with $L = W = L_0$. The cell is subjected to incremental normal tension or compression in the transverse direction by imposing $\dot{\Delta}_3$ as well as to out-of-plane incremental shear specified by $\dot{\Delta}_{23}$, as shown in Fig. 2b.

The cell contains a random distribution of 70 monosized fibers of radius $R_f = 0.1 L_0$ leading to the fiber volume fraction of $\sim 60\%$ and void volume fraction of 1—5%, which are realistic values for composites of good quality. The nearest fiber distance is set to a minimum value to avoid fiber overlap during the generation of the RVE. The majority of this porosity is in voids trapped between fibers and the rest are isolated voids dispersed in the matrix. Fibers and voids intersecting the cell edges were split and copied to the opposite sides of the square cell to create a periodic microstructure. Periodic boundary conditions were applied to the edges of the cell to ensure the continuity between neighboring cells (which may deform like jigsaw puzzles). The periodic boundary conditions can be expressed in terms of the prescribed displacement vectors $\vec{U}_2$ and $\vec{U}_3$ which relate the displacements, $\vec{u}$, between opposite edges according to

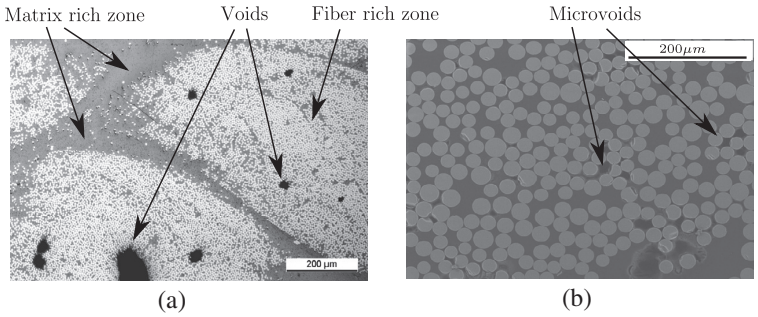

Fig. 1. Shape and size of voids in composites used in wind turbine blades. (a) Large voids, as compared to the fiber diameter. (b) Position and shape of microvoids whose size is comparable or smaller than the fiber diameter.

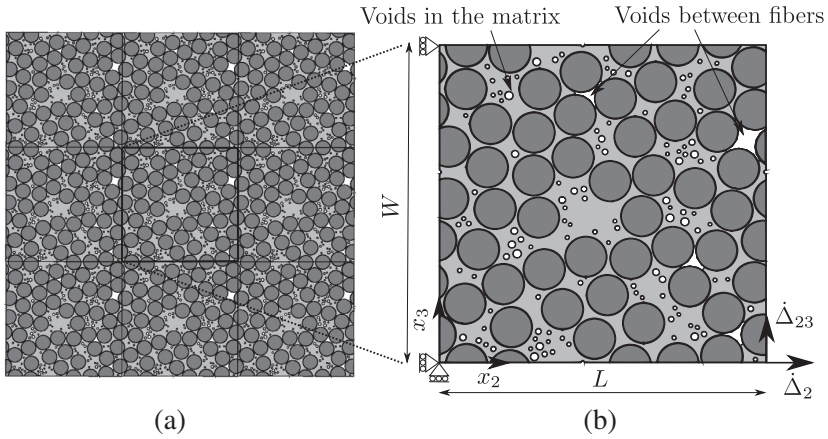

Fig. 2. (a) Illustration of the fiber and void distribution in a cross-section of a fiber-reinforced composite. (b) Unit cell of the porous fiber-reinforced composites. The dimensions, loads and the coordinate system are shown. The cell can be subjected to transverse tension/compression by applying $\dot{\Delta}_2$ and out-of-plane shear by applying $\dot{\Delta}_{23}$.

$$\begin{aligned}\vec{u}(0,x_3)-\vec{u}(L_0,x_3)&=\vec{U}_2\\ \vec{u}(x_2,0)-\vec{u}(x_2,L_0)&=\vec{U}_3\end{aligned} \tag{1}$$

Combined uniaxial tension/compression along the x_2-axis and out-of-plane shear are imposed with $\vec{U}_2=(\Delta_2,\Delta_{23})$ and $\vec{U}_3=(u_2,u_3)$, where Δ_2 denotes the compression or tension load depending on the sign of Δ_2 and Δ_{23} defined the shear deformation. While the component of u_2 is determined from the condition of mechanical equilibrium, u_3 is computed so that the average normal stresses perpendicular to the tension/compression axis (x_2) is zero. The incremental tensile/compressive and shear strains are given by

$$\dot{\epsilon}_2=\frac{\dot{\Delta}_2}{L_0}\quad\text{and}\quad\dot{\gamma}_{23}=\arctan\left(\frac{\dot{\Delta}_{23}}{L_0}\right) \tag{2}$$

The corresponding normal and shear stresses are computed from the resultant normal and tangential forces acting on the edges divided by the actual cross-section, A, as

$$\sigma_2=\frac{1}{A}\int T_2 t dx_3\Big|_{x_2=L_0}\quad\text{and}\quad\tau_{23}=\frac{1}{A}\int T_3 t dx_3\Big|_{x_2=L_0} \tag{3}$$

where t is the unit thickness of the cell in the x_1-direction and T_2 and T_3 denote the normal and shear traction at the edge $x_2=L_0$, respectively.

3. Material model

3.1. Isotropic modified Drucker–Prager model

The matrix behavior corresponds to an isotropic epoxy resin and fails at a very low strain in a brittle fashion under uniaxial tension [16]. Under uniaxial compression or shear, epoxy resins undergo considerable plastic deformation and the flow stress is pressure-dependent [16–18]. The Drucker–Prager yield criterion has often been used to model the mechanical behavior of these materials. As illustrated in Fig. 3, this model is a modification of the von Mises criterion with different tensile and compressive yield stress (shown as a dashed-line in Fig. 3). In addition, the Drucker–Prager yield criterion includes the effect of hydrostatic stresses on the flow stress by including an additional term in the von Mises expression, according to

$$F(I_1,J_2)=\sqrt{3J_2}+\alpha I_1-c=0 \tag{4}$$

where I_1 is the first invariant of the stress tensor, J_2 is the second invariant of the deviatoric stress tensor and c is the flow stress under pure shear. The pressure-sensitivity parameter, α, can be determined by Lubliner et al. [19]

$$\alpha=\frac{\frac{\sigma_m^{b0}}{\sigma_m^{c0}}-1}{2\frac{\sigma_m^{c0}}{\sigma_m^{t0}}-1} \tag{5}$$

Here, σ_m^{c0}, σ_m^{b0} and σ_m^{t0} denote the matrix uniaxial compressive yield stress, the biaxial compressive yield stress and the uniaxial tensile yield stress, respectively, see Fig. 3. In order to include the brittle behavior of the epoxy matrix in tension, the modified Drucker–Prager model developed by Lubliner et al. [19] and Lee and Fenves [20] was used in this investigation to simulate the matrix behavior. It is expressed by

$$F(I_1,J_2,\sigma_l,\beta,\alpha)=\frac{1}{1-\alpha}\left(\sqrt{3J_2}+\alpha I_1+\beta\langle\sigma_l\rangle\right)-\sigma_m^{c0}=0 \tag{6}$$

where σ_l is the maximum principal stress, $\langle\rangle$ denotes the Macaulay brackets (which return the argument if positive and zero otherwise), and β is a function of the tensile, σ_m^{t0}, and compressive, σ_m^{c0}, yield stress according to

$$\beta=\frac{\sigma_m^{c0}}{\sigma_m^{t0}}(1-\alpha)-(1+\alpha) \tag{7}$$

The yield surface corresponding to the modified Drucker–Prager criterion is depicted in Fig. 3. It follows the standard Drucker–Prager yield criterion with an associated flow rule under compression, which has been experimentally validated for glassy polymers [17]. Chew et al. [12] and Quinson et al. [17] discussed that the pressure-sensitivity reduces the load-carrying capacity and influences the strain for void coalescence, and also showed that plastic dilatancy effects are relatively milder. Thus, for the sake of simplicity, an associated flow rule is considered to simulate the plastic flow of the matrix. The epoxy behavior in tension was controlled by the maximum principal stress and the yield surface was cut off by the tensile yield stress, σ_m^{t0}, as shown with the straight dashed lines in Fig. 3.

The stress–strain behavior of the matrix under uniaxial compression and uniaxial tension is shown in Fig. 4. Plastic deformation at constant flow stress occurred in compression after yielding, leading to failure by the localization of a shear band. In Fig. 4, σ_m^{cu} denotes the matrix ultimate compressive strength. Conversely, the behavior in tension was brittle due to microcracking and this is accounted for by a softening law [21]. The energy dissipated by a unit volume during tensile cracking is G_m which is the area under the tensile stress–strain curve for $\epsilon_m>0$. Residual

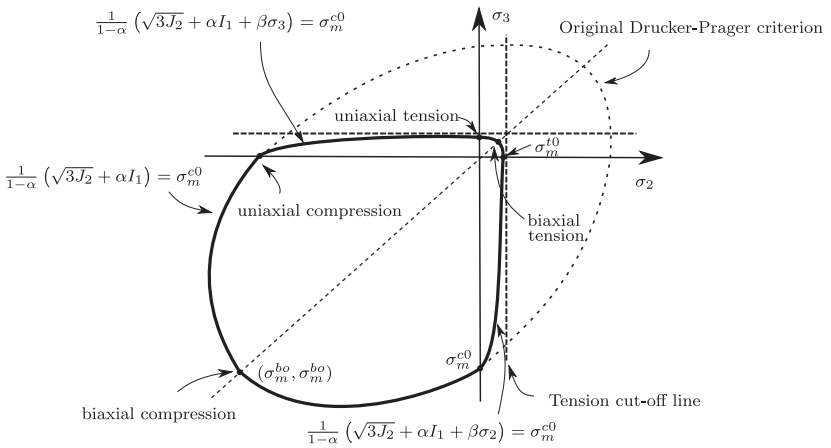

Fig. 3. Yield surface of the modified Drucker–Prager criterion. The dashed-line denotes the original Drucker–Prager criterion.

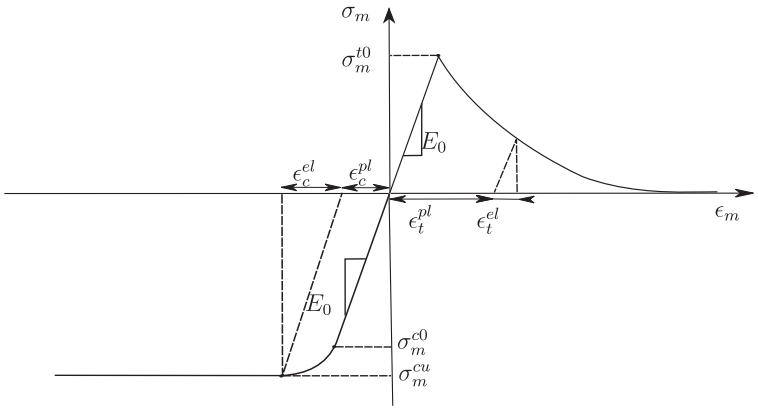

Fig. 4. Stress–strain behavior of the matrix under uniaxial tension and uniaxial compression.

stresses due to chemical cure shrinkage and cooling from processing temperature were not taken into account, as this investigation was focussed in the effect of porosity.

Glass-fibers were modeled as isotropic, elastic materials whereas the matrix properties correspond to typical values used in the modified Drucker–Prager model for an epoxy matrix [21]. The pressure-sensitivity parameter was chosen to be $\alpha = 0.13$ which is within the range reported by Quinson et al. [17] and Chew et al. [12].

3.2. Cohesive zone model

The fiber/matrix interface was modeled using a cohesive zone model, which relates the normal and tangential stresses transferred through the crack with the normal and tangential crack opening [22]. In this model, λ is defined as a non-dimensional parameter describing the separation between the crack faces as

$$\lambda = \sqrt{\left(\frac{u_n}{\delta_n^c}\right)^2 + \left(\frac{u_t}{\delta_t^c}\right)^2} \tag{8}$$

such that damage initiation starts at a specified value, $\lambda = \lambda_2$, and fully damage occurs when $\lambda \geqslant 1$. δ_n^c and δ_t^c stand for the normal and tangential characteristic cohesive lengths, respectively, and u_n and u_t are the normal and tangential separation between the crack faces, respectively. As shown in Fig. 5, $\sigma(\lambda)$ defines a traction potential as

$$G_{int} = \delta_n^c \int_0^{\lambda} \sigma(\lambda) d\lambda \tag{9}$$

where the area under $\sigma(\lambda)$ represents the fracture energy, G_{int}. Therefore, the normal, T_n, and tangential, T_t, tractions acting on the interfaces are defined from Eq. (9) as

$$T_n = \frac{\partial G_{int}}{\partial u_n} = \frac{\sigma(\lambda)}{\lambda}\frac{u_n}{\delta_n^c}, \qquad T_t = \frac{\partial G_{int}}{\partial u_t} = \frac{\sigma(\lambda)}{\lambda}\frac{\delta_n^c}{\delta_t^c}\frac{u_t}{\delta_t^c} \tag{10}$$

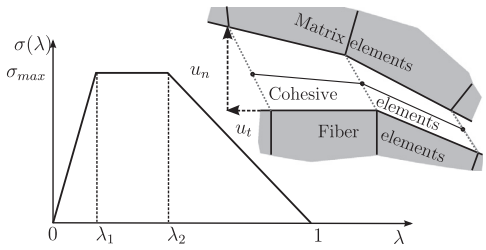

Fig. 5. Traction–separation law used to characterize interface separation.

The incremental traction vector is related to the displacement increments across the interface as

$$\begin{bmatrix} \dot{T}_t \\ \dot{T}_n \end{bmatrix} = \begin{bmatrix} \frac{\partial T_t}{\partial u_t} & \frac{\partial T_t}{\partial u_n} \\ \frac{\partial T_n}{\partial u_t} & \frac{\partial T_n}{\partial u_n} \end{bmatrix} \begin{bmatrix} \dot{u}_t \\ \dot{u}_n \end{bmatrix} \tag{11}$$

where the matrix on the right hand side is the cohesive tangent modulus.

The interface behavior is controlled by the cohesive strength, σ_{max}, and the interface fracture energy, G_{int}. The cohesive strength was chosen to be equal to 50 MPa, following the experimental results obtained by Canal et al. [21]. The interface fracture energy was $G_{int} = 10\,\mathrm{J/m^2}$, one tenth of the matrix fracture energy, $G_m = 100\,\mathrm{J/m^2}$. As the interface fracture energy is given by the area under the cohesive traction–separation law, it follows

$$G_{int} = \frac{\sigma_{max}(1 + \lambda_2 - \lambda_1)\delta_n^c}{2} \tag{12}$$

where $\lambda_1 = 10^{-3}$ and $\lambda_2 = 10^{-1}$. Substituting σ_{max}, G_{int}, λ_1 and λ_2 into Eq. (12) yields $\delta_n^c = \delta_t^c \simeq 0.4\,\mu\mathrm{m}$.

4. Numerical methods

Simulations are carried out with Abaqus/Standard [23] under plane strain conditions within the framework of the finite deformations theory with the initial unstressed state as reference. The matrix and the fibers were automatically meshed using 3-node isoparametric triangles. An example of finite element mesh is shown in Fig. 6. In addition, 4-node interface elements were inserted at the fiber/matrix interface to include the effect of interface decohesion. The converged finite element discretization includes around 48,000 solid elements, 3350 cohesive elements and 56,000 nodes. Totry et al. [5] discussed that different arrangement of fibers in an RVE including 30 fibers with interface debonding under uniaxial compression shows up to 7% deviation in the ultimate failure stress. This scatter can be even larger when the RVE includes voids. This work does not aim at studying an RVE which macroscopically represents the lamina but focuses on the effect of voids randomly distributed in the matrix.

5. Results and discussion

5.1. Influence of porosity on the failure mechanisms

The matrix properties, as a typical thermosetting epoxy, are $E_m = 3$ GPa, $\nu_m = 0.3$, $\sigma_m^{c0} = 85$ MPa, $\sigma_m^{cu} = 95$ MPa, $\sigma_m^{t0} = 65$ MPa, $\alpha = 0.13$ and $G_m = 100\,\mathrm{J/m^2}$ and the material properties of the glass fibers are $E_f = 70$ GPa and $\nu_f = 0.21$. While the cohesive parameters are assumed to be $\delta_n^c = \delta_t^c = 0.4\,\mu$m, $\sigma_{max} = 50$ MPa and $G_{int} = 10\,\mathrm{J/m^2}$. These material parameters are unchanged throughout the paper.

Fig. 7a shows the macroscopic stress–strain under transverse tension for an RVE containing a fiber volume fraction V_f = 60% and void volume fraction V_v = 2%. The initial elastic response is followed by a non-linear hardening region up to a maximum (point A in Fig. 7a). Afterwards, the load bearing capacity is rapidly reduced as a result of unstable crack growth in the fiber/matrix interfaces along the RVE. The damage sequence within the RVE is shown in Fig. 7d for the points A, B, and C, respectively, in the stress–strain curve. These plots show that the first damage mechanism, responsible for the non-linearity above 25 MPa and for the maximum strength, was interface decohesion. Interface cracks initiated around voids trapped between fibers (Fig. 7b). The composite strength was ≈ 37 MPa, below the matrix strength in tension (σ_m^{t0} = 65 MPa) and the interface strength (σ_{max} = 50 MPa), and this was due to the presence of the voids, that triggered the onset of interface decohesion at lower stresses. Damage propagated by the successive fracture of interfaces (Fig. 7c) and the crack path was also influenced by the location of interfiber voids. Load was carried by the matrix ligaments between decohered interfaces in the last stages of deformation (Fig. 7d), and final fracture occurred by the link up of interface cracks through the epoxy resin. This series of events is in excellent agreement with recent *in situ* fracture tests under transverse tension carried out within a scanning electron microscope, which showed the same sequence of damage [21].

The influence of the size of the circular voids within the matrix on the stress–strain response under transverse tension is plotted in Fig. 8a, which includes the curves corresponding to the composite without voids and the composite with a void volume fraction V_v = 1.5%. The fiber volume fraction (60%) and the fiber spatial distribution was identical in all cases. As in the previous case, two types of voids were placed in the composite: voids trapped

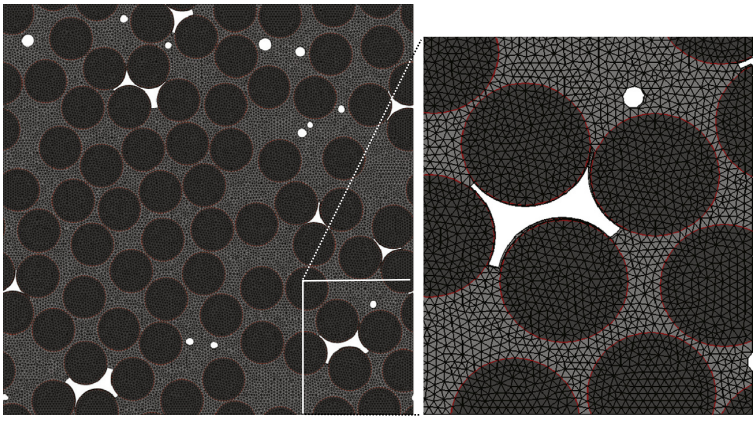

Fig. 6. Finite element mesh of the cell. The mesh includes around 48,000 solid elements, 3350 cohesive elements and 56,000 nodes. The red line between the fibers and the matrix denotes the cohesive elements. (For interpretation of the references to colour in this figure legend, the reader is referred to the web version of this article.)

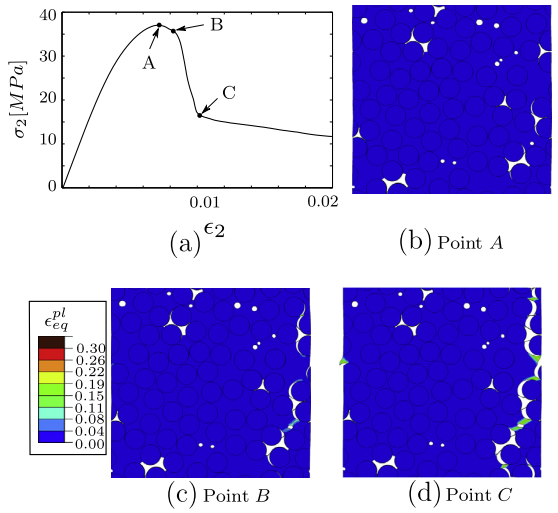

Fig. 7. (a) Stress–strain response under transverse tension of an RVE containing $V_f = 60\%$ and $V_v = 2\%$. Contour plot of the equivalent plastic strain within the RVE for: (b) Point A in the stress–strain curve. (c) Point B in the stress–strain curve. (d) Point C in the stress–strain curve. The displacements are magnified by a factor of 3 in the contour plots.

between fibers and circular isolated voids dispersed in the matrix. While the size and distribution of the interfiber voids were the same in all RVEs, different values of the average radius of the circular voids, $\bar{R}_v = 0.2R_f$, $0.3R_f$ and $0.4R_f$, were chosen for each RVE. The void-free material presented the highest strength, which was close to the interface strength (50 MPa), indicating that interface fracture controlled the maximum bearing capacity of the composite under transverse tension. The analysis of the failure micromechanisms close to the peak load ($\epsilon_2 = 0.9\%$) showed that interface decohesion perpendicular to the tensile stress was the dominant fracture mode Fig. 8b.

The presence of 1.5% porosity reduced the composite strength by ≈20% but the size of the circular voids within the matrix did not influence the transverse tensile strength (Fig. 8a). There were, however, significant changes in the post-peak behavior because the damage localization path changed with the void size, as shown in the contour plots of the equivalent plastic strain depicted in Fig. 8e. While the initial damage (and, thus, the strength) was always controlled by the interfiber voids, the final crack path depended on the circular void size. Large voids can change the path of cracks (Fig. 8e) while the crack path was insensitive to the presence of small voids (Fig. 8c). This effect of the void size (or void distribution) on the post-peak behavior is equivalent to the influence of the fiber spatial distribution because the final damage localization path is very sensitive to the microstructural details (fiber and void spatial distribution and size) of the RVE.

The effect of porosity and of the void size on the mechanical response under transverse compression is shown in Fig. 9a. The RVE corresponding to the four stress–strain curves are identical to those used to compute the mechanical behavior under transverse tension in Fig. 8. The numerical simulations showed that the presence of 1.5% of voids reduced the compressive strength only by ≈14%, as compared with a reduction of ≈20% under transverse tension. These differences can be attributed to the change in the failure mechanisms which control fracture upon tension or compression. Failure under transverse compression takes place by the localization of the plastic strain in the matrix, which leads to the formation of a shear band (Fig. 9b). The angle between the shear band and the direction perpendicular to the loading axis was slightly higher than 45° (in the range of 50–56°) and this was attributed to the pressure sensitivity of matrix yield strength [4]. The contour plots of the void-free and porous RVEs after the peak load are depicted in Fig. 9b–e and demonstrate that the presence of voids did not change the dominant failure mechanism. In addition, the orientation of the shear band was around 55°, within the expected range for fully-dense composites. More detailed analysis of these plots show that the localization band started at interfiber voids, which acted as stress concentrators, and were again responsible for the reduction in strength. The final localization path was controlled by the pressure sensitivity of the matrix and also by the presence of the circular voids in the matrix, which attracted the shear band. This effect of the circular voids seemed

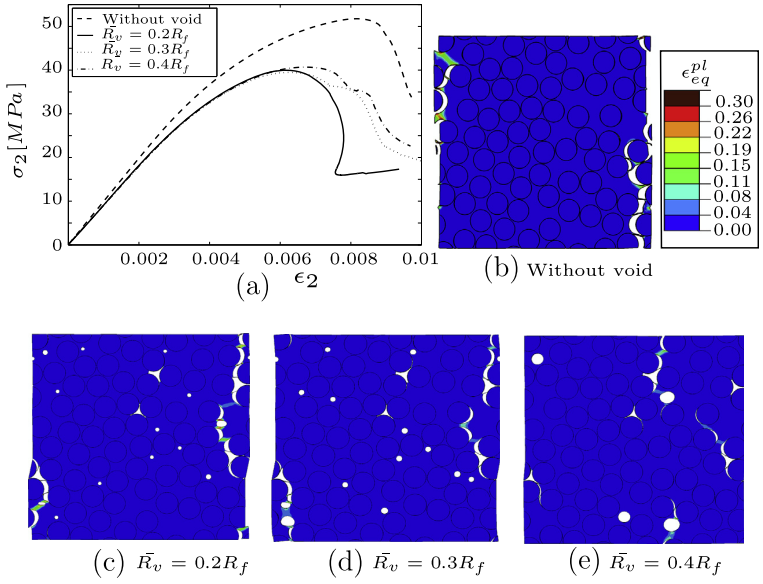

Fig. 8. Effect of void size on the mechanical behavior under transverse tension of an RVE containing $V_f = 60\%$ and $V_v = 1.5\%$. (a) Stress–strain response. Contours plots of the equivalent plastic strain at $\epsilon_2 = 0.009$ in the RVE for: (b) Void-free material. (c) Porous material with an average radius of the circular voids $\overline{R_v} = 0.2R_f$, (d) $\overline{R_v} = 0.3R_f$ and (e) $\overline{R_v} = 0.4R_f$. The displacements are magnified by a factor of 3 in the contour plots.

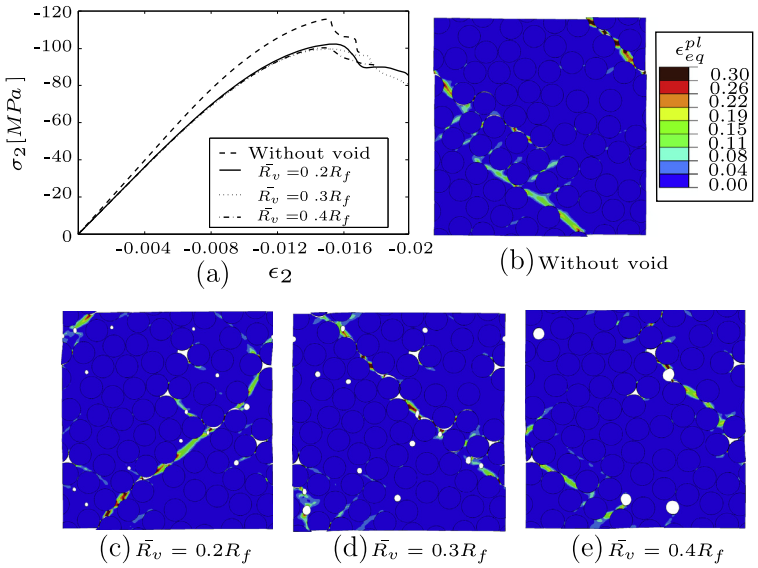

Fig. 9. Effect of void size on the mechanical behavior under transverse compression of an RVE containing $V_f = 60\%$ and $V_v = 1.5\%$. (a) Stress–strain response. Contours plots of the equivalent plastic strain at $\epsilon_2 = -0.016$ in the RVE for: (b) Void-free material. (c) Porous material with an average radius of the circular voids $\overline{R_v} = 0.2R_f$, (d) $\overline{R_v} = 0.3R_f$ and (e) $\overline{R_v} = 0.4R_f$. The displacements are magnified by a factor of 3 in the contour plots.

to increase with the void size, as it happened under transverse tension.

The overall effect of the void volume fraction in the mechanical behavior under transverse tension and compression can be found in the stress–strain curves plotted in Fig. 10a and b, respectively. The curves in these plots were obtained in an RVE containing a fiber volume fraction of 60% and porosity levels in the range 0–5%. The proportion of interfiber voids was 0.7%, 1.5% and 2.5% in the RVEs with V_v = 1%, 2% and 5%, respectively and the remaining were the circular voids embedded in the matrix. This porosity range was selected because composite materials for aerospace require porosity levels below 1–2% while porosity of up to 5% can be tolerated in other applications [24]. In both cases (tension and compression), porosity reduced the composite strength. No experimental results on the effect of porosity on the transverse compressive strength were found in the literature. Olivier et al. [8] has detailed information about the influence of porosity on the transverse tensile strength of UD composites. The experimental data in that paper reported that the transverse tensile strength was reduced by approximately 7% and 20% in the presence of 5% of porosity in two different carbon-fiber/epoxy composites with 60% fiber volume fraction. The numerical predictions in Fig. 10a for 5% porosity were slightly higher (around 30%). Moreover, the numerical study highlighted different influences of voids under transverse tension and compression. On the former events, small amounts of porosity (1%) reduced markedly the transverse tensile strength and increasing the void volume fraction up to 5% did not have very negative effects on the strength. This behavior was a result of the dominant failure mechanism, brittle interface decohesion. Interfiber voids were very efficient to promote interface decohesion at low stresses and the stress concentration at the crack tip propagated damage rapidly through the microstructure. Only one or two voids are necessary to trigger this process and increasing the void volume fraction did not reduce much further the tensile strength. The formation of a shear band through the matrix is, however, a ductile process and the maximum bearing capacity of the composite is not only controlled by the initiation of the shear band but by the propagation throughout the microstructure. This latter process is easier in the presence of larger porosity and thus the transverse compressive strength decreased rapidly with the void volume fraction.

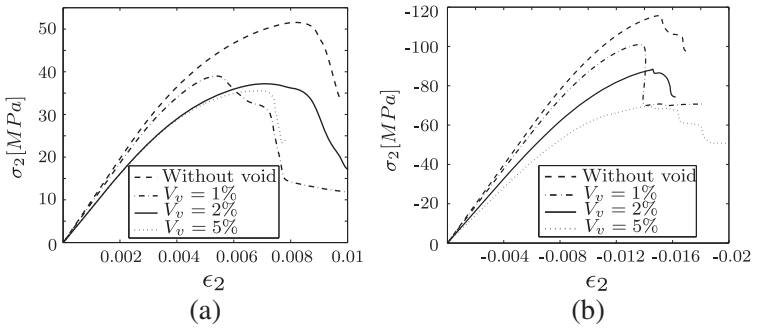

Fig. 10. Effect of void volume fraction on the mechanical behavior of UD fiber-reinforced composites. (a) Transverse tension. (b) Transverse compression.

5.2. Influence of porosity on the failure envelope

Laminate design is based on failure criteria in the stress space which are formed by the intersection of various smooth surfaces, each one representing the critical condition for a given fracture mode. There are different classical failure criteria such as Tsai–Hill, Tsai–Wu, the recently developed NU theory [25] and Puck's criterion all to be used in composite design. Puck's criterion has been largely consistent with the experimental results of the failure envelope of a composite made up of a brittle epoxy matrix reinforced with either glass or C fibers [26] as well as with the numerical results obtained for these composites using computational micromechanics [5]. Puck's criterion is based on the Hashin's failure criterion [27], who distinguished between fiber- and matrix-dominated fracture, and each one was further subdivided into tensile and compressive modes. Furthermore, he assumed that failure was due to the normal and tangential stresses acting on the fracture plane, which is parallel to the fibers in the case of matrix-dominated failure in tension. Puck and Schürmann [18] improved Hashin's model by assuming that failure was caused by the normal, σ_n, and tangential, τ_t, stresses acting on the failure plane, which forms a fracture angle, θ_f, with the direction perpendicular to the tensile stresses. The fracture angle was explicitly determined for each combination of normal, σ_2, and shear, τ_{23}, stresses acting on the lamina. The fracture angle under compression is predicted to be 50°. Puck's failure criterion is then expressed as

$$\sqrt{\left[\left(\frac{1}{Y_T}-\frac{2p_{\perp\perp}(1+p_{\perp\perp})}{Y_C}\right)\sigma_n(\theta_f)\right]^2+\left[\frac{2(1+p_{\perp\perp})}{Y_C}\tau_t(\theta_f)\right]^2}+\frac{2p_{\perp\perp}(1+p_{\perp\perp})}{Y_C}\sigma_n(\theta_f)=1 \quad \text{for} \quad \sigma_n \geqslant 0 \tag{13}$$

$$\sqrt{\left[\frac{2(1+p_{\perp\perp})}{Y_C}\tau_t(\theta_f)\right]^2+\left[\frac{2p_{\perp\perp}(1+p_{\perp\perp})}{Y_C}\sigma_n(\theta_f)\right]^2}+\frac{2p_{\perp\perp}(1+p_{\perp\perp})}{Y_C}\sigma_n(\theta_f)=1 \quad \text{for} \quad \sigma_n < 0 \tag{14}$$

with

$$\begin{aligned}\sigma_n(\theta_f) &= \sigma_2\cos^2\theta_f+2\tau_{23}\sin\theta_f\cos\theta_f\\ \tau_t(\theta_f) &= -\sigma_2\sin\theta_f\cos\theta_f+\tau_{23}\left(\cos^2\theta_f-\sin^2\theta_f\right)\end{aligned} \tag{15}$$

where Y_T and Y_C stand for the transverse tensile and compressive strength of composite, respectively. θ_f denotes the fracture plane orientation under transverse compression, which is always 0° under transverse tension. The inclination coefficient, $p_{\perp\perp}$, is a fitting parameter in the range of 0.20—0.25 for glass-fiber/epoxy composites [18]. Puck's model is controlled by the tensile and the compressive transverse strength. This information for composite with different void volume fraction can be obtained from the numerical simulation, as shown in the previous section.

The failure locus in σ_2–τ_{23} stress space is plotted in Fig. 11 for a composite lamina containing 60% of glass fibers and different porosities (no voids and V_v = 1%, 2% and 5% of which the proportion of interfiber voids was 0.7%, 1.5% and 2.5%, respectively and the remaining were circular voids embedded in the matrix). The predictions of Puck's model with $p_{\perp\perp} = 0.22$ can be compared in Fig. 11 with solid points provided by computational micromechanics. They were obtained by the numerical simulation of an RVE subjected to a different loading paths characterized by different ratios of the normal to the shear displacement, Δ_2/Δ_{23} while $\sigma_3 = 0$. The strength under biaxial loading (transverse tension or compression and out-of-plane shear) was determined by the point at which one (or often both) normal and shear stresses began to decrease as the normal and shear displacements increase.

In addition to Fig. 10 which indicated the effect of porosity in reduction of transverse tension and compression, Fig. 11 also shows the large influence of porosity on the transverse shear strength of UD fiber-reinforced composites. Several authors reported experimental results on the influence of porosity on the shear strength of UD fiber-reinforced composites [8–11]. The composites were reinforced with either glass or carbon fibers and with similar fiber volume fraction to our RVE. The experimental reduction in the shear strength for a porosity of 5% was in the range 15–40%, which is in good agreement with the numerical predictions in Fig. 11 which shows 35% reduction for V_v = 5%. Again, the experimental scatter seems to be controlled by the size, shape and spatial distribution of voids and the present numerical strategy seems to be a promising tool to capture the effect of these factors.

The predictions of the Puck's model (based on the computationally provided values of the strength under transverse tension and compression) were in very good agreement with the results provided by computational micromechanics. This comparison supports the validity of the computational model to predict different physical failure mechanisms occurring in UD laminates and the shape of the failure envelope for the combined transverse normal and shear loading conditions. This agreement indicates that the dominant damage mechanisms are not modified although porosity reduced the strength of composites by triggering damage at lower stresses. However, it should be noted that the available failure criteria (such as Puck's model) cannot explicitly predict the strength reduction due to porosity as they need experimental data (strength in tension and compression of the porous composite) as input. On the contrary, micromechanics simulations are able to determine

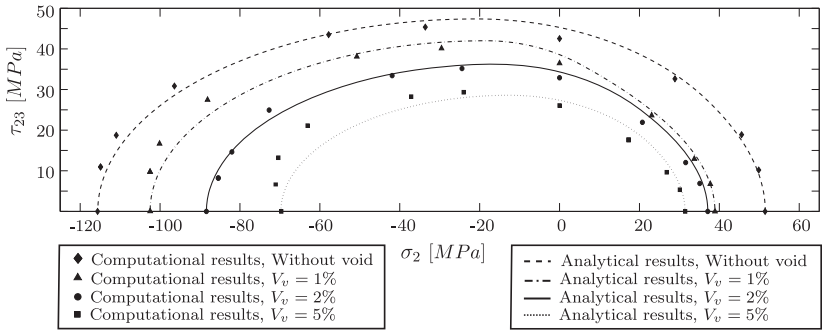

Fig. 11. Failure locus of a UD fiber-reinforced composite in the σ_2–τ_{23} stress space as function of porosity. The lines correspond to the predictions of the Puck's model [18]. The solid symbols stand for the numerical predictions obtained from the numerical simulation of an RVE of the microstructure.

the failure locus based on the microstructural features (e.g., the fiber, matrix and interface properties, and the shape, size and location of fibers and voids).

6. Conclusion

The influence of the porosity on the transverse mechanical response of UD fiber-reinforced composites was analyzed by means of computational micromechanics. To this end, an RVE of the composite microstructure with different void volume fractions was generated and the mechanical behavior was simulated using the finite element method. Two different population of voids were explicitly represented in the RVE of the microstructure: Interfiber voids and circular voids within the matrix. The fiber behavior was elastic and isotropic while the matrix was an elasto-plastic solid following the modified Drucker–Prager yield surface proposed by Lubliner [19]. Brittle matrix failure in tension and fiber/matrix interfacial debonding were accounted for.

Porosity reduced markedly the strength of composite under transverse tension and compression although it did not modify the dominant failure mechanisms. Failure under tension was controlled by interface decohesion while in compression it was dominated by the localized plastic shear band throughout the matrix. In both cases, interfiber voids acted as stress concentrators which triggered the onset of failure at lower stresses. Circular voids in the matrix affected the localization path throughout the microstructure.

The model was also used to determine numerically the failure envelope in the σ_2–τ_{23} stress space of composite containing V_v = 0%, 1%, 2% and 5%. They were in good agreement with the predictions of Puck's model (based on the transverse tensile and compressive strength provided by the computational micromechanics). This supports the validity of the computational model to predict different failure mechanisms based on the microstructural features.

Acknowledgments

The authors would like to thank Prof. Bent F. Sørensen and Dr. L.P. Canal for their ideas and comments and Mr. T. Løgstrup Andersen for providing Fig. 1. This work was supported by the Danish Council for Strategic Research (Grant No.: 09-067212) under the Danish Center for Composite Structures and Materials for Wind Turbines (DCCSM) and by the Spanish Ministry of Economy and Competitiveness under Grant MAT2012-37552.

References

[1] París F, Correa E, Cañas J. Micromechanical view of failure of the matrix in fibrous composite materials. Compos Sci Technol 2003;63:1041–52.
[2] Correa E, Mantič V, París F. A micromechanical view of inter-fibre failure of composite materials under compression transverse to the fibres. Compos Sci Technol 2008;68:2010–21.
[3] Romanowicz M. A numerical approach for predicting the failure locus of fiber reinforced composites under combined transverse compression and axial tension. Comput Mater Sci 2012;51:7–12.
[4] González C, Llorca J. Mechanical behavior of unidirectional fiber-reinforced polymers under transverse compression: microscopic mechanisms and modeling. Compos Sci Technol 2007;67:2795–806.
[5] Totry E, González C, Llorca J. Failure locus of fiber-reinforced composites under transverse compression and out-of-plane shear. Compos Sci Technol 2008;68:829–39.
[6] Thomason JL. The interface region in glass fibre-reinforced epoxy resin composites: 2. Water absorption, voids and the interface. Composites 1995;26:477–85.
[7] Hernández S, Sket F, Molina-Aldareguía JM, González C, Llorca J. Effect of curing cycle on void distribution and interlaminar shear strength in polymer–matrix composites. Compos Sci Technol 2011;71:1331–41.
[8] Olivier P, Cottu JP, Ferret B. Effects of cure cycle pressure and voids on some mechanical properties of carbon/epoxy laminates. Composites 1995;26:509–15.
[9] Jeong H. Effects of voids on the mechanical strength and ultrasonic attenuation of laminated composites. J Compos Mater 1997;31:276–92.
[10] Costa ML, Rezende MC, Almeida SFM. Strength of hygrothermally conditioned polymer composites with voids. J Compos Mater 2005;39:1943–61.
[11] Zhang AY, Li DH, Zhang DX, Lu HB, Xiao HY, Jia J. Qualitative separation of the effect of voids on the static mechanical properties of hygrothermally conditioned carbon/epoxy composites. eXPRESS Poly Lett 2005;5:708–16.
[12] Chew HB, Guo TF, Cheng L. Effects of pressure-sensitivity and plastic dilatancy on void growth and interaction. Int J Solids Struct 2006;43:6380–97.
[13] Cheng L, Guo TF. Void interaction and coalescence in polymeric materials. Int J Solids Struct 2007;44:1787–808.
[14] Moraleda J, Segurado J, Llorca J. Finite deformation of porous elastomers: a computational micromechanics approach. Philos Mag 2007;87:5607–27.
[15] Little JE, Yuan X, Jones MI. Characterisation of voids in fibre reinforced composite materials. NDT & E Int 2012;46:122–7.
[16] Kinloch AJ, Young RJ. Fracture behaviour of polymers. Elsevier Applied Science Publishers; 1983.
[17] Quinson R, Perez J, Rink M, Pavan A. Yield criteria for amorphous glassy polymers. J Mater Sci 1997;32:1371–9.
[18] Puck A, Schürmann H. Failure analysis of FRP laminates by means of physically based phenomenological models. Compos Sci Technol 2002;62:1633–62.
[19] Lubliner J, Oliver J, Oller S, Oñate E. A plastic-damage model for concrete. Int J Solids Struct 1989;25:299–329.
[20] Lee J, Fenves GL. Plastic-damage for cyclic loading of concrete structures. J Eng Mech 1998;124:892–900.
[21] Canal LP, González C, Segurado J, Llorca J. Intraply fracture of fiber-reinforced composites: microscopic mechanisms and modeling. Compos Sci Technol 2012;72:1223–32.
[22] Tvergaard V, Hutchinson JW. The influence of plasticity on mixed mode interface toughness. J Mech Phys Solids 1993;41:1119–35.
[23] Abaqus. Analysis user's manual, version 6.12. Simulia; 2012.
[24] Ghiorse SR. Effect of void content on the mechanical properties of carbon/epoxy laminates. SAMPE Quart 1993;1:54–9.
[25] Daniel IM, Luo JJ, Schubel PM, Werner BT. Interfiber/interlaminar failure of composites under multi-axial states of stress photoelastic investigation of composites. J Compos Mater 2009;69:764–71.
[26] Hinton MJ, Soden PD, Kaddour AS. Failure criteria in fiber reinforced polymer composites: the world wide failure exercise. Elsevier; 2004.
[27] Hashin Z. Failure criteria for unidirectional fiber composites. J Appl Mech 1980;47:329–34.

Publication [P5]

A micromechanical study of porous composites under longitudinal shear and transverse normal loading

A micromechanical study of porous composites under longitudinal shear and transverse normal loading

Danial Ashouri Vajari*

Department of Mechanical Engineering, Solid Mechanics, Technical University of Denmark, DK-2800 Kgs. Lyngby, Denmark

Abstract

The mechanical response of porous unidirectional composites under transverse normal and longitudinal shear loading is studied by means of the finite element analysis. The 3D model includes discrete and random distribution of fibers and voids. The micromechanical failure mechanisms are taken into account by considering the mixed-mode interfacial debonding and the pressure-dependent yielding of the matrix using the modified Drucker-Prager plasticity model. The effect of the micromechanical factors on the overall response of composite is discussed with a focus on the effect of microvoids and interfacial toughness. Finally, the computational prediction of the porous composite in the transverse normal-longitudinal shear stress space is obtained and compared with Puck's model. It is shown that the microstructral modeling is a powerful tool to predict different failure mechanisms originating from micro-scale features. The results show that both interfaces with low fracture toughness as well as microvoids with even small void volume fraction can significantly reduce the macroscopic strength of composite. The size and shape of microvoids can also microscopically lead to different crack paths.

Keywords: Micromechanics, Glass-reinforced epoxy composites, Microvoids, Failure criterion

*Corresponding author
Email address: dvaj@mek.dtu.dk (Danial Ashouri Vajari)

1. Introduction

In laminate design, there is still an essential need for strength analysis considering the critical micromechanical failure mechanisms occurring in composites. Hashin (1980) proposed a phenomenological failure model for unidirectional (UD) fiber composites using the Mohr yield criterion which was appropriate for brittle materials such as composites. He distinguished between fiber- and matrix-dominated fracture in tensile or compressive modes. Puck and Schürmann (2002) improved Hashin's model by assuming that failure is caused by the normal and shear stresses acting on the failure plane, which forms an angle with respect to the direction perpendicular to the tensile stresses. The fracture angle is explicitly determined for each combination of normal and shear stresses acting on the lamina. The predictions of Puck's model have been largely consistent with the experimental results of the failure surface of a composite made up of a brittle epoxy reinforced with either glass or carbon fibers (Hinton et al., 2004). However, the prediction of both Hashin's and Puck's model require the laminate strengths provided by the mechanical tests. On the other hand, in fibre-reinforced polymer composites voids have been found to reduce the mechanical properties such as the interlaminar shear strength, longitudinal and transverse strength as well as Young's modulus, and also fatigue resistance (Thomason, 1995). The effect of porosity is not explicitly considered in the current available analytical failure criteria such as Puck's model.

The presense of porosity is an unavoidable imperfection in composite materials due to the process of manufacturing and inhomogeneous nature of composites. Costa et al. (2001) studied the influence of voids on the interlaminar shear strength of carbon/epoxy and carbon/bismaleimide laminates in terms of the corresponding fracture parameters as well as the shape and the location of the voids. They showed that cracks emanate from voids under interlaminar shear strength test. The author's experimental observations also show that microvoids can lead to crack initiation in composites subjected to uniaxial transverse tension, see Fig. 1. In microscopic point of view, voids can lead to crack initiation at smaller amount of loading due to, e.g., stress concentration around the voids which can consequently trigger interfacial debonding or matrix cracking.

The increase of the computer power has made it possible to predict numerically the mechanical response of composites by considering the micromechanical failure mechanisms. Fiber failure, matrix cracking, fiber/matrix

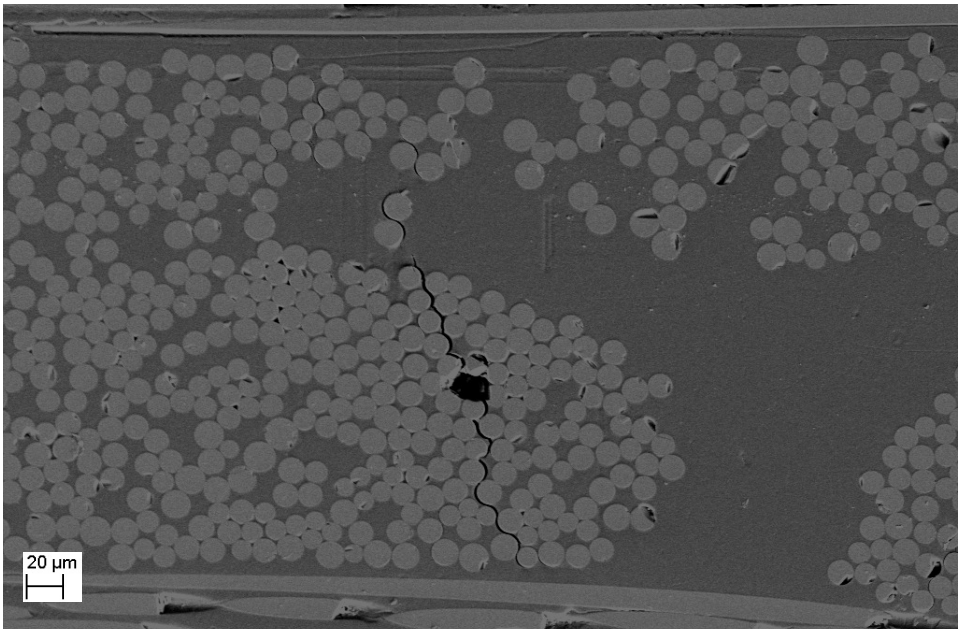

Figure 1: The author's *in-situ* SEM observation of a $[0/90]_s$ laminate subjected to tension perpendicular to the 90° ply. The figure shows a crack initiating from a microvoid.

interfacial debonding and porosity are the main features controlling micro-scale failure. Interfacial debonding has been widely studied as one of the main factors on crack initiation and propagation in composites (París et al., 2003, 2007; Correa et al., 2007; Vajari et al., 2013). The brittle behavior of epoxy resins used in the polymeric composites was studied by Kinloch and Young (1983). González and Llorca (2007a,b), Totry et al. (2008a) and Romanowicz (2012) studied the pressure-dependent behavior of epoxy in composites. Vajari et al. (2014) studied numerically the effect of microvoids on the mechanical response of composites in the transverse normal-longitudinal shear, $\sigma_2 - \tau_{23}$, stress space within the framework of multi-void/fiber RVEs in which both are randomly distributed in the matrix. It was found that stress concentration around a void can lead to onset of interfacial debonding as well as matrix cracking in lower load-bearing capacity. Vajari et al. (2014) found that even 1% void volume fraction can significantly reduce the macroscopic mechanical response of composites.

In the present study the mechanical properties and the failure behavior of a glass-fiber reinforced epoxy composite is numerically investigated under different loading conditions in $\sigma_2 - \tau_{12}$ stress space. This study aims at using the same strategy as Vajari et al. (2014) by considering a discrete and random distribution of multi-fibers and micro voids embedded in the matrix. The focus is on the effect of microvoids and the interfacial fracture toughness. The obtained macroscopic mechanical behavior is used to study the effect of microvoids on different failure modes in $\sigma_2 - \tau_{12}$ stress space from harmless failure due to transverse tensile stress to the dangerous failure caused by severe transverse compression combined by longitudinal shear. Here, Puck's model will be used as an analytical reference for a comparison with numerically obtained failure locus.

2. Problem Formulation

A schematic of the microstructure of UD composites including fibers, matrix and microvoids is depicted in Fig. 2a. The chosen cell includes a random distribution of circular fibers, circular microvoids and microvoids isolated between the fibers. This model considers that all voids and fibers are cylindrical. A Cartesian reference coordinate system, x_i, is placed at the bottom-left corner of the cell and aligned with its edges (Fig. 2a). The dimension of the cell is determined by the length, L, the width, W, the thickness, t, and the radius of the N_f monosized fibers, R_f, which yields

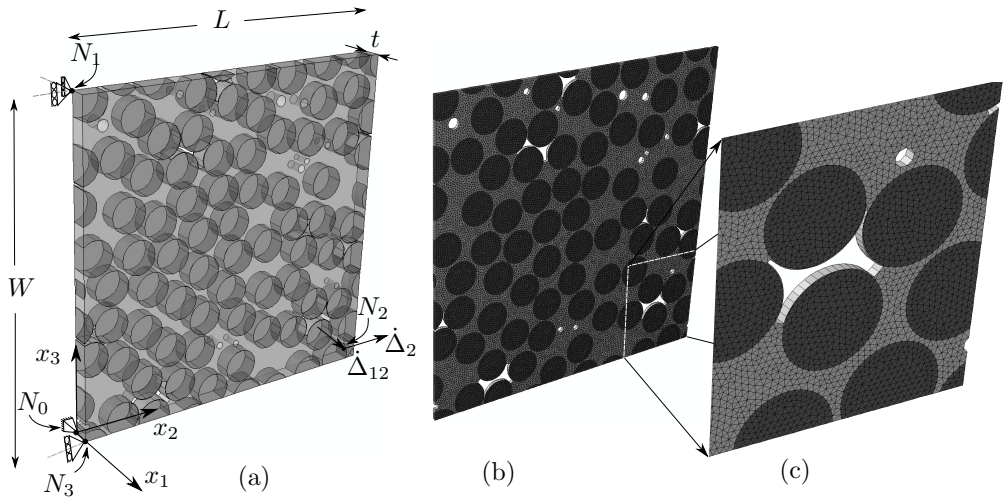

Figure 2: a) Illustration of the fiber and void distribution in a cross-section of a fiber-reinforced composite. The dimensions, loads and the coordinate system are shown. The cell can be subjected to transverse tension/compression by applying $\dot{\Delta}_2$ and in-plane shear by applying $\dot{\Delta}_{12}$. b) Finite element mesh of the cell. The mesh includes around 48,000 solid elements, 3,350 cohesive elements and 56,000 nodes. c) A close view of the mesh near a trapped void is shown.

the fiber volume fraction $V_f = N_f \pi R_f^2 / WL$. The total void volume fraction, V_v, is the sum of the void volume fraction of the N_v circular voids of radius R_v^i, $\sum_{i=1}^{N_v} \pi {R_v^i}^2 / WL$, plus the void volume fraction due to the trapped voids isolated between the fibers. The cell in these analyses is always a square cell with $L = W = L_0$.

All the volume elements considered in this study contain a random distribution of 70 monosized fibers of radius $R_f = 0.1 L_0$ leading to the fiber volume fraction of $\sim 60\%$ while the void volume fraction varies from 0% to 5%, which is a realistic range for composites of good quality. The majority of this porosity is found in voids trapped between fibers while some isolated voids are also dispersed in the matrix. Fibers and voids intersecting the cell edges were split and copied to the opposite sides of the square cell to create a periodic microstructure.

As shown in Fig. 2a, the boundary conditions are applied on a master node, N_0, and three slave nodes, N_1, N_2 and N_3. The cell is subjected to incremental normal tension or compression in the transverse direction by imposing $\dot{\Delta}_2$ as well as the in-plane incremental shear specified by $\dot{\Delta}_{12}$, as shown in Fig. 2b at node N_2. The boundary condition is imposed as shown in Fig. 2a by

$$\begin{aligned} &\dot{u}_1 = \dot{u}_2 = \dot{u}_3 = 0 && \text{at } N_0 = (0,0,0) \\ &\dot{u}_1 = \dot{u}_2 = 0 && \text{at } N_1 = (0,0,L_0) \\ &\dot{u}_1 = \dot{\Delta}_{12}, \dot{u}_2 = \dot{\Delta}_2 && \text{at } N_2 = (0,L_0,0) \\ &\dot{u}_2 = 0 && \text{at } N_3 = (t,0,0) \end{aligned} \tag{1}$$

where $\vec{\dot{u}} = (\dot{u}_1, \dot{u}_2, \dot{u}_3)$ is the incremental displacement vector, $\dot{\Delta}_2$ denotes the compression or tension imposed incremental displacement depending on the sign of $\dot{\Delta}_2$ and $\dot{\Delta}_{12}$ defines the incremental in-plane shear deformation. The location of N_i is given on the coordinate system by (x_1, x_2, x_3) vector. Periodic boundary conditions were applied to the edges of the cell to ensure the continuity between neighboring cells. The periodic boundary conditions can be expressed in terms of the prescribed incremental displacement vectors $\vec{\dot{U}}_1$, $\vec{\dot{U}}_2$ and $\vec{\dot{U}}_3$ which relate the incremental displacements, $\vec{\dot{u}}$, between opposite edges according to

$$\begin{aligned}\vec{U}_1 &= \vec{u}(0, x_2, x_3) - \vec{u}(t, x_2, x_3) \\ \vec{U}_2 &= \vec{u}(x_1, 0, x_3) - \vec{u}(x_1, L_0, x_3) \\ \vec{U}_3 &= \vec{u}(x_1, x_2, 0) - \vec{u}(x_1, x_2, L_0)\end{aligned} \tag{2}$$

Combined uniaxial tension/compression along the x_2-axis and in-plane shear deformation are imposed with $\vec{U}_2 = (\dot{\Delta}_{12}, \dot{\Delta}_2, 0)$. While the component of $\vec{U}_1$ and $\vec{U}_3$ are chosen so that the average normal and shear forces acting on the cell surfaces are zero (besides those corresponding to transverse tension/compression and longitudinal shear). The incremental tensile/compressive and shear strains are given by

$$\dot{\epsilon}_2 = \frac{\dot{\Delta}_2}{L_0} \quad \text{and} \quad \dot{\gamma}_{12} = \arctan\left(\frac{\dot{\Delta}_{12}}{L_0}\right) \tag{3}$$

The corresponding normal and shear stresses are computed from the resultant normal and tangential forces acting on the edges divided by the cross-section, A, as

$$\sigma_2 = \frac{1}{A}\int T_2 t dx_3\Big|_{x_2=L_0} \quad \text{and} \quad \tau_{12} = \frac{1}{A}\int T_{12} t dx_3\Big|_{x_2=L_0} \tag{4}$$

where $A = L_0 \times t$ and t is the unit thickness of the cell in the x_1-direction and T_2 and T_{12} denote the normal and in-plane shear tractions at the edge $x_2 = L_0$, respectively.

3. Material Model

3.1. Isotropic Modified Drucker-Prager Model

The matrix behavior corresponds to an isotropic epoxy resin and fails at a very low strain in a brittle fashion under uniaxial tension (Kinloch and Young, 1983). Under uniaxial compression or shear, epoxy resins undergo considerable plastic deformation and the flow stress is pressure-dependent (Quinson, 1997; Puck and Schürmann, 2002; Kinloch and Young, 1983). The Drucker-Prager yield criterion has often been used to model the mechanical behavior of these materials. The Drucker-Prager model is illustrated in Fig. 3 and it is a modification of the von Mises criterion with different tensile and compressive yield stress (shown as a dashed-line in Fig. 3). In addition, the

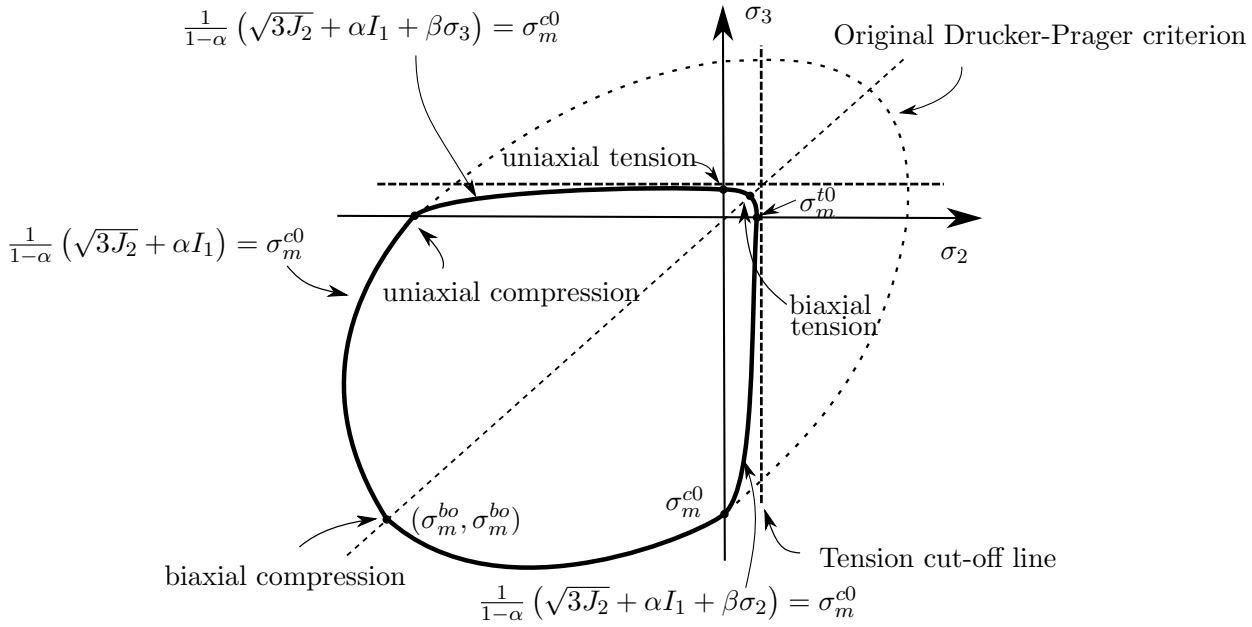

Figure 3: Yield surface of the modified Drucker-Prager criterion. The dashed-line denotes the original Drucker-Prager criterion.

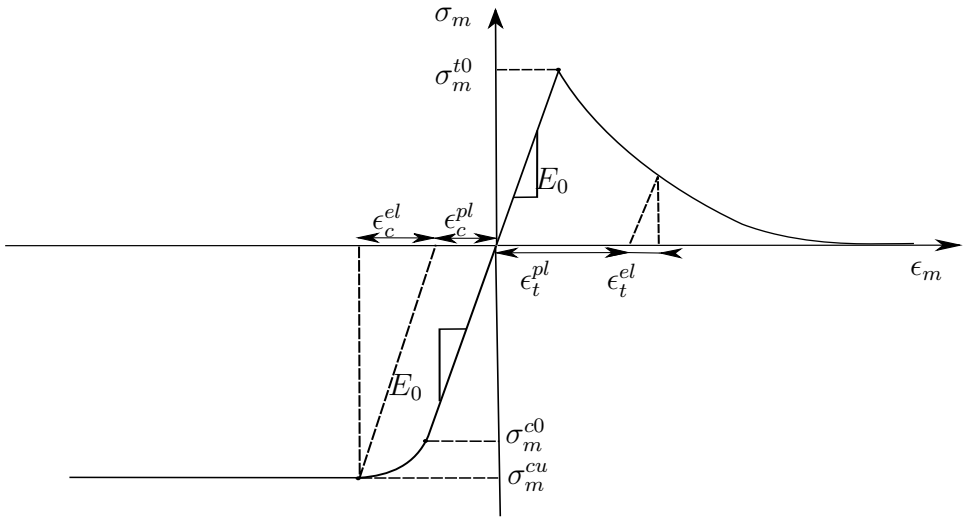

Figure 4: Stress-strain behavior of the matrix under uniaxial tension and uniaxial compression.

Drucker-Prager yield criterion includes the effect of hydrostatic stresses on the flow stress by including an additional term in the von Mises expression, according to

$$F(I_1, J_2) = \sqrt{3J_2} - \alpha I_1 - c = 0 \tag{5}$$

where I_1 is the first invariant of the stress tensor, J_2 is the second invariant of the deviatoric stress tensor and c is the flow stress under pure shear. The pressure-sensitivity parameter, α, can be determined by (Lubliner, 1989)

$$3\alpha = \frac{\frac{\sigma_m^{b0}}{\sigma_m^{c0}} - 1}{2\frac{\sigma_m^{c0}}{\sigma_m^{t0}} - 1} \tag{6}$$

Here, σ_m^{c0}, σ_m^{b0} and σ_m^{t0} denote the matrix uniaxial compressive yield stress, the biaxial compressive yield stress and the uniaxial tensile yield stress, respectively, see Fig. 3. In order to include the brittle behavior of the epoxy matrix in tension, the modified Drucker-Prager model developed by Lubliner (1989) and Lee (1998) was used in this investigation to simulate the matrix behavior. It is expressed by

$$F(I_1, J_2, \sigma_I, \beta, \alpha) = \frac{1}{1-\alpha}\left(\sqrt{3J_2} - \alpha I_1 + \beta \langle \sigma_I \rangle\right) - \sigma_m^{c0} = 0 \tag{7}$$

where σ_I is the maximum principal stress, $\langle\rangle$ denotes the Macaulay brackets (which return the argument if positive and zero otherwise), and β is a function of the tensile, σ_m^{t0}, and compressive, σ_m^{c0}, yield stress according to

$$\beta = \frac{\sigma_m^{c0}}{\sigma_m^{t0}}(1-\alpha) - (1+\alpha) \tag{8}$$

The yield surface corresponding to the modified Drucker-Prager criterion is depicted in Fig. 3. It follows the standard Drucker-Prager yield criterion with an associated flow rule under compression, which has been experimentally validated for glassy polymers (Puck and Schürmann, 2002; Quinson, 1997). Quinson (1997) and Chew et al. (2006) discussed that the pressure-sensitivity reduces the load-carrying capacity and influences the strain for void coalescence, and also showed that plastic dilatancy effects are relatively milder. Thus, for the sake of simplicity, an associated flow rule is considered to simulate the plastic flow of the matrix. The epoxy behavior in tension was

Fiber		Matrix						
E_f $[GPa]$	ν_f	E_m $[GPa]$	ν_m	σ_m^{c0} $[MPa]$	σ_m^{cu} $[MPa]$	σ_m^{t0} $[MPa]$	G_m $[\frac{J}{m^2}]$	α
70	0.21	3	0.3	85	95	65	100	0.13

Table 1: Parameters of the constitutive models of the fibers, the epoxy matrix.

controlled by the maximum principal stress and the yield surface was cut off by the tensile yield stress, σ_m^{t0}, as shown with the straight dashed lines in Fig. 3.

The stress-strain behavior of the matrix under uniaxial compression and uniaxial tension is shown in Fig. 4. Plastic deformation at constant flow stress occurred in compression after yielding, leading to failure by the localization of a shear band. In Fig. 4, σ_m^{cu} denotes the matrix ultimate compressive strength. Conversely, the behavior in tension was brittle due to microcracking and this is accounted for by a softening law (Canal et al., 2012). The energy dissipated by a unit volume during tensile cracking is G_m which is the area under the tensile stress-strain curve for $\epsilon_m > 0$. The assumed stress-strain behavior shown in Fig. 4 for both tension and compression loading is in good agreement with the experimental results reported by Fiedler et al. (2001).

Glass fibers were modeled as isotropic, elastic materials with the elastic constants given in Table. 1. The matrix properties are also shown in Table. 1 and they correspond to typical values used in the modified Drucker-Prager model for an epoxy matrix (Canal et al., 2012). The pressure-sensitivity parameter was chosen to be $\alpha = 0.13$ which is within the range reported by Quinson (1997) and Chew et al. (2006).

4. 3D bilinear cohesive zone model

The cohesive zone model defined in ABAQUS assumes initially linear elastic behavior followed by the initiation and evolution of damage, see Fig. 5a. The elastic behavior of the cohesive traction-separation law can be given as

$$\begin{bmatrix} \dot{T}_n \\ \dot{T}_s \\ \dot{T}_t \end{bmatrix} = \begin{bmatrix} K_{nn} & K_{ns} & K_{nt} \\ K_{ns} & K_{ss} & K_{st} \\ K_{nt} & K_{st} & K_{tt} \end{bmatrix} \begin{bmatrix} \dot{u}_n \\ \dot{u}_s \\ \dot{u}_t \end{bmatrix} \tag{9}$$

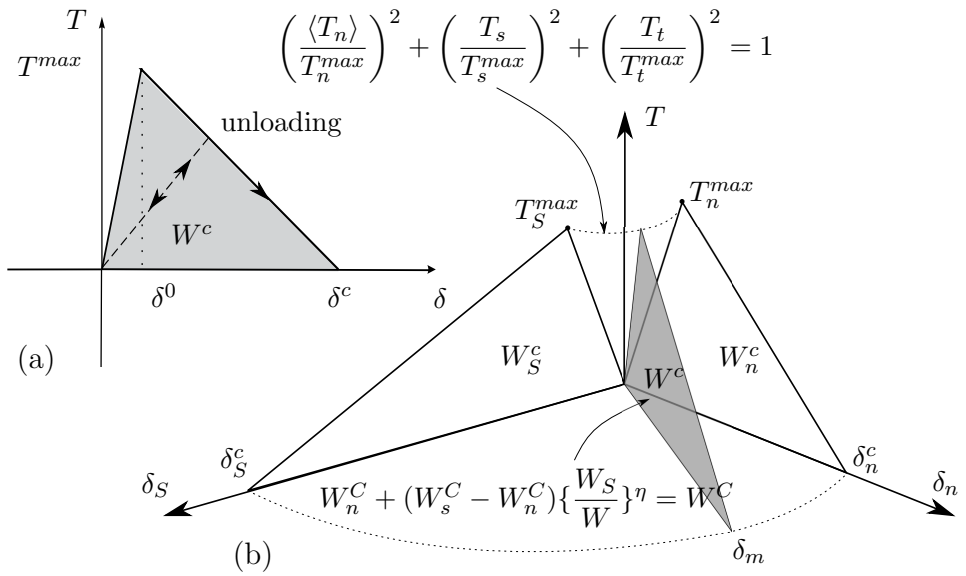

Figure 5: a) Bilinear traction-separation law including unload-reloading. b) The mixed mode response of 3D cohesive elements. Damage initiation is specified by quadratic stress criterion while damage evolution uses a mixed-mode energy based criterion proposed by Benzeggagh and Kenane (1996).

where $\dot{T}_i$ and $\dot{u}_i$ denotes the incremental traction and displacement components, respectively where the subscript n stands for normal debonding while s and t denote the tangential openings perpendicular and parallel to the fiber direction, respectively. K_{ij} are the stiffness components. Damage in a cohesive element consists of three ingredients: a damage initiation criterion, a damage evolution law and a choice of damage removal upon reaching a completely damaged state (Abaqus, 2012). As shown in Fig. 5a, the damage initiation specifies the beginning of degradation in traction-separation law. Damage is assumed to initiate based on the quadratic nominal stress criterion defined as

$$\left(\frac{\langle T_n \rangle}{T_n^{max}}\right)^2 + \left(\frac{T_s}{T_s^{max}}\right)^2 + \left(\frac{T_t}{T_t^{max}}\right)^2 = 1 \tag{10}$$

where T_n^{max} denotes the maximum normal traction while T_s^{max} and T_t^{max} are the maximum tangential tractions. The Macaulay brackets, $\langle\rangle$, indicate that pure compressive deformation does not lead to damage initiation. Once

the damage initiation criterion is met the degradation of cohesive stiffness triggers. As shown in Fig. 5a, a linear softening behavior is considered. The damage evolution is determined by a mixed-mode fracture criterion proposed by Benzeggagh and Kenane (1996) which is based on the dissipated interfacial fracture energy, W, as

$$W_n^C + (W_s^C - W_n^C)\{\frac{W_S}{W}\}^\eta = W^C \tag{11}$$

where the work per unit area of the normal traction is denoted by W_n and by W_s and W_t for shear, respectively. The superscript C denotes the critical energy dissipated due to failure and η is a material parameter. The portion of the total work done by the shear tractions and the corresponding relative displacement components is represented by $W_S = W_s + W_t$. The Benzeggagh-Kenane fracture criterion is particularly useful when the critical fracture energies during deformation purely along the first and the second shear directions are the same; i.e., $W_s^C = W_t^C$ (Abaqus, 2012).

Fig. 5b schematically illustrates the mixed-mode traction-separation law in the 3D cohesive elements. The traction on the vertical axis is versus the normal displacement, δ_n, and the portion of the total tangential displacement, δ_S. Two unshaded triangles shown in Fig. 5b represent the traction-separation law under pure normal or tangential mode. For any mixed-mode condition, Eq. 10 and 11 provide the mixed traction-separation law shown by the gray triangle. By determining the mixed critical traction and fracture energy from Eq. 10 and 11 the corresponding mixed critical cohesive length, δ_m can be obtained. However, it should be noted that this type of cohesive law is path dependent, so that the total work of the tractions may not be the gray area, see Sørensen and Goutianos (2014).

Finally, as shown in Fig. 5a, unloading after the damage initiation is always assumed to occur linearly toward the origin of the traction-separation plane and reloading subsequent to unloading also occurs along the same linear path until it reaches the softening envelope is reached.

5. Numerical Methods

Three-dimensional simulations are carried out with Abaqus/Standard (Abaqus, 2012) within the framework of the finite deformations theory with the initial unstressed state as reference.

Interface			
W_n^C $[\frac{J}{m^2}]$	$W_s^C = W_t^C$ $[\frac{J}{m^2}]$	T_n^{max} $[MPa]$	$T_s^{max} = T_t^{max}$ $[MPa]$
10	25	50	75

Table 2: Parameters of the fiber/matrix interface.

The matrix and the fibers were automatically meshed using 6-node linear triangular element (C3D6). In addition, 8-node three-dimensional cohesive elements (COH3D8) were inserted at the fiber/matrix interface to include the effect of interface decohesion. An example of finite element mesh is shown in Fig. 2a and c. The converged finite element discretization includes around 48,000 solid elements, 3,350 cohesive elements and 56,000 nodes.

6. Results and Discussion

6.1. Effect of void volume fraction

The stress–strain curves obtained from the numerical simulation of four different cells under transverse uniaxial tension, transverse uniaxial compression and longitudinal shear are plotted in Fig. 6a, b and c, respectively. All cells contain 70 monosized fibers with the same fiber distribution giving 60% fiber volume fraction. The difference between the cells is the arrangement of 2% void volume fraction which are randomly distributed in the matrix. Some simulations are stopped due to numerical instabilities after the stress drop was attained. Fig. 6 shows that regardless of different void distribution the elastic response of the cells are almost the same while the nonlinear response differs which subsequently leads to different ultimate stress. Totry et al. (2008a) discussed that different arrangement of fibers in an RVE including 30 fibers with interface debonding under uniaxial compression shows up to 7% deviation in the ultimate failure stress. This scatter can be even larger when the same RVE includes voids. Fig. 6 shows that with the same arrangement of 70 fibers, different spatial distribution of 2% void volume fraction can lead to approximately 17%, 12% and 15% deviation in the ultimate stress under transverse uniaxial tension, transverse uniaxial compression and longitudinal shear, respectively. However, this study does not aim at studying an RVE which represents the whole macroscopic behavior of the lamina but focuses on the effect of different micromechanical failure mechanisms on a specific

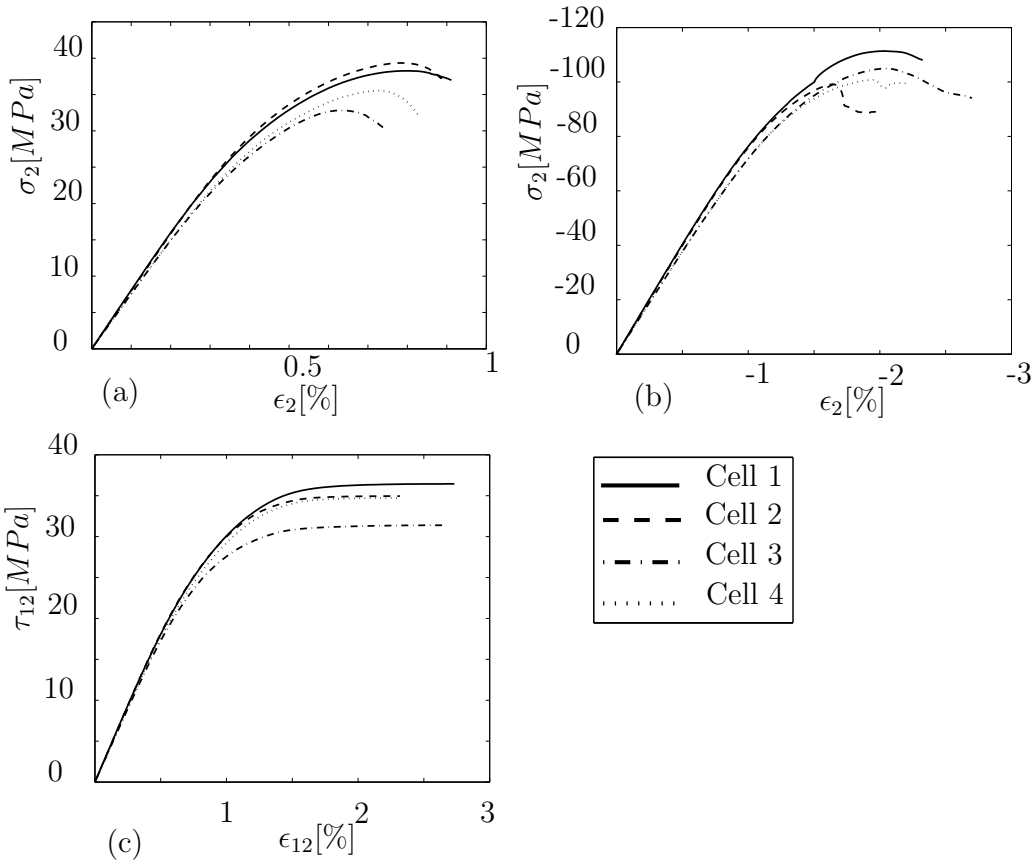

Figure 6: a) The overall stress-strain response of four cells with different randomly distribution of 2% void volume fraction under a) pure transverse tension, b) pure transverse compression and c) pure longitudinal shear loading. The fiber distribution in all cases is the same and is generated by 70 monosized fibers giving 60% fiber volume fraction.

configuration of a lamina which contains several fibers and voids randomly distributed in the matrix.

The effect of void volume fraction on the overall stress-strain response of a cell under combined transverse tension and longitudinal shear, $\Delta_{12}/\Delta_2 = 1$, dominant longitudinal shear combined with transverse compression, $\Delta_{12}/\Delta_2 = -10$ and dominant transverse compression combined with longitudinal shear, $\Delta_{12}/\Delta_2 = -0.5$ is shown in Fig. 7a, b and c, respectively. Fig. 7 shows that increase of void volume fraction leads to decrease the macroscopic stress-strain response of cells under all these three loading conditions. This reduction effect is due to the micromechanical effect of voids which triggers

interfacial debonding or matrix cracking at smaller amount of loading. This micromechanical effect is shown in Fig. 7 where even 1% void volume fraction can decrease 25%, 10% and 15% of the ultimate stress in Fig. 7a, b and c, respectively. Different reduction values in Fig. 7a, b and c is due to various failure mechanisms occurring under different loading conditions. In Fig. 7a, the dominant failure mechanism is due to normal interfacial debonding while in Fig. 7b the matrix deformation and tangential interfacial debonding leads failure and in Fig. 7c failure is caused by matrix shear band with subsequent interfacial debonding. Thus, as the results show, under transverse tension the effect of void volume fraction is more pronounced.

Puck and Schürmann (1998) proposed physically based phenomenological models to predict the failure locus of fiber-reinforced composites. They distinguish between fiber failure and inter-fiber failure mechanisms. Furthermore, their fracture criteria is based on the normal, σ_n, and shear stresses, τ_{1n} and τ_{tn}, acting on the fracture plane and not the actual stresses subjected to the action plane, see Fig. 8b. Their fracture criteria make a distinction between different fracture modes namely; Mode-A, -B and -C. Mode-A is shown in Fig. 8a on the failure curve from point a to b. In mode-A, the composite is under combined transverse tension and in-plane shear which leads to a fracture plane perpendicular to the tensile loading direction, i.e. the fracture angle is $\theta_{fp} = 0^\circ$. With the similar fracture angle as mode-A, mode-B is determined for the dominant longitudinal shear combined with transverse compression (the path from point b to c). Mode-C is defined for the dominant transverse compression combined with longitudinal shear where inclined fracture planes occur (the path from point c to d). For a given $(\sigma_2 - \tau_{12})$ stress state, the Puck's criteria under mode-A with $\theta_{fp} = 0^\circ$ is given by (Puck and Schürmann, 1998)

$$\sqrt{\left(\frac{\tau_{12}}{S_{12}}\right)^2 + \left(1 - P_{\perp\parallel}^{(+)}\frac{Y_T}{S_{12}}\right)^2\left(\frac{\sigma_2}{Y_T}\right)^2} + P_{\perp\parallel}^{(+)}\frac{\sigma_2}{S_{12}} = 1 \qquad \text{for } \sigma_2 \geq 0 \tag{12}$$

while under mode-B with $\theta_{fp} = 0^\circ$ is expressed by

$$\frac{1}{S_{12}}\left(\sqrt{\tau_{12}^2 + \left(P_{\perp\parallel}^{(-)}\sigma_2\right)^2} + P_{\perp\parallel}^{(-)}\sigma_2\right) = 1 \qquad \text{for } \sigma_2 < 0 \quad \text{and} \quad 0 \leq |\frac{\sigma_2}{\tau_{12}}| \leq \frac{R_{\perp\perp}^A}{|\tau_{12c}|} \tag{13}$$

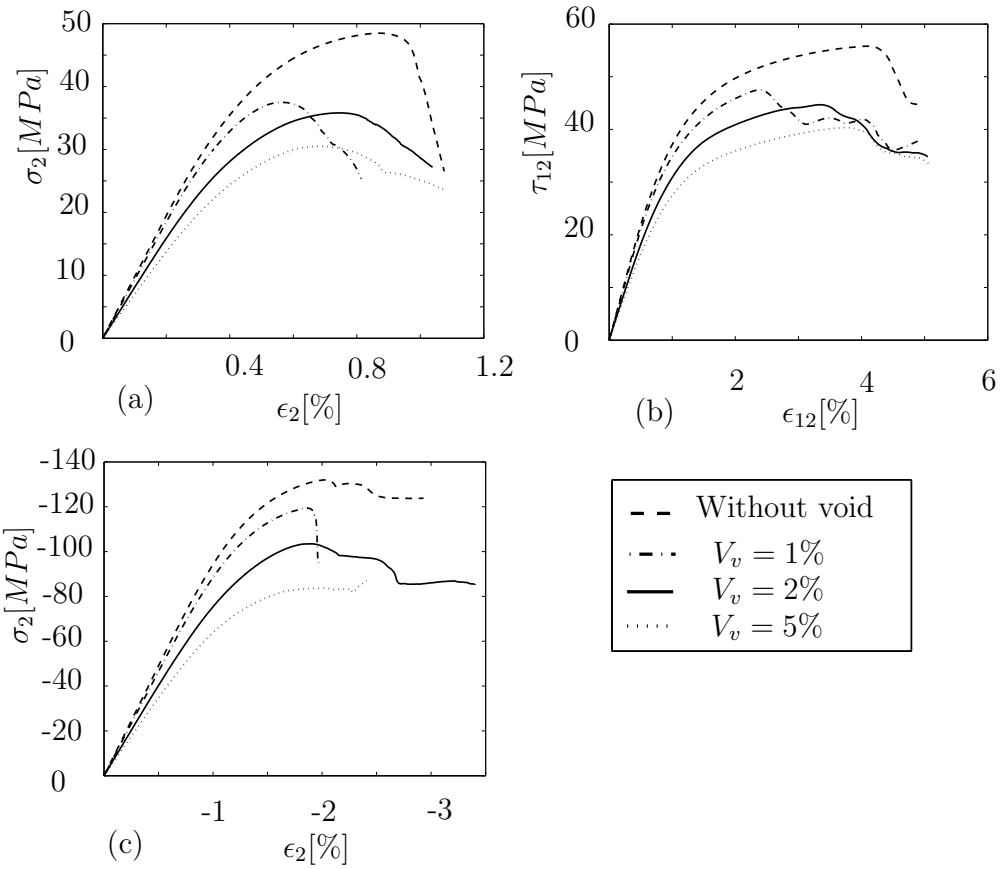

Figure 7: Effect of void volume fraction on the overall stress-strain response of UD fiber-reinforced composites under a) combined transverse tension and longitudinal shear, $\Delta_{12}/\Delta_2 = 1$, b) dominant longitudinal shear combined with transverse compression, $\Delta_{12}/\Delta_2 = -10$ and c) dominant transverse compression combined with longitudinal shear, $\Delta_{12}/\Delta_2 = -0.5$. The curves are plotted in the corresponding dominant loading stress.

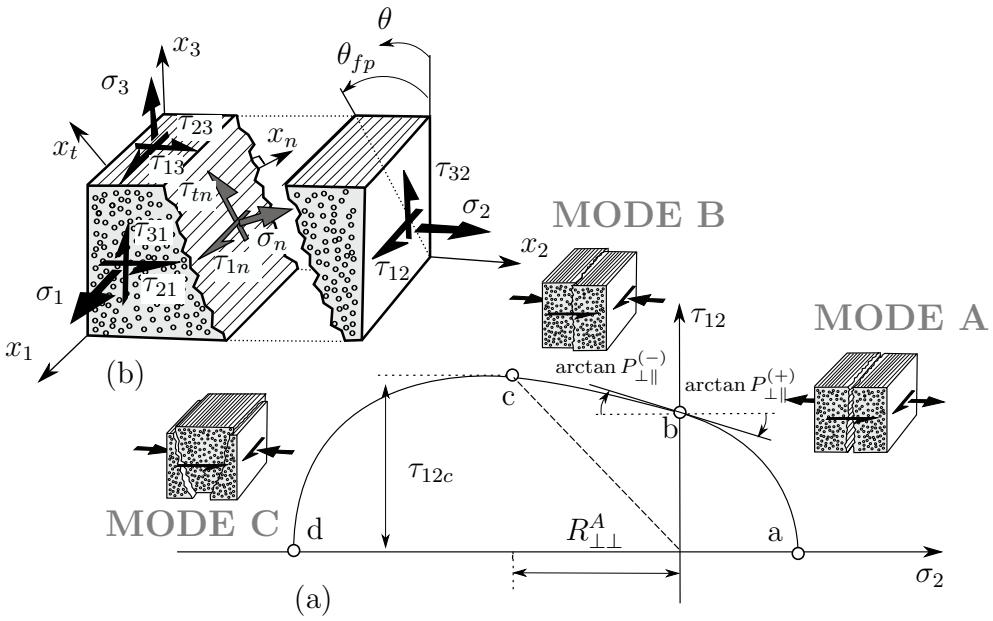

Figure 8: a) Illustration of the analytical $\sigma_2 - \tau_{12}$ fracture envelope for $\sigma_1 = 0$ proposed by Puck and Schürmann (1998). Three different fracture modes (A, B and C) are shown which are distinguished based on different loading conditions and the fracture angle. b) Three dimensional stresses, (σ_n, τ_{n1}, τ_{nt}) acting on the fracture plane. The (x_1, x_n, x_t) coordinate system is rotated by the fracture angle, θ_{fp}, with respect to the (x_1, x_2, x_3) coordinate system.

and in mode-C having $\cos\theta_{fp} = \sqrt{\frac{R^A_{\perp\perp}}{(-\sigma_2)}}$ is given by

$$\left[\left(\frac{\tau_{12}}{2(1+P^{(-)}_{\perp\perp})S_{12}}\right)^2 + \left(\frac{\sigma_2}{Y_C}\right)^2\right]\frac{Y_C}{(-\sigma_2)} = 1 \qquad \text{for } \sigma_2 < 0 \quad \text{and} \quad 0 \le |\frac{\tau_{12}}{\sigma_2}| \le \frac{|\tau_{12c}|}{R^A_{\perp\perp}} \tag{14}$$

where Y_T, Y_C and S_{12} denote the tensile strength, the compressive strength and the shear strength of composite, respectively. The so-called inclination parameters, $P_{\perp\parallel}$ and $P_{\perp\perp}$, are the slopes of the failure curve in $\sigma_2 - \tau_{12}$ plane (as shown in Fig. 8a) and in $\sigma_2 - \tau_{tn}$ plane, respectively. The inclination parameters should be experimentally determined. In this study, $P^{(-)}_{\perp\parallel} = 0.2$ and $P^{(+)}_{\perp\parallel} = 0.25$ which are in the range recommended by (Puck and Schürmann, 2002) for glass-epoxy composites are used. The superscripts $(+)$ and $(-)$ stand for tension and compression loading conditions, respectively. While the subscripts $\perp$ and $\parallel$ denote the transverse, x_t, and longitudinal, x_1, directions on the fracture plane. Finally, according to some relationships the fracture resistance in the fracture plane due to transverse/transverse shear, $R^A_{\perp\perp}$, the inclination parameter, $P^{(-)}_{\perp\perp}$, and the shear stress at the border of mode-B and -C, τ_{12c}, (shown as point c in Fig. 8a) are defined as (Puck and Schürmann, 1998)

$$\begin{aligned} R^A_{\perp\perp} &= \frac{Y_C}{2(1+P^{(-)}_{\perp\perp})} = \frac{S_{12}}{2P^{(-)}_{\perp\parallel}}\left(\sqrt{1+2P^{(-)}_{\perp\parallel}\frac{Y_C}{S_{12}}} - 1\right) \\ P^{(-)}_{\perp\perp} &= P^{(-)}_{\perp\parallel}\frac{R^A_{\perp\perp}}{S_{12}} \\ \tau_{12c} &= S_{12}\sqrt{1+2P^{(-)}_{\perp\perp}} \end{aligned} \tag{15}$$

The Puck's model needs some parameters such as Y_T, Y_C, S_{12} and $P_{\perp\parallel}$ to be determined experimentally for a given material. However, experimentally measuring of the mechanical properties is sometimes difficult and costly. Alternatively, one can use the numerical modeling considering the micromechanical mechanisms occurring in fiber, matrix and interfaces to predict the

mechanical properties of composites. In this study, the numerically predicted values of the mechanical strengths of composites are used to calculate the Puck's failure locus. Subsequently, the analytical failure locus is compared with the computationally predicted failure locus to check the effectiveness of the numerical results for the combined $\sigma_2 - \tau_{12}$ loading conditions. In Fig. 9 the failure envelopes of UD composite in the $\sigma_2 - \tau_{12}$ stress space is plotted for the cells with 60% fiber volume fraction and three different void volume fractions ($V_v = 1\%$, 2% and 5%) which are compared with a void-free case. To cover the entire failure locus each cell is subjected to 14 different loading conditions produced by different ratios of the shear displacement, Δ_{12}, to the normal displacement, Δ_2, while $\sigma_1 = 0$. The strength under biaxial loading (transverse tension or compression and in-plane shear) was determined by the point at which one (or often both) normal and shear stresses began to decrease as the normal and shear displacements increase. The results show a good agreement between the computational and the analytical predictions for all void volume fractions. However, there are small scatters in the combined transverse tension and longitudinal shear loading conditions (mode-A). The failure mechanism in mode-A is controlled by the normal interfacial debonding which has weaker strength than the matrix tensile strength. Furthermore, the presence of the voids triggers the onset of interface decohesion at lower stresses. Therefore, the scatters seen in mode-A can be due to the fact that these micromechanical mechanisms are not considered in the Puck's model. Comparing the results for different void volume fractions indicates that even very small amount of void volume fraction can significantly reduce the macroscopic failure locus of composites in all different modes shown in Fig. 9. This reduction effect from a void-free composite to a composite with $V_v = 5\%$ is up to 38% in mode-A, 30% in mode-B and up to 24% in mode-C.

Several authors reported experimental results on the influence of porosity on the tensile and shear strengths of UD fiber-reinforced composites (Olivier et al., 1995; Jeong, 1997; Costa et al., 2005; Zhang et al., 2011). However, no experimental results on the effect of porosity on the transverse compressive strength were found in the literature. Olivier et al. (1995) has detailed information about the influence of porosity on the transverse tensile strength of UD composites. The experimental data in that paper reported that the transverse tensile strength was reduced by approximately 7% and 20% in the presence of 5% of porosity in two different carbon-fiber/epoxy composites with 60% fiber volume fraction. The numerical predictions in Fig. 7a for 5% porosity were higher (around 38%). Zhang et al. (2011) reported that the

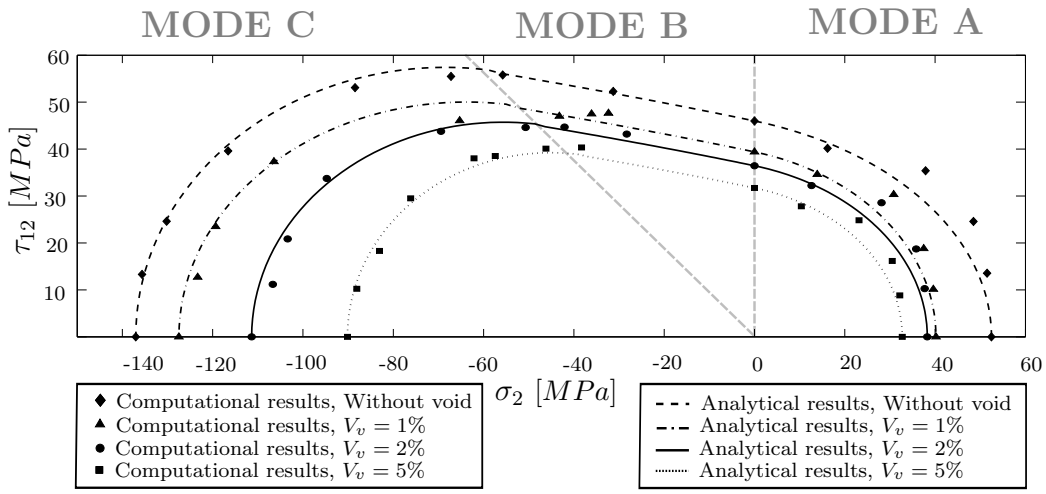

Figure 9: Failure locus of a UD fiber-reinforced composite in the $\sigma_2 - \tau_{12}$ stress space as function of porosity. The lines correspond to the predictions of the Puck's model (Puck and Schürmann, 2002). The solid symbols stand for the numerical predictions obtained from the numerical simulation of an RVE of the microstructure.

shear strength of the aged carbon/epoxy composites can decrease 11.8% and 14.2% with porosity of $V_v = 0.33\%$ and $V_v = 1.5\%$, respectively, which is in a good agreement with the numerical results shown in Fig. 7c giving 13% for $V_v = 1\%$. The scatter in the experimental results can be controlled by the size, shape and spatial distribution of voids and the present numerical strategy seems to be a promising tool to capture the effect of these factors.

In order to check the ability of the numerical modeling to predict different failure modes, the contour plots of the equivalent plastic strain of a cell without porosity under six different loading conditions are plotted in Fig. 10. Fig. 10a and b denote the failure under mode-A while Fig. 10c and d represent the mode-B failure and Fig. 10e and f show the failure under mode-C. The results predict the fracture angles in good agreements with the Puck's predictions. Fig. 10a, b, c and d give $\theta_{fp} = 0^\circ$ while Fig. 10e and f show an oblique failure plane slightly higher than 45° with $\theta_{fp} = 50^\circ$ and $\theta_{fp} = 56^\circ$, respectively. This oblique failure plane is attributed to the pressure sensitivity of matrix yield strength (González and Llorca, 2007a) and the predictions are in the range reported by (Puck and Schürmann, 2002). Furthermore, Fig. 10a and b indicate that in mode-A the failure is controlled by normal interfacial debonding which leads to crack initiation at fiber/matrix interfaces. The crack propagates along the debonded interfaces perpendicular to the trans-

verse normal stress. The localized deformation of matrix in the ligament of the debonded interfaces can be also seen. In mode-B, as shown in Fig. 10c and d, the failure is controlled by matrix deformation which subsequently leads to tangential interfacial opening along the fibers. Fracture controlled by matrix deformation occurs when the cohesive tangential strength is high, $T_t^{max} = 75MPa$, following the experimental results obtained by Canal et al. (2012). This value is larger than the ultimate strength of the matrix, $\sigma_m^{t0} = 65MPa$. In addition, as Puck and Schürmann (1998) also discussed, in the mode-B the transverse compressive stress impedes the shear fracture leading to an internal friction. The effect of this phenomena is schematically shown in the path from point b to c in Fig. 8a. Fig. 9 shows this effect in the analytical predictions which are perfectly followed in the numerical predictions as well. Finally, it is worth to notice that the simulation predicts a wedge shaped transverse compressive fracture under mode-C which is due to the sliding of composite along the shear bands and the debonded interfaces under large compressive deformation. This failure which is known as the "explosive effect"can cause delamination and local buckling which is dangerous compared to the fairly harmless crack forming due to transverse tensile stress (Puck and Schürmann, 1998).

Fig. 11 shows the contour plots of the accumulated plastic strain of a cell with the same fiber distribution as Fig. 10 but including 2% void volume fraction. The results show that porosity not only can macroscopically shrinkage the failure envelope of composite but can also microscopically provoke crack initiation and propagation leading to different crack paths. Comparing Fig. 11 with Fig. 10 indicates that in all different modes the crack paths are affected by the location of the larger voids. Fig. 11a and b in mode-A and Fig. 11c and d in mode-B show the fracture angles higher than zero. Whereas in mode-C, the fracture angles in both Fig. 11e and f are $\theta_{fp} = 47°$ which differ with the corresponding cases in Fig. 10. The wedge effect in mode-C is also more pronounced in the porous composites such that under pure compression at $\epsilon_2 = 2.5\%$ the maximum strain in the x_3-direction of void-free composite is $\epsilon_3 = 1.7\%$ while it is $\epsilon_3 = 2.4\%$ for the composite with $V_v = 2\%$.

6.2. Effect of interfacial toughness on porous composite

As it was discussed in Fig. 10 and 11, due to the loading conditions in mode-A a fracture plane normal to the transverse tension is generated. This fracture plane normally leads to a failure mechanism mainly controlled by the

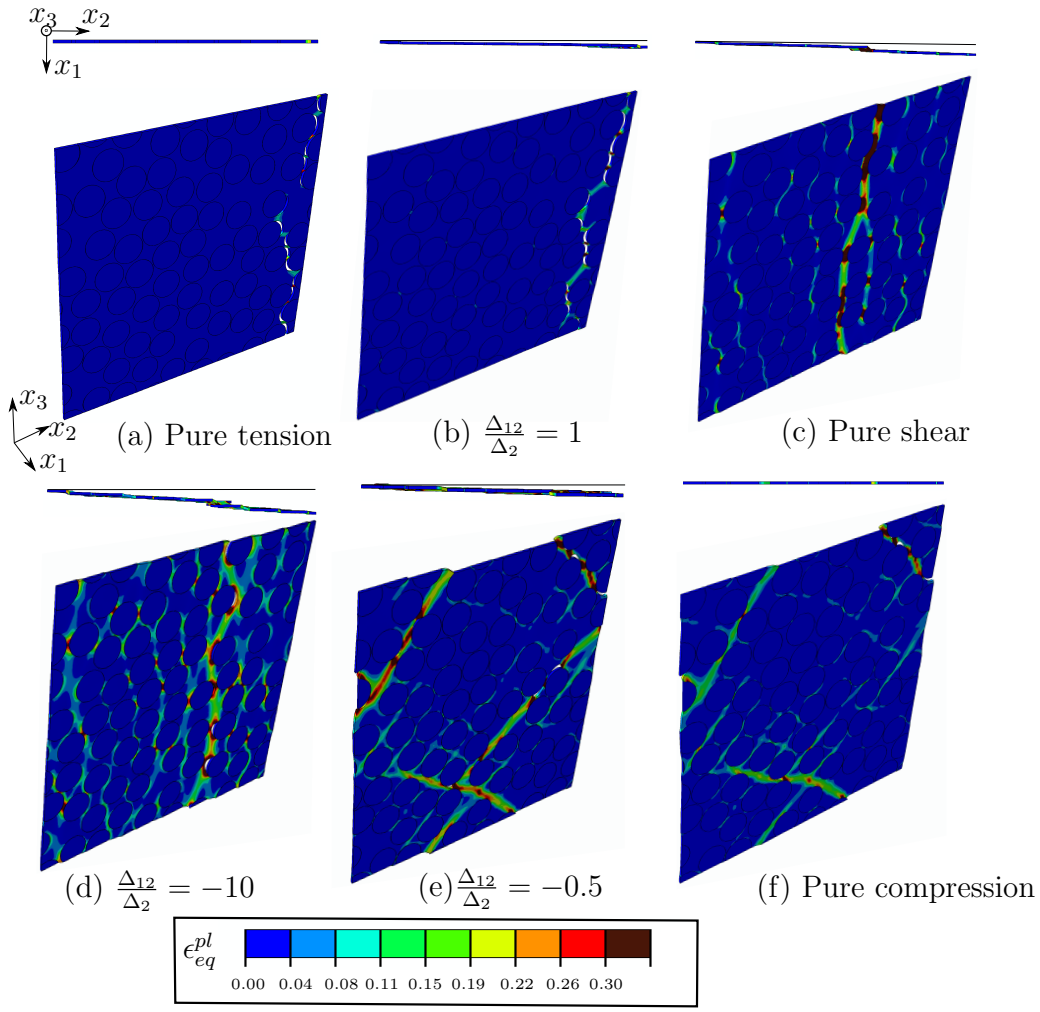

Figure 10: Contour plots of the accumulated plastic strain of a cell without porosity subjected to a) pure transverse tension, b) combined transverse tension and longitudinal shear with $\Delta_{12}/\Delta_2 = 1$, c) combined transverse compression and longitudinal shear with $\Delta_{12}/\Delta_2 = -10$, d) pure compression, e) combined transverse compression and longitudinal shear with $\Delta_{12}/\Delta_2 = -0.5$ and f) pure shear. Figures (a) and (b) are at $\epsilon_2 = 1.5\%$ and Figures (c) is at $\epsilon_2 = 4\%$ while the rest are at the dominant strain, ϵ_2 or $\epsilon_{12} = 2.5\%$. All the figures are magnified by factor 2.

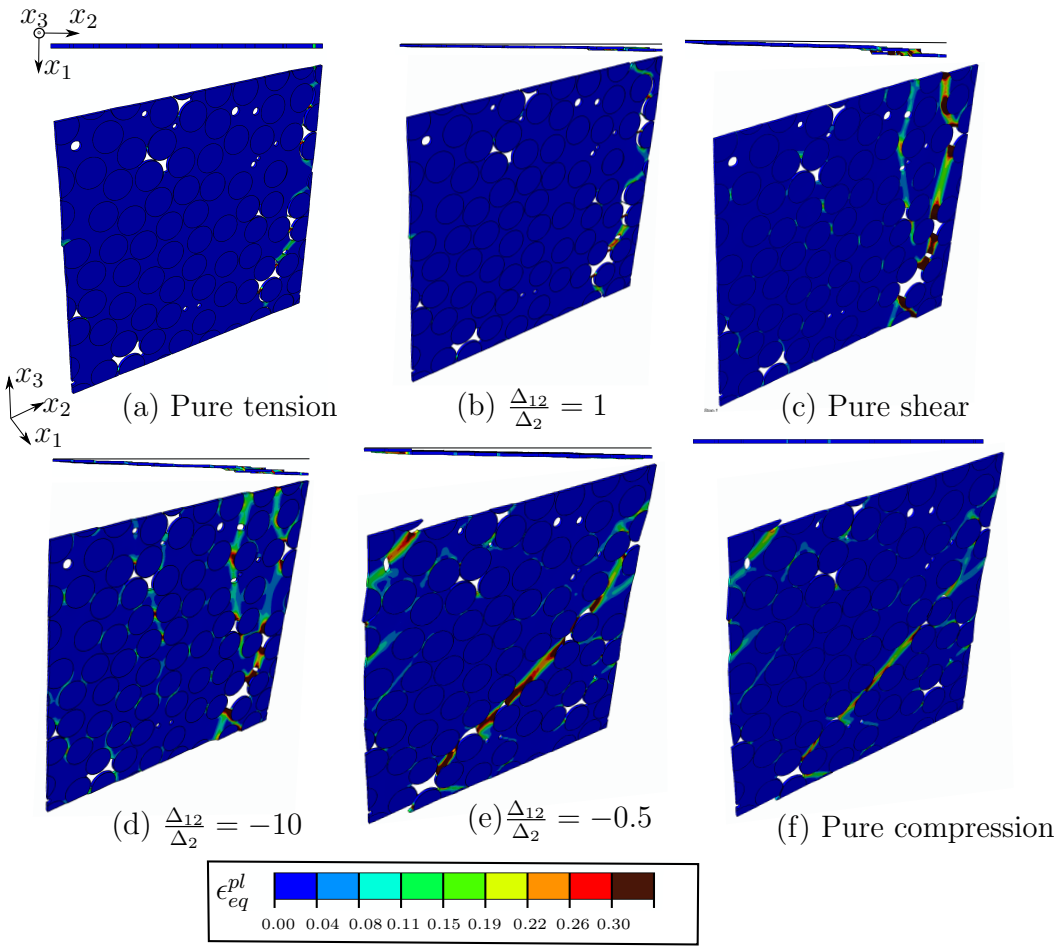

Figure 11: Contour plots of the accumulated plastic strain of a cell with $V_v = 2\%$ subjected to a) pure transverse tension, b) combined transverse tension and longitudinal shear with $\Delta_{12}/\Delta_2 = 1$, c) combined transverse compression and longitudinal shear with $\Delta_{12}/\Delta_2 = -10$, d) pure compression, e) combined transverse compression and longitudinal shear with $\Delta_{12}/\Delta_2 = -0.5$ and f) pure shear. Figures (a) and (b) are at $\epsilon_2 = 1.5\%$ while the rest are at the dominant strain, ϵ_2 or $\epsilon_{12} = 2.5\%$. All the figures are magnified by factor 2.

normal interfacial debonding. While in the dominant transverse compression the loading condition produces an oblique fracture plane which causes the interfaces to be under tangential debonding perpendicular to the fiber direction more than normal opening. Since the shear strength of the interface is larger than the normal interfacial strength and often the matrix tensile strength the matrix deformation normally controls failure. However, different interfacial properties may also change the influence of the interfacial debonding and matrix cracking in the failure mechanism of composite. In this section the effect of interfacial toughness on the failure mechanisms of porous composites is studied. Moreover, the contribution of microvoids in damage evolution based on different interfacial fracture toughness is discussed.

The effect of interfacial toughness on the strength of composites with different void volume fractions is shown in Fig. 12. Cells with $V_v = 0, 1, 2$ and 5% are chosen under a) uniaxial transverse tension, b) uniaxial transverse compression and c) pure longitudinal shear. Fig. 12 demonstrates the results of the overall composite strength for a cell with respect to five different interfacial toughness: *I*) $W_n^C = 1J/m^2, W_t^C = 2.5J/m^2$, *II*) $W_n^C = 10J/m^2, W_t^C = 25J/m^2$ (the baseline value of Table. 2), *III*) $W_n^C = 20J/m^2, W_t^C = 75J/m^2$, *IV*) $W_n^C = 50J/m^2, W_t^C = 125J/m^2$ and *V*) $W_n^C = 100J/m^2, W_t^C = 250J/m^2$. Both the normal and tangential fracture energies of the interfaces increase such that the ratio $W_t^C/W_n^C = 2.5$ holds for all cases. The results of Fig. 12a and b corresponding to uniaxial transverse tension and compression loading conditions, respectively, show that interfaces with very small interfacial toughness significantly reduce the overall tensile and the compressive strengths of composite. Consequently, the composite strength rises with increase of interfacial toughness until a certain amount of interfacial fracture energy $\sim W_n^C = 50J/m^2, W_t^C = 125J/m^2$ at which the composite strength is not influenced by higher interfacial toughness. This is due to the fact that the strength of the composite mainly controlled by interfacial debonding in the case of very weak interfaces. On the other hand, when the interfaces are not weak enough in comparison with the matrix the overall response of composite is controlled by the matrix deformation which is the case occurring in Fig. 12a and b at high values of W_n^C and W_t^C. However, no effect of interfacial toughness is detected under pure longitudinal shear, see Fig. 12c. This can be explained by the pure tangential debonding along the fibers which is the only interfacial failure mechanism under pure longitudinal shear. In this case tangential interface debonding is prevented due to very strong tangential cohesive stress, $T_t^{max} = 75MPa$, which is chosen to be larger than the ma-

trix ultimate tensile strength, $\sigma_m^{t0} = 50MPa$. It is also worth to notice that the behavior of composite strength versus the interfacial toughness does not change under different void volume fractions. This implies that microvoids can not modify the dominant failure mechanism from interfacial debonding to matrix deformation or vice versa although they may trigger the onset of damage at smaller load carrying capacity. This is discussed in more detail in Fig. 13 and Fig. 14.

Fig. 13 shows the effect of the interface fracture energy on the overall stress-strain and on the contour plots of the accumulated plastic strain of the cell with $V_f = 60\%$ and $V_v = 2\%$. The cell is under combined transverse tension and longitudinal shear with $\Delta_{12}/\Delta_2 = 1$. Simulations are performed with the same cell and three different interface fracture energies: $W_n^C = 1J/m^2, W_t^C = 2.5J/m^2$, $W_n^C = 10J/m^2, W_t^C = 25J/m^2$ and $W_n^C = 100J/m^2, W_t^C = 250J/m^2$. Following the discussion in Fig. 12, comparing Fig. 13b-d shows that interface debonding is the dominant failure mechanism when the interface fracture energy is much smaller than the matrix fracture energy. On the other hand, the localized deformation in the matrix is the first phenomenon when the interface is very strong, Fig. 13d. However, for both mechanisms damage initiates around the trapped voids. Deformations around the cylindrical voids appear when the matrix failure is more dominant, see Fig. 13d. Furthermore, smaller fracture energy with a constant maximum cohesive stress, T_{max}, gives a decrease in the characteristic cohesive lengths, δ_n^c and δ_S^c, leading to more brittle behavior. This brittle behavior can be seen by a sudden stress drop occurring at smaller macroscopic strain without a considerable hardening deformation. As shown in Fig. 13a, very brittle fiber/matrix interfaces with $W_n^C = 1J/m^2, W_t^C = 2.5J/m^2$ significantly reduces the strength of composite. In Fig. 13a, the difference between the ultimate stress in curves with $W_n^C = 10J/m^2, W_t^C = 25J/m^2$ and $W_n^C = 100J/m^2, W_t^C = 250J/m^2$ is small although the stress drop occurs earlier in $W_n^C = 10J/m^2, W_t^C = 25J/m^2$ due to more brittle interfaces.

The effect of different interfacial fracture energies in a cell with $V_f = 60\%$ and $V_v = 2\%$ subjected to combined transverse compression and longitudinal shear with $\Delta_{12}/\Delta_2 = -0.5$ is shown in Fig. 14. Similar to Fig. 13a, the stress-strain curves in Fig. 14a show that a weak fiber/matrix interfaces with $W_n^C = 1J/m^2, W_t^C = 2.5J/m^2$ leads to very brittle response of composite which has very linear stiffness up to failure with very low ultimate stress. Fig. 14b demonstrates corresponding contour plot of the accumulated plastic strain for $W_n^C = 1J/m^2, W_t^C = 2.5J/m^2$. In Fig. 14b the failure

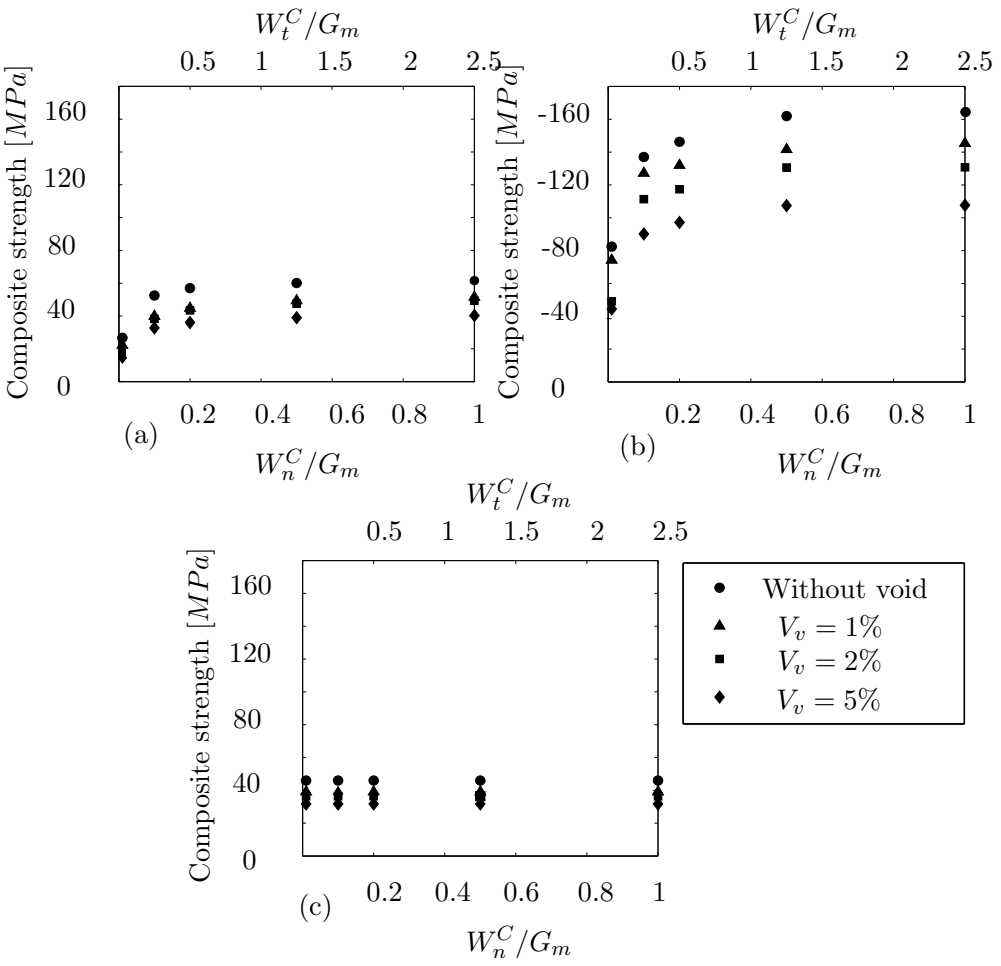

Figure 12: Effect of interfacial fracture energy on the macroscopic strength of UD fiber-reinforced composites under a) pure transverse tension, b) pure transverse compression and c) pure longitudinal shear.

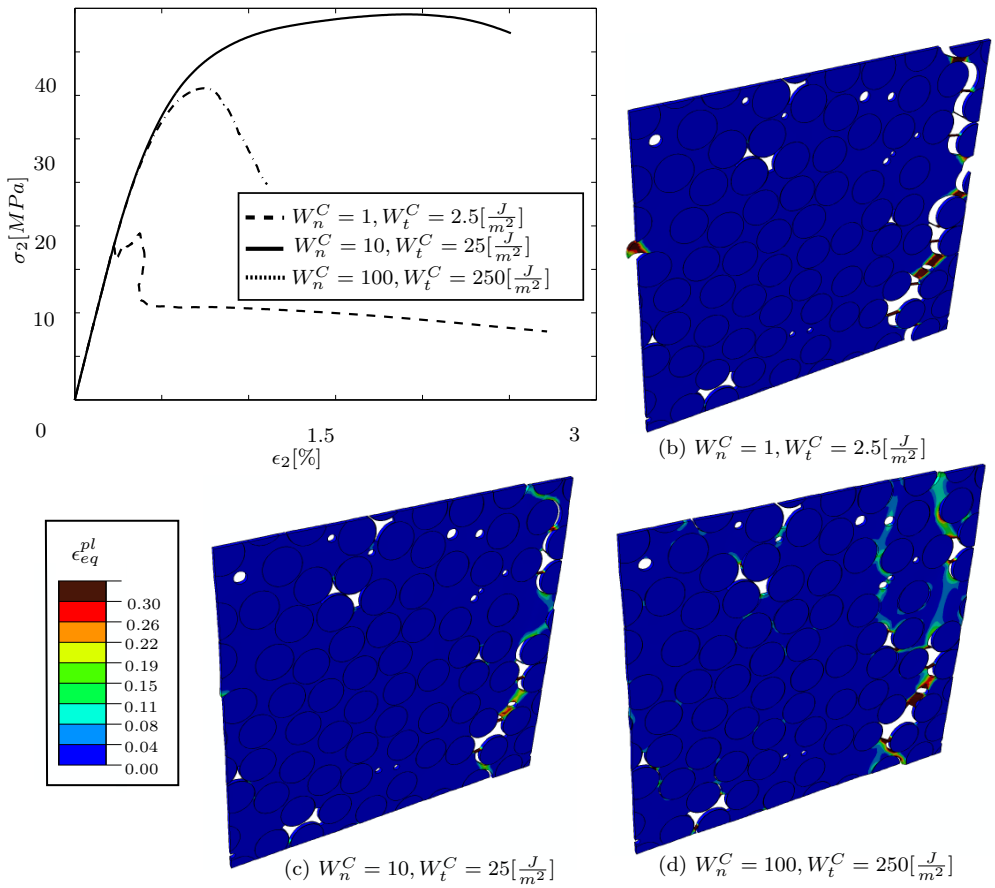

Figure 13: The effect of the interface fracture energy on the mechanical behavior of the cell with $V_f = 60\%$ and $V_v = 2\%$ under combined transverse tension and longitudinal shear with $\Delta_{12}/\Delta_2 = 1$. Contour plots of the accumulated plastic strain are shown at $\epsilon_2 = 1.2\%$ in b) $W_n^C = 1J/m^2, W_t^C = 2.5J/m^2$, c) $W_n^C = 10J/m^2, W_t^C = 25J/m^2$ and d) $W_n^C = 100J/m^2, W_t^C = 250J/m^2$.

is due to interfacial debonding initiating from the trapped voids and after the ultimate stress reaches the subsequent matrix shear band generates along the fracture plane. The overall stress-strain response of the cell with $W_n^C = 10J/m^2, W_t^C = 25J/m^2$ shows more hardening before failure with larger overall strength. This can be explained by the contour plot in Fig. 14c where the failure initiates due to the matrix shear band deformation and subsequently interfacial debonding along the shear band leads to a stress drop on the stress-strain curve. The stress-strain curve of the cell containing very strong interfaces with $W_n^C = 100J/m^2, W_t^C = 250J/m^2$ shows very ductile behavior with a remarkably large nonlinear hardening, see Fig. 14a. This ductile behavior is due to the failure mechanism which is only controlled by the matrix plastic deformation. The interfacial debonding does not contribute in failure due to very large interfacial fracture energy and tangential cohesive stress. Comparing Fig. 14b-d also indicates that cracks always initiate from the trapped voids in all cases. However, deformation of cylindrical voids occurs when the matrix shear band is the dominant failure mechanism.

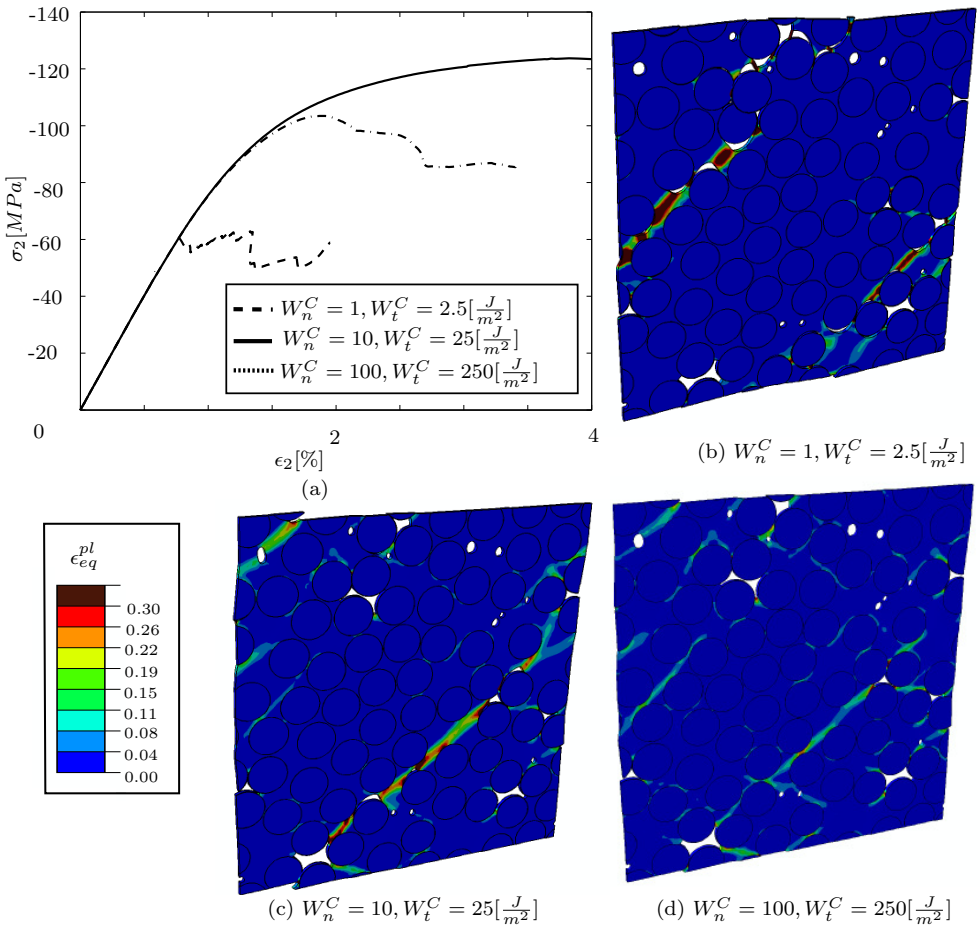

Figure 14: The effect of the interface fracture energy on the mechanical behavior of the cell with $V_f = 60\%$ and $V_v = 2\%$ under combined transverse compression and longitudinal shear with $\Delta_{12}/\Delta_2 = -0.5$. Contour plots of the accumulated plastic strain are shown at $\epsilon_2 = 2\%$ in b) $W_n^C = 1J/m^2, W_t^C = 2.5J/m^2$, c) $W_n^C = 10J/m^2, W_t^C = 25J/m^2$ and d) $W_n^C = 100J/m^2, W_t^C = 250J/m^2$.

7. Conclusion

A computational model was established to study the micromechanical failure mechanisms in UD glass-fiber/epoxy composites. The model includes randomly distribution of fibers and microvoids embedded in the matrix. Two different population of voids were explicitly represented in the microstructure: Inter-fiber voids and circular voids within the matrix. The fibers are

assumed to be isotropic elastic while the matrix behaves isotropically elasto-plastic. The matrix followed the modified Drucker-Prager yield surface proposed by Lubliner (1989) which includes the inherent pressure-dependency of the epoxy resins. Matrix failure, fiber/matrix interfacial debonding and microvoids were the micromechanical imperfections considered in this study.

The results showed that two factors can significantly reduce the macroscopic ultimate strength of composites: Increase of the void volume fraction and decrease of the fiber/matrix interfacial toughness. It was shown that a weak interface remarkably reduced the overall composite strength under dominant transverse tension or transverse compression. It was also found that damage often initiates around the inter-fiber trapped voids while the role of the cylindrical microvoids appears when the matrix deformation is the dominant failure mechanism in comparison with interfacial debonding. In general, stress concentration around the larger voids leads to trigger the onset of damage in lower load-carrying capacities. Deformation of larger microvoids are decisive for crack initiations while the smaller microvoids may influence the path of crack propagation.

This model was also exploited to computationally predict the failure locus of UD composites in the $\sigma_2 - \tau_{12}$ stress space. It was found that the failure envelope of composite is significantly reduced by the presence of voids. The results were compared with the phenomenological model of Puck and Schürmann (2002). This comparison shows that the numerical model can precisely predict different modes of failure due to different loading conditions. The results indicate that the effect of microscale features such as fiber/matrix interfacial debonding and voids are significantly decisive in the macroscopic behavior of composites which are not directly included in the current classical phenomenological failure models. This work indicates that even milder void volume fractions of less than 5% of composites is a crucial parameter that defines the strength of fiber composites.

8. Acknowledgments

The author would like to thank Prof. Bent F. Sørensen and Assoc. Prof. Brian N. Legarth at Technical University of Denmark (DTU) for their ideas, discussions and comments. The support by Prof. Javier Llorca and Dr. Carlos González from IMDEA Materials Institute is also gratefully appreciated. This work was supported by the Danish Council for Strategic Research

(grant no.: 09-067212) under the Danish Center for Composite Structures and Materials for Wind Turbines (DCCSM).

References

Abaqus, 2012. Analysis user's manual, version 6.12. Simulia.

Ashouri Vajari, D., Legarth, B. N. and Niordson, C. F., 2013. Micromechanical modeling of unidirectional composites with uneven interfacial strengths. European Journal of Mechanics - A/Solids 42, 241-250.

Ashouri Vajari, D., González, C., Llorca, J. and Legarth, B. N., 2014. A numerical study of the influence of microvoids in the transverse mechanical response of unidirectional composites. Journal of Composite Science and Technology. (under review)

M. L. Benzeggagh and M. Kenane. Measurement of mixed-mode delamination fracture toughness of unidirectional glass/epoxy composites with mixed-mode bending apparatus. Composites Science and Technology 56, 439-449, 1996.

Canal L.P., González C, Segurado J, Llorca J., 2012. Intraply fracture of fiber-reinforced composites: Microscopic mechanisms and modeling. Compos Sci Technol 72, 1223-1232.

Cheng, L., Guo, T.F., 2007. Void interaction and coalescence in polymeric materials. Int J Solids Struct 44, 1787-1808.

Chew, H.B., Guo, T.F., Cheng, L., 2006. Effects of pressure-sensitivity and plastic dilatancy on void growth and interaction. Int J Solids Struct 43, 6380-6397.

Correa, E., Gamstedt, E.K., París, F., Mantič, V., 2007. Effects of the presence of compression in transverse cyclic loading on fibrematrix debonding in unidirectional composite plies. Composites Part A 38, 2260-2269.

Costa, M.L., Sérgio, F.A., M., Rezende, M.C., 2001. The influence of porosity on the interlaminar shear strength of carbon/epoxy and carbon/bismaleimide fabric laminates. Compos Sci Technol 61, 2101-2108.

Costa ML, Rezende MC, Almeida SFM. Strength of hygrothermally conditioned polymer com- posites with voids. Journal of Composite Materials 2005;39:1943-61.

Fiedler, B., Hojo, M., Ochiai, S., Schulte, K. and Ando., M., 2001. Failure behavior of an epoxy matrix under different kinds of static loading. Composites Science and Technology, 61, 1615-1624.

González, C., Llorca, J., 2007. Mechanical behavior of unidirectional fiber-reinforced polymers under transverse compression: Microscopic mechanisms and modeling. Compos Sci Technol 67, 2795-2806.

González, C., Llorca J., 2007. Numerical simulation of the fracture behavior of Ti/ SiC composites between 20 $^{\circ}C$ and 400 $^{\circ}C$. Metall Mater Trans A 38, 169-79.

Hashin, Z., 1980. Failure criteria for unidirectional fiber composites. J Appl Mech 47, 329334.

Hernández, S., Sket, F., Molina-Aldareguía, J.M., González, C., Llorca, J., 2011. Effect of curing cycle on void distribution and interlaminar shear strength in polymer-matrix composites. Compos Sci Technol 71, 1331-1341.

Hernández, S., Sket, F., González, C., Llorca, J., 2012. Optimization of curing cycle in carbon fiber-reinforced laminates: void distribution and mechanical properties. Compos Sci Technol 85, 73-82.

Hinton, M.J., Soden, P.D., Kaddour, A.S., 2004. Failure criteria in fiber reinforced polymer composites: the world wide failure exercise. Elsevier.

Jeong H. Effects of voids on the mechanical strength and ultrasonic attenuation of laminated composites. J Compos Mater 1997;31:276-292.

Kinloch, A.J., Young, R.J., 1983. Fracture behaviour of polymers. Elsevier Applied Science Publishers.

Lee, J., Fenves, G.L., 1998. Plastic-damage for cyclic loading of concrete structures. J Eng Mech 124, 892-900.

Little, J.E., Yuan, X., Jones, M.I, 2012. Characterisation of voids in fibre reinforced composite materials. NDT & E International 46, 122-127.

Lubliner, J., Oliver J., Oller S, Oñate, E., 1989. A plastic-damage model for concrete. Int J Solids Struct 25, 299-329.

Moraleda, J., Segurado, J., Llorca, J., 2007. Finite deformation of porous elastomers: a computational micromechanics approach. Philos Mag 87, 5607-27.

Olivier P, Cottu JP, Ferret B. Effects of cure cycle pressure and voids on some mechanical properties of carbon/epoxy laminates. Composites 1995;26:509-515.

París, F., Correa, E., Cañas, J., 2003. Micromechanical view of failure of the matrix in fibrous composite materials. Compos Sci Technol 63, 1041-1052.

París, F., Correa, E., Mantič, V., 2007. Kinking of Transversal Interface Cracks Between Fiber and Matrix. J Appl Mech 74, 703-716.

Puck, A., Schürmann, H., 1998. Failure analysis of FRP laminates by means of physically based phenomenological models. Compos Sci Technol 58, 1045-1067.

Puck, A., Schürmann, H., 2002. Failure analysis of FRP laminates by means of physically based phenomenological models. Compos Sci Technol 62, 1633-62.

Quinson, R., Perez, J., Rink, M., Pavan, A., 1997. Yield criteria for amorphous glassy polymers. J Mater Sci 32, 1371-9.

Romanowicz, M., 2012. A numerical approach for predicting the failure locus of fiber reinforced composites under combined transverse compression and axial tension. Comput Mater Sci 51, 7-12.

Sørensen, B.F., Goutianos, S., 2014. Mixed Mode cohesive law with interface dilatation. Mech Mater 70, 76-93.

Thomason, J.L., 1995. The interface region in glass fibre-reinforced epoxy resin composites: 2. Water absorption, voids and the interface. Composites 26, 477-485.

Totry, E., González, C., Llorca, J., 2008. Prediction of the failure locus of C/PEEK composites under transverse compression and longitudinal shear through computational micromechanics. Compos Sci Technol 68, 3128-36.

Totry, E., González, C., Llorca J., 2008. Failure locus of fiber-reinforced composites under transverse compression and out-of-plane shear. Compos Sci Technol 68, 829-839.

Zhang AY, Li DH, Zhang DX, Lu HB, Xiao HY, Jia J. Qualitative separation of the effect of voids on the static mechanical properties of hygrothermally conditioned carbon/epoxy composites. eXPRESS Polymer Letters 2005;5:708-716.

DTU Mechanical Engineering
Section of Solid Mechanics
Technical University of Denmark

Nils Koppels Allé, Bld. 404
DK- 2800 Kgs. Lyngby
Denmark
Phone (+45) 4525 4250
Fax (+45) 4593 1475
www.mek.dtu.dk
ISBN: 978-87-7475-379-7

DCAMM
Danish Center for Applied Mathematics and Mechanics

Nils Koppels Allé, Bld. 404
DK-2800 Kgs. Lyngby
Denmark
Phone (+45) 4525 4250
Fax (+45) 4593 1475
www.dcamm.dk
ISSN: 0903-1685